LUND UNIVERSITY

The Milky Way as seen through Neutron-Capture Elements

Forsberg, Rebecca

2023

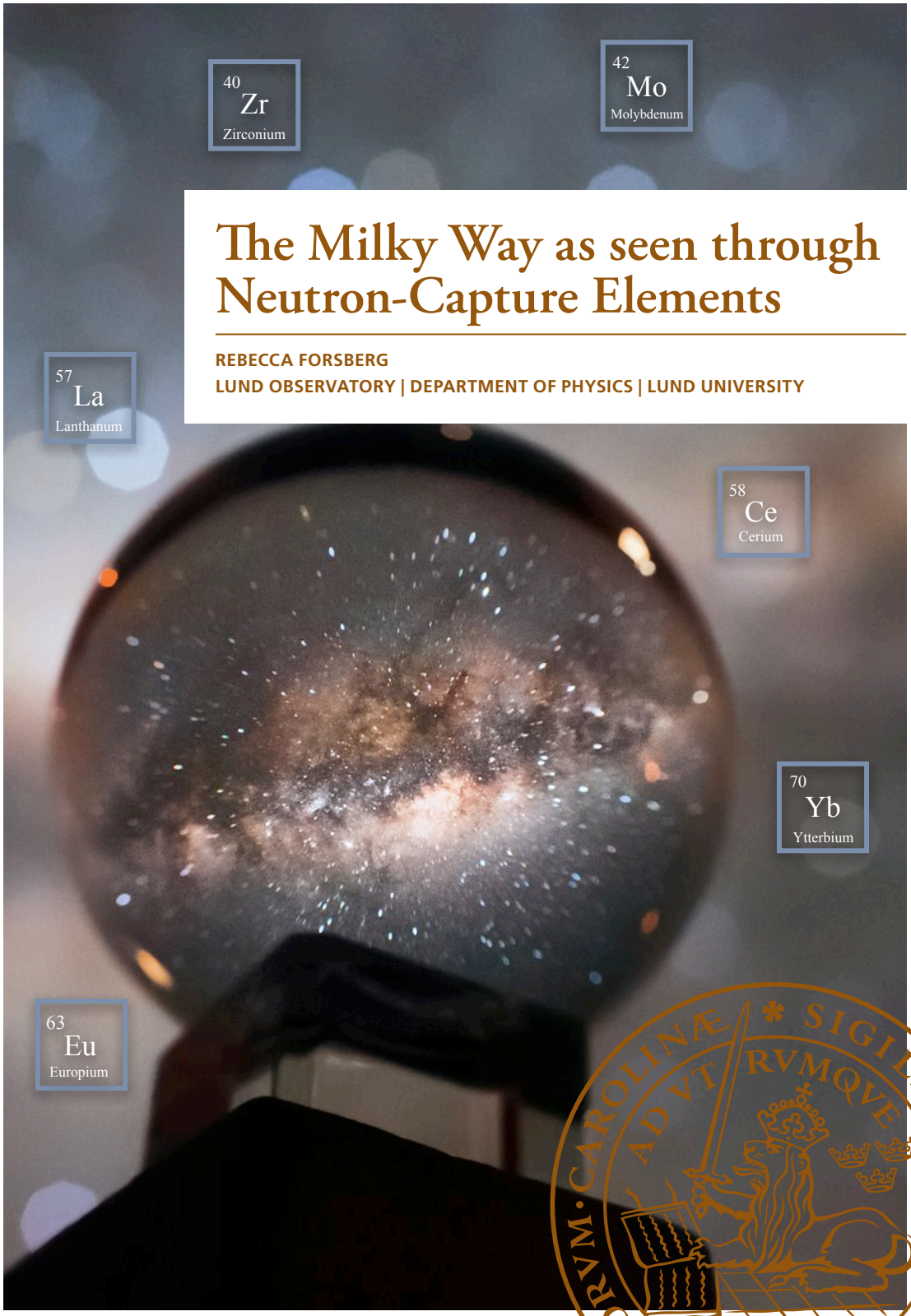

The Milky Way as seen through Neutron-Capture Elements

REBECCA FORSBERG
LUND OBSERVATORY | DEPARTMENT OF PHYSICS | LUND UNIVERSITY

The Milky Way as seen through Neutron-Capture Elements

Rebecca Forsberg

LUND
UNIVERSITY

Thesis for the degree of Doctor of Philosophy

Thesis advisor: Professor Nils Ryde
Co-advisors: Docent Henrik Jönsson, Professor Anders Johansen,
Faculty opponent: Astronome Alejandra Recio-Blanco

To be presented, with the permission of the Faculty of Science of Lund University, for public criticism in the Lundmark lecture hall (Lundmarksalen) at the Division of Astrophysics, Department of Physics on Friday, 3rd of November 2023 at 9:00.

Organization
LUND UNIVERSITY
Lund Observatory, Division of Astrophysics,
Department of Physics
Box 43, SE-221 00, Lund, Sweden

Author(s)
Rebecca Forsberg

Document name
DOCTORAL DISSERTATION

Date of issue
2023-10-10

Sponsoring organization

Title and subtitle
The Milky Way as seen through Neutron-Capture Elements

Abstract
Through stars, the formation and evolution of the Galaxy goes hand-in-hand with the cosmic origin of the elements. As stars form, they carry chemical fingerprints of their birthclouds, providing us with chemical timestamps of the Galaxy.

The detailed history of the Galactic disk and bulge is still to be untagled. The same goes for the origin of elements – where some still have elusive origins. Disentagling the origin of the Galaxy and the elements can only be acchived by continued efforts by combining the most accurate and precise data with the latest state-of-the art theoretical models.

In this thesis, I present high-precision chemical abundances of red giant stars in the Galactic disk and bulge, obtained by careful analysis of high-resolution optical and infrared spectra. Using red giant stars in the bulge and disk populations allows for an unique differential comparison of the two Galactic components. I focus the analysis to obtain abundances of neutron-capture elements, which can shed new light on the origin of the Galactic components.

The abundance trends of the Galactic bulge show great similarities with the Galactic (thick) disk, pointing at a similar history. However, there are possible enrichements in both lanthanum and molybdenum, which require further follow-up studies to confirm. I identify a chemically-peculiar star in the bulge, standing out by its high abundances of europium and molybenum.

Finally, I demonstrate the need for high-resolution and spectra in order to access abundances of neutron-capture elements in the infrared. Including heavy elements is essential in getting the full chemical view of the Galaxy, which is shown in this thesis.

Key words
Chemical abundances; Galactic archaeology; Galactic chemical evolution; Galactic bulge; Galactic disk; heavy elements; chemically peculiar star

Supplementary bibliographical information

Language
English

ISSN and key title

ISBN
ISBN: 978-91-8039-715-5 (print)
ISBN: 978-91-8039-714-8 (pdf)

Number of pages: 151

Price

Security classification

The Milky Way as seen through Neutron-Capture Elements

Rebecca Forsberg

LUND
UNIVERSITY

Faculty Opponent

Astronome Alejandra Recio-Blanco
UMR Lagrange, L'Observatoire de la Côte d'Azur,
Nice, France

Evaluation Committee

Professor Tamara Mishenina
Astronomical Observatory, Odessa National University
Odessa, Ukraine

Professor Birgitta Nordström
Niels Bohr Institute, Copenhagen University,
Copenhagen, Denmark

Professor Dirk Rudolph
Department of Physics, Lund University,
Lund, Sweden

Cover: Photograph of the Milky Way through a crystal ball, captured by Juan Carlos Muñoz-Mateos at ESO's sites in Paranal, Chile. I have added the neutron-capture elements studied in this thesis to the image. Credit: Juan Carlos Muñoz-Mateos/ESO
Funding information: This thesis work is financially supported by the Göran Gustafsson Fundation for Research in Natural Sciences and Medicine and the Royal Physiographic Society of Lund through the Stiftelsen Walter Gyllenbergs fond and Märta och Erik Holmbergs donation.

Faculty of Science, Department of Physics

ISBN: 978-91-8039-715-5 (print)
ISBN: 978-91-8039-714-8 (pdf)

Printed in Sweden by Media-Tryck, Lund University, Lund 2023

Media-Tryck is a Nordic Swan Ecolabel certified provider of printed material. Read more about our environmental work at www.mediatryck.lu.se

MADE IN SWEDEN

Dedicated to me, for my endless curiosity

Contents

List of publications

This thesis is based on the following peer-reviewed publications:

I **Abundances of disk and bulge giants from high-resolution optical spectra IV. Zr, La, Ce, Eu**
R. Forsberg, H. Jönsson, N. Ryde, and F. Matteucci (2019)
Astronomy & Astrophysics, Volume 631, id.A113

II **Abundances of disk and bulge giants from high-resolution optical spectra V. Molybdenum: The p-process element**
R. Forsberg, N. Ryde, H. Jönsson, R. M. Rich, and A. Johansen (2022)
Astronomy & Astrophysics, Volume 666, id.A125

III **First r-process enhanced star confirmed as a member of the Galactic bulge**
R. Forsberg, R. M. Rich, N. Nieuwmunster, H. Jönsson, M. Schultheis, N. Ryde, and B. Thorsbro (2023)
Astronomy & Astrophysics, Volume 669, id.A17

IV **Chemical evolution of ytterbium in the Galactic disk**
M. Montelius, **R. Forsberg**, N. Ryde , H. Jönsson, M. Afşar, A. Johansen, K. F. Kaplan, H. Kim, G. Mace, C. Sneden, and B. Thorsbro (2022)
Astronomy & Astrophysics, Volume 665, id.A135

Work not included in the thesis

Peer-reviewed publications not included in this thesis:

I **Stellar abundance of binary stars: their role in determining the formation location of super-Earths and ice giants**
B. Bitsch, **R. Forsberg**, F. Liu, and A. Johansen (2018)
Monthly Notices of the Royal Astronomical Society, Volume 479, Issue 3

II **Modelling the chemical evolution of Zr, La, Ce, and Eu in the Galactic discs and bulge**
V. Grisoni, G. Cescutti, F. Matteucci, **R. Forsberg**, H. Jönsson, and N. Ryde (2020)
Monthly Notices of the Royal Astronomical Society, Volume 492, Issue 2

III **Fluorine in the Solar Neighborhood: The Need for Several Cosmic Sources**
N. Ryde, H. Jönsson, G. Mace, Katia Cunha, E. Spitoni, M. Afşar, D. Jaffe, **R. Forsberg**, K.F. Kaplan, Benjamin T. Kidder, J. Lee, H. Oh, V.V. Smith, C. Sneden, K.R. Sokal, E. Strickland, and B. Thorsbro (2020)
The Astrophysical Journal, Volume 893, Issue 1, id.37, 12 pp.

IV **The Mantis Network IV: Expanding the limits of chemical searches within ultra hot-Jupiters – New detections of Ca I, V I, Cr I, Ni I, Sr II, Ba II, and Tb II in KELT-9 b**
N.W. Borsato, H.J. Hoeijmakers, B. Prinoth, B. Thorsbro, **R. Forsberg**, D. Kitzmann, K. Jones, and K. Heng (2023)
Astronomy & Astrophysics, Volume 673, id.A158

V **A Wide Metallicity Range for Gyr-old Stars in the Nuclear Star Cluster**
B. Thorsbro, **R. Forsberg**, G. Kordopatis, A. Mastrobuono-Battisti, R.P. Church, M. Rich, N. Ryde, M. Schultheis, and S. Nishiyama
Submitted

Notable outreach work

- Founder and host of the Lund Observatory podcast, *the Meridian*.
- Science reporter for Sweden's leading magazine for popularising astronomy and space research, *Populär Astronomi*, including a feature article on the Gaia space telescope.
- Science reporter for Sweden's oldest student magazine *Lundagård*, including live-reporting from the announcement of the 2021 Nobel Price in Physics.
- Science Communication Internship at the European Southern Observatory (ESO), 6 months in 2022 at ESO headquarters in Germany.
- Multiple instances of communicating astronomy to the general public through participation on local radio and news outlets, and through public speaking, including giving the invited talk at the Värmland Starparty 30 years jubilee.

”Be humble, for you are made of earth.
Be noble, for you are made of stars.”

Serbian proverb

Popular summary

How do we study the galaxy where we live? It is a bit like being asked to draw a map of the city you live in, without being able to leave your house. You might be able to peer through the windows and see some features like streets and tall buildings, but most will be hidden by nearby houses.

Imagine that you also have to figure out how your city used to look like before your time, and when and how it was formed – just by looking out of your windows. Astronomers face this challenge when we want to map our home galaxy, the Milky Way. We sit within the Milky Way, and as we look up in the sky we see the hazy stellar band of our Galaxy, and clouds of dust obscuring its inner parts.

In this thesis I do not draw a map of the Milky Way, rather I contribute details of what its disk and central parts look and have looked like, from a chemical point of view. The lightest elements: hydrogen, helium, and lithium, were created in the Big Bang, but the rest – the ones that constitute our bodies and everything around us – have been created in stars and via processes involving stars. By studying the composition of stars, we can open up a window on to the history of the Galaxy.

When lighter elements merge into heavier ones, energy is released – a process called fusion that takes places in the interior of stars. For the heaviest stars, which have higher pressures and temperatures, fusion continues until energy is no longer released, which occurs when the entire core of the star consists of iron, and the lighter elements have been used up.

In order to create elements heavier than iron, a process called neutron capture must take place. In this process, neutrons are captured by atomic nuclei, which in turn can decay to heavy elements. We call these neutron-capture elements, and they are suggested to be formed, for instance, in the final stages of low-mass stars, in supernovae and in mergers of neutron stars. We are still not entirely sure of all the cosmic processes that lie behind their origin, and by studying the neutron-capture elements in stars, we can also obtain clues to the origin of the Milky Way.

Stars consist of recycled stellar material, with each new generation of stars containing increasing concentrations of heavier elements. This makes them chemical fossils, or time capsules, from earlier epochs of the Galaxy. The Milky Way consists of hundreds of billions of stars, most of which sits in the disk and in the central part of the Galaxy: we call the latter "the bulge". When we study the composition of stars of different ages, we get clues about what the Milky Way looked like chemically when the stars were formed. This gives us an insight into what chemical processes were active and how the Milky Way has evolved over time.

How the bulge formed is one of the unanswered questions in Milky Way research. Whether it formed first or at the same time as the disk, or whether it emerged later out of the disk, is still uncertain. Our Solar system is in the disk, so this is a bit, to revert to the analogy at the beginning, like trying to study the centre of your city while you live in the suburbs.

To study the bulge of the Milky Way, we use red giant stars. These are very bright and can be observed from a great distance. We collect spectroscopic data from stars located in both the disk (to serve as comparison sample) and in the bulge to determine their chemical composition. The light of the stars is like a fingerprint that reveals which elements they are composed of.

As the chemical analysis of red giant stars is complex, the major part of this thesis has been devoted to carefully overcoming these difficulties and developing a method that can be used in future research studies.

Using this method, I determine the abundance of six neutron-capture elements in stars in the disk and bulge. I observe a chemical agreement between the two components, indicating that they have a strong shared history and origin.

Despite this agreement, there are interesting features in one of the elements, molybdenum – an element whose origin is still not fully understood. It is also one of the less-studied elements in the bulge of the Milky Way. Through my research, I have contributed to one of the clearest and most precise pictures of molybdenum in the Milky Way, which will facilitate comparisons with models and form a basis for continued observational studies – both to understand the origins of the Milky Way and of molybdenum itself.

I also identify a chemically peculiar star in the bulge, which exhibits high levels of molybdenum and europium. Stars with similar chemistry have been found in the outer parts of the Milky Way, but never before with such high confidence in the bulge. The star's chemistry suggests that the bulge may have had episodes of intense star formation.

Finally, U also demonstrate the power of using high-resolution spectroscopic data to study neutron-capture elements in the infrared. Infrared light allows us to see through the dust in the disk and to study the bulge in even greater detail (a bit like mapping your city with X-ray vision), which is highly relevant for future surveys of our Galaxy.

In my thesis I study our home galaxy, the Milky Way, with very high precision and with greater detail than before. I provide a unique insight into the history of the Milky Way, showing that its various components most likely have a common origin, but that much still remains to be discovered.

Populärvetenskaplig sammanfattning

Hur studerar vi galaxen där vi bor? Det är som att försöka rita en karta över staden du bor i, utan att kunna lämna ditt hus. Du kan titta ut genom fönstren och se vissa gator och höga byggnader, men mycket av staden kommer att döljas av dina väggar och närliggande hus.

Tänk att du i sin tur ska lista ut hur staden har sett ut bakåt i tiden och hur den har bildats – bara genom att kolla ut genom fönstret. Detta är samma utmaning som astronomer har när vi vill kartlägga vår hemgalax Vintergatan. Vi befinner oss i Vintergatans skiva, och när vi tittar upp mot himlen ser vi det disiga stjärnbandet av vår hemgalax och stoftet som skymmer dess inre delar.

I denna avhandling ritar jag inte en detaljerad karta av Vintergatan, men bidrar med detaljer om hur dess skiva och centrala delar ser ut och har sett ut, från en kemisk synvinkel. De enklaste grundämnena, väte, helium och litium, skapades i Big Bang, men resten av grundämnena, de som bygger upp oss, har bildats i stjärnor och processer som involverar stjärnor. Genom att studera grundämnen i stjärnor, kan vi öppna ytterligare ett fönster till Vintergatans historia.

Inuti stjärnor pågår fusion, sammanslagning av lättare grundämnen till tyngre, en process som frigör energi. För dem tyngsta stjärnorna, som har högre tryck och temperaturer, pågår fusion tills dess att energi inte längre frigörs, vilket sker när hela stjärnans mitt består av järn.

För att kunna skapa tyngre ämnen än järn, måste en process som kallas neutroninfångning ske – de bildas då när neutroner tränger in i atomkärnor som i sin tur sönderfaller till tyngre ämnen. Vi kallar dessa för neutroninfångningsämnen och de bildas bland annat i slutstadiet av lätta stjärnor, i supernovor samt vid kollisioner av neutronstjärnor. Men vi är fortfarande inte helt säkra på vilka alla kosmiska processer som ligger bakom deras ursprung. Genom att studera neutroninfångningsämnen kan vi få unika ledtrådar till både deras och Vintergatans historia.

Stjärnor består av återanvänt stjärnmaterial, där varje ny generation av stjärnor innehåller tyngre grundämnen. Detta gör dem till kemiska fossiler, eller tidskapslar, från den urtida galaxen. Vintergatan består av några hundra miljarder stjärnor, där de flesta finns i skivan och den centrala delen. När vi studerar innehållet hos stjärnor av olika åldrar får vi ledtrådar om hur Vintergatan såg ut kemiskt när stjärnorna skapades. Detta låter oss tolka vilka kemiska processer som var aktiva och hur Vintergatan har utvecklats över tid.

En av de stora obesvarade frågorna inom Vintergatsforskning är hur galaxens centrala del bildades: om den bildades först eller samtidigt som skivan, eller om

den bildades senare ur skivan. Vårt solsystem finns i skivan, så detta är lite som, för att knyta an till analogin i början, att försöka studera centrumet i din stad medan du är fast i en förort.

För att studera Vintergatans centrala del använder vi oss av röda jättestjärnor. Dessa är väldigt ljusstarka och kan observeras på långt avstånd. Vi samlar in spektroskopisk data från stjärnor som befinner sig i skivan och i den centrala delen för att kunna bestämma deras kemiska innehåll. Stjärnornas ljus är nämligen som ett fingeravtryck som avslöjar vilka ämnen de består av.

Då analysen av röda jättestjärnors fingeravtryck är komplex har den största delen av denna avhandling ägnats åt att noggrant överkomma dessa svårigheter och utveckla en fungerande metod som kan användas i framtida forskningstudier.

Genom denna metod bestämmer jag halten av sex stycken neutroninfångningsämnen hos stjärnor i skivan och centrala delen. Jag presenterar en stor kemisk överensstämmelse mellan de två komponenterna, över alla tidsepoker som datan täcker in. Detta indikerar att de har ett starkt gemensamt förflutet.

Trots detta finns det intressanta drag i ett av grundämnena, molybden, som skulle kunna bära ytterligare information om Vintergatans historia. Molybden är nämligen ett ämne vars ursprung fortfarande är okänt. Det är även en av dem mindre studerade ämnena i Vintergatans centrala del. Genom min forskning bidrar jag till den tydligaste och mest precisa bilden av molybden i Vintergatan, vilket kommer underlätta jämförelser med modeller och fortsatta observationella studier – både för att förstå Vintergatans och molybdens ursprung.

Jag identifierar även en kemiskt annorlunda stjärna i den centrala delen, som uppvisar höga halter av molybden och europium. Stjärnor med liknande kemi har påträffats i dem yttre delarna av Vintergatan, men aldrig tidigare med såhär pass hög säkerhet i dess centrala del. Stjärnans kemi antyder att den centrala delen kan ha haft episoder av intensiv stjärnbildning.

Slutligen visar jag också på styrkan av att använda högupplöst spektroskopisk data för att noggrant studera neutroninfångningsämnen i infrarött ljus. Infrafött ljus låter oss se igenom stoft i Vintergatans skiva och studera centrala delen i ännu högre detalj (lite som att kartlägga din stad med röntgensyn), vilket är högaktuellt för framtida kartläggningar.

I min avhandling studerar jag vår stad, vår hemgalax, med mycket hög precision och med större detaljrikedom än tidigare. Genom att studera grundämnen med komplexa ursprung ger jag en unik inblick i Vintergatans historia, som visar på att dess olika komponenter troligtvis har ett gemensamt ursprung, men att det fortfarande finns mycket kvar att lära.

Acknowledgements

To even begin acknowledging all of the people who made this thesis possible seems harder than writing the thesis itself. Many people have contributed along the way, many more than I probably can list here. To everyone — thank you.

Thank you Nils, for seeing me, for taking me under your wings, and for always supporting and believing in me. Thank you for letting dive into nerdy topics (what is the p-process, anyway?) and for bringing out the best of the scientists in me.

Thank you Henrik; from the very beginning you made me feel like a colleague and you have always been a keen listener and helped whenever I needed it. Thank you for bringing me along to the NOT, and for letting me be part of your exciting projects in studying the Galaxy.

Thank you Anders, for valuable discussions about molybdenum (hell of an element?), and for providing support and resources when I needed it the most.

Thanks goes to all current and previous members of the ISA group, Brian, Erik, Emelie, Govind, Martin, Maria, Niels, Ivalu, Jess, for alongside me, learning, as well as teaching me about the beautiful art that is stellar spectroscopy.

Special thanks goes to everyone who helped proof read and give very helpful comments to the manuscript of this thesis, including Nils, Henrik, Brian, Colin, Santi, Bibi and Martin (glad to know some people have struggled to the end!).

To everyone at Lund Observatory who has made my days brighter and cleared the skies on even the cloudiest of November days. Thank you Ross for teaching me about the beauty of stars. Thank you Alvaro, Oscar, Florent, Eric and Santi for teaching me about galaxy formation and the dark magic (brr...) of galactic simulations. To Paul for patiently answering my endless questions about Gaia and potentials (and especially for the shared love of James Acaster). Thank you to Bibi, Madeleine, Santi, Simon, Michal, Lucian, and many many more for karaoke, board games, and mental health circles to keep the spirits up.

Thank you Colin for being a, may I say, substitute grandfather here in the windy south. For keeping your door open, for all support, well wishes, and for help with English, gardening and how to boil perfect rice.

Thank you Eva for all the help with the labyrinth that is university administration, for keeping your door open and always doing your very best to help.

To my office mates, Linn and Nic, thank you for keeping up with me always interrupting with silly questions and running in-and-out of the office (sorry!). Nic, you will always be my number 1 podcast partner, and *the Meridian* is one of the fondest treasures from my time at the observatory. Thank you Anna for making the podcast happen, and for your support with everything outreach related.

Speaking of outreach, thank you Juan Carlos and everyone at ESO communications for welcoming me into your group. You made me feel valued, competent, knowledgeable and confident in a way that made the last year of my PhD easier to push through. The stay with you, and all the friends I made at ESO, will always be one of the fondest memories in my life.

The same goes to my editors: Robert, Katrin, Alexandra, Viktor, and Theo. Populär Astronomi and Lundagård not only gave me a broader view of science and how to communicate it, but has been the main contributor in setting out the path in my life to come. Thank you for your energy and support – I will always cherish having being part of your team of writers.

Thanks goes to all my friends I have made during my time in Lund, both through studies, involvement in student organisations, and other friends. Especially to Daniel, for listening to all of the whining and ranting on even then rainiest of Tuesday runs, and for providing endless support.

Thank you to my scientific collaborators outside of Lund Observatory who has shared their knowledge with me. Special thanks goes to Mike and Mathias, for help with making the third paper become real, and for many interesting talks over bottles of wine.

Tack till min familj och min utökade familj. Tack mamma för att du alltid lyssnar, alltid stöttar, alltid finns här för mig. Tack Viking för din snällhet och för att du alltid bara är ett sms bort. Tack pappa för att du svarade på alla tusentals frågor den där nyfikna sjuåringen hade om, ja, exakt allt? Ert stöd har varit ovärderligt.

Deepest of thanks to Johan, the sunshine of my life. I could not have done this without you.

Lastly, I'd like to thank a seven-year old version of me, who inhaled everything astronomy, physics and maths from the minute she learnt that astronomers had determined that the Milky Way "consists of *at least* 200 billion stars". A staggering number, larger than a seven-year old probably could comprehend. But I could grasp the concept of the Milky Way, our home, and more so — that there are people who spend their day studying it. Thank you me for staying curious.

With this, there is nothing more to say than that producing this thesis has pushed me in way I could not have imagined, there has been many up and downs, and, as James Acaster so brilliantly put it,

"Started making it.
Had a breakdown.
Bon Appetit!"

Historical Preface

The Milky Way is one galaxy among many, but this has only been accepted knowledge for less than a hundred years. Although both Wright (1750) and Kant (1755) described a galaxy to be an isolated collection of stars (an *Island Universe*), the question still remained if the spiral-shaped "nebulae" (Latin for clouds), as observed by Caroline and William Herschel and Charles Messier in the late 1700s (Messier, 1781; Herschel, 1786), were components of the Milky Way, or their own Island Universes. With the advancements of astrophysical observations of nebulae a paradigm-shifting discussion took place that would change the view of our place in the Universe for good.

In the early 1900s, Harlow Shapley measured the distribution of globular clusters – old, massive collections of stars – in the Milky Way. He found them to be in a spherical arrangement around what he correctly assumed to be the centre of the Galaxy. This allowed him to estimate the physical size of the Milky Way to be a staggering 300 000 light years, or 90 kpc, in diameter. Today we know that the luminous disk of the Milky Way is closer to 30-35 kpc in diameter, but the magnitude of its size made him conclude that *"it appears unlikely that spiral nebulae can be considered separate galaxies of stars"* (Shapley, 1918).

Around the same time, Heber Curtis in the US and Knut Lundmark in Sweden, were taking a closer look at the spiral-shaped "Andromeda nebula" – the largest of all known nebulae. Curtis measured the optical spectrum of Andromeda, arguing for its resemblance to the Milky Way, leading to his conclusion that there in fact existed galaxies outside of our own. Lundmark, inspired by earlier work by Curtis on distance measurements using novae, took this method as a starting point to determine the distance to Andromeda. Lundmark devoted most of his doctoral thesis to the method itself and, using data from four novae in Andromeda, he calculated the distance to be 650 000 light years, or 200 kpc (Lundmark, 1920). Even though this only was about a quarter of the modern determined distance of around 780 kpc, it placed Andromeda well outside of the Milky Way.

These coeval discoveries led to the pivotal discussion among astronomers, especially Shapley and Curtis, regarding the status of Andromeda as a separate galaxy or as a nebulous cloud within the Milky Way. This discussion, called *"the Great Debate"* (Shapley & Curtis, 1921), took place in 1920 a the Smithsonian Museum of Natural History, in Washington, D.C., United States. Shapley argued that nothing could be as large as the Milky Way, but even so, the debate was settled in Curtis's and Lundmark's favour when, a few years later, Edwin Hubble measured the distance to stars in Andromeda, putting them 10 times further away than the most distant stars in the Milky Way (Hubble, 1929). This marked the beginning of a new era in astronomy, recognising that the observable size of the Universe was much bigger than previously thought, and that the Milky Way was a galaxy within the Universe.

As such, Lundmark's thesis, presented in 1920 at Uppsala University in Sweden, deals with nothing less than modern astronomical history and contributed to a paradigm shift of an almost Copernican style. His mark on astronomical history spans from the discovery of dark matter (Lundmark, 1930; Günter, 2015) and the expansion of the universe (Lundmark, 1924), to *the Great Debate* and the commissioning of the Lund Milky Way Panorama (see Figure 1), to foster a new generation of modern astronomers. As a professor at Lund Observatory, Lundmark supervised the astronomer Erik Holmberg, who undertook pioneering galactic work, conducting some of the very first galaxy simulations using a set of light bulbs as proxy for gravitation (Holmberg, 1941).

Erik Holmberg in turn supervised Bengt Gustafsson, astronomer at Uppsala University whose models of stellar atmospheres are still being used today (indeed, in the studies presented in this very thesis). He brought his knowledge on to Kjell Eriksson and in turn Nils Ryde, stellar spectroscopist who has been investigating the formation and evolution of the Milky Way, especially its central parts, using the chemical abundances of stars. For the past few years, Nils Ryde has been supervising me in the arts of stellar spectroscopy and Galactic archaeology, and so what started with Lundmark has now landed here, with me.

It is a honour that I have been handed the torch of Lundmark, in exploring our place in the Universe and our home galaxy, and it is with pride that I will defend this thesis in the lecture hall named after Knut Lundmark at Lund Observatory.

Rebecca Forsberg
Lund University

Nils Ryde
Uppsala University

Kjell Eriksson
Uppsala University

Bengt Gustafsson
Uppsala University

Erik Holmberg
Lund University

Knut Lundmark
Uppsala University

Östen Bergstrand
Uppsala University

Nils Dunér
Uppsala University

D M Axel Möller
Lund University

J Mortimer Agardh
Lund University

Carl Adolf Agardh
Lund University

Olof Peter Swartz
Academy of Sciences, Stockholm

Carl von Linné
Uppsala University

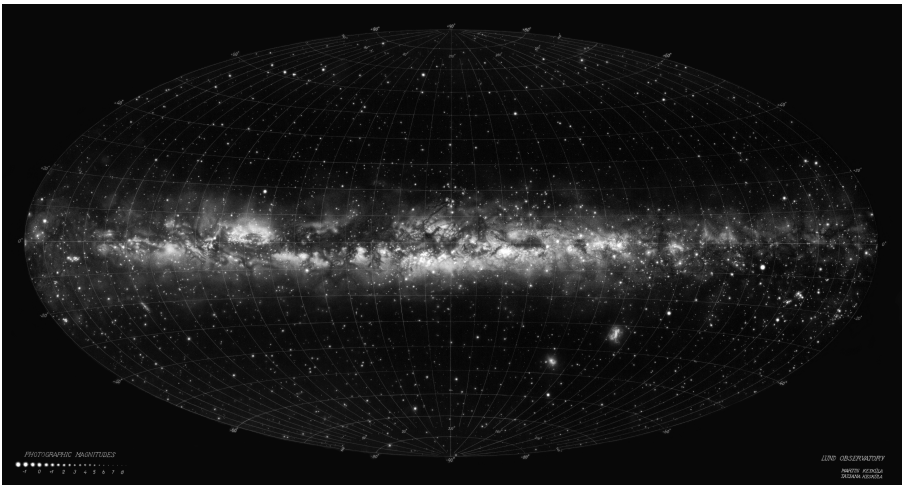

Figure 1: Early 1950s, Knut Lundmark commissioned Martin and Tatjana Kesküla to paint a map of our galaxy, known as the Lund Panorama of the Milky Way. By hand, they added the positions of about 7000 individual stars, with their to-scale magnitudes, to create an, at the time, unprecedented drawing of the Milky Way. The 2-by-1-metre map took two years to paint and can still be seen at Lund Observatory, Sweden. *Reproduced with permission from Lund Observatory.*

Part I

Research context

Summary of Scientific Publications

My thesis concerns the chemical evolution of the Milky Way, focusing on two of its main stellar components: the Galactic disk and bulge. I study the evolution of these by considering the abundance of neutron-capture elements in red giant stars in these stellar components.

To that end, this thesis includes a differential comparison of the disk and bulge populations, examples of how to obtain high-precision abundances in red giant stars, and provides an extensive view of the neutron-capture elements in the disk and bulge. The research content of this thesis consists of four papers, summarised below.

Paper I: *Abundances of disk and bulge giants from high-resolution optical spectra IV. Zr, La, Ce, Eu*
We determine the abundances of the neutron-capture elements Zr, La, Ce and Eu in two stellar samples: a bulge sample of 45 red giant stars and a disk sample of 291 red giant stars. The spectra are obtained with the optical high-resolution spectrographs UVES and FIES, respectively. We determine the abundances using synthetic spectra produced with the tool Spectroscopy Made Easy (SME). In order to use SME, we identify usable spectral lines and continuum points in the stellar spectra. We find that i) the giant stars can produce reliable chemical abundances, comparable with previous studies of dwarf stars and that ii) the bulge abundance trends follow closely those of the thick disk abundance trends, pointing at a similar origin of these two stellar components.

Paper II: *Abundances of disk and bulge giants from high-resolution optical spectra V. Molybdenum: The p-process element*
We determine the abundance of the element molybdenum (Mo) in the two stellar samples presented in Paper I, using the same methodology to analyse the stellar spectra. Molybdenum has a complex nucleosynthetic origin, making it particularly interesting to study. In this paper we present – as far as we are aware – one of the first abundance trends of Mo in the bulge. We find that the Mo-abundance trends in the disk and bulge look like a mixture between an s- and r-process element, which is expected from the theory of the cosmic origin of this element. Additionally, we find a possible enrichment in [Mo/Fe] in the bulge, as compared to the disk, which would be intriguing for the origin of both Mo and the bulge if confirmed in future measurements.

Paper III: *First r-process enhanced star confirmed as a member of the Galactic bulge*
In this paper we present the chemically peculiar bulge star 2MASS-J18082459-2548444. From Paper I and Paper II, we discover that this star was high in both [Eu/Fe] and [Mo/Fe], whilst having nominal bulge abundances in other elements. We confirm its bulge membership by considering its distance and orbital parameters, using Gaia kinematics and `galpy`. In this paper we also consider the bulge membership of a previously proposed, r-process enriched, bulge star – placing it outside of the bulge.

Paper IV: *Chemical Evolution of Ytterbium in the Galactic Disk*
We present Yb abundances for a sample of 30 local disk red giant stars, determined from high-resolution, high signal-to-noise, infrared spectra in the H-band. Whilst Paper I, II and III we present abundances obtained from spectra in the optical wavelength regime, in Paper IV we consider infrared spectra obtained with the IGRINS spectrograph. We find that with a careful and detailed analysis of high-resolution spectra, adequate infrared Yb abundances can be determined. This is promising for the future since it opens up the r-process channel in the infrared.

Note that parts of this thesis will have similarities to and be based upon the licentiate thesis of Forsberg (2021) and of the papers included in this thesis.

Chapter 1

The Milky Way

Our Galaxy itself contains a hundred billion stars,
It's a hundred thousand light years side to side,
It bulges in the middle, sixteen thousand light years thick,
But out by us, it's just three thousand light years wide,
We're thirty thousand light years from Galactic central point,
We go 'round every two hundred million years,
And our Galaxy is only one of millions of billions,
In this amazing and expanding universe,

– Monty Python, The Galaxy Song

The formation and evolution of galaxies is one of the main topics of research in the field of astrophysics. In that pursuit the Milky Way plays a crucial role, not only because it is the galaxy that we live in, but because it is the galaxy that we can study in the most detail. However, studying a galaxy that we sit within is not without its difficulties, and mapping out the large scale structures of the Galaxy is not trivial. Nonetheless, studying the Milky Way in the pursuit of understanding how its different components come to be and how they relate to each other, can help us to understand galaxies at large.

From observational studies, the Milky Way is in general accepted to be a barred spiral galaxy consisting of several stellar components, or *stellar populations*, commonly talked about as the halo, the disk and the central region known as the bulge[1]. This thesis focuses on the latter two components – the disk and the bulge – since these are the most stellar-rich parts of the Galaxy (and as such, the halo will not be discussed to the same extent).

[1] Throughout this thesis, for readability, the *disk, halo* and *bulge* refers to the Milky Way components, even though they are spelt with lower case letters.

Thanks to the proximity, individual stars of the Milky Way can be resolved and observed individually. Spectroscopic studies of the stellar light, in combination with theory and models, enable for intricate studies of stars, allowing us to determine many of their properties, such as the temperature, and – most notably for this work – their chemical composition.

The very lightest elements, hydrogen, helium and trace amounts of lithium and beryllium, were synthesised shortly after the Big Bang. All heavier species beyond these have been, and still are, created by different processes involving stars at different stages of their lives. This includes the interior of stars, the environments linked to their death, and the collision and mergers of stars and their final stages.

The observation of different chemical species, such as atoms and molecules, are a consequence of, and hence a witness to, the existence of these nucleosynthetic processes. Which process is the cause of the formation of different elements is dependent on several factors, most notably the mass of the star and whether or not the star is part of a binary star system (Prialnik, 2000). As stars end their lives, the elements they have synthesised become part of the material that will form new stars. This is the cosmic cycle, where star material is being re-used and, in a way, upgraded to heavier elements with each generation of stars. This makes stars key to the field of Galactic and Universal exploration, since they carry an imprint of the interstellar medium (ISM) from the time at which they were formed. This in turn means that their elemental composition is a timestamp of the elemental composition of that part of the Galaxy at that time – rendering stars fossils of the Galaxy as it has evolved – a trait that has given birth to the field of Galactic archaeology.[2]

Galactic archaeology makes the assumption that the stellar photosphere remains relatively unchanged during the life of the star (e.g. Jofré et al., 2019). Thus, observing the photospheres of stars with spectroscopy and determining their chemical compositions using abundance analysis allows for observations of the evolution of the Galactic ISM as it was. Such abundances can be compared with Galactic chemical evolution models in order to draw conclusions on the characteristics of the processes involved in the evolution of the Galaxy, such as time scales and relative importance of different nucleosynthetic channels.

[2]I want to mention that there is a debate on the naming of the field. Archaeology is defined as the scientific study of human-made artefacts and structures to learn about people and cultures, whereas palaeontology is the scientific study of fossils to learn about the pre-historic, non-human, life on Earth. As such, Galactic palaeontology would be a better suited name, but as with many nomenclatures in astronomy, they are not always the most logical and tend to stick once given. In this thesis, I will use the "Galactic archaeology" when refering to this field.

There are several important ingredients to include when producing Galactic chemical evolution models. The star formation rate (SFR) and the mass distribution of the stars formed (the initial mass function, IMF, see e.g. Madau & Dickinson, 2014) are key for understanding the pace and characteristics of Galactic formation and evolution (Matteucci, 2012). In addition to the star formation rate and the initial mass function, well-developed theories and knowledge of stellar structure and evolution is necessary in order to construct models on how stars evolve (Prialnik, 2000). In particular, theories allow us to model both the photon transport in the stellar photosphere, i.e. *radiation transport*, as well as the amount of different chemical species that are synthesised in stars that are later scattered into the surrounding ISM, known as the *yield*.

Even from simple modelling of the enrichment of the ISM over time we can conclude that the very first stars should have contained only the very lightest of elements synthesised in the Big Bang, while progressively younger stars should show higher abundances of heavier elements. Thus, the chemical composition of stars provides an avenue for exploring the history of the Milky Way and its components. Not only can we learn about the Galactic history, but by observing the chemical composition of stars, we can put constraints on how and where these elements are synthesised – fundamental research that links to the origin of mankind itself.

Even though the field of studying galaxies is one of the oldest in astrophysics, the formation and evolution processes of galaxies is extremely complex, and therefore still not well understood. In order to take further steps in understanding the formation of galaxies, we need to expand our observational evidence and compare more extensively with the increasingly complex theoretical simulations and models of our Galaxy. Only with the most accurate knowledge of chemical abundances can we compare with the most sophisticated models. To that end, in this thesis my aim is to contribute to this endeavour by observationally determining trends of elements in the most stellar-rich components of the Milky Way: the bulge and the disk.

The bracket notation

Before we describe the details of the bulge and the disk, I want to introduce the notation commonly used when determining and discussing elemental abundances. It is less common to talk about absolute abundances, since for us it is more relevant to consider the evolution of elements over a proxy of time. As such, we use the ratio of two elements in a star, compared to those in the Sun by using the bracket-notation of [X/Y], where X and Y represents the elements of interest.

This notation is defined as

$$[\mathrm{X/Y}] \equiv \log\left(\frac{N_\mathrm{X}}{N_\mathrm{Y}}\right)_\mathrm{star} - \log\left(\frac{N_\mathrm{X}}{N_\mathrm{Y}}\right)_\mathrm{Sun}, \tag{1.1}$$

where N_X and N_Y are the number densities of element X and Y per unit volume, e.g. [cm^{-3}], respectively. This is a logarithmic expression that involves normalisation to the solar abundance ratio of the elements, meaning that all [X/Y] ratios of the Sun are exactly zero by definition. It is common to take the ratio of the element to iron. We do so because the cosmic origin of iron is relatively well known and can thus acts as the proxy for time. Additionally, there typically are many iron lines to determine an iron abundance from. As such, the [X/Fe]-ratio is usually compared to the iron-over-hydrogen ratio, [Fe/H], referred to as metallicity. Let us now return to the Galaxy and its components.

1.1 The Bulge

The Galactic bulge is the structure that makes up the central part of the galaxy, containing at least one third of all stars in the Milky Way with mass estimates around $2 \times 10^{10}\,\mathrm{M}_\odot$ (Valenti et al., 2016). However, constraining its properties and origin has proven to be a tricky task, partly because the region is crowded by stars, obscured by dust, and rather distant to us.

Early studies of the bulge considered its morphology, density and distribution and tried to put it into the context of extragalactic bulges. Indeed, in *Origin of Bulges* by Renzini (1999) he concluded that *"it appears legitimate to look at bulges as ellipticals that happen to have a prominent disk around them"* – a view which was adopted for the Milky Way bulge as well. However, from extragalactic observations (e.g. de Souza & Dos Anjos, 1987; Lütticke et al., 2000) and in early N-body simulations (e.g. Athanassoula & Misiriotis, 2002), another type of bulge appeared: the X-shaped bulges, also called "boxy/peanut" (BP).

These two, the ellipticals and the BP-bulges, outline two kinds of morphological bulges with differing formation scenarios (Kormendy & Kennicutt, 2004), being:

- The *classical* scenario where the bulge forms early on by mergers of primordial structures, implying that it should be one of the oldest components of the Galaxy. In this scenario the bulge is typically massive compared to the disk, as well as spheroidal and isotropic. This is the type of bulge that Renzini (1999) was referring to.

- The secular internal evolution of the disk via gas and stars transferring to the central part, forming what Kormendy & Kennicutt (2004) call a *pseudo-bulge*. These are flatter than the merger-built bulges and have younger stars thanks to star formation, such as recent starbursts. Due to vertical instabilities, from the formation of a bar, the bulge becomes puffed up and assumes the BP-shape (Shen & Zheng, 2020).

There are some grey areas to be considered here. Saha (2015) suggested that small classical bulges can be lost due to secular evolution. Additionally, some galaxies have been observed to have both a classical and a peanut-bulge component, indicating that there might not exist a strict grouping between the two cases (Erwin et al., 2015). Furthermore, the presence of a BP-bulge can also be described as a puffed up bar seen edge-on (Bland-Hawthorn & Gerhard, 2016). This latter kind of bulge is the view of the Milky Way bulge that has emerged over time, an artist's impression of which can be seen in Figure 1.1.

To arrive at a clear understanding of the Galactic bulge's formation and evolution provides quite a challenge due to its large coverage of at least 400 deg^2 of heavily dust extincted sky. On top of that, the definition of what belongs to the bulge or not varies among astronomers. One of the more common definitions is to use the Galactic coordinates longitude (l) and latitude (b), with the bulge being confined to $(l, b) \leq (|10°|, |10°|)$ (Barbuy et al., 2018).

Figure 1.1: An artist's impression of how the Milky Way would appear as seen edge on. The central bulge shows up as the boxy/peanut-shaped region of stars and the disk and its associated dust clouds form a narrow band. *Credit: ESO/NASA/JPL-Caltech/M. Kornmesser/R. Hurt*

However, this only sets the line-of-sight positions of bulge stars, which need to be complemented with distances. Distance estimates to stars, especially to bulge stars, are still cumbersome, making contamination of the foreground field stars a problem when observing the bulge. Nonetheless, distances to the individual stars are crucial to determine whether they are part of the bulge or not.

The above introduction to the bulge is based on morphology, and the BP-shape points at the bulge evolution being strongly linked to the Galactic evolution as a whole, with timescales over billion of years. For further constrains on the nature of the Galactic bulge, detailed chemodynamical surveys and simulations have contributed enormously.

The first attempts to make detailed models of the formation of the Galactic bulge were through chemical evolution models where the fundamental idea was formation on short timescales and a high star formation rate (Matteucci & Brocato, 1990). The high star formation rate was strongly supported by early observations of so-called α-abundances, such as oxygen, magnesium, and silicon, where the so-called knee in α-over-iron-abundance, [α/Fe], appeared to be located at higher metallicities when compared to the disk (Rich, 1988; Zoccali et al., 2006; Lecureur et al., 2007). The knee is a result of the onset of iron-production by supernovae (SNe) type Ia, where the placement of the knee depends on the star formation rate of the region. A region with a higher star formation rate (i.e. a classical bulge) reaches higher metallicities before the SNe type Ia onset. See Figure 1.2 for a visualisation of this α-knee and its dependence on star formation rate and initial mass function.

Newer observations however points to the bulge having a large chemical overlap with the inner thick disk, pointing to a similar origin of these (Meléndez et al., 2008; Jönsson et al., 2017b; Lomaeva et al., 2019). Still the endeavour remains to disentangle the stellar populations of the bulge and search for possible dissimilarities.

The metallicity of the bulge is found to have a broad distribution spanning $-3 <$ [Fe/H] $< +1$ (Ness & Freeman, 2016), with the bulk of the bulge stars are found within $-1.5 <$ [Fe/H]$< +0.5$. It is estimated that the stellar population is generally older than 10 Gyr (Barbuy et al., 2018). However, Bensby et al. (2017) found that at least 18 % of stars in the bulge might be younger than 5 Gyr, with an even higher fraction at supersolar metallicities. Although these are results that later have been questioned as too optimistic (Joyce et al., 2023), it is evident that the stars of the bulge have a broad span of metallicities and ages.

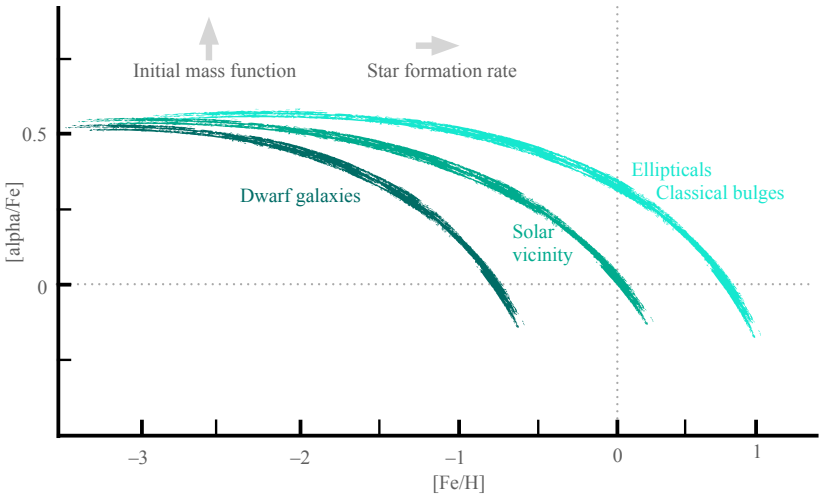

Figure 1.2: Matteucci & Brocato (1990) predicted that the α-knee in the trend of [O/Fe] with [Fe/H] depends on the star formation rate (SFR), indicated in the figure. systems with high star formation rate, like classical bulges and elliptical galaxies, should show enhanced [α/Fe] to high [Fe/H], whilst dwarf galaxies with low star formation rate show reduced [α/Fe] relative to the Solar vicinity. Also shown in this figure is how the initial mass fraction, specifically with an enhanced fraction of massive stars, would shift the trends upwards in [α/Fe]-direction.

When relating these age findings to the metallicity distribution functions in the bulge, it strongly indicates that the bulge consists of several stellar populations. In general, it seems as though the metallicity distribution function has a bimodal shape, with roughly half of the population consisting of an older, metal-poor component that traces a structure more compatible with a spheroid, whilst a more metal-rich component with younger stars, better traces the BP-shape (Debattista et al., 2017; Rojas-Arriagada et al., 2019). These younger stars are kinematically colder, which could be why they would be more sensitive to instabilities caused by the bar (Ness et al., 2013; Di Matteo, 2016).

To conclude, there is very strong evidence for the Milky Way to have a typical BP-shape and observations point towards the bulge forming through secular evolution by buckling instabilities in the disk. Even so it also seems likely that the Milky Way bulge does not consist of a unique single stellar population. As such, the question still stands as to whether there are remains of a classical bulge or not.

By considering the kinematics of bulge stars in simulations, Shen et al. (2010) puts an upper limit on the mass of such a component to 8 % of the disk mass. This translates to 16 % of the bulge mass assuming that the bulge is approximately half the stellar mass of the disk. Although this is a small part of the bulge as a whole, it is a non-negligible part of it, and mapping all components of the bulge are within our quest of mapping the entire Milky Way.

1.2 The Disk

The Milky Way disk, in which we find the Sun, contains the majority of the stellar mass in the Galaxy and is concentrated in the Galactic mid-plane. Compared to the bulge, which is more distant and substantially obscured by dust, the stars of the disk – and especially the local regions around the solar neighbourhood – has historically been easier to study in higher detail.

Gilmore & Reid (1983) showed that the local disk needs two density profiles to fit the total vertical density distribution of the disk – which represent es the birth of viewing the Milky Way disk as bimodal with two components. Due to the vertical distributions of the two components (Gilmore & Reid, 1983), they are often referred to as the thin and the thick disk, originating from the different scale-heights of the components. The thinner one has a scale height of about 300 pc, whilst the thicker disk extends to roughly 1 kpc. A schematic, simplified view of the Milky Way and its stellar components is seen edge on in Figure 1.3.

Following this finding, the disk has been investigated further in chemodynamical studies, showing that it indeed does consist of two stellar populations, distinguished by chemical abundances, ages and kinematics. The stars in the thick disk have been shown to be relatively higher in [α/Fe], typically older, and kinematically hotter compared to the stars of the thin disk. (e.g. Bensby et al., 2007, 2014; Adibekyan et al., 2011; Jönsson et al., 2017a, among others).

These properties of the disks point to different formation time scales, where the older, α-enhanced, and metal-poor disk is believed to have formed early on in the Galaxy. This could have been either through episodes of intense star formation driven by the infall of pristine gas from the accretion of smaller satellite galaxies, or as a result of a merger event between the Milky Way and a massive dwarf galaxy (e.g. Helmi et al., 2018).

Such a merger would not only have brought pristine gas and ex-situ stars, but also would have caused a significant disturbance in the Galaxy, leading to the formation of the thick disk. Traces of such a merger can be seen in the local stellar

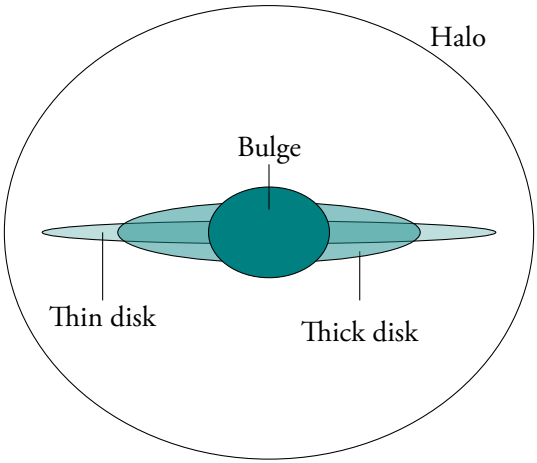

Figure 1.3: Schematic view of the Milky Way and its stellar components seen edge on. Although a simplified view, it showcases the locations and extent of the halo, bulge and disk components.

halo when combining data from large spectroscopic surveys and kinematical data from the Gaia space telescope (Gaia Collaboration et al., 2016, 2018). Discovered by Helmi et al. (2018) and Belokurov et al. (2018) the merging galaxy has been given the name the Gaia-Enceladus-Sausage (GES).

Although there are many findings supporting the merger of the GES-galaxy with the Milky Way roughly 9 billion years ago, the discussion of the origin of the disk bimodality is still not settled (see e.g. Garver et al., 2023, on a discussion of the evolution of massive clumps). In fact, the distinguishing of these two components is debated, and even though two populations emerge from the data, there is no clear cut distinction in either abundances, ages, kinematics or geometric distribution, and the question remains as to whether there is a clear separation rather a continuum. One suggestion is instead that of an inner and an outer disk, supported by findings in e.g. Hayden et al. (2015) where an α-poor component stretches further out in the disk. This study finds a positive skewness of the outer-disk metallicity distribution, which largely is attributed to the radial migration of stars in the outer disk.

These findings fits well with the theory that the Milky Way disk formed through inside-out formation, with the inner regions of the Galactic disk having formed before the outer regions. This is supported by theoretical models of galaxy formation, which predict that galactic disks grow from the inside-out, suggesting that

the chemical enrichment and formation of stars occurred in a sequential manner, resulting in abundance gradients (see e.g. Haywood et al., 2015; Minchev et al., 2015; Ratcliffe et al., 2023).

The fact that stars indeed migrate and move through the Milky Way disk causes a problem when it comes to Galactic archaeology. Although Galactic archaeology makes the assumption of stars providing a chemical timestamp of their respective birth clouds, the migration of stars blurs their respective origin, since they necessarily did not form on the same orbit as we find them today.

What is important to remember is that the Milky Way did not form in isolation. Today, galaxy formation simulations in a cosmological context are on the verge of producing high-resolution Milky Way analogues. For instance the VINTERGATAN-simulation[3] (Agertz et al., 2021; Renaud et al., 2021a,b), combines a hydrodynamics and an N-body code to investigate the Milky Way's formation history. From that simulation, they show that the Milky Way formed through episodes of mergers and gas flows in filaments under the influence of tidal forces. By including a GES-similar merger in the simulation, they do produce a bimodality in the α-abundance trends, providing further clues to the origin of the disk structure.

The truth situation lies probably in a combination of all theories above – the Milky Way has not formed in isolation, and stars will radially move throughout the Galaxy (Imig et al., 2023). The best way in which we can disentangle the stellar populations and their formation histories is to compare theoretical models that include all relevant processes with chemodynamical data. But only with extremely high-precision abundances can we start talking about chemical tagging of stars, i.e. to find their true origin in the Galaxy.

In the field of Galactic archaeology, several groups of chemical species have been studied already in this context – the α-elements as well as the metallicity and the iron-peak elements. A third group of elements is the heavier ones, the *neutron-capture elements*. This group of elements provides an alternative timeline for astrophysical phenomena and processes throughout the history of the Galaxy. Moreover, since the neutron-capture elements comprise more than two thirds of the periodic table, the study of these is crucial to an understanding of the full element production throughout the Universe. In the next chapter I will shed light on the cosmic origin of these elements, and what there still is to learn.

[3] "Vintergatan" being the name of the Milky Way in Swedish, directly translates to "the winter street", since in old Nordic folklore, the shape of the Milky Way was used to infer the weather of the upcoming winter. Naturally, the name also links to that at our northern latitudes the Milky Way is easiest observed during the dark winters.

Chapter 2

Stellar nucleosynthesis

If you wish to make an apple pie from scratch,
you must first invent the universe.

– Carl Sagan, Cosmos

Carl Sagan was right, because everything around us is composed of stardust. The very lightest of elements, hydrogen and helium, are the most abundant in the Universe and were created just after the Big Bang. All other elements, apart from small amounts of lithium and unstable beryllium, have been produced within stars or through stars in different stages of their life. Therefore, the elements that make us up have not only been created by and within stars, but we are made up of recycled star material.

In this Chapter I will take us through the life cycle of stars and go into some depth on the nuclear and stellar processes that contribute to the creation of the elements, with a focus on the heavy elements that have been studied in this thesis. These elements, due to their cosmic origin, can provide another perspective as compared to the lighter elements. As such, for us to be able to link their presence in stars with the evolution of the Galaxy, it is important to understand the processes, environments and time scales behind the origin of these elements. In order to take us through this chapter, I will use notation and nomenclature commonly used within nuclear physics.

2.1 Stellar structure and evolution

The conditions in the interior of stars, with high temperatures and pressures, enable fusion to occur in their cores. The main fusion process is that of hydrogen into helium, an exothermic reaction that releases energy through radiation. This radiation results in an outward pressure that, as long as the fusion of hydrogen and helium is active, prevents the star from collapsing under its own gravity.

The star spends most of its life in this state, called the main-sequence (MS) phase. This nomenclature, like many of the names of stages in the stellar life cycle, comes from the Hertzsprung-Russell (HR) diagram. This diagram is used in astronomy to show the relationship between the temperature or spectral type of stars and their luminosity or absolute magnitude. It is a fundamental tool in the study of stellar evolution and provides valuable insights into the life cycle of stars, for instance by tracing the evolutionary path of stars. Figure 2.1 below shows the path of a typical solar mass star.

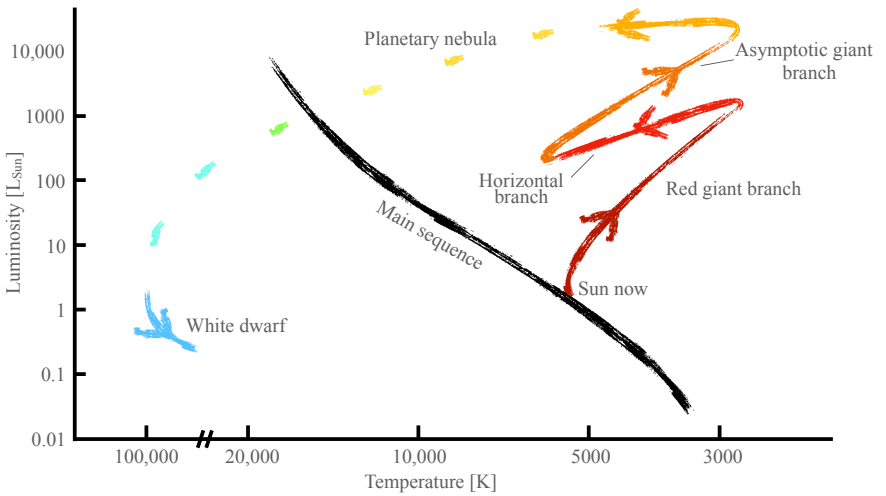

Figure 2.1: Schematic of the evolutionary path of a solar mass star in the HR-diagram, from the main-sequence to the final stage as a white dwarf. Note that this is a simplified view and that the different branches on the giant branch lays much closer to each other in temperature and luminosity than pictured here.

Eventually, the hydrogen in the core of the star runs out, marking the end of its period on the main-sequence. It is important to note that the more massive the star, the shorter it will remain on the main-sequence. With more mass comes a higher gravitational pressure, that increases the core temperature, in turn increasing the rate of fusion in the core.

At the conclusion of the main-sequence phase, the final stages in the life of the star begin. Despite their relatively short timespan, the final stages are of great significance in the nucleosynthesis of elements. As hydrogen fusion stops in the core, there is a reduction in the outward radiation pressure. Consequently, the core starts to shrink under gravitational pressure. In order to conserve gravitational potential energy, the outer parts of the star – called the envelope – expand. At the same time, the core temperature increases, and the expanding envelope cools, conserving the thermal energy of the star. This turns the star into a red giant which moves it up on the red giant branch (RGB), as seen in Figure 2.1. As a red giant, hydrogen fusion still takes place but only in a hydrogen-shell surrounding the, what is now, a helium core.

The core continues to heat up from compression, and as the core becomes hot enough to fuse helium into carbon, what is known as a helium-core flash kicks in, moving the star onto the horizontal branch. This is mostly relevant for solar-mass stars, since a minimum mass of about 0.5 solar masses is required for the star to experience a helium-core flash. Stars with less mass do not have cores hot enough to ignite helium, and their degenerate helium core will keep on contracting and finally become a helium white dwarf. On the other hand, stars with mass greater than about 2.2 solar masses, see Figure 2.2 on the next page for a reference of the mass limits, start to fuse helium without their core becoming degenerate, and as such do not experience the helium-core flash.

Nonetheless, with helium fusion in the core, eventually the core becomes depleted helium depleted too. At this stage, an outer shell of helium joins the residual hydrogen-shell, now separated by a helium intershell. This causes the star to enter the asymptotic giant branch (AGB) phase. It becomes an AGB star, see Figure 2.3 for a schematic of the stellar interior during this phase. These types of stars are essential in synthesising roughly half of the heavy elements.

Low and intermediate-mass stars with masses of 9 $M_\odot$ or less eventually evolve into white dwarfs. These have a carbon-oxygen core and are surrounded by a planetary nebula (so named historically but with no connection to planets). The nebula is the remnant from the large convective stellar envelope that, during episodic cycles, has been thrown out and detached from the core.

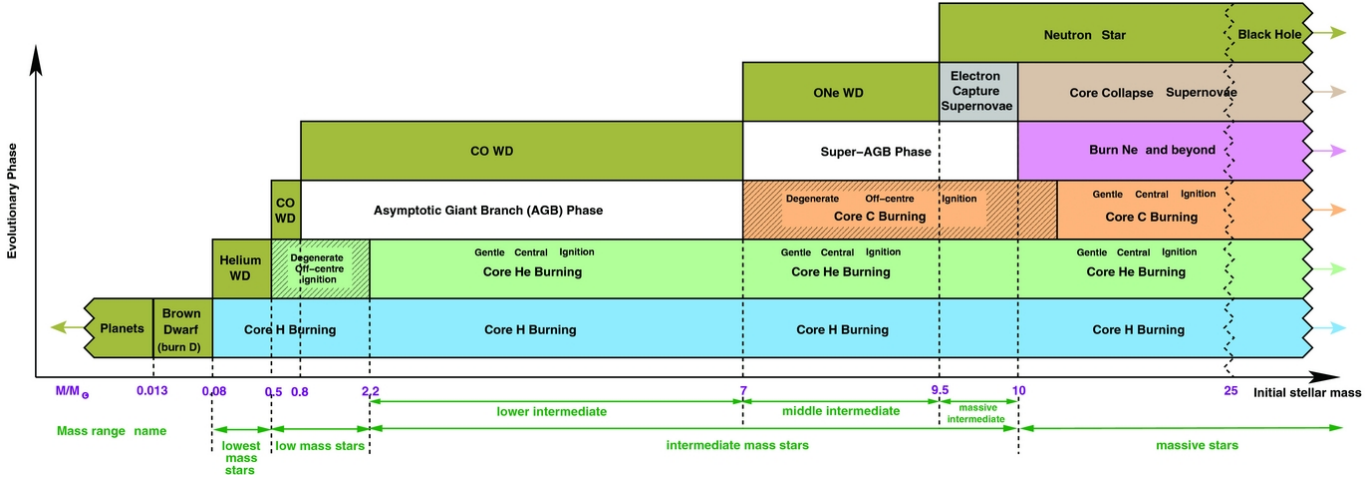

Figure 2.2: Schematic from Karakas & Lattanzio (2014) that shows the different phases of stars with solar metallicities, depending on the initial stellar mass. Note that the mass limits are often not well determined theoretically, depend on metallicity, and should be seen as rough estimates. *Figure from Karakas & Lattanzio (2014), reproduced with permission.*

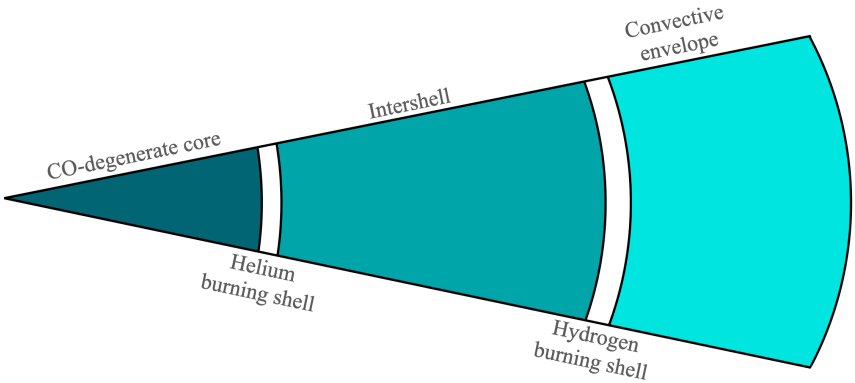

Figure 2.3: Schematic of the interior of an AGB star, showing the relative positions of the core, convective envelope, hydrogen- and helium-burning shells, and the intershell between them. The intershell is an important region for the production of s-process elements.

The more massive stars (refer to Figure 2.2 again for the various mass limits) continue to fuse elements in their cores until they reach iron. At this point, the fusion of elements is no longer energetically favourable. As stars have negative heat capacity, a star heats up as it loses energy through radiation. This temperature increase enables photo-dissociation of the iron nuclei in the stellar core, a highly endothermic reaction. This leads to loss of energy and pressure, so severe that the star starts to collapse in on itself.

The collapse results in such high densities that free protons capture electrons, creating neutrons which results in an energy loss and a reduced number of particles. As such, the collapse continues until neutron-degeneracy pressure is reached. Depending on the initial mass (and metallicity) of the progenitor star, the collapse could reach its halt here, leaving behind a neutron star. If even more massive, the collapse will continue, leaving behind a black hole. These latter stages can also be associated with a supernova explosion.

In the field of Galactic archaeology, it is common to group elements by their cosmic origin. We do this because the origin of different elements, along with the timescale of their respective nucleosynthetic processes, is one of the essential aspects we want to trace. When elements fuse in the stellar core, they create heavier elements. One of these fusion reactions is through reactions with helium-nuclei, also known as α-particles. Elements that are created by the adding of α-particles

are called α-elements, with oxygen, magnesium, and silicon being among them. To create the intermediate elements, other fusion reactions including e.g. free protons are involved.

The elements close to iron in the Periodic Table, are called the iron-peak elements. There some iron-peak elements heavier than iron, such as cobolt, nickel, and copper, that are produced by the rapid capture of α-particles in supernova explosions. However, what about the even heavier elements? In the following section, I will go through how and where they are created.

2.2 Synthesis of heavy elements

When compiling the abundances of elements in the Sun, Suess & Urey (1956) noticed distinctive peaks in the abundances of heavy elements — peaks that lined up closely with the magic numbers. Magic numbers are the number of protons or neutrons (nucleons) at which the energy levels of an atomic nucleus is filled, making it more stable than other nuclei (similar to the energy levels of an electron in the atom). They found two peaks at each of the neutron magic numbers of N = 50, 82 and 126, one sharp peak at the position of the magic numbers, and one smoother a few mass numbers below. We can see this in Figure 2.4 where a sharp peak can be found at e.g. barium with N = 82 and mass number A = 138.

Suess & Urey (1956) concluded that such distinctive peaks can be produced by considering the process of neutron-capture, where the sharp peak could be produced from a bottleneck of isotopes due to low neutron-capture cross sections close to the valley of stability (the black isotopes in the chart of isotopes, Figure 2.5). The smooth peak on the other hand they suggested could be produced by neutron-captures on the neutron-rich side of the valley of stability, followed by radioactive β^- decay (a nuclear reaction that was discovered by Fermi, 1934, awarding him the Nobel Prize in Physics in 1938).

Building on the work of Suess & Urey, Burbidge et al. (1957) formalised the concept of stellar synthesis of heavier elements that we know of today – through neutron-capture processes.

It should be noted that when I write "nucleosynthesis", what I refer to is nucleosynthesis by stars (or via processes involving stars). Heavy elements can be produced not only in extreme environments in outer space, but also in processes taking place in e.g. laboratories here on Earth. One such process is the heavy ion transfer reaction where a beam of ions is accelerated onto a thin foil. On occasions, a nucleus from the beam merges with a nucleus in the foil to form a new

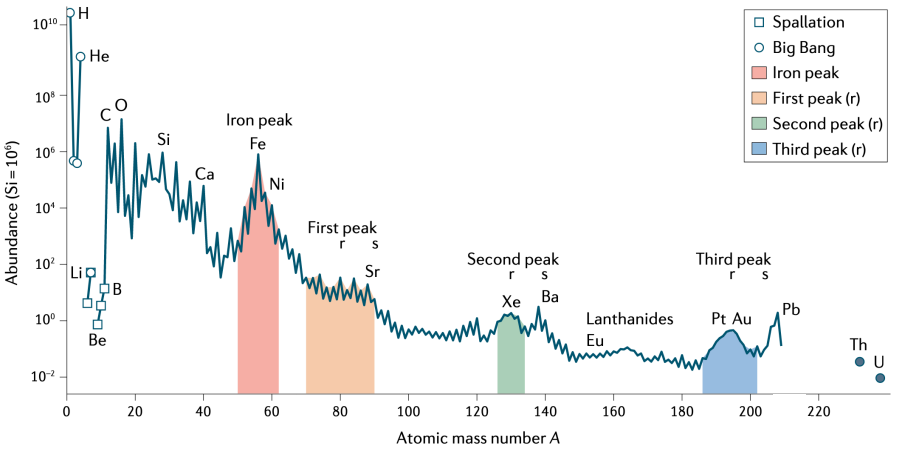

Figure 2.4: Observed abundances of isotopes as a function of atomic mass number A. Beyond the iron-peak elements (red) the characteristic peak structures of the s-process and r-process are evident (note that only the r-process peaks are indicated by colour). The abundance peaks are caused by the low neutron-capture rates at magic numbers. Specifically, the peaks near A = 80, 130, and 195 originate from the decays of r-process progenitors with N = 50, 82, and 126 (magic numbers). The peaks at A = 90, 138, and 208 results from s-process stable nuclei also with N = 50, 82, and 126. Due to the r-process producing nuclei farther away from the valley of stability (compared to the s-process), the r-process will access the magic numbered shells at lower mass number, causing the offset between the s– and r-process peaks. *Figure from Siegel (2022), reproduced with permission.*

nucleus, creating a heavier element. In the case of super-heavy elements, these are very low on neutrons and thus extremely unstable and decay within a few seconds. If the reader is interested in super-heavy element production on Earth, I recommend reading the doctoral thesis *"Element 115"* by my namesake, Forsberg (2016), issued at Lund University.

Since free neutrons are rare in nature, it would seem that neutron-capture is an inefficient way to create heavier elements. Fortunately, neutrons have no charge which make it easier for them to be captured by an atomic nucleus, in comparison to a positively charged proton that would have to overcome the Coulomb barrier. As such, neutrons are essential when building up and creating heavier elements.

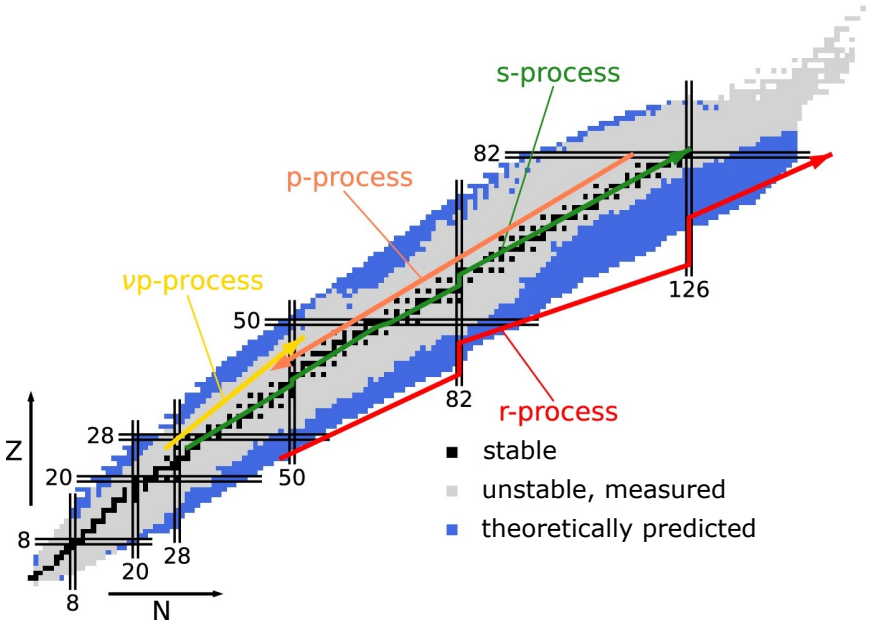

Figure 2.5: The Table of Nuclides. Isotopes with a certain number of neutrons N on the same horizontal line correspond to an element with a fixed number of protons, Z. Stable isotopes are marked with black. This is known as the valley of stability. Nuclei that have been produced in the laboratory are grey; and exotic isotopes that have been predicted theoretically and could be produced in rare isotope facilities are blue. The nucleosynthesis processes are indicated by coloured lines. The r-process path (red) turns vertical at the double vertical lines that indicate magic numbers. A nucleus on an r-process path eventually β-decays to the valley of stability to become an r-process stable isotope. *Figure from Arcones & Thielemann (2023), reproduced with permission.*

But, what is the neutron-capture process, and how does it actually create the heavy elements? There are two main nuclear physical reactions involved in the process:

1. The capture of neutrons by an atomic nuclei containing Z protons,

2. β^- decay where a neutron transforms into a proton, electron and a neutrino.

When a neutron interacts with an atomic nucleus, a heavier isotope is formed that may or may not be stable. If the resulting nucleus is stable, it can either remain in this state or continue capturing neutrons. While a stable nucleus can undergo another neutron capture, an unstable nucleus can alternatively undergo β-decay, which increases the proton number, creating a new element with Z+1. At this stage, successive neutron captures can continue until another unstable isotope is reached, and another heavier element is created through subsequent β-decay.

The neutron-capture process can be divided into two categories primarily distinguished by the amount of available neutrons, or the neutron flux. These categories are the *slow*- and *rapid*-process (s- and r-processes).

In the s-process neutron absorption by a stable nucleus leads to the creation of a different stable nucleus and so on until the nucleus produced is unstable. It then β-decays to form a nucleus with atomic number Z+1. This is inherently a slow process, taking place over thousands of years.

In contrast, the r-process involves a high flux of neutrons leading to an increase in the mass number that is faster than the β-decay of the unstable nucleus. This is inherently a rapid process, taking place in less than seconds.

These two processes represent two different formation channels or paths for creating isotopes of heavy elements, matching the predictions and observations made by Suess & Urey (1956).

Whilst some isotopes can be produced by both s- and r-process paths, some can only be reached through one of these processes, called shielding. For instance, s-only isotopes are blocked from the r-process by stable isobars[1] of charge $Z-1$ (or $Z-2$). An example of shielding is shown in Figure 2.6 on the next page.

However, determining the actual path of the different processes is not trivial. In comparison to β-decay, the time scale for neutron capture is not constant and depends on the neutron density and the neutron absorption cross section of the isotope. As such, one thing to take into account is the branching at unstable isotopes with semi-long decay lives of a few days to years, where both β-decay

[1]Isobars have constant same mass number A, i.e. the same number of nucleons, but not necessarily the same number of neutrons and/or protons. These are diagonally traced from the upper left to the lower right in the chart of isotopes, as indicated in Figure 2.6

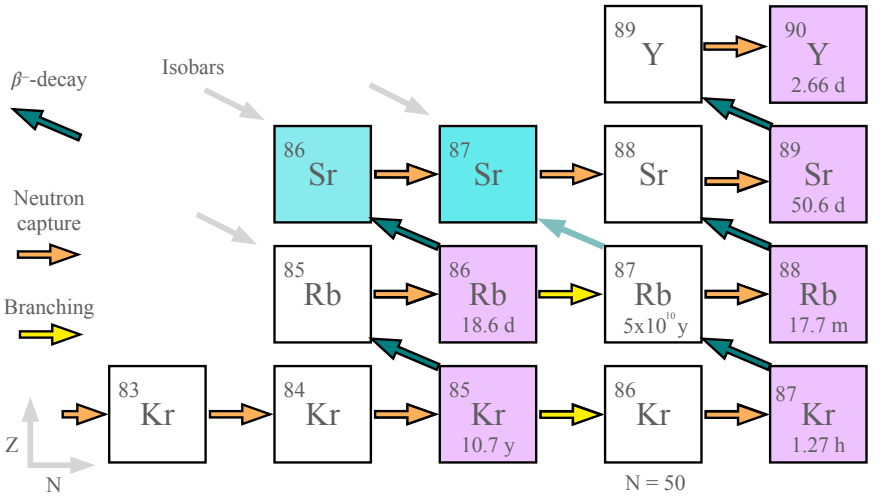

Figure 2.6: Part of the Table of Nuclides, showing the s-process pathin the region of the isotopes of krypton, rubidium and strontium. Stable isotopes are white and unstable isotopes are pink, with their half-lives indicated. This shows an example of shielding where the ^{86}Sr isotope (cyan) is a pure-s isotope. Nuclei that would be produced by the r-process (from the lower right) would end up via β-decay in the stable isotope ^{86}Kr, blocking any contribution to ^{86}Sr. In the same way, ^{87}Sr (cyan) is in practice pure-s, since its isobar ^{87}Rb has a long half-life comparable to the age of the Universe, and r-process decays from the next isobar ^{87}Kr are shielded. The yellow arrows to ^{86}Kr and ^{87}Rb show where neutron capture competes with decays causing the nucleosynthesis path to branch, called branching. In this case, all branches combine at ^{88}Sr, which has a closed neutron shell of N =50 and, hence, a very small neutron-capture cross section.

and neutron capture can take place. An example of branching is also included in Figure 2.6 above.

Nonetheless, in order for neutron capture to take place and progress through the various paths, the s-process operates at neutron densities equal to or less than 10^{11} neutrons/cm^3 (Busso et al., 1999) and the r-process somewhere between $10^{24} - 10^{28}$ neutrons/cm^3 (Kratz et al., 2007). These neutron densities differs on several orders of magnitude, which provides constraints on the environments where the s- and r-processes can take place.

The s-process

The s-process is composed of three different sub-processes, the weak, main, and strong s-process, that depend upon the environment where they take place, and the nuclear reaction from which the neutrons originate. The weak and main s-process can synthesise most of the s-process element, but to create the heaviest ones, the strong s-process is necessary. In this section I will focus on describing the mechanisms of the first two processes, since none of the heaviest s-process elements created by the strong s-process have been part of this thesis.

The main s-process occurs in the interior of AGB stars. As described previously in this Chapter, the interior structure of these stars is characterised by a carbon and oxygen core, enclosed by a helium and a hydrogen shell. These shells are separated by the helium intershell, which is enriched in both helium and carbon.

During the AGB phase, the star experiences instabilities known as thermal pulses. These release energy that drives convective flows across the entire intershell for a brief period of time. One of these pulses sees partial fusing producing a large quantity of ^{12}C. This is linked to what is called the *third dredge-up*, where the convection zone extends all the way from the star's surface down to the intershell, bringing hydrogen down from the surface. As a result, a ^{13}C-pocket forms in between the burning shells through the reaction:

$$^{12}\mathrm{C}(\mathrm{p},\gamma)\ ^{13}\mathrm{N}(\beta,\nu)\ ^{13}\mathrm{C}. \tag{2.1}$$

The s-process nucleosynthesis occurs inside this ^{13}C-pocket, as ^{13}C fuses with α-particles in the intershell, $^{13}\mathrm{C}(\alpha,\mathrm{n})\ ^{16}\mathrm{O}$, leading to the release of neutrons into the pocket, which then interact with heavy nuclei already present in the star.

The weak s-process is conceptually similar to the main s-process, but instead of ^{13}C as the primary neutron source, the neutrons originate from the reaction $^{22}\mathrm{Ne}(\alpha,\mathrm{n})\ ^{25}\mathrm{Mg}$. This reaction is endothermic, meaning it requires higher temperatures than the $^{13}\mathrm{C}(\alpha,\mathrm{n})$-reaction, and occurs at the end stages of hotter and more massive stars. Specifically, it is believed that the weak s-process occurs during the helium core burning phase and partly in the subsequent convective carbon burning shell phase of massive stars (Couch et al., 1974). Due to their intrinsic higher temperature, this reaction can also occur in the most massive AGB stars.

The elements produced by the s-process can furthermore be divided into the three abundance peaks identified in Suess & Urey (1956). These are the first, second and third peak s-process elements. During the third dredge-up, the first-peak s-process elements are synthesised first and, as the neutron exposure increases, the second-peak s-process elements are created. In AGB stars with masses greater

than 4 $M_{\odot}$, the ^{22}Ne(α,n)-reaction occurs due to the high temperatures (Karakas & Lattanzio, 2014). This leads to an increase in the neutron density, in addition to shrinking the ^{13}C-pocket. Furthermore, the neutron exposure of the ^{22}Ne(α,n)-reaction is lower than that of the ^{13}C-reaction. This results in a smaller quantity of s-process elements being produced, particularly the heavier ones. To conclude, massive AGB stars produce relatively fewer second-peak elements in comparison to low-mass AGB stars. Moreover, at lower metallicities fewer iron seeds are available per neutron, implying that second- and third-peak elements are more likely to be produced, compared to first-peak elements (Busso et al., 1999).

The s-process can produce more or less all the stable isotopes and stops at ^{209}Bi. This is due to the low neutron-capture cross-section of ^{209}Pb, which decays back to ^{209}Bi, resulting in a blocked loop. While the s-process forms elements over a timescale of thousands of years, the r-process can create heavy stable elements in less than a second. It is important to note that because low-to-intermediate mass stars spend a longer time on the main sequence, as compared to more massive stars, there is a delay in the production of s-process elements in AGB stars. Therefore, any observed s-process-dominated element before this onset must be due to at least one additional production channel, most likely the r-process at early times.

The r-process

While the s-process stops at ^{209}Bi, the r-process has no such limit and can continue until radioactive decay prevails over the neutron-capture time scales. Like the s-process, the r-process can be divided into two sub-processes: the weak and the main r-process. The difference lies is the rate of neutron capture, where the weak r-process has a slower succession of neutron captures, and can produce elements up until the second peak of the r-process.

The weak r-process is thought to take place in the neutrino-driven winds of core-collapse supernovae (CC SNe) and accretion disks around collapsars. But in order to form all of the heavy elements up to uranium, the main r-process is required. This works under higher neutron fluxes, requiring an extreme abundance of available neutrons, which have been proposed to be available in various explosive environments, such as CC SNe and compact binary mergers (neutron star-neutron star or neutron star-black hole mergers, commonly abbreviated to NSM).

Confirmation of the presence of NSM was achieved through the detection of gravitational waves from the GW170817 merger (Abbott et al., 2017) and the emission of electromagentic radiation from the associated kilonova AT2017gfo. The observation of this kilonova shows that these energetic and neutron-rich events

do produce heavy elements, particularly from detections of the neutron-capture element strontium (Tanvir et al., 2017; Drout et al., 2017).

Despite measuring about 0.05 $M_{\odot}$ – which is adequate to explain all Universal r-process production – the amount of r-process material generated from this event has been difficult to replicate in theoretical models. The amount of r-process elements produced in a neutron star merger ejecta depends significantly on the adopted equation of state (Matteucci et al., 2014), rendering it difficult to constrain the yields for Galactic chemical evolution models. Uncertainty in nuclear inputs, including nuclear masses and β-decay rates, is another source of variation in calculating r-process yields.

Since GW170817/AT2017gfo, studies have debated whether neutron star mergers are the primary source or even a relevant source of r-process elements (e.g. Côté et al., 2019; Siegel, 2022; Van der Swaelmen et al., 2023), but still no consensus has been reached. Additionally, another type of rare supernova has emerged as a candidate production site for the r-process. These are called magneto-rotational supernovae (MRSNe) and when included in Galactochemical evolution models, they manage to reproduce the observed abundance trends of r-process elements, whilst the contribution from neutron star mergers appears to be relatively low, primarily at lower metallicities. This can be seen for e.g. europium in the models of Kobayashi et al. (2020) and Lian et al. (2023), see Figure 32 in Kobayashi et al. (2020) and Figure 2.7 on the next page, respectively.

However, some studies (e.g. Côté et al., 2019; Skúladóttir & Salvadori, 2020; Lian et al., 2023) point towards the necessity of combining two sources with different delay-times to replicate the observed abundance trends in the Milky Way and its satellite dwarf galaxies. One of these sources would be fast and early enrichment by (MR-)supernovae, and the other would be neutron star mergers that could have longer delay time of more than 1 Gyr.

Nonetheless, it is evident that the production site(s) of the r-process is still uncertain and determining their contribution is an active area of research. Having high-quality observational data to compare against models is crucial in this ongoing effort.

The p-process

Neutron-capture processes are not sufficient to create all of the heavy stable isotopes; 32 isotopes are shielded both by the s- and the r-process, and are created by what Burbidge et al. (1957) called the "proton-capture", or p-process. While the production site of the r-process is not well constrained, the production site of the

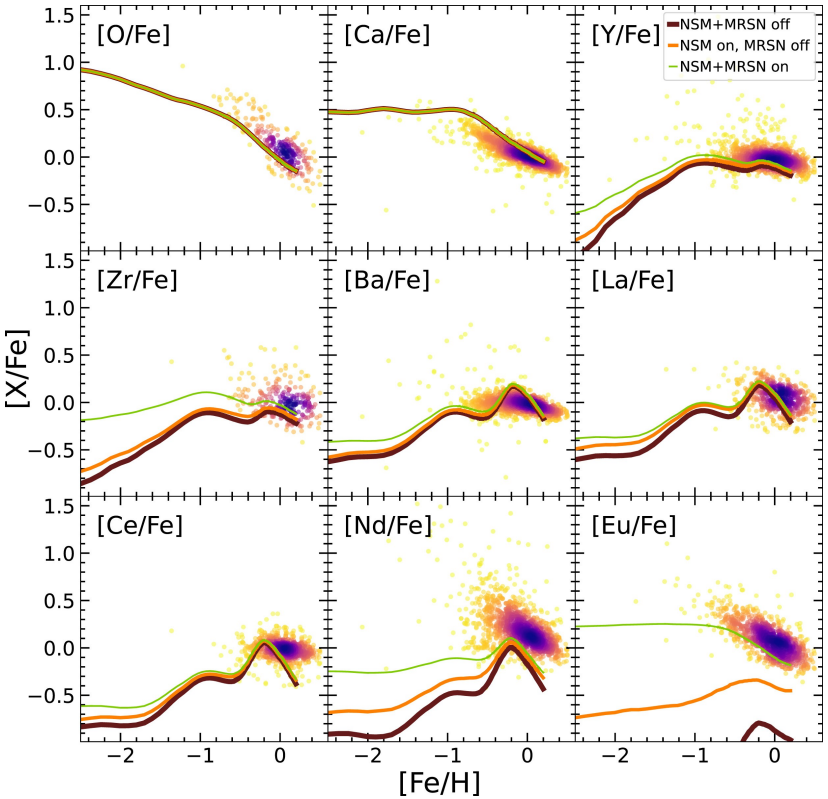

Figure 2.7: The abundances of neutron-capture elements from the final data release of the Gaia-ESO survey compared with Galactic chemical evolution models. The models showcase the impact of including NSM and MRSNe, or not. Three models with different scenarios are included: no NSM or MRSN contribution (dark red), NSM only (orange), and including both NSM and MRSN (green). *Figure from Lian et al. (2023), reproduced with permission.*

p-process remains even more elusive. Cameron (1957) and Burbidge et al. (1957) suggested that the p-process occurs in the hydrogen-rich layers of type II supernovae, and although the term ”p-process” refers to proton-capture, it has been demonstrated that this is not necessarily the only way for creating these ”p-rich” isotopes, and that there could be several mechanisms behind their cosmic origin (Rauscher et al., 2013).

In the case of actual proton capture, one of the processes is the rapid proton-capture process. This is known as the rp-process, which takes place in extremely

proton-rich environments with more than 10^{28} protons/cm^3 through (p,γ)-reactions and has been suggested to occur in explosive hydrogen– and helium-burning on the surface of mass-accreting neutron stars (Koike et al., 2004). These are also known as type I X-ray bursts and they are the result of mass transfer in binary systems consisting of a neutron star and an evolved companion star.

Type I X-ray bursts are caused by thermonuclear runaway, where the mass transferred from the companion star accumulates on the surface of the neutron star until it ignites and fuses in a burst, producing X-rays.

Similarly to neutron capture, proton capture continues to create isotopes until the timescale of decay dominates the timescale of proton-capture. The rp-process is usually halted at isotopes having a combination of long half-lives and small proton-capture cross sections, causing "waiting points" (Schatz et al., 2001). These waiting points can be overcome by either the pn- or the νp-processes.

- For the pn-process, (n,p)-reactions have been suggested to take place in a subclass of type Ia supernovae which is caused by the disruption of a sub-Chandrasekhar CO-white dwarfs due to a thermonuclear runaway in He-rich accretion layers (Goriely et al., 2002). Models suggest that this process can efficiently produce the light p-nuclides from Se to Ru but when compared to observations, the models overproduces them in relation to the heavier ones.

- In the νp-process, neutrons are created through anti-neutrino interactions with protons. This process, which takes place in proton-rich ejecta in core-collapse SNe, has been in favour as a mechanism for making some of the lightest p-isotopes, including ^{92,94}Mo (Fröhlich et al., 2006).

A different approach to creating the p-isotopes is through the γ-process which is the photo-disintegration of neutrons in heavy, neutron-rich isotopes that have been synthesised through neutron-capture processes. The stripping of the neutrons is caused by highly energetic gamma-photons in (γ,n)-reactions, giving the process its name. It has been proposed to take place in the explosive O/Ne-shell burning stages of core-collapse SNe. Although some models suggest that the γ-process encounters problems in creating the lighter p-isotopes (Arnould & Goriely, 2003), in Travaglio et al. (2015) they show that type Ia SNe can produce all mass ranges of p-isotopes through the γ-process, and as such it is one of the most favoured explanations for creating p-isotopes. Nonetheless, there is evidently a plethora of different mechanisms and sites that potentially could produce the p-isotopes.

2.3 Final remarks on nucleosynthesis

In the fields of Galactic archaeology and abundance analysis, neutron-capture element are often classified as either an r-process or s-process element. It is important to note that what we are referring to is the dominant origin from either of the processes for producing the elements. What matters is how the isotopes that make up the elements are created, and how much they contribute to the overall abundance of the element.

Consequently, there is no clear separation in either the Periodic Table of Elements or the Table of Nuclides between the s-process and r-process because both processes, alongside the p-process, often are involved in producing an element. Prantzos et al. (2020) have estimated the contribution to isotopes in the abundance of elements, shown in Figure 2.8. This indicates that, for instance, europium is a typical r-process element, which has two stable isotopes, ^{151}Eu and ^{153}Eu, primarily produced by the r-process.

Indeed, europium is the element used in the papers of this thesis as a tracers for the r-process. Similarly, lanthanum and cerium are used as tracers for the s-process. Having these tracers are important for comparing contributions to the production of elements, e.g. for the 50/50 s–/r-process element ytterbium that we measure in a sample of disk stars in Paper IV.

It is important to note that, as I will touch upon in the following Chapter when describing isotope shift, measuring abundances of isotopes is extremely cumbersome and requires extremely high resolution, which is beyond the scope of this thesis. As such, the abundances presented in this thesis are abundances of the elements.

Light Element Primary Process

Despite being the most well-understood of the nucleosynthetic processes of heavy elements, obtaining theoretical estimates of s-process yields is difficult due to its dependence on a wide range of physical parameters. Partly, there is a metallicity-dependent yield from the already pre-existing atomic iron seeds, on which the neutron capture takes place. Furthermore, neutron poisons, such as the ^{14}N(n, p)^{14}C-reaction that decelerates the neutron-capture process, need to be considered. Furthermore, the dependence of the size and properties of the ^{13}C-pocket in AGB stars is one of the main challenges when estimating yields.

Such challenges led to the disagreements between observations and theoretical models which in turn led to the introduction of the Light Element Primary Process

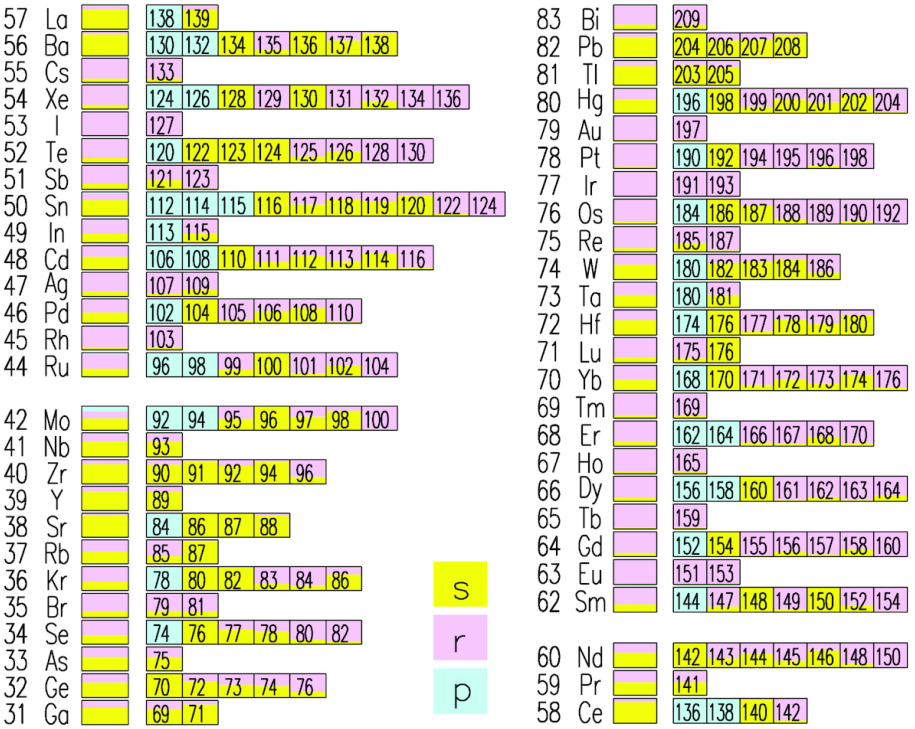

Figure 2.8: Contribution of the s-, r-, and p-process to the isotopic and elemental according to the work of Prantzos et al. (2020). The contribution of each process is proportional to the coloured area of the corresponding box. *Figure from Prantzos et al. (2020), reproduced with permission.*

(LEPP) by Travaglio et al. (2004). LEPP was proposed to offer a potential explanation for the high abundances of strontium, yttrium, and zirconium (the first s-process peak) observed in metal-poor stars. However, as theoretical models on stellar structure and nucleosynthesis have become more refined, the necessity for LEPP has decreased. Trippella et al. (2014) and Cristallo et al. (2015) discovered that by enlarging the ^{13}C-pocket and accounting for stellar rotation, a satisfactory amount of the first s-process peak elements could be synthesised. For a more in-depth discussion on the significance of the size of the ^{13}C-pocket, refer Bisterzo et al. (2017). The involvement of rotating massive stars in the s-process production, specifically in low metallicity environments, is backed by several studies (e.g. Cescutti et al., 2013; Frischknecht et al., 2016; Prantzos et al., 2020).

On the other hand, Kobayashi et al. (2020) developed Galactic chemical evolution models that match the observations of the first s-process peak elements, without the need to include rotating massive stars. Instead, they incorporated so-called electron-capture supernovae as well. However, it should be noted that the model cannot fully replicate the second s-process peak elements, especially at lower metallicities of [Fe/H] < -1.

The intermediate process

Another proposed process to take into account, that could explain the high abundances of first-peak s-process elements at low metallicities, is the intermediate process. As mentioned earlier in this Chapter, the neutron densities for the s- and the r-process differ by several orders of magnitude and it has been suggested that a third process could exist in the intermediate gap with neutron densities of $10^7 - 10^{15}$ neutrons/cm^3 (Cowan & Rose, 1977).

This intermediate process (i-process) has been proposed to give an explanation to the puzzling abundances of barium enchanced stars in open clusters (Mishenina et al., 2015) and some carbon-enhanced metal-poor (CEMP) stars in the Galactic halo (Hampel et al., 2016; Hansen et al., 2023). A significant amount of CEMP stars show enrichment in either s- or r-process elements, with a subset enhanced in elements from both processes, called CEMP-r/s or CEMP-i stars. The easiest way to explain these abundances would be a process that can create elements otherwise typically prescribed to the s- and the r-process, i.e. the intermediate process.

Furthermore, as shown by Côté et al. (2018), including i-process yields from rapidly-accreting white dwarfs in Galactic chemical evolution models, can produce sufficient amounts of the first s-process peak elements at low metallicities to remove the need for LEPP. A rapidly-accreting white dwarf is a binary system consisting of a carbon-oxygen or oxygen-neon white dwarf primary, and a main-sequence, or evolved star companion. The white dwarf accretes hydrogen from the companion, resulting in hydrogen fusion in a shell. Eventually fusion takes place in a helium shell that can experience thermal flashes, similar to the thermal pulses in AGB stars that led to s-process synthesis.

Although the i-process and its production sites is yet to be confirmed, both the rapidly-accreting white dwarfs and low-metallicity low-mass AGB stars are the favoured sources in the literature (Choplin et al., 2021, 2022).

To unravel the p-process

To study the origin of the p-process, which is highly elusive, the best approach is to examine the element molybdenum, as illustrated in Figure 2.8. Usually, the p-isotopes contribute very little to the element's abundance, but in the case of molybdenum, the isotopes ^{92}Mo and ^{94}Mo have been estimated to constitute around a quarter of the molybdenum abundance in the Sun — a noticeable proportion (Lodders et al., 2009; Prantzos et al., 2020).

Next in line with a noticeable abundance of p-isotopes is ruthenium, with a roughly 7% contribution to its overall solar abundance from ^{96}Ru and ^{98}Ru. As such, molybdenum is the elements to study in order to put constraints on the mechanisms and cosmic sites behind the production of p-isotopes. Abundances of molybdenum for stars in the bulge and disk are presented in Paper II of this thesis.

To summarise, the complex cosmic origin of the neutron-capture elements are different to the more studied α- and iron-peak elements. This difference provides additional constraints to the evolution of the Galaxy and its stellar components. These elements comprise more than two thirds of the periodic table of elements, making the study of them crucial to understanding the full production of elements in the Universe.

Chapter 3

How we study stellar light

I will love the light for it shows me the way;
yet I will endure the darkness for it shows me the stars.

— Augustine "Og" Mandino

Studying the stars provides insights into both Galactic evolution and the origin of elements. Encoded in the stellar light there is an abundance of information, provided one knows how to decode it. This chapter will describe the process of identifying the information contained in stellar light, its creation, and the method for determining stellar abundances by decoding it. This thesis focuses on a specific class of stars, red giants. Details relating to their characteristics and analysis will also be elaborated upon.

3.1 The information in the light

There are many ways to define when the field of astrophysics was born, one of which suggests that its birth coincides with the astronomers' integration of spectrographs onto their telescopes. The previously red and blue, faint and bright stars and galaxies now showed their true colours in the rainbow light revealed by the prisms of the spectrographs. In 1814, the physicist Joseph von Fraunhofer provided one of the earliest illustrations of this type of study, discovering dark lines within the solar spectrum. The absorption of light in the solar photosphere was identified as being caused by the presence of chemical species. By comparing this to laboratory measurements of the wavelengths observed at which the light was absorbed, it was possible to identify the chemical species.

The possibility of obtaining star spectra has provided a new way to study the Galaxy. However, a comprehension of underlying physics is necessary before using theory and modelling to extract information from the light. To perform such modelling, one needs to know about atomic and molecular physics, stellar photospheres, and radiation transport. These topics will be reviewed in the following sections, and a more extensive and detailed description can for example be found in the book on *The Observation and Analysis of Stellar Photospheres* by Gray (2005), especially Chapter 13.

Let there be light

Considering the atomic model of Niels Bohr, the electrons are located in shells around the nucleus. Although a simplified picture of a quantum mechanical system, it helps when imagining the processes that creates light. The electrons are found in discrete energy levels, and as the atom interacts with an energy source of the same, or greater, energy as one of these discrete energy levels, it can trigger a transition of the electron to a lower energy state. In the process, it emits the energy as a photon. The photon will have the energy, i.e. wavelength, of the transition made by the electron. Having precise knowledge of these wavelengths is the foundation for identifying the spectral lines.

Identifying all energy transitions that exist in all elements and their isotopes is truly an astronomical task. Furthermore, molecular data — that also have energy transitions — needs to be taken into account for a complete understanding of the spectra. Fortunately, in the optical wavelength regime that we are targeting in Paper I-Paper III, the elements have been fairly well studied in the laboratory. However, as Paper IV suggests, the infrared regime is less abundant with atomic spectral lines, and a large number of them are yet to be accurately measured.

The stellar atmosphere

The photosphere is the region of a star where radiation — its light — is emitted. The properties of the photosphere have a significant impact on the observable spectra of stars. As covered in Chapter 2, fusion within the core of the star results in an energy flux. Subsequently, radiated energy flux travels via radiation transport mechanisms, i.e. photon scattering and convection before it reaches the photosphere, taking hundreds of thousands to millions of years.

The ability to detect chemical species in stars is influenced by the temperature and pressure gradients found within the photosphere. Modelling the photosphere and determining global stellar parameters, which define the star through fundamental equations, must be considered:

- Effective temperature T_{eff}, which is the surface temperature,
- Surface gravity $\log(g)$,
- Metallicity, that we usually measure from iron-lines, and define as [Fe/H] using the notation introduced in Chapter 1, eq. 1.1.

Movements in the photosphere must also be taken into account. For the sake of simplicity, the photosphere is often modelled in the radial direction using 1D models. Modelling the photosphere in full-scale 3D can generate more precise calculations of the heat transportation by convection, which affects the temperature distribution. Creating a complete 3D model would allow a better comprehension of the the movements in the photosphere, known to impact the spectra of stars. Unfortunately, it is currently not feasible to observe the surface of most stars, and 3D modelling both increases computational time and can induce the risk for redundant complexity.

Thus, these motions are taken into account by including turbulence parameters in the 1D modelling, which include micro- and macroturbulence. Macroturbulence takes into account line broadening mechanisms, while microturbulence is used to account for non-thermal motions in the star's atmosphere. These movements are smaller than a mean-free path of photons, influencing line formation and radiative transfer, similar to thermal movements.

In environments with a high particle density, particle collisions dominate the energy distribution; this is unlike less dense environments where photon interactions dominate. We say that the environment where collisions dominate is in local thermodynamic equilibrium (LTE). In LTE, the atomic and molecular level populations and degree of ionisation is set by the local temperature, as is the radiation field and source of light, given by Planck's black body radiation field, significantly simplifying the physical modelling of the photosphere. However, this holds true only in the dense parts of the photosphere. The outer regions of the photosphere are less dense, which leads to deviations from LTE, referred to as non-LTE (or NLTE). In this case, an intricate interplay between radiation and thermal motions determines the level populations and sources of photons.

Opacity and line formation

How are spectral lines, similar to those observed in the solar spectrum by Fraunhofer, formed in the photospheres of stars? The absorption of photons varies with wavelength, causing wavelength-dependent differences in the escape of light from the star. If there is no chemical species present to interact with light of a specific wavelength, the photon escaping from the star can originate from regions deeper in the star, which are hotter. Conversely, if the wavelength of light matches that of a strong energy transition, most of the light at that wavelength will be absorbed, and only the photons originating from the topmost layer of the star's surface are capable of escaping. These layers are most often cooler, leading to less light at that wavelength, explaining the dark Fraunhofer lines. We refer to the phenomenon of wavelength-dependent strength of light absorption as opacity.

In the regions of the spectrum where there are no spectral lines, light is not emitted from a transition between levels in an atom or molecule. Rather, photons originate from non-discrete photon-matter interactions. Thus, one of the significant type of opacities is the continuum opacity. In cool stars, the continuum opacity originates from two main processes involving hydrogen, known as H^- free-free and H^- bound-free. Photon absorption in both of these processes shows a weak dependence on photon wavelength and establishes the minimum opacity of the star, which limits how deep we can probe into the star.

Transitions between energy levels in chemical species are known as bound-bound absorption. Where strong transitions exists, the opacity becomes very high, manifesting as a strong spectral line in the spectrum. We make the assumption that weaker spectral lines and the continuum originate from deeper in the photosphere, while stronger absorption lines, especially the core of these lines, form further out in the photosphere. Consequently, coming back to the topic of LTE, we usually assume that LTE conditions hold both for the continuum and weaker lines.

The spectral lines of a chemical species are not only affected by their intrinsic strengths, the oscillator strength, and the opacity, but – fortunately for us – by the abundance. The line strength can be expected to increase with increased chemical abundance, but the change in line profile and width of the spectral line is not always a simple proportionality. Weak lines are commonly used when determining abundances since they tend to be less affected by deviations from LTE and are more sensitive to the abundance; for weak lines, the depth of the line grows in proportion with the abundance. As a line grows deeper, the line saturates, meaning that the light in the core of the spectral line originates from the outermost parts of the photosphere, and grows asymptotically with a low dependence on the abundance.

Hyperfine splitting and isotope shift

Before covering how we determine the abundances, there are additional processes to consider which can affect the shape and width of spectral lines of interest.

Nuclei with an odd number of nucleons, in particular those with an odd number of protons (such as lanthanum and europium), have a nuclear spin which gives rise to hyperfine splitting (HFS). This arises due to interactions between the magnetic moments of the spin of the nucleus and the electrons, causing the energy levels of the atom to split into several levels. The splitting of the levels is usually small, and most astronomical observations are not able to resolve it. However, the splitting nonetheless broadens the spectral line, and as such it is important to take HFS into account, since it can cause de-saturation of the line (e.g. Thorsbro et al., 2018).

Another mechanism for line broadening is the isotope shift, which occurs in elements that have more than one stable isotope. The difference in the number of neutrons in the isotopes of these elements causes a shift in the mass and volume of the nucleus, subsequently shifting the atomic energy levels. The understanding is that an orbital electron experiences a weaker charge per unit volume or mass from the nucleus, making it less bound. As the atom becomes more massive, the isotope shift is predominantly influenced by the change in volume rather than mass. Nevertheless, as highlighted in the Gaia-ESO line list by Heiter et al. (2021), isotope shifts are generally much smaller than what our spectrographs can resolve and often can be disregarded in the analysis.

3.2 Abundance analysis

The abundances of a star are measured by solving the radiation equations using the stellar parameters introduced earlier in this chapter, whilst considering the intensities of the elemental spectral lines of interest.

There are different ways of going about doing these calculations. In the papers comprising this thesis we have determined the abundances by comparing the observed spectrum with a modelled synthetic spectrum. There are a few tools available for this, but for our purpose we are using the tool Spectroscopy Made Easy (SME, Valenti & Piskunov, 1996; Piskunov & Valenti, 2017). SME creates a synthetic spectrum that allows both nearby, blending spectral lines and hyperfine structures to be taken into consideration. To create a synthetic spectrum, SME requires a set of input parameters:

- The stellar parameters, including the chemical abundances. The latter we keep as free parameter(s) in the analysis.
- A model of the stellar atmosphere that describes the temperature and pressure distributions in the star, as a function of (optical) depth. We use a grid of 1D, spherically symmetric models called MARCS (Gustafsson et al., 2008), which are well-suited for the type of stars in our stellar sample.
- NLTE grids to better account for deviations from LTE. However, NLTE calculations for the neutron-capture elements are extremely limited, and as such we synthesise these lines under the assumption of LTE.
- A list with data of atomic and/or molecular lines, including the wavelength, ionisation state, lower state excitation energy, oscillator strength and damping parameters.

In order to enable a precise and accurate comparison between models and observation, a majority of the work for the studies in this thesis was concentrated on finding suitable spectral lines and defining the line- and continuum locations. After synthesising spectra with SME, and finding the best fit between modelled and observed lines by a χ^2-minimisation, all synthetic spectra were visually checked with the observed spectra, in order to make sure that blends, spectral wings and depths were modelled properly. Spectra that ended up not being modelled properly, usually due to the low signal-to-noise ratio or strong blending, were not included in the final sample. This work is both time consuming and requires patience and attention to detail – but is necessary in order to obtain the high precision we get.

3.3 Spectral analysis of red giant stars

Historically, dwarf stars have been used in Galactic archaeology studies, partly because they have not evolved much since forming, which has allowed them to maintain their initial chemical composition. They are also similar to the most well studied star there is, the Sun, facilitating atmospheric modelling.

In the studies of Rich (1988); Zoccali et al. (2006); Lecureur et al. (2007), where they found the bulge to be overabundant in α- and iron-peak elements as compared to the disk, they compared giant and dwarf stars, respectively. Being very different objects, systematic differences may exist, sometimes severe, which means that one should preferably use similar types of stars when comparing properties of different populations. As noted by, for example, Meléndez et al. (2008),

there are good reasons to believe that the abundances obtained from dwarf and red giant stars might differ systematically, since heavy elements have been suggested to sediment in the stellar atmosphere over time – effectively depleting the photospheres of old main-sequence stars. These elements are later brought up to the stellar surface due to the increased depth of convective zones as the star evolve and becomes a red giant star. The consequence of such a depletion in dwarf stars is that they may not provide a fully representative chemical view of the Galactic cloud from which they formed. Therefore, one should be cautious when comparing abundances obtained from different types of stars (and with different analysis methods, see e.g. Jofré et al., 2019).

In order to make high-precision abundances of stars, high signal-to-noise data is required. To obtain such signal-to-noise for the more distant, and thus fainter, bulge stars, it is the best to observe giant stars that are intrinsically brighter (unless using micro-lensed dwarf stars in the bulge, e.g. Bensby et al., 2011, 2017). As such, the general norm of using giant and dwarf stars to compare the populations of the bulge and disk, respectively, has been applied by various studies that determine neutron-capture abundances (e.g. Johnson et al., 2012; Van der Swaelmen et al., 2016).

In my research, to make sure that we do not end up comparing apples to oranges, we have used high-resolution spectra of red giant stars in both the bulge and disk populations. Comparing the same types of stars, using the same atomic lines, data and analysis methods enable a differential assessment of the stellar components while minimising systematic uncertainties (see Nissen & Gustafsson, 2018; Jofré et al., 2019, for the necessity of using constant methodology).

One of the main reasons giant stars are used in the bulge instead of dwarf stars is their higher luminosity, which facilitates high-resolution spectroscopic measurements with higher signal-to-noise at the large distances where bulge stars are located. A better understanding of analysing spectra from giant stars can enhance our precision in studying more distant stars, like those in the Milky Way outer disk, halo or satellite galaxies.

However, spectroscopic analysis of red giant stars is not without its difficulties:

- Red giant stars have low effective temperatures of around 3000 to 5000 K, which cause molecules to form in the stellar atmosphere, crowding the stellar spectrum with molecular lines. These lines can blend with the atomic lines of interest, which, if not modelled properly, can affect the abundance determination. This crowding of lines can also make the continuum harder to define which can severely impact abundance measurements; abundances

are determined by measuring the contrast of the atomic line and continuum opacities.

- Red giant stars have low surface gravities, leading to lower electron pressures. This lowers the continuum opacity which in turn, in general, increases the line strength. Although this increases the risk of saturated lines, which are less sensitive to the abundance, this also strengthens otherwise too weak lines which can not be found in dwarf stars. Some examples are the forbidden [O I] line (Jönsson et al., 2017a), the HF line (Ryde et al., 2020), and the Yb line in Paper IV which are more favourably measured in red giant stars for this reason.

- Most of the spectral lines in the optical region arise due to absorption of photons by neutral element species. At the lower effective temperatures of red giants, the proportion of atoms being neutral increases (in comparison to ionised atoms), and consequently the strength of the spectral lines increases too.

Considering these challenges, red giant stars require a careful analysis and intricate detailed work to get proper abundances. Therefore, it is of great importance to select lines that have both good atomic data and are of suitable line strength in the type of star used.

Figure 3.1: A majority of the disk spectra have been obtained with the FIES spectrograph at the Nordic Optical Telescope at Observatorio del Roque de los Muchachos, La Palma. These photos are from one of my observational visits to the telescope.

Chapter 4

A neutron-capture view of the Galaxy

I don't know anything with certainty,
but seeing the stars makes me dream.

— Vincent van Gogh

Abundances of neutron-capture elements in solar neighbourhood stars have been investigated for many years, with some very early work of elemental abundances in G-type dwarfs already published in 1960 by Aller & Greenstein (1960). Over the years, the field has developed with more sophisticated analyses and ever larger samples of stars. Results revealed the complexity of the cosmic origin of the neutron-capture elements, making them an important tool in constraining the evolution of the Galaxy and its components. As we have seen in Chapter 1 and Chapter 2, these heavy elements are essential to study the Galactic scale, as well as the stellar scale, with complex processes within stars and their environments, including the final stages of stars.

In the papers of this thesis, specifically Paper I and Paper II, the abundances of several neutron-capture elements have been determined, both in the bulge- and disk populations (disk only in Paper IV). In these papers, we show the necessity of having a high-quality giant disk sample to compare with abundances for the bulge giants - an endeavour that delves into probing the distant parts of our Galaxy in higher detail. In Paper III we show the strength of combing chemical abundances with kinematical data, and – although on a small scale – provide an example for the future that lies ahead. Finally, we show the necessity of using high-resolution

spectra to get as high-precision abundances as possible. Although this thesis has a focus on obtaining the abundances from high-resolution optical spectra, in Paper IV we investigate the possibility of accessing another neutron-capture element in the infrared using high-resolution spectra, allowing us to study both the r- and s-processes in dust-covered areas of the Galaxy.

In this Chapter I will take some of the main results and conclusions from these studies, put them into context of recent and ongoing work and elaborate on the status of the neutron-capture view of the Milky Way. To conclude, I will look to the future and – from what I have learnt during the years of working on this thesis – share my thoughts and perspectives for what lies ahead in the coming times for the field of Galactic archaeology.

4.1 Comparing my results with previous studies

Many of the studies pre-dating the ones published in this thesis, e.g. Mishenina et al. (2013); Battistini & Bensby (2016); Delgado Mena et al. (2017); Guiglion et al. (2018) have used dwarf stars for probing Galactic chemical evolution. As discussed more thoroughly at the end of Chapter 3, there are several advantages of working with dwarf stars. However, they are not as bright as giant stars, thus limiting the distance at which they can reliably be observed at the same signal-to-noise ratio using the same instrumentation.

Both in Paper I and Paper II we compare our abundance trends with such literature studies in the disk. We do this to ensure that our analysis of giant stars is of the right quality before making the differential comparison with the bulge stars. We find that our method of determining abundances of heavy elements in giant stars sufficiently reproduces the abundance trends in the previous studies, see Figure 4.1. As noted earlier, to make a direct comparison of abundances obtained from dwarf and giant stars is not without risk; instead we look at the overall shapes of the trends to reassure ourselves that we properly trace the local Galactic trends.

Additionally our estimated uncertainties are, in general, smaller in comparison with the literature studies. This can also be inferred from the fact that we present tighter abundance trends with less scatter. Both the tightness and general shape-overlap of these trends points to an efficient and accurate determination of giant stellar abundances, both in the Milky Way disk and in the bulge.

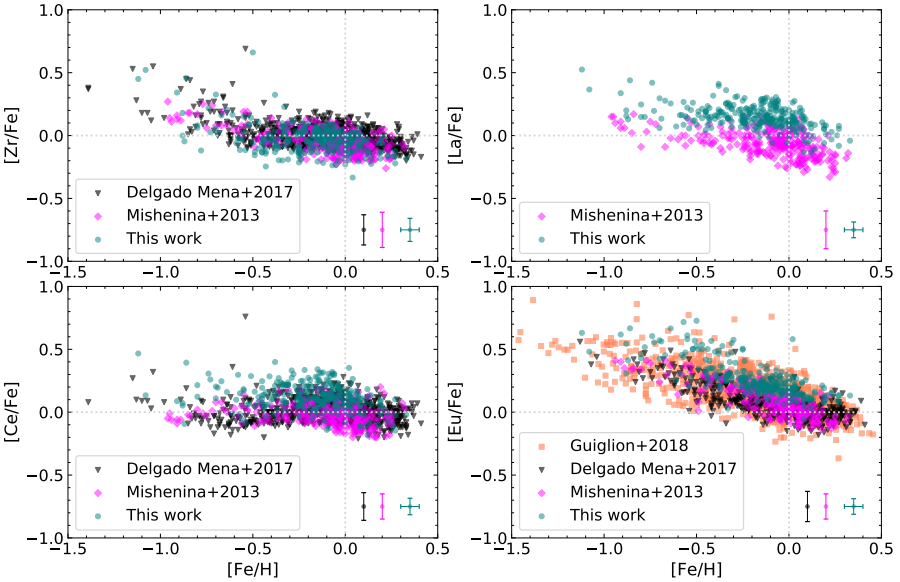

Figure 4.1: Abundance trends for [Zr,La,Ce,Eu/Fe] for the disk giants in Paper I (teal circles) and literature comparison samples (Mishenina et al., 2013; Delgado Mena et al., 2017; Guiglion et al., 2018). These plots show the overall shapes of the s- and r-process elements, as well as the tight trends produced by our method in Paper I. *Figure originally from Paper I, reproduced with permission from ESO.*

4.2 The view of the disk

In addition to noting that our observed trends have similar overall shapes to previous studies, we see that the trend for the first-peak s-process element zirconium is flatter at subsolar metallicities compared to the other two second-peak s-process elements lanthanum and cerium. This is most probably due to the different production mechanisms of first- and second-peak s-process elements (as described in Chapter 2), where lower-mass AGB stars more efficiently produce the heavier s-process elements.

As for lanthanum and cerium, they have more of a tilted, what is now in general known as a, "banana"-shape. This shape is associated with a transition from dominant production by explosive environments (e.g. supernovae) to production in AGB stars. The AGB stars are more efficient at producing the s-process elements, leading to an increase in [*s*/Fe] with metallicity. However, because 1) the

iron production in supernovae type Ia, and 2) the metallicity-dependent yields of AGB stars, producing less s-process elements at higher metallicities, the [*s*/Fe] decreases over time, resulting in the banana shape.

We can see that the r-process element europium resembles that of a typical α-element, which is to be expected with an origin from fast-evolving explosive environments (as seen by the flat europium-over-magnesium ratio in Figure 8 in Paper I). This is what similar studies in the optical has also shown, e.g. Figure 4.1.

The need for high-precision abundances are not only key for mapping the chemical history of the Milky Way, but also to untangle the cosmic origin of other elements, such as fluorine that has a suggested origin in AGB stars and can be compared to with s-process elements, e.g. lanthanum and cerium. Indeed the cerium abundances from (Paper I) was used in Ryde et al. (2020), finding that AGB stars are important for the production of fluorine from when they start enriching the interstellar medium up until solar metallicities.

A reference view for surveys

With the high precision of the abundances that we have presented, we are also happy to see that they have been adopted as a reference sample within the Galactic archaeology community. In the 16th data release of the Galactic APOGEE survey, abundances of cerium for close to 140,000 stars in the Milky Way were presented. These abundances, determined from infrared spectra on almost an industrial scale, were compared with the cerium abundances presented in Paper I. With our sample of close to 300 disk stars in Paper I, we share an extensive overlap of 105 stars with the APOGEE survey. As such, the Jönsson et al. (2020)-paper demonstrates the benefits of having high-precision abundances of giant stars to compare with, especially when moving into the less explored infrared regime.

Similarly, the 3rd data release from the Gaia space telescope included stellar parameters and abundances for 5.6 million stars (Gaia Collaboration et al., 2023). Included in these are abundances of cerium for roughly 30,000 stars (Contursi et al., 2023), that are compared with Galactic chemical evolution models to put constraints on the history of the Galactic disk, finding an overlap with the suggested three-infall model of Spitoni et al. (2023).

Although these surveys generate consistency thanks to their numbers, drawing out the chemical brushstrokes of the Galaxy, we still need to venture carefully. Indeed, in the review article on the Galactic chemical evolution of the bulge by McWilliam (2016), the need for accurately-measured abundances in the disk to serve as a reference sample for bulge measurements is emphasised.

We have seen how the sample of high-precision abundances in Paper I can be used as a reference sample in e.g. APOGEE (Jönsson et al., 2020), Gaia (Gaia Collaboration et al., 2023; Contursi et al., 2023) and Gaia-ESO (Lian et al., 2023). As such, we have chiselled out a stepping stone in high-precision and accurate abundances of red giant stars in the disk. As the next step in this endeavour, we are expanding the disk sample in this thesis to include 500 giant stars in the local disk.

Giants in the Local Disk

With the Giants in the Local Disk (GILD) sample, we are including the whole optical wavelength regime accessed by the FIES spectrograph on the Nordic Optical Telescope, opening up access to the abundances of many more elements to be determined.

With the addition of over 200 stars to the original sample presented in the papers of this thesis, we much clearer see the identified banana-shape in the disk for the s-process dominated elements, e.g. lanthanum and cerium, but it is also very prominent in the first s-process peak elements, yttrium and zirconium, see Figure 4.2 on the next page where I show some preliminary results from GILD.

We also very clearly see a transition of the trends when moving from s-process-dominated elements (e.g. lanthanum and cerium) to those having a 50/50 % contribution from the s– and r-process (e.g. praseodymium and neodymium) all the way to the r-process-dominated elements (e.g. europium and gadolinium). This transition is characterised by a decrease in the banana-shape, and more of a tilt/α-like trend as moving towards the r-process dominated elements.

Additionally, when separating the disk into high- and low-αcomponents (what I have chosen to call thick and thin disk components, respectively), as I have done in Figure 4.2 we see that they behave differently. The banana is much more prominent in the thin disk compared to the thick disk that has a flatter trend at subsolar metallicities for the s-process elements.

Lastly, we shows the high-precision of GILD, with s-process-enriched stars standing out from the otherwise tight abundance trends. The work with GILD is still due to be published, but will be important in the continued efforts of studying the Galactic scale, as well as the stellar scale with the nucleosynthetic origin of the elements.

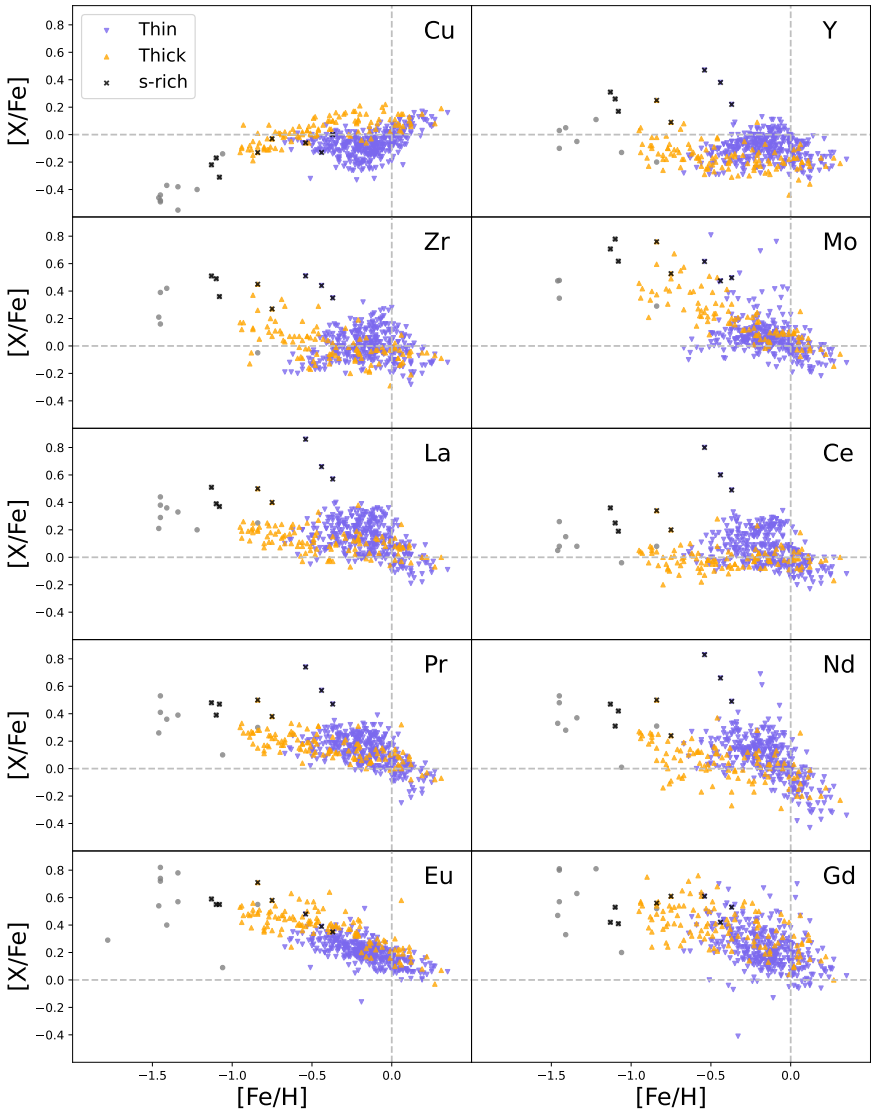

Figure 4.2: Preliminary abundance trends of neutron-capture elements from the to-be-published GILD sample. The thin (blue) and thick (yellow) disk are separated by α-abundances. Moving left to right, up to down, we can see the transition from weak s-process (Cu) to main s-process in the first s-peak (Y and Zr) and second s-peak (La and Ce) to the r-process (Eu and Gd). Stars identified as enriched in s-process, especially standing out in lanthanum and cerium, are indicated by black crosses. Abundances are normalised to solar values from Grevesse et al. (2015).

4.3 The view of the bulge

From our disk and bulge comparison in Paper I and Paper II, see Figure 4.3, it becomes evident that the bulge shows great chemical similarities with the thick disk, both for the s- and the r-process elements. There is a possible enrichment in the bulge of ~ 0.1 dex for [Mo/Fe], especially at subsolar metallicities, which can also be seen for [La/Fe] in Figure 7 in Paper I.

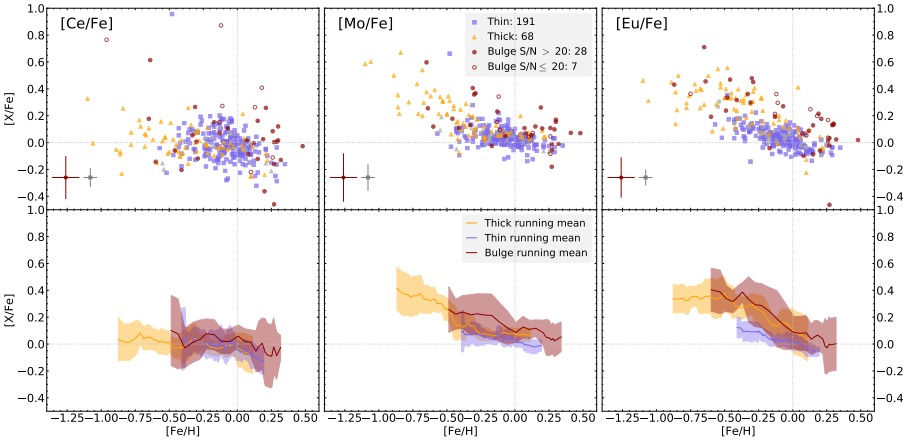

Figure 4.3: Abundance trends for [Ce,Mo,Eu/Fe] for the bulge (red), the thick disk (yellow) and thin disk (blue). The top row shows the scatter plots, with the estimated typical uncertainties indicated in the lower left corner. The bottom row shows the running mean of the data, with the shaded regions of 1 σ. *Figure originally from Paper II, reproduced with permission from ESO.*

The s-process view

In the study by Razera et al. (2022), they identify 58 bulge stars as belonging to the classical/spherodial bulge. They find the abundances for the elements studied (C, N and α-elements) to be similar to those of other bulge stars, but point out an enrichment in the s-process elements cerium. Such an enrichment in old, classical bulge stars could be due to early generations of fast-rotating massive stars. As noted in Chapter 2, the rotation of stars has been suggested to affect the s-process yields. Although we do not see such a strong enrichment of [Ce/Fe] in our bulge stars, the possible [La/Fe] enrichment is intriguing and requires further detailed studies with higher signal-to-noise spectra.

It is worthwhile noting that Johnson et al. (2012) do also find differences in [La/Fe] between the inner disk/metal-poor bulge and the thick disk. However, whilst we find a possible [La/Fe]-enrichment at subsolar metallicities in the bulge, they find a [La/Fe]-depletion.

All in all, this shows that there are still questions to resolve here, and we can only do so by combining the highest-resolution spectra with the most sophisticated stellar models and analysis tools. Possible NLTE-corrections could help in resolving this matter.

The curious case of molybdenum

When it comes to the possible [Mo/Fe] enrichment in the bulge, this could be due to the complex cosmic origin of molybdenum. Since we do not see any difference between the disk and bulge stellar populations in either [Ce/Fe] or [Eu/Fe], the high molybdenum abundance in the bulge could be linked to the p-process. In Lomaeva et al. (2019) and in Paper I, there are indications of possible enrichment in [V, Co, La/Fe] for the bulge, but these differences are not consistent with a single type of nucleosynthetic origin, meaning that – all elements considered – it cannot be concluded with confidence that the bulge is distinguishable from the thick disk in the amount and rate of SNe type I and II.

In turn, this means that the p-process sites linked to SNe type II and white dwarf sources most probably cannot produce the possible difference in the thick disk and the bulge [Mo/Fe]. Out of the suggested p-process mechanisms, the one then remaining is the rp-process, which is linked to burning on mass-accreting neutron stars (as discussed in Chapter 2). Since the stellar density is higher in the bulge compared to the disk, it could be that the fraction of binaries is higher in the bulge, leading to a higher fraction of mass-accretion neutron stars. That – to me – is the most likely explanation, since either an elevated star formation rate or a top-heavy initial mass function would make the bulge stand out in α-elements as well. However, due to the relatively low number of stars in the bulge and with the present scatter in the bulge, the above reasoning is very speculative.

It is worth noting that the molybdenum abundance is determined from one single spectral line, and although the overlap between our [Mo/Fe]-disk trend and the one published in Mishenina et al. (2019) is large, the scatter in the bulge stars is too large for any firm conclusions to be drawn. As such, since the thick disk and bulge track each other in both the s- and r-process elements [Ce/Fe] and [Eu/Fe], respectively, our results strongly suggests a similar history of the two populations.

A chemically peculiar star

The discussion on whether or not there is an old, classical component in the Milky Way bulge is still open. In Paper III we present the star B3-B8 (or MASS J18082459-2548444), a relatively metal-rich r-process-rich star in the bulge. From a literature study, we compile 22 elemental abundances (including iron) of B3-B8, finding it to have bulge-nominal abundances in all elements except for [Mo, Eu/Fe] that are enriched, see Figure 6 in Paper III.

Such a star has been discovered before in the bulge, by Johnson et al. (2013), with which our chemically peculiar star has a very similar chemical fingerprint. With the exception of metallicity where our star is close to 1 dex higher, again Figure 6 in Paper III. However, in Johnson et al. (2013), they raised uncertainties with the bulge membership of their star, referring to, at the time, upcoming kinematical data from Gaia to better constrain its membership.

Close to a decade later, such data is available. Using the kinematical data provided by Gaia, we tested the bulge-membership of the Johnson et al. (2013) star and B3-B8. We considered their distances and orbital parameters, placing B3-B8 well within the bulge, whilst the Johnson et al. (2013) star most likely is a visiting halo/thick disk star, appearing in the line-of-sight towards the bulge, see Figure 1 in Paper III

The r-process enrichment of B3-B8 is interesting both from the Galactic and the stellar/nucleosynthetic point of view. This is not the only r-enriched star observed in the Galaxy. The R-process Alliance (Holmbeck et al., 2020) have compiled over 300 stars with anomalously high [Eu/Fe]-abundances. Their presence could indicate that its birth cloud could have been close to an enriching event (such as a neutron star mergers), boosting its molybdenum and europium content. Such mechanisms has been suggested to be responsible for the enrichment in the ultra-faint dwarf galaxy Reticulum II (Ji et al., 2016; Hayes et al., 2023).

Indeed, in the simulation study of Hirai et al. (2022) they use a combined N-body/hydrodynamics code to show that r-enriched stars with low metallicities, $[\mathrm{Fe/H}] < -2.5$ dex, are likely formed in accreted low-mass dwarf galaxies. In the case of our star, its high metallicity of $[\mathrm{Fe/H}] \sim -0.65$ dex points to an *in situ* formation from locally enhanced clumps. The detection of the enriched B3-B8 star could point towards the bulge being inhomogeneously mixed. Together with that, it could also point to the existence of a classical part of the bulge, that experienced high and fast star formation early on, leading to high metallicities with local regions of high r-process content.

4.4 The low-metallicity regime

Whilst the stellar populations studied in this thesis have relatively high metallicities of [Fe/H] ≥ -2, we note an interesting scatter at very low metallicities in the halo that ties together with the discussion above. As seen in Figure 4.4, both molybdenum and ytterbium (Paper II; Paper IV), which have a significant origin from the r-process, show a large scatter in the trends at lower metallicities. This extent of scatter is not observed for the α-elements, where r-process elements otherwise share very similar trends at solar- and subsolar metallicities. The scatter is too large to have its origin in faulty abundances, that typically are on the order of a few 0.1 dex. Instead it indicates the true nature of the behaviour of neutron-capture elements at low metallicities.

It is more probable that the origin lies with inhomogeneities in the Galactic interstellar medium at low metallicites, in combination with that the sources that produce the neutron-capture elements likely are rare. This creates isolated stellar groups of high and low r-process abundances. This behaviour of an r-process-dominated element at low metallicities has been reproduced both by Hirai et al. (2022), as mentioned above, and in the stochastic chemical evolution models in Cescutti et al. (2015), which take inhomogeneous mixing into account. As seen in Figure 4.4, the scatter decreases substantially at higher metallicities, a result of a more homogeneous stellar disk.

This showcases the need for including the neutron-capture elements in chemical studies to get the full historical view of the Milky Way.

4.5 The combined view with Galactochemical evolution models

Although not the main topic of this thesis, I will take the opportunity to mention some of the continued efforts with theoretical models of the elemental abundance trends in the Galactic stellar components. Such models serve as a way of disentangling both the stellar scale (cosmic origin of the elements) and the Galactic scale (formation and history of the stellar populations). Indeed, Paper I was followed up with a paper in collaboration with Grisoni et al. (2020) to do just that.

When constructing such models, they typically build on an assumed initial mass function, a star formation efficiency and rate, and the yields for the chemical species. The first two can be set to be different depending upon the assumed characteristics of the stellar components of interest, in order to compare with the

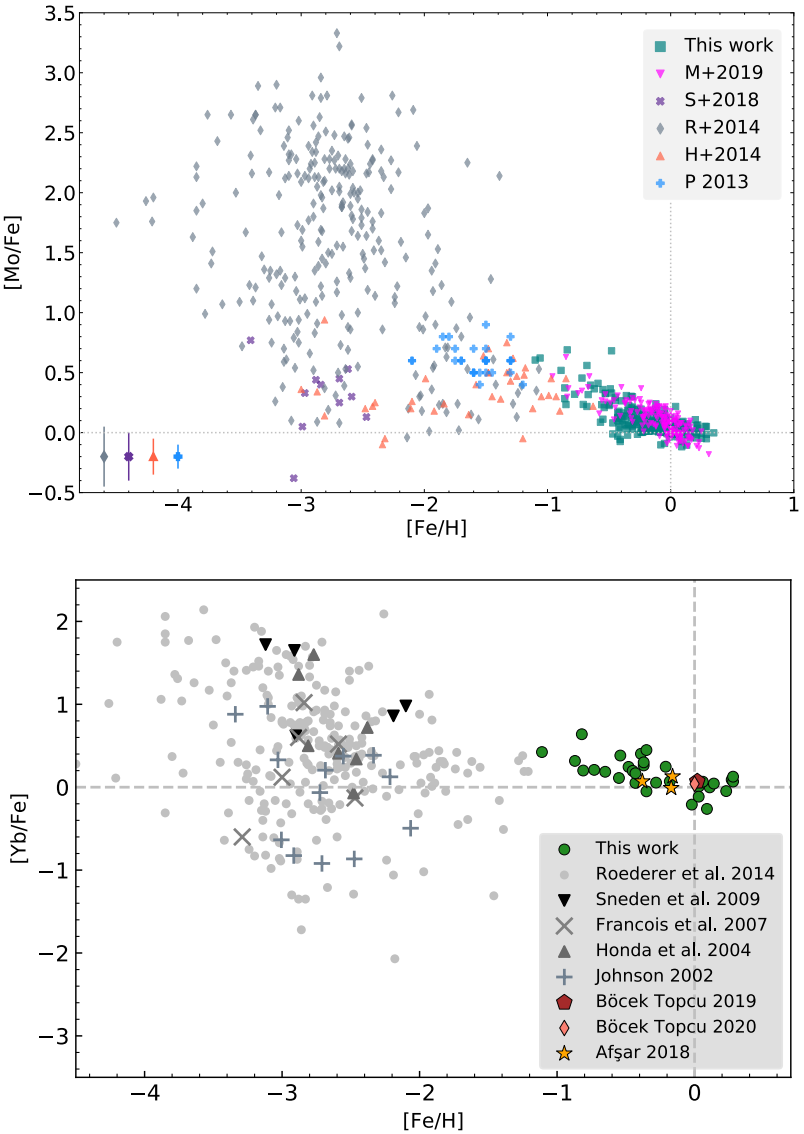

Figure 4.4: [Mo/Fe] (top) and [Yb/Fe] (bottom) as a function of [Fe/H] from observational studies, including those presented in Paper II and Paper IV, respectively. The plots showcases the large scatter found at low metallicities, which distinguishes the r-process elements from the α-elements and shows the local enrichment and inhomogeneous mixing in the early Galaxy. *Figure originally from Paper II and Paper IV, reproduced with permission from ESO.*

observed abundances. On top of that, infall of pristine gas can be modelled as well. Since the observations contain both the Galactic and stellar scales and dependencies, these are heavily complex systems to model.

Nonetheless, today such models can, to a large extent, reproduce the observed abundance trends. For instance, in the recent models by e.g. Lian et al. (2023); Molero et al. (2023) and Van der Swaelmen et al. (2023) they include r-process yields from both neutron star mergers and magneto-rotational supernovae, and rotations of massive stars, that is usually implemented to reproduce trends for s-process elements. In Lian et al. (2023) they construct models to compare with the data from Gaia-ESO, and manage to reproduce the banana-shape of the s-process, especially for the second peak s-process elements of barium, lanthanum and cerium, see Figure 2.7. Additionally, they show that, in order to reproduce the trends of [Eu/Fe], magneto-rotational supernovae have to be included.

One element that still generates difficulties in being reproduced from models is the complex element molybdenum. It is consistently underestimated (e.g. Mishenina et al., 2019; Van der Swaelmen et al., 2023; Molero et al., 2023), an issue that could be linked to the poor understanding of its cosmic origin, especially the p-isotopes. Molybdenum is in many ways the poster child indicating that there is still a lot to learn, not only when it comes to understanding the modelling of the Galaxy, but also the origin of the elements that are essential for our existence.

4.6 Looking towards the future

From my work, we can clearly see that the neutron-capture elements are important in order to arrive at a complete picture of Galactic chemical evolution. These elements make up a majority of the elements in the periodic table and can tell a story which other elements fail to tell, namely that of AGB stars, neutron star mergers, magneto-rotational supernovae, and that of the metal-poor Galaxy.

In spite of much progress, both observationally and theoretically, it is evident that we still do not have a complete picture of the Milky Way's formation history nor a full understanding of how and where the different chemical elements are created. With help from large Galactic spectroscopy surveys such as APOGEE, GALAH, LAMOST, Gaia-ESO, WEAVE, the upcoming 4MOST and MOONS, in combination with Gaia, the chemodynamical picture of the Milky Way is becoming much clearer.

The aforementioned large spectroscopic surveys all determine their stellar parameters and chemical abundances using pipelines, resulting in industrially determined abundances. For very large data-sets, the task to determine abundances manually truly is a too time-consuming task, however, it is nonetheless important that these industrial abundances can be compared to high-quality ones determined in a careful way.

Since GILD will give us access to the whole optical wavelength range, more lines will be available for the abundance determination, not only extending the range of elements studied, but also increasing the precision of the already determined abundances. This will make the GILD sample both a reference sample towards industrial abundances of giant stars as well as a reference of the local Galactic disk to be used when comparing with other populations in the Galaxy, or beyond.

Along the line-of-sight towards the Galactic bulge the optical extinction of light is high due to the large amount of dust, making it quite challenging to observe bulge stars in the optical wavelength region. However, in the bulge sample we have selected stars in fields where the optical extinction is lower, whilst still being as close to the centre of the bulge as possible.

A way to peer through the dust, is to study the stars in the infrared instead – a natural step for Galactic archaeology to take. Infrared radiation can, to a greater extent, penetrate the dust-covered areas of the Galactic disk and bulge, making it possible to observe otherwise inaccessible regions of the Galaxy such as the Galactic nucleus. This is key for gaining a better understanding of the various Galactic stellar populations.

APOGEE has successfully derived abundances for 26 elements using mid-resolution spectra in the in H-band, however the field of working with stellar spectra in the infrared is still under development and will be continued (Paper IV). This will be done partly with the mid-resolution near-infrared spectrograph MOONS on VLT, which will work in a similar wavelength regime as APOGEE.

Although MOONS will be more efficient with a large amount of fibres mounted on a large telescope, the challenges they confront of are similar to those that have already been, to a large extent, overcome by the optical community. That is, specifically having knowledge about usable lines for parameter and abundance determination. Our sample of precise data from optical spectra will play, and already has played, a role in evaluating results from the infrared field.

Nonetheless, even though APOGEE has successfully measured Ce, the best analysis options for getting abundances of (known) neutron-capture elements lie in the optical wavelength regime, due to the lack of (identified) neutron-capture

element spectral lines of suitable strength in these instruments' wavelength coverages. Europium (Eu) is the only r-process-dominated element that has been measured adequately in the bulge, making the r-process branch an unexplored area within this research field. However, with Paper IV, we show that with careful, detailed analysis of high-resolution infrared spectra, adequate abundances of the the 50/50 s/r-process element ytterbium can be determined.

Thus, given the mid-resolution of MOONS, one of the best surveys for future studies of the bulge is the optical higher-resolution survey 4MOST. However, it too has its setbacks since it will not probe very deeply, and roughly beyond 3-4 degrees out of the plane, thus avoiding the dust obscured Galactic plane. Even further into the future there is the suggested Gaia-NIR, for which I hope that a spectrograph will be incorporated, but alas there is the risk that the resolution will not be high enough for abundances of both the r- and s-process channels (through ytterbium and cerium, respectively) to be adequately determined.

Finally, the planned first-generation instruments ANDES and MOSAIC for ESO's Extremely Large Telescope (ELT), will observe in optical and near infrared using mid-resolution and high-resolution spectra, respectively. With the 39-metre mirror of the ELT, obtaining high signal-to-noise spectra with high-resolution of distant objects (such as bulge stars) will be timely cheaper.

However, with ELT being close to a decade into the future, and likely to be a very busy telescope, the sample of abundances for bulge giants presented in this thesis, is to this date, and for the near future, one of the most precise samples there is of neutron-capture elements in this important quest of understanding the formation of out home Galaxy.

References

Abbott, B. P., Abbott, R., Abbott, T. D., et al. 2017, PhRvL, 119, 161101, doi: 10.1103/PhysRevLett.119.161101

Adibekyan, V. Z., Santos, N. C., Sousa, S. G., & Israelian, G. 2011, A&A, 535, L11, doi: 10.1051/0004-6361/201118240

Agertz, O., Renaud, F., Feltzing, S., et al. 2021, MNRAS, 503, 5826, doi: 10.1093/mnras/stab322

Aller, L. H., & Greenstein, J. L. 1960, The Astrophysical Journal Supplement Series, 5, 139, doi: 10.1086/190054

Arcones, A., & Thielemann, F.-K. 2023, A&A Rv, 31, 1, doi: 10.1007/s00159-022-00146-x

Arnould, M., & Goriely, S. 2003, PhR, 384, 1, doi: 10.1016/S0370-1573(03)00242-4

Athanassoula, E., & Misiriotis, A. 2002, MNRAS, 330, 35, doi: 10.1046/j.1365-8711.2002.05028.x

Barbuy, B., Chiappini, C., & Gerhard, O. 2018, ARA&A, 56, 223, doi: 10.1146/annurev-astro-081817-051826

Battistini, C., & Bensby, T. 2016, A&A, 586, A49, doi: 10.1051/0004-6361/201527385

Belokurov, V., Erkal, D., Evans, N. W., Koposov, S. E., & Deason, A. J. 2018, MNRAS, 478, 611, doi: 10.1093/mnras/sty982

Bensby, T., Feltzing, S., & Oey, M. S. 2014, A&A, 562, A71, doi: 10.1051/0004-6361/201322631

Bensby, T., Zenn, A. R., Oey, M. S., & Feltzing, S. 2007, ApJL, 663, L13, doi: 10.1086/519792

Bensby, T., Adén, D., Meléndez, J., et al. 2011, A&A, 533, A134, doi: 10.1051/0004-6361/201117059

Bensby, T., Feltzing, S., Gould, A., et al. 2017, A&A, 605, A89, doi: 10.1051/0004-6361/201730560

Bisterzo, S., Travaglio, C., Wiescher, M., Käppeler, F., & Gallino, R. 2017, ApJ, 835, 97, doi: 10.3847/1538-4357/835/1/97

Bland-Hawthorn, J., & Gerhard, O. 2016, ARA&A, 54, 529, doi: 10.1146/annurev-astro-081915-023441

Burbidge, E. M., Burbidge, G. R., Fowler, W. A., & Hoyle, F. 1957, Reviews of Modern Physics, 29, 547, doi: 10.1103/RevModPhys.29.547

Busso, M., Gallino, R., & Wasserburg, G. J. 1999, Annual Review of Astronomy and Astrophysics, 37, 239, doi: 10.1146/annurev.astro.37.1.239

Cameron, A. G. W. 1957, PASP, 69, 201, doi: 10.1086/127051

Cescutti, G., Chiappini, C., Hirschi, R., Meynet, G., & Frischknecht, U. 2013, A&A, 553, A51, doi: 10.1051/0004-6361/201220809

Cescutti, G., Romano, D., Matteucci, F., Chiappini, C., & Hirschi, R. 2015, A&A, 577, A139, doi: 10.1051/0004-6361/201525698

Choplin, A., Siess, L., & Goriely, S. 2021, A&A, 648, A119, doi: 10.1051/0004-6361/202040170

—. 2022, A&A, 667, A155, doi: 10.1051/0004-6361/202244360

Contursi, G., de Laverny, P., Recio-Blanco, A., et al. 2023, A&A, 670, A106, doi: 10.1051/0004-6361/202244469

Côté, B., Denissenkov, P., Herwig, F., et al. 2018, ApJ, 854, 105, doi: 10.3847/1538-4357/aaaae8

Côté, B., Eichler, M., Arcones, A., et al. 2019, ApJ, 875, 106, doi: 10.3847/1538-4357/ab10db

Couch, R. G., Schmiedekamp, A. B., & Arnett, W. D. 1974, ApJ, 190, 95, doi: 10.1086/152851

Cowan, J. J., & Rose, W. K. 1977, ApJ, 212, 149, doi: 10.1086/155030

Cristallo, S., Abia, C., Straniero, O., & Piersanti, L. 2015, ApJ, 801, 53, doi: 10.1088/0004-637X/801/1/53

de Souza, R. E., & Dos Anjos, S. 1987, A&AS, 70, 465

Debattista, V. P., Ness, M., Gonzalez, O. A., et al. 2017, MNRAS, 469, 1587, doi: 10.1093/mnras/stx947

Delgado Mena, E., Tsantaki, M., Adibekyan, V. Z., et al. 2017, A&A, 606, A94, doi: 10.1051/0004-6361/201730535

Di Matteo, P. 2016, PASA, 33, e027, doi: 10.1017/pasa.2016.11

Drout, M. R., Piro, A. L., Shappee, B. J., et al. 2017, Science, 358, 1570, doi: 10.1126/science.aaq0049

Erwin, P., Saglia, R. P., Fabricius, M., et al. 2015, MNRAS, 446, 4039, doi: 10.1093/mnras/stu2376

Fermi, E. 1934, La ricerca scientifica, 5, 1921

Forsberg, R. 2021, Abundances of Neutron-Capture Elements in the Galactic Bulge and Disk from High-Resolution Spectra, Lund University Licentiate Thesis

Forsberg, R., Jönsson, H., Ryde, N., & Matteucci, F. 2019, A&A, 631, A113, doi: 10.1051/0004-6361/201936343

Forsberg, R., Rich, R. M., Nieuwmunster, N., et al. 2023, A&A, 669, A17, doi: 10.1051/0004-6361/202244305

Forsberg, R., Ryde, N., Jönsson, H., Rich, R. M., & Johansen, A. 2022, A&A, 666, A125, doi: 10.1051/0004-6361/202244013

Forsberg, U. 2016, Element 115 (Lund University)

Frischknecht, U., Hirschi, R., Pignatari, M., et al. 2016, MNRAS, 456, 1803, doi: 10.1093/mnras/stv2723

Fröhlich, C., Martínez-Pinedo, G., Liebendörfer, M., et al. 2006, PhRvL, 96, 142502, doi: 10.1103/PhysRevLett.96.142502

Gaia Collaboration, Prusti, T., de Bruijne, J. H. J., et al. 2016, A&A, 595, A1, doi: 10.1051/0004-6361/201629272

Gaia Collaboration, Brown, A. G. A., Vallenari, A., et al. 2018, A&A, 616, A1, doi: 10.1051/0004-6361/201833051

Gaia Collaboration, Recio-Blanco, A., Kordopatis, G., et al. 2023, A&A, 674, A38, doi: 10.1051/0004-6361/202243511

Garver, B. R., Nidever, D. L., Debattista, V. P., Beraldo e Silva, L., & Khachaturyants, T. 2023, ApJ, 953, 128, doi: 10.3847/1538-4357/acdfc6

Gilmore, G., & Reid, N. 1983, MNRAS, 202, 1025, doi: 10.1093/mnras/202.4.1025

Goriely, S., José, J., Hernanz, M., Rayet, M., & Arnould, M. 2002, A&A, 383, L27, doi: 10.1051/0004-6361:20020088

Gray, D. F. 2005, The Observation and Analysis of Stellar Photospheres, 3rd Edition (Cambridge University Press, 2005.), 550

Grevesse, N., Scott, P., Asplund, M., & Sauval, A. J. 2015, A&A, 573, A27, doi: 10.1051/0004-6361/201424111

Grisoni, V., Cescutti, G., Matteucci, F., et al. 2020, MNRAS, 492, 2828, doi: 10.1093/mnras/staa051

Guiglion, G., de Laverny, P., Recio-Blanco, A., & Prantzos, N. 2018, A&A, 619, A143, doi: 10.1051/0004-6361/201833782

Günter, M. 2015, Dagens Nyheter

Gustafsson, B., Edvardsson, B., Eriksson, K., et al. 2008, A&A, 486, 951, doi: 10.1051/0004-6361:200809724

Hampel, M., Stancliffe, R. J., Lugaro, M., & Meyer, B. S. 2016, ApJ, 831, 171, doi: 10.3847/0004-637X/831/2/171

Hansen, T. T., Simon, J. D., Li, T. S., et al. 2023, A&A, 674, A180, doi: 10.1051/0004-6361/202346168

Hayden, M. R., Bovy, J., Holtzman, J. A., et al. 2015, ApJ, 808, 132, doi: 10.1088/0004-637X/808/2/132

Hayes, C. R., Venn, K. A., Waller, F., et al. 2023, arXiv e-prints, arXiv:2306.04804, doi: 10.48550/arXiv.2306.04804

Haywood, M., Di Matteo, P., Snaith, O., & Lehnert, M. D. 2015, A&A, 579, A5, doi: 10.1051/0004-6361/201425459

Heiter, U., Lind, K., Bergemann, M., et al. 2021, A&A, 645, A106, doi: 10.1051/0004-6361/201936291

Helmi, A., Babusiaux, C., Koppelman, H. H., et al. 2018, Nature, 563, 85, doi: 10.1038/s41586-018-0625-x

Herschel, W. 1786, Philosophical Transactions of the Royal Society of London Series I, 76, 457

Hirai, Y., Beers, T. C., Chiba, M., et al. 2022, MNRAS, 517, 4856, doi: 10.1093/mnras/stac2489

Holmbeck, E. M., Hansen, T. T., Beers, T. C., et al. 2020, ApJS, 249, 30, doi: 10.3847/1538-4365/ab9c19

Holmberg, E. 1941, ApJ, 94, 385, doi: 10.1086/144344

Hubble, E. 1929, Proceedings of the National Academy of Science, 15, 168, doi: 10.1073/pnas.15.3.168

Imig, J., Price, C., Holtzman, J. A., et al. 2023, arXiv e-prints, arXiv:2307.13887, doi: 10.48550/arXiv.2307.13887

Ji, A. P., Frebel, A., Chiti, A., & Simon, J. D. 2016, Nature, 531, 610, doi: 10.1038/nature17425

Jofré, P., Heiter, U., & Soubiran, C. 2019, ARA&A, 57, 571, doi: 10.1146/annurev-astro-091918-104509

Johnson, C. I., McWilliam, A., & Rich, R. M. 2013, ApJL, 775, L27, doi: 10.1088/2041-8205/775/1/L27

Johnson, C. I., Rich, R. M., Kobayashi, C., & Fulbright, J. P. 2012, ApJ, 749, 175, doi: 10.1088/0004-637X/749/2/175

Jönsson, H., Ryde, N., Nordlander, T., et al. 2017a, A&A, 598, A100, doi: 10.1051/0004-6361/201629128

Jönsson, H., Ryde, N., Schultheis, M., & Zoccali, M. 2017b, A&A, 600, C2, doi: 10.1051/0004-6361/201629129e

Jönsson, H., Holtzman, J. A., Allende Prieto, C., et al. 2020, AJ, 160, 120, doi: 10.3847/1538-3881/aba592

Joyce, M., Johnson, C. I., Marchetti, T., et al. 2023, ApJ, 946, 28, doi: 10.3847/1538-4357/acb692

Kant, I. 1755, Allgemeine Naturgeschichte und Theorie des Himmels

Karakas, A. I., & Lattanzio, J. C. 2014, PASA, 31, e030, doi: 10.1017/pasa.2014.21

Kobayashi, C., Karakas, A. I., & Lugaro, M. 2020, ApJ, 900, 179, doi: 10.3847/1538-4357/abae65

Koike, O., Hashimoto, M.-a., Kuromizu, R., & Fujimoto, S.-i. 2004, ApJ, 603, 242, doi: 10.1086/381354

Kormendy, J., & Kennicutt, Robert C., J. 2004, ARA&A, 42, 603, doi: 10.1146/annurev.astro.42.053102.134024

Kratz, K.-L., Farouqi, K., Pfeiffer, B., et al. 2007, ApJ, 662, 39, doi: 10.1086/517495

Lecureur, A., Hill, V., Zoccali, M., et al. 2007, A&A, 465, 799, doi: 10.1051/0004-6361:20066036

Lian, J., Storm, N., Guiglion, G., et al. 2023, MNRAS, doi: 10.1093/mnras/stad2390

Lodders, K., Palme, H., & Gail, H.-P. 2009, Solar system, 712

Lomaeva, M., Jönsson, H., Ryde, N., Schultheis, M., & Thorsbro, B. 2019, A&A, 625, A141, doi: 10.1051/0004-6361/201834247

Lundmark, K. 1920, Kungl. Svenska Vetenskapsakademiens Handlingar, 60, 1

Lundmark, K. 1924, Monthly Notices of the Royal Astronomical Society, Vol. 84, p. 747-770, 84, 747

Lundmark, K. 1930, Meddelanden fran Lunds Astronomiska Observatorium Serie I, 125, 1

Lütticke, R., Dettmar, R. J., & Pohlen, M. 2000, A&AS, 145, 405, doi: 10.1051/aas:2000354

Madau, P., & Dickinson, M. 2014, ARA&A, 52, 415, doi: 10.1146/annurev-astro-081811-125615

Matteucci, F. 2012, Chemical Evolution of Galaxies, doi: 10.1007/978-3-642-22491-1

Matteucci, F., & Brocato, E. 1990, ApJ, 365, 539, doi: 10.1086/169508

Matteucci, F., Romano, D., Arcones, A., Korobkin, O., & Rosswog, S. 2014, MNRAS, 438, 2177, doi: 10.1093/mnras/stt2350

McWilliam, A. 2016, PASA, 33, e040, doi: 10.1017/pasa.2016.32

Meléndez, J., Asplund, M., Alves-Brito, A., et al. 2008, A&A, 484, L21, doi: 10.1051/0004-6361:200809398

Messier, C. 1781, Catalogue des Nébuleuses et des Amas d'Étoiles (Catalog of Nebulae and Star Clusters), Connoissance des Temps ou des Mouvements Célestes, for 1784, p. 227-267

Minchev, I., Martig, M., Streich, D., et al. 2015, ApJL, 804, L9, doi: 10.1088/2041-8205/804/1/L9

Mishenina, T., Pignatari, M., Gorbaneva, T., et al. 2019, MNRAS, 489, 1697, doi: 10.1093/mnras/stz2202

Mishenina, T., Pignatari, M., Carraro, G., et al. 2015, MNRAS, 446, 3651, doi: 10.1093/mnras/stu2337

Mishenina, T. V., Pignatari, M., Korotin, S. A., et al. 2013, A&A, 552, A128, doi: 10.1051/0004-6361/201220687

Molero, M., Magrini, L., Matteucci, F., et al. 2023, MNRAS, 523, 2974, doi: 10.1093/mnras/stad1577

Montelius, M., Forsberg, R., Ryde, N., et al. 2022, A&A, 665, A135, doi: 10.1051/0004-6361/202243140

Ness, M., & Freeman, K. 2016, PASA, 33, e022, doi: 10.1017/pasa.2015.51

Ness, M., Freeman, K., Athanassoula, E., et al. 2013, MNRAS, 432, 2092, doi: 10.1093/mnras/stt533

Nissen, P. E., & Gustafsson, B. 2018, A&A Rv, 26, 6, doi: 10.1007/s00159-018-0111-3

Piskunov, N., & Valenti, J. A. 2017, A&A, 597, A16, doi: 10.1051/0004-6361/201629124

Prantzos, N., Abia, C., Cristallo, S., Limongi, M., & Chieffi, A. 2020, MNRAS, 491, 1832, doi: 10.1093/mnras/stz3154

Prialnik, D. 2000, An Introduction to the Theory of Stellar Structure and Evolution (Cambridge University Press)

Ratcliffe, B., Minchev, I., Anders, F., et al. 2023, MNRAS, doi: 10.1093/mnras/stad1573

Rauscher, T., Dauphas, N., Dillmann, I., et al. 2013, Reports on Progress in Physics, 76, 066201, doi: 10.1088/0034-4885/76/6/066201

Razera, R., Barbuy, B., Moura, T. C., et al. 2022, MNRAS, 517, 4590, doi: 10.1093/mnras/stac2136

Renaud, F., Agertz, O., Andersson, E. P., et al. 2021a, MNRAS, 503, 5868, doi: 10.1093/mnras/stab543

Renaud, F., Agertz, O., Read, J. I., et al. 2021b, MNRAS, 503, 5846, doi: 10.1093/mnras/stab250

Renzini, A. 1999, in Spiral Galaxies in the Near-IR: Proceedings of the ESO/MPA Workshop Held at Garching, Germany, 7–9 June 1995, Springer, 95–104

Rich, R. M. 1988, AJ, 95, 828, doi: 10.1086/114681

Rojas-Arriagada, A., Zoccali, M., Schultheis, M., et al. 2019, A&A, 626, A16, doi: 10.1051/0004-6361/201834126

Ryde, N., Jönsson, H., Mace, G., et al. 2020, ApJ, 893, 37, doi: 10.3847/1538-4357/ab7eb1

Saha, K. 2015, ApJL, 806, L29, doi: 10.1088/2041-8205/806/2/L29

Schatz, H., Aprahamian, A., Barnard, V., et al. 2001, PhRvL, 86, 3471, doi: 10.1103/PhysRevLett.86.3471

Shapley, H. 1918, PASP, 30, 42, doi: 10.1086/122686

Shapley, H., & Curtis, H. D. 1921, Bulletin of the National Research Council, 2, 171

Shen, J., Rich, R. M., Kormendy, J., et al. 2010, ApJL, 720, L72, doi: 10.1088/2041-8205/720/1/L72

Shen, J., & Zheng, X.-W. 2020, Research in Astronomy and Astrophysics, 20, 159, doi: 10.1088/1674-4527/20/10/159

Siegel, D. M. 2022, Nature Reviews Physics, 4, 306, doi: 10.1038/s42254-022-00439-1

Skúladóttir, Á., & Salvadori, S. 2020, A&A, 634, L2, doi: 10.1051/0004-6361/201937293

Spitoni, E., Recio-Blanco, A., de Laverny, P., et al. 2023, A&A, 670, A109, doi: 10.1051/0004-6361/202244349

Suess, H. E., & Urey, H. C. 1956, Reviews of Modern Physics, 28, 53, doi: 10.1103/RevModPhys.28.53

Tanvir, N. R., Levan, A. J., González-Fernández, C., et al. 2017, ApJL, 848, L27, doi: 10.3847/2041-8213/aa90b6

Thorsbro, B., Ryde, N., Schultheis, M., et al. 2018, ApJ, 866, 52, doi: 10.3847/1538-4357/aadb97

Travaglio, C., Gallino, R., Arnone, E., et al. 2004, ApJ, 601, 864, doi: 10.1086/380507

Travaglio, C., Gallino, R., Rauscher, T., Röpke, F. K., & Hillebrandt, W. 2015, ApJ, 799, 54, doi: 10.1088/0004-637X/799/1/54

Trippella, O., Busso, M., Maiorca, E., Käppeler, F., & Palmerini, S. 2014, ApJ, 787, 41, doi: 10.1088/0004-637X/787/1/41

Valenti, E., Zoccali, M., Gonzalez, O. A., et al. 2016, A&A, 587, L6, doi: 10.1051/0004-6361/201527500

Valenti, J. A., & Piskunov, N. 1996, A&AS, 118, 595

Van der Swaelmen, M., Barbuy, B., Hill, V., et al. 2016, A&A, 586, A1, doi: 10.1051/0004-6361/201525709

Van der Swaelmen, M., Viscasillas Vázquez, C., Cescutti, G., et al. 2023, A&A, 670, A129, doi: 10.1051/0004-6361/202243764

Wright, T. 1750, An original theory or new hypothesis of the universe: founded upon general phaenomena of the visible creation; and particularly the Via the laws of nature, and solving by mathematical principles, doi: 10.3931/e-rara-28672

Zoccali, M., Lecureur, A., Barbuy, B., et al. 2006, A&A, 457, L1, doi: 10.1051/0004-6361:20065659

Part II

Scientific Publications

Author contributions

A summary of my contribution to each of the papers included in this thesis.

Paper I

Abundances of disk and bulge giants from high-resolution optical spectra IV. Zr, La, Ce, Eu
R. Forsberg, H. Jönsson, N. Ryde, and F. Matteucci (2019)
In this study, I led the abundance determination of the elements, including identifying lines, placing continuum– and linemasks for the spectra and visually inspecting the fits of all of the synthetic spectra. I used the previously determined stellar parameters from my co-supervisor Henrik Jönsson, and did the analysis in close collaboration with him. I led the writing of the paper.

Paper II

Abundances of disk and bulge giants from high-resolution optical spectra V. Molybdenum: The p-process element
R. Forsberg, N. Ryde, H. Jönsson, R. M. Rich, and A. Johansen (2022)

In this study, I led the abundance determination of molybdenum, including identifying the line, placing continuum– and linemasks for the spectra and visually inspecting the fits of all of the synthetic spectra. The method built on the one in Paper I, and similarly I used the previously determined stellar parameters from my co-supervisor Henrik Jönsson. I led the writing of the paper.

Paper III

First r-process enhanced star confirmed as a member of the Galactic bulge
R. Forsberg, R. M. Rich, N. Nieuwmunster, H. Jönsson, M. Schultheis, N. Ryde, and B. Thorsbro (2023)

In this study, I contacted experts in the field to discuss and contribute to the ideas that resulted in the paper, especially R. Michael Rich. As such, I complied the literature studies and determined the orbital parameters to confirm the bulge membership. The distance estimates were done in close collaboration with Mathias Schultheis. I led the writing of the paper.

Paper IV

Chemical evolution of ytterbium in the Galactic disk
M. Montelius, **R. Forsberg**, N. Ryde , H. Jönsson, M. Afşar, A. Johansen, K. F. Kaplan, H. Kim, G. Mace, C. Sneden, and B. Thorsbro (2022)

In this study, I participated greatly in the development of the ideas behind the paper, supporting Martin Montelius in the analysis of the data. I co-wrote the paper together with Martin Montelius, where I focused on the aspects of the Galactochemical evolution of ytterbium in the disk and how it compares with other neutron-capture elements.

Paper I

A&A 631, A113 (2019)
https://doi.org/10.1051/0004-6361/201936343

Astronomy & Astrophysics

Abundances of disk and bulge giants from high-resolution optical spectra

IV. Zr, La, Ce, Eu⋆,⋆⋆

R. Forsberg[1], H. Jönsson[1,2], N. Ryde[1,3], and F. Matteucci[4,5,6]

[1] Lund Observatory, Department of Astronomy and Theoretical Physics, Lund University, Box 43, 221 00 Lund, Sweden
e-mail: rebecca@astro.lu.se
[2] Materials Science and Applied Mathematics, Malmö University, 205 06 Malmö, Sweden
[3] Université Côte d'Azur, Observatoire de la Côte d'Azur, CNRS, Laboratoire Lagrange, Bd de l'Observatoire, CS 34229, 06304 Nice Cedex 4, France
[4] Dipartimento di Fisica, Sezione di Astronomia, Università di Trieste, via G.B. Tiepolo 11, 34131 Trieste, Italy
[5] INAF – Osservatorio Astronomico di Trieste, via G.B. Tiepolo 11, 34131 Trieste, Italy
[6] INFN – Sezione di Trieste, via Valerio 2, 34134 Trieste, Italy

Received 18 July 2019 / Accepted 18 September 2019

ABSTRACT

Context. Observations of the Galactic bulge suggest that the disk formed through secular evolution rather than gas dissipation and/or mergers, as previously believed. This would imply very similar chemistry in the disk and bulge. Some elements, such as the α-elements, are well studied in the bulge, but others like the neutron-capture elements are much less well explored. Stellar mass and metallicity are factors that affect the neutron-capture process. Due to this, the enrichment of the ISM and the abundance of neutron-capture elements vary with time, making them suitable probes for Galactic chemical evolution.
Aims. In this work, we make a differential comparison of neutron-capture element abundances determined in the local disk(s) and the bulge, focusing on minimising possible systematic effects in the analysis, with the aim of finding possible differences/similarities between the populations.
Methods. Abundances are determined for Zr, La, Ce, and Eu in 45 bulge giants and 291 local disk giants, from high-resolution optical spectra. The abundances are determined by fitting synthetic spectra using the SME-code. The disk sample is separated into thin- and thick-disk components using a combination of abundances and kinematics.
Results. We find flat Zr, La, and Ce trends in the bulge, with a ∼0.1 dex higher La abundance compared with the disk, possibly indicating a higher s-process contribution for La in the bulge. [Eu/Fe] decreases with increasing [Fe/H], with a plateau at around [Fe/H] ∼ −0.4, pointing at similar enrichment to α-elements in all populations.
Conclusions. We find that the r-process dominated the neutron-capture production at early times both in the disks and bulge. Further, [La/Eu] ratios for the bulge are systematically higher than for the thick disk, pointing to either a) a different amount of SN II or b) a different contribution of the s-process in the two populations. Considering [(La+Ce)/Zr], the bulge and the thick disk follow each other closely, suggesting a similar ratio of high-to-low-mass asymptotic giant branch stars.

Key words. stars: abundances – Galaxy: bulge – solar neighborhood – Galaxy: evolution

1. Introduction

Our view of the structure and formation of the Galactic bulge has changed dramatically over the past decade. Earlier, the prevailing view was that the bulge is a spheroid in a disk formed in an early, rapid, dissipative collapse (e.g. Immeli et al. 2004), naturally resulting from major mergers for example, converting disks to classical bulges (e.g. Shen & Li 2016). However, with new findings and an accumulation of data, what we call the bulge is today predominately considered to be mainly the inner structures of the Galactic bar seen edge-on (e.g. Portail et al. 2017). The details of its structure and timescales for its formation are nevertheless unclear (e.g. Barbuy et al. 2018).

Metallicity distributions and abundance-ratio trends with metallicity provide important means to determine the evolution of stellar populations, also in the bulge. Trends of different element groups formed in different nucleosynthetic channels provide strong complementary constraints. Also, comparisons of trends between different stellar populations, for example the local thick disk, can be used to constrain the history of the bulge. Whether or not there is an actual difference in abundance trends with metallicity between the bulge and the local thick disk is unclear (McWilliam 2016; Barbuy et al. 2018; Zasowski et al. 2019; Lomaeva et al. 2019). Some elements such as Sc,

⋆ Full Tables A.1–A.4 are only available at the CDS via anonymous ftp to cdsarc.u-strasbg.fr (130.79.128.5) or via http://cdsarc.u-strasbg.fr/viz-bin/cat/J/A+A/631/A113

⋆⋆ Based on observations made with the Nordic Optical Telescope (programs 51-018 and 53-002) operated by the Nordic Optical Telescope Scientific Association at the Observatorio del Roque de los Muchachos, La Palma, Spain, of the Instituto de Astrofisica de Canarias, spectral data retrieved from PolarBase at Observatoire Midi Pyrénées, and observations collected at the European Southern Observatory, Chile (ESO programs 71.B-0617(A), 073.B-0074(A), and 085.B-0552(A)).

V, Cr, Co, Ni, and Cu show differences in some investigations, whereas others show great similarities. New abundance studies minimising systematic uncertainties are clearly needed.

An important nucleosynthetic channel that has not yet been thoroughly investigated in the bulge is that of the heavy elements, namely the neutron-capture elements. These can be divided into two groups: the slow (s)- and rapid (r)-process elements, depending on the timescales between the subsequent β-decay and that of the interacting neutron flux (Burbidge et al. 1957). The neutron flux in the s-process is such that the timescale of interaction is slower than the subsequent β-decay, making the elements created in this process stable and generally found in the so-called valley of stability, whilst it is the other way around for the r-process, resulting in the creation of heavier elements. As a point of reference, the s-process therefore produces the lighter elements after iron ($A \geq 60$), whereas the r-process is the dominating production process for the heaviest elements. Nonetheless, it is important to keep in mind that the production of heavier elements is a combination of the two processes and an "s- or r-process element" simply refers to an element with a dominating contribution from one of the processes. The neutron densities required for the s- and r-processes are $\leq 10^{7}-10^{15}$ cm^{-3} (Busso et al. 1999; Karakas & Lattanzio 2014) and somewhere between $10^{24}-10^{28}$ cm^{-3} (Kratz et al. 2007), respectively, putting some constraints on the astrophysical sites where they can occur.

The s-process can in turn be divided into three sub-processes: the weak, main and strong s-processes taking place in massive stars (weak) and asymptotic giant branch (AGB) stars (main, strong). Furthermore, the s-process elements can be divided into the light, heavy, and very heavy s-process elements, the naming originating from their atomic masses of A = 90, 138 and 208 (around Zr, La, and Pb, respectively). A build-up is created at these stable nuclei (N = 50, 82, and 126, also known as magic numbers) due to isotopes with low neutron cross sections, creating bottlenecks in the production of heavier elements and in turn, peaks of stable isotopes. Thus, the naming first-second-, and third-peak s-process is often also used for the light, heavy and very heavy s-process elements. In this work, light and heavy s-process elements produced in the main s-process will be analysed (Zr, La, Ce).

The main s-process takes place in the interior of low- and intermediate-mass AGB stars (Herwig 2005; Karakas & Lattanzio 2014) with the neutrons originating from the reactions ^{13}C$(\alpha, n)^{16}$O and ^{22}Ne$(\alpha, n)^{25}$Mg. The second reaction takes place at higher temperatures in AGB stars with initial masses of >4 $M_{\odot}$. The process takes place in the so-called ^{13}C-pocket in between the hydrogen and helium burning shells during the third dredge-up (TDU; Bisterzo et al. 2017). Since AGB stars have an onset delay on cosmic scales, a non-negligible fraction of the s-process-dominated elements is likely to originate from the r-process at early times. Furthermore, the light s-process elements (first-peak s-process) can have a possible production from the weak s-process, taking place in helium core burning and in the subsequent convective carbon-burning-shell phase in massive stars (Couch et al. 1974). However, previous observations cannot fully explain the abundance of the light s-process elements at early times, and other possible origins have therefore been proposed (e.g. LEPP; Travaglio et al. 2004; Cristallo et al. 2015).

The production site(s) for r-process elements is yet to be constrained, but the proposed sites are various neutron-rich (violent) events, such as core-collapse supernovae (CC SNe), collapsars, and the mergers of heavy bodies in binaries, such as neutron star mergers (Sneden et al. 2000; Thielemann et al. 2011, 2017). The electromagnetic counterpart to the observed neutron merger GW170817 (Abbott et al. 2017) indeed showed r-process elements. Research is still ongoing to determine whether or not neutron star mergers are the only, or even the dominating, source of r-process elements (e.g. Thielemann et al. 2018; Côté et al. 2019; Siegel et al. 2019; Kajino et al. 2019).

In order to put constraints on the neutron capture yields, it is important to have reliable observational abundances to compare with the models. In the review paper on the chemical evolution of the bulge by McWilliam (2016), the necessity of having properly measured abundances for the disk in order to have a reference sample for bulge measurements is stressed, and these are provided in this work.

Regarding the determination of neutron-capture elements in bulge stars, such analyses have been made previously by Johnson et al. (2012), Van der Swaelmen et al. (2016), and Duong et al. (2019). Johnson et al. (2012) studied stars in Plaut's field ($b = -8°$) observed with the Hydra multifibre spectrograph at the Blanco 4m telescope, determining the abundances of Zr, La, Nd, and Eu. Their [La/Fe] trend versus metallicity of the stars in the bulge field is clearly different from that of the thick disk. These latter authors therefore concluded that the metal-poor bulge, or the inner disk, is likely chemically different from that of the thick disk. Van der Swaelmen et al. (2016) studied Ba, La, Ce, Nd and Eu in 56 Galactic bulge giants observed with FLAMES/UVES at the VLT, finding that the s-process elements Ba, La, Ce, and Nd have decreasing [Ba,La,Ce,Nd/Fe] abundances with increasing metallicity, separating them from the flatter thick-disk trends. Additionally, in the work by Duong et al. (2019), Zr, La, Ce, Nd and Eu are measured for a large bulge sample at latitudes of $b = -10°$, $-7.5°$ and $-5°$, observed with the HERMES spectrograph on the Anglo-Australian Telescope. These latter authors find indications of the bulge having a higher star formation rate than that of the disk.

Johnson et al. (2012) and Van der Swaelmen et al. (2016) compare their bulge abundances with previously determined disk abundances, mainly from dwarf stars, which might obstruct the interpretation of the comparative abundances due to the risk of systematic uncertainties between analyses of dwarf and giant stars[1]. Previous studies by Meléndez et al. (2008) and Gonzalez et al. (2015) stressed the importance of comparing stars within the same evolutionary stage. Furthermore, in investigations of atomic diffusion and mixing in stars (Korn et al. 2007; Lind et al. 2008; Nordlander et al. 2012; Gruyters et al. 2016; Souto et al. 2019; Liu et al. 2019), it has been shown that dwarf stars might have systematically lower elemental abundances compared to evolved stars, suggesting that abundances measured from dwarf stars are too low. The magnitude of this depletion is measurable and should, in general, be considered for the relevant elements in order to properly probe the Galactic composition and its evolution based on dwarf stars.

In this paper, we study the four neutron-capture elements Zr, La, Ce, and Eu determined from optical spectra of giants observed with FLAMES/UVES for the bulge sample. We compare the obtained abundance-ratio trends with that of the local disk obtained from a comparison sample of similarly analysed giants (observed with FIES at high resolution in the same wavelength range). Section 2 describe the bulge and disk samples. The same methodology for determining the stellar parameters

[1] Duong et al. (2019), to as large an extent as possible, use the same atomic data and analysis method in their work as their comparison sample, GALAH (Buder et al. 2018), to minimise systematic offsets.

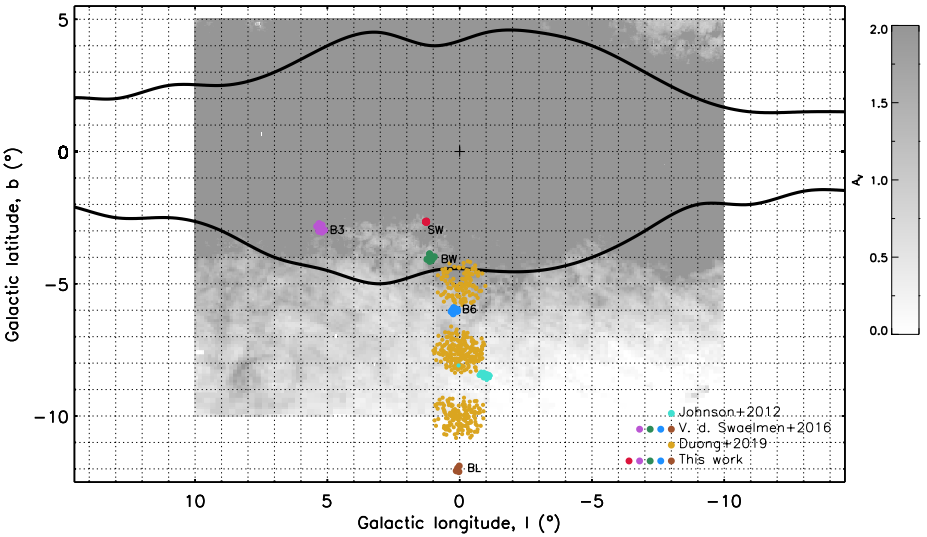

Fig. 1. Map of the Galactic bulge showing the five analysed fields (SW, B3, BW, B6, and BL). The bulge samples from Johnson et al. (2012), Van der Swaelmen et al. (2016), and Duong et al. (2019) are also marked in the figure. The dust extinction towards the bulge is taken from Gonzalez et al. (2011, 2012) and scaled to optical extinction (Cardelli et al. 1989). The scale saturates at $A_V = 2$, which is the upper limit in the figure. The COBE/DIRBE contours of the Galactic bulge, in black, are from Weiland et al. (1994).

and abundances (a carefully chosen set of spectral lines) ensures a minimisation of the systematic uncertainties in the comparison of the two samples, following the same methodology as the previous papers in this series; Jönsson et al. (2017a,b); Lomaeva et al. (2019), see Sect. 3. We present the results in Sect. 4 and discuss these in Sect. 5.

2. Observations

2.1. Bulge sample

Since large amounts of dust lies in the line of sight towards the Galactic centre resulting in a high optical extinction, observing bulge stars can be challenging at optical wavelengths. Our ambition was to include fields as close to the centre of the bulge as possible, whilst keeping to regions where the extinction is manageable.

The Galactic bulge sample consists of 45 giants (see Table A.1). The spectra were obtained using the spectrometer FLAMES/UVES mounted on the VLT, Chile, observed in May-August 2003-2004. Twenty-seven of these spectra were also analysed in Van der Swaelmen et al. (2016). In addition to these, 18 spectra from the Sagittarius Window, $(l, b) = (1.29°, -2.65°)$, lying closer to the Galactic plane in a region with relatively low extinction, are added to the sample analysed here. These were observed in August 2011 (ESO programme 085.B-0552(A)). In total, five bulge fields are included in the bulge sample: SW (the Sagittarius Window), BW (Baade's Window), BL (the Blanco field), B3, and B6[2]. The fields can be seen in Fig. 1, overlaid on an optical extinction map, together with the fields analysed in Johnson et al. (2012) and Duong et al. (2019). From Fig. 1 one can see that the SW field lies in a region of relatively low extinction and closer to the Galactic plane than the other fields.

The FLAMES/UVES instrument allows for simultaneous observation of up to seven stars. Depending on the extinction and local conditions, each setting in our observations required an integration time of somewhere between 5 and 12 h. The achieved signal-to-noise ratios (S/N) of the recorded bulge spectra are between 10 and 80. The resolving power of the spectra is $R \sim 47\,000$ and the usable wavelength coverage is limited to the range 5800–6800 Å.

The distances to our bulge stars are estimated to range between 4 and 12 kpc from the solar system (Bailer-Jones et al. 2018), placing the stars within the Galactic regions classified as the bulge by Wegg et al. (2015). Although it should be noted that distance estimation can be rather troublesome and *Gaia* DR2 (Gaia Collaboration 2016, 2018) reports a parallax uncertainty higher than 20% for the majority of our bulge stars.

2.2. Disk sample

The disk sample consists of 291 giants stars, a majority of these placed within 2 kpc of the solar system (see Table A.2). The bulk of the sample is observed at the Nordic Optical Telescope (NOT), La Palma, using the FIbre-fed Echelle Spectrograph (FIES; Telting et al. 2014), under the programme 51-018 (150 stars) in May–June 2015 and 53-002 (63 stars) in June 2016. Forty-one spectra were taken from the stellar sample in Thygesen et al. (2012), also observed using the FIES at the NOT. An additional 18 spectra were downloaded from the FIES archive. Lastly, 19

[2] The naming of the fields follows the convention seen in Lecureur et al. (2007).

spectra were taken from the PolarBase data base (Petit et al. 2014) where NARVAL and ESPaDOnS were used (mounted on Telescope *Bernard Lyot* and Canada–France–Hawaii Telescope, respectively). The FIES and PolarBase have similar resolving powers of $R \sim 67\,000$ and $R \sim 65\,000$, respectively.

All three spectrometers cover wide regions in the optical domain, but in order to maximise the coherency in this work, the wavelength region used is restricted to that of the bulge spectra: 5800–6800 Å. The resulting S/N of the FIES spectra are around 80–120 per data point in the reduced spectrum. Similar values can be found for the PolarBase spectra whereas the Thygesen et al. (2012) spectra have a lower S/N of about 30–50. Details of how the S/N was calculated can be found in Jönsson et al. (2017a).

The reduction of the FIES spectra was preformed using the standard FIES pipeline and the Thygesen et al. (2012) and PolarBase data was already reduced. A crude normalisation of all spectra was done initially with the IRAF task `continuum`. Later in the analysis, the continuum is re-normalised more carefully by a manual placement of continuum regions and subsequently fitting a straight line to these, allowing a higher precision of the abundance determination (more on this in Sect. 3.3).

Telluric lines have not been removed from the spectra. Instead a telluric spectrum from the Arcturus atlas (Hinkle et al. 2000) has been plotted over the appropriately shifted observed spectra and affected regions have been avoided on a star-by-star basis.

3. Analysis

The analysis of the spectra and the determination of the stellar abundances follows the same methodology as described in the previous papers in this series: Jönsson et al. (2017a,b) and Lomaeva et al. (2019). This section describes the general methodology as well as the specific details relevant for this work.

3.1. General methodology

To determine the stellar abundances, synthetic spectra are modelled using the tool Spectroscopy Made Easy (SME, Valenti & Piskunov 1996; Piskunov & Valenti 2017). For a given set of stellar parameters ($T_{\rm eff}$, $\log g$, [Fe/H], and microturbulence, $\xi_{\rm micro}$), SME interpolates in a grid of pre-calculated model atmospheres and calculates a synthetic spectrum of a region of choice. By defining line and continuum masks over spectral regions of interest, SME can simultaneously fit, using χ^2-minimisation (Marquardt 1963), both stellar photospheric parameters and/or stellar abundances. Figure 2 shows the line definitions and continuum placements for the bulge star B6-F1 and the spectral lines used in the analysis.

The stellar parameters of the stars analysed are determined as described in Sect. 3.2 below. Metallicity-scaled solar abundances (Grevesse et al. 2007) are assumed in SME, except for the α-elements that have already been determined in Jönsson et al. (2017b).

Spectroscopy Made Easy uses a grid of MARCS models[3] (Gustafsson et al. 2008) that adopts spherical symmetry for $\log g < 3.5$, which is the case for the majority of our stars, but otherwise adopts plane parallel symmetry. Some non-local thermodynamic equilibrium (NLTE) effects have been reported for the elements analysed here: Zr is shown by Velichko et al. (2010) to be weakly dependent on temperature; and Mashonkina & Gehren (2000) find that they need small NLTE corrections

[3] Available at `marcs.astro.uu.se`

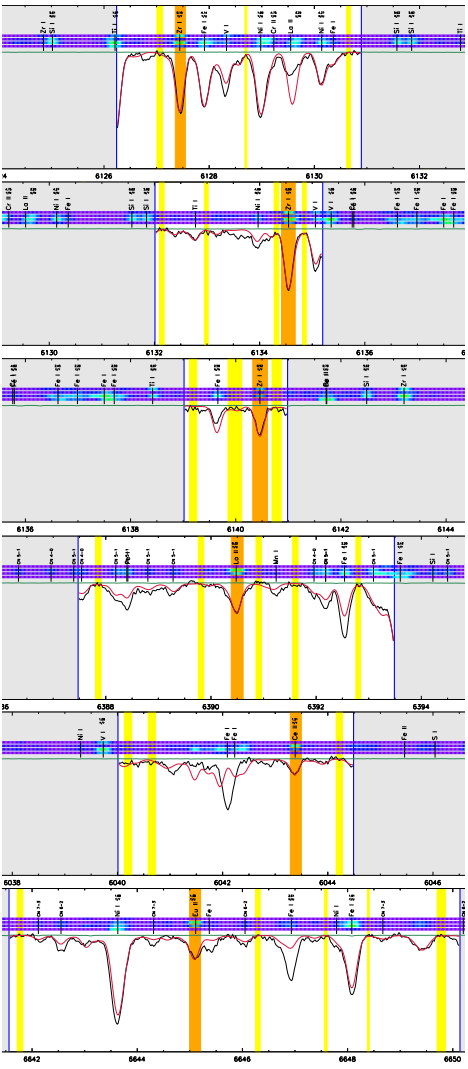

Fig. 2. Observed spectrum (black) of the bulge star B6-F1 (S/N = 54). The lines for abundance determination of Zr (three lines), La, Ce, and Eu (one line each) are marked out as the orange regions. The yellow regions are the manually placed continuum and the red spectrum is the synthetic one. The segments within which the synthetic spectrum is modelled are marked as the white wavelength regions between the blue vertical lines in each panel. The four horizontal lines above each spectrum indicate the lines' sensitivity in the stellar parameters $T_{\rm eff}$, $\log g$, [Fe/H] and $\xi_{\rm micro}$, respectively, where green is more sensitive than blue.

of the order of +0.03 dex for Eu in their analysis of cool dwarfs. Nonetheless, the analysis in this work is done under the assumption of LTE.

3.2. Stellar parameters

The stellar parameters used are determined in Jönsson et al. (2017a,b) (where a more detailed description can be found) by fitting synthetic spectra for unsaturated and unblended Fe I and Fe II lines, Ca I lines, and $\log g$ sensitive Ca I line wings, while $T_{\rm eff}$, $\log g$, [Fe/H], $\xi_{\rm micro}$, and [Ca/Fe] were set as free parameters in SME. The Fe I line has NLTE corrections adopted from Lind et al. (2012). The reported uncertainties for these parameters in Jönsson et al. (2017a,b) for a typical disk star of $S/N \sim 100$ are $T_{\rm eff}$ ±50 K, $\log g \pm 0.15$ dex, [Fe/H] ± 0.05 dex, and ± 0.1 km s^{-1} for $\xi_{\rm micro}$. For a typical bulge star, the S/N is significantly lower (median of 38), and hence the uncertainties greater; $T_{\rm eff} \pm 100$ K, $\log g \pm 0.30$ dex, [Fe/H] ± 0.10 dex and $\xi_{\rm micro} \pm 0.2$ km s^{-1}. These values are later used in the uncertainties estimations; see Sect. 4.2.

3.3. Abundance determination

The atomic line data used for the abundance determination are collected from the *Gaia*-ESO line list version 6 (Heiter et al. 2015, and in prep.). From here we get wavelengths, excitation energies, and transition probabilities (as well as broadening parameters, when existing). The transition probabilities for the elements investigated here, Zr, La, Ce, and Eu, come from Biemont et al. (1981), Lawler et al. (2001a), Lawler et al. (2009), and Lawler et al. (2001b), respectively. All available lines for these elements in the given wavelength region (5800–6800 Å) were investigated individually in order to exclude lines that could not be modelled properly (due to blends, bad atomic data, or other systematics). As for Zr, where three separate lines were suitable for abundance determination, the lines were ultimately fitted simultaneously. Finally, the determined SME abundances were, in the post-process, re-normalised to the most up-to-date solar values provided by Grevesse et al. (2015). The final set of lines used for abundance determination is presented in Table 1. Apart from the atomic lines, we include the molecules C_2 (Brooke et al. 2013) and CN (Sneden et al. 2014) in the synthesis.

For La and Eu, hyperfine splitting (hfs) had to be taken into account. By not taking hfs into account there is a risk of overestimating the measured abundance (Prochaska & McWilliam 2000; Thorsbro et al. 2018). Additionally, isotopic shift (IS) has to be considered for Zr, Ce, and Eu. The shift is caused by the isotopes having shifted energy levels, resulting in radiative transitions with shifted wavelengths. Isotopic shift is included by manually identifying the set of transitions for each isotope in the line list and scaling the $\log(gf)$ to the relative solar isotopic abundances; see Table 2.

3.4. Population separation

The classification of the stellar populations in the disk (thin/thick) can be done in several ways, namely by kinematics, age, geometry, and chemistry. Even so, the separation of these two components is somewhat debated and the transition between them might be a gradient rather than a clear separation. The results by Hayden et al. (2015) show that the scale length of the thin disk extends further out than that of the thick disk. The thick disk has been shown to be enriched in α-elements compared to that of the thin disk, in addition to thick disk stars having higher total velocities but slower rotational velocities (Bensby et al. 2014).

In Lomaeva et al. (2019) the separation into the two populations is computed for our disk sample, using a combination of stellar metallicity, abundances ([Ti/Fe] as determined in Jönsson et al. 2017b) and kinematics. The radial velocities from Table A.2, proper motions from *Gaia* DR2 (Gaia Collaboration 2016, 2018) and distances from McMillan (2018) are used to calculate the total velocities[4]. In total, kinematic data were available for 268 stars in the disk sample. The clustering method `Gaussian Mixture Model` (GMM), obtained from the `scikit-learn` module for Python (Pedregosa et al. 2011), is used to cluster the disk data into the two components. We refer to Lomaeva et al. (2019) for more details.

Table 1. Atomic lines used in the analysis.

Element	Wavelength [Å]	$\log(gf)$	$\chi_{\rm exc}^{\rm low}$ [eV]
Zr I	6127.440	−1.06	0.15
Zr I	6134.550	−1.28	0.00
Zr I	6140.460	−1.41	0.51
La II	6390.457	−2.01	0.32
La II	6390.469	−2.08	0.32
La II	6390.486	−1.90	0.32
La II	6390.501	−2.08	0.32
Ce II	6043.373	−0.48	1.21
Eu II	6645.057	−0.84	1.38
Eu II	6645.060	−0.78	1.38
Eu II	6645.068	−2.13	1.38
Eu II	6645.074	−0.84	1.38
Eu II	6645.083	−0.91	1.38
Eu II	6645.086	−0.90	1.38
Eu II	6645.098	−0.60	1.38
Eu II	6645.101	−0.95	1.38
Eu II	6645.121	−1.01	1.38
Eu II	6645.137	−1.09	1.38
Eu II	6645.149	−1.19	1.38

Notes. The elements and ionisation stages are given in Col. 1, the transition wavelengths in Col. 2, and the $\log(gf)$ values are listed in Col. 3. The excitation energies of the transitions lower level are given in Col. 4. **References.** The $\log(gf)$ data included in the *Gaia*-ESO line lists comes from Biemont et al. (1981) (Zr), Lawler et al. (2001a) (La), Lawler et al. (2009) (Ce) and Lawler et al. (2001b) (Eu).

Table 2. Isotope information of the elements.

Element(Z)	Baryon number	Relative abundance	Reference
Zr(40)	90:91:92:94:96	51:11:17:17:3	Nomura et al. (1983)
La(57)	139	100	de Laeter & Bukilic (2005)
Ce(58)	140:142	88:11	Chang et al. (1995)
Eu(63)	151:153	48:52	Chang et al. (1994)

Notes. Column 2 gives the baryon number of the stable isotopes that contribute to at least 1% to the solar system abundance. Column 3 gives the corresponding relative isotopic abundances of the stable isotopes as measured in the Sun, with references in the last column.

[4] $V_{\rm tot}^2 = U^2 + V^2 + W^2$.

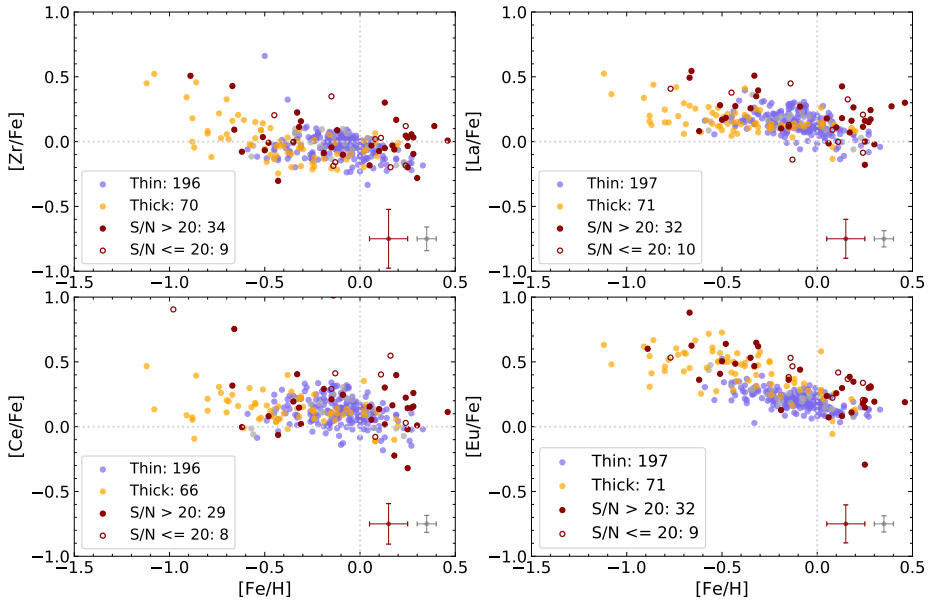

Fig. 3. Abundance ratio trends with metallicity, [X/Fe] against [Fe/H], for the thin- (blue) and thick-disk (yellow) stars as well as the bulge stars (red). Since it was not possible to determine all abundances in all spectra, the number of stars in each sample is included in the legend. Filled dark red circles indicate bulge stars with a S/N above 20, whereas the hollow red circles indicate a S/N equal to or less than 20. Some of the disk stars could not be classified as thick or thin disk stars; these are marked as grey dots. The typical uncertainty for the disk and the bulge sample, as described in Sect. 4.2, is marked in the lower right corner of every plot.

4. Results

4.1. Abundances

Our derived abundance ratios, [X/Fe], for Zr, La, Ce, and Eu, are plotted against [Fe/H] in Fig. 3. The population separation is applied to the disk sample and the number of stars in each population for which we could determine the abundance in question is noted in every panel. The bulge sample is plotted on top of the disk trends, where for the bulge we differentiate between spectra of high and low S/N, with a separation of $S/N = 20$. The typical uncertainties are noted in the plots, and the estimation of these is described in Sect. 4.2.

4.2. Uncertainties

Systematic errors generally originate from incorrectly determined stellar parameters, model atmosphere assumptions, continuum placement, and atomic data. This makes these errors hard to estimate. To get a sense of the systematic uncertainties, one can compare to reference stars. In Jönsson et al. (2017a) they compare the determined stellar parameters to those of three overlapping *Gaia* benchmark stars determined in Jofré et al. (2015) and find that these are within the uncertainties of the *Gaia* benchmark parameters.

All spectra are analysed using the same line and continuum masks as well as the same atomic data, minimising possible random uncertainties. Therefore, the random uncertainties are to primarily be found in the (random) uncertainties of the stellar parameters. An approach to estimate the random uncertainties due to changes in the stellar parameters, is to analyse a typical spectrum several times using parameters that all vary within given distributions. The same method for estimating the uncertainties was used in Lomaeva et al. (2019).

Using the FIES spectrum of the standard star Arcturus[5], uncertainties were added to its initial stellar parameters, meaning that the stellar parameters were changed simultaneously, for a set of 500 runs with modified stellar parameters. A Gaussian distribution is used to generate the uncertainties, using the reported stellar parameter uncertainties as standard deviation (see Sect. 3.2). In the uncertainty estimation of the bulge abundances, we have not degraded the FIES Arcturus spectrum (with a resolution of 67 000) to match that of the bulge spectra (R of 47 000), but separate tests have shown this slightly lower resolution to have a negligible effect on the determined abundance.

The abundance uncertainties coming from the uncertainties in the stellar parameters are then calculated as

$$\sigma A_{\text{parameters}} = \sqrt{|\delta A_{T_{\text{eff}}}|^2 + |\delta A_{\log g}|^2 + |\delta A_{[\text{Fe/H}]}|^2 + |\delta A_{v_{\text{micro}}}|^2}, \quad (1)$$

[5] The giant star Arcturus (also known as α-Boo or HIP69673) has been analysed extensively due to its brightness, being the fourth brightest in the night sky, and is suitable as a reference of a typical giant star.

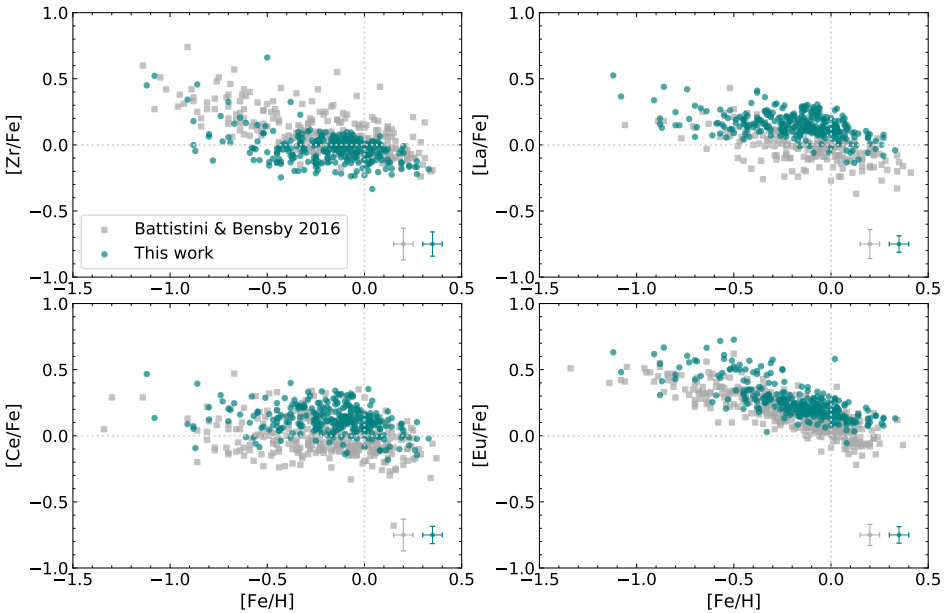

Fig. 4. Determined disk abundances in this work (teal) compared with the determined abundances from Battistini & Bensby (2016) (grey). The typical uncertainties for both data sets are indicated in the lower right corner of every plot, where the uncertainties are taken from Table 6 in Battistini & Bensby (2016).

Table 3. Estimated typical uncertainties for the disk and bulge sample using a generated set of stellar parameters for the giant star α-Boo.

$\sigma A_{\text{parameters}}$	Zr	La	Ce	Eu
Disk [dex]	0.09	0.06	0.07	0.06
Bulge [dex]	0.23	0.15	0.16	0.15

where, for non-symmetrical abundance changes, the mean value is used in the squared sums. The resulting uncertainties can be seen in Table 3.

5. Discussion

In this section we elaborate on the results. Firstly, we compare our separate abundance trends for the disks and bulge with previous literature studies in Sect. 5.1. Secondly, and this is the core of this investigation, in Sect. 5.2 we consider a more in-depth comparative analysis between our abundances for the bulge and disks populations, both determined in the same way. This is done to minimise the systematic uncertainties as much as possible. We then proceed in considering and discussing comparative abundance ratios such as [Eu/Mg], [Eu/La], and [second-peak s/first-peak s], also in Sect. 5.2 as well as Sect. 5.3.

To highlight features of the trend-plots, the running means of the samples are calculated and plotted (with a 1σ scatter). The number of data points in the running window is set to roughly 15% of the sample sizes (thin disk, thick disk, bulge). As a result, the running mean (and scatter) does not cover the whole trend range. For the bulge sample, only data points with $S/N > 20$ are included in the running mean. Henceforth, the running mean-trend is the one referred to when describing [X/Fe] or [X/Y] ratios (except for Sect. 5.1.1).

5.1. Comparison with selected literature trends

5.1.1. Disk sample

In Fig. 4 we compare our determined disk abundances with those determined for dwarf stars in the disk by Battistini & Bensby (2016). In general, the trends are similar for all elements, as well as the scatter in the determined abundance. The abundances of [La, Ce, Eu/Fe] seem to be systematically higher than those of Battistini & Bensby (2016) whereas the [Zr/Fe]-abundances appear to be slightly lower. The typical abundance uncertainties for Battistini & Bensby (2016) are 0.12, 0.11, 0.12, and 0.08 dex for Zr, La, Ce, and Eu, respectively (their Table 6), which is somewhat higher than ours (see Table 3). The possible shifts in the abundances could be due to systematic differences in dwarf and giant stars or in differing atomic data such as using different lines in the abundance determination. Indeed, there is no overlap in the atomic lines used in these two data sets, except for the La line at 6390 Å, although Battistini & Bensby (2016) use three additional lines for the La abundance determination.

Zirconium is a first-peak s-process element whereas La and Ce are second-peak s-process elements. [Zr,La/Fe] have

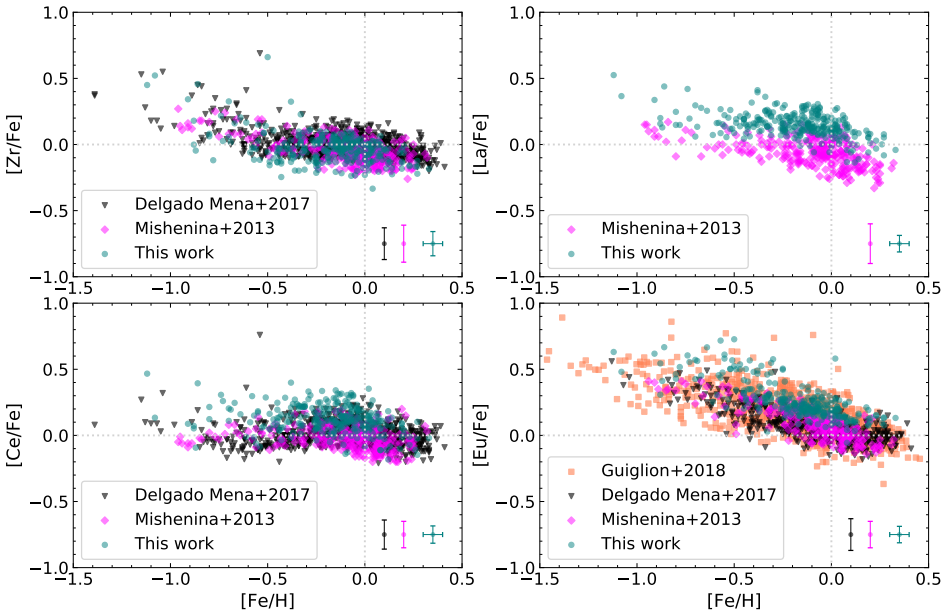

Fig. 5. Determined disk abundances in this work (teal) compared with selected literature trends: Mishenina et al. (2013) (pink), Delgado Mena et al. (2017) (black), and Guiglion et al. (2018) (orange). The typical uncertainties, when available, are indicated in the lower right corner of every plot, where the uncertainties from Mishenina et al. (2013) and Delgado Mena et al. (2017) (their Tables 3 and 4, respectively) are for a low $T_{\rm eff}$ star.

somewhat decreasing abundances with increasing metallicities, with a flattening of abundances for [Fe/H] above approximately −0.4. The [Ce/Fe] trend is flatter than [Zr/Fe] and [La/Fe], explained by the higher s-process contribution in the Ce production (66, 76 and 84% s-process contribution for Zr, La and Ce, respectively Bisterzo et al. 2014).

The scatter for the [La/Fe] abundances is higher, ∼0.5 dex, over the metallicity range [−0.2, 0], compared to the rest of the metallicity domain with ∼0.3 dex. This indicates that AGB stars produce the bulk of their s-elements through the main s-process. The increase in scatter can most likely be explained by the mass range of AGB stars, which enables (1) stars to produce s-process elements at different metallicities (times) as well as (2) different amounts of production of the first-/second-peak s-process for AGB stars with different masses (see Sect. 5.3). The increasing abundances when [Fe/H] is below −0.5 for the s-process elements Zr and La point at a production by the r-process at early times (see [Eu/Fe]). In addition to Battistini & Bensby (2016), our results are comparable to those reported in Mishenina et al. (2013) (Zr, La, Ce, Eu) and Delgado Mena et al. (2017) (Zr, Ce, Eu), on dwarf stars in the local disk; see Fig. 5. The typical uncertainties from Mishenina et al. (2013) and Delgado Mena et al. (2017) are chosen from their estimates of low $T_{\rm eff}$ stars; see their Tables 3 and 4, respectively.

For Eu, the trend decreases with increasing metallicity throughout our metallicity range, except for a plateau around [Fe/H] < −0.6. Europium has a reported r-process contribution of 94% (Bisterzo et al. 2014) and the observed trend indicates that the r-process has a continuous enrichment in the Galaxy, similar to that of the α-elements. Our Eu abundances compare well with those of Guiglion et al. (2018), including some subgiant and giant stars in their sample; see Fig. 5. We note that our measurements, and those of Battistini & Bensby (2016) and Guiglion et al. (2018), show, on average, slightly supersolar [Eu/Fe] abundances at solar metallicities, which is not seen in either Mishenina et al. (2013) or Delgado Mena et al. (2017). Of all the trends, ours is systematically high, not passing through the solar value at any metallicities.

5.1.2. Bulge sample

In Fig. 6 we compare our bulge trend with those observed in Johnson et al. (2012), Van der Swaelmen et al. (2016), and Duong et al. (2019). Twenty-seven of our stars and their spectra overlap with those of Van der Swaelmen et al. (2016), and the same spectral lines are used for the abundance determination. Nonetheless, we observe different trends as well as measure Zr in these stars.

Zirconium. In general, our [Zr/Fe] trend with metallicity is flat, with an increase at lower metallicities [Fe/H] < −0.5. It should be noted that the running mean is rather poorly defined at the edges and the feature is based primarily on the two most metal-poor stars in Fig. 3. Our trend agrees well with that of Johnson et al. (2012) within our overlapping metallicity ranges, whereas Duong et al. (2019) has overall decreasing abundances with increasing metallicities. Above [Fe/H] ∼ 0.1, our [Zr/Fe]

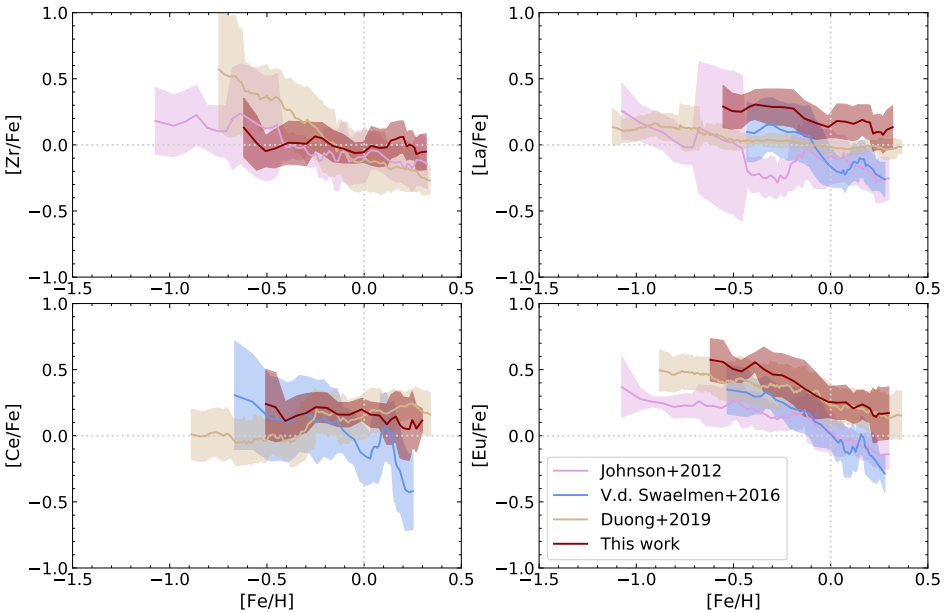

Fig. 6. Running mean for the bulge abundances determined in this work (red solid line) compared with the calculated running mean based on the abundances in Johnson et al. (2012) (pink solid line),Van der Swaelmen et al. (2016) (blue solid line), and Duong et al. (2019) (beige solid line), with a 1σ scatter (shaded regions, same colours as solid lines).

is solar while Johnson et al. (2012) and Duong et al. (2019) have subsolar [Zr/Fe], ours pointing at a higher s-process contribution in the production of Zr.

Lanthanum. Johnson et al. (2012) reports a dip in [La/Fe] abundance around [Fe/H] ~ -0.4 which is not observed in either of the other studies, or ours. Both Johnson et al. (2012) and Van der Swaelmen et al. (2016) produce decreasing [La/Fe] abundances with increasing metallicities, whilst both ours and that of Duong et al. (2019) exhibit only a very small decrease of [La/Fe] with increasing [Fe/H]. In general, our [La/Fe] abundances are higher than the other studies, which possibly could point at a higher s-process production in the bulge compared to previous work. However, we note that our bulge abundances, similarly to the disk abundances, are expected to suffer from a systematic offset in the determined [La/Fe] abundance ratios, preventing us from making a firm claim.

Cerium. Our [Ce/Fe] trend is flat throughout our metallicity range. Duong et al. (2019) also find a flat trend at solar scaled values, but with a slight step-wise increase at [Fe/H] ~ -0.3, thereafter following our trend. Van der Swaelmen et al. (2016) find a different [Ce/Fe] trend with decreasing [Ce/Fe] values with increasing metallicities.

Europium. All the published [Eu/Fe] bulge trends and ours decrease with increasing metallicity, although with slightly different slopes and different offsets. The Johnson et al. (2012) study covers the lowest metallicities of all the samples. The trend of Duong et al. (2019) and ours trace each other closely with super-solar abundances at all metallicities. The Johnson et al. (2012) and Van der Swaelmen et al. (2016) trends follow each other well in their overlapping metallicity region, with subsolar abundances above solar metallicities. There is an observable "knee" in the trend around [Fe/H] ~ -0.4, seen in all four studies mentioned above. Similarly to [La/Fe], our [Eu/Fe] abundances are higher than those in previous studies, although due to the possible systematic offsets we cannot draw any firm conclusions from this. However, since the main purpose of this work is to make a differential analysis between the disk and bulge abundances in this work, the possible systematic offset in our analysis is of less importance.

5.2. Disk and bulge comparison of the current study

In this section we compare our abundance-ratio trends, that is [X/Fe], for the bulge, the thin disk, and the thick disk as a function of the metallicity for the s-process elements Zr, La, and Ce, and the r-process element Eu. In Fig. 7 we directly compare the bulge population trends with those of the thin and the thick disk populations, determined in the same way in the present study.

The bulge and the disks have very similarly shaped s-process element trends (Zr, La, Ce). The bulge trend of [La/Fe] is slightly higher overall, especially at subsolar metallicities where [La/Fe] is ~0.1 dex higher than for the disk. We note that this is the opposite to findings in Duong et al. (2019). The metallicities of

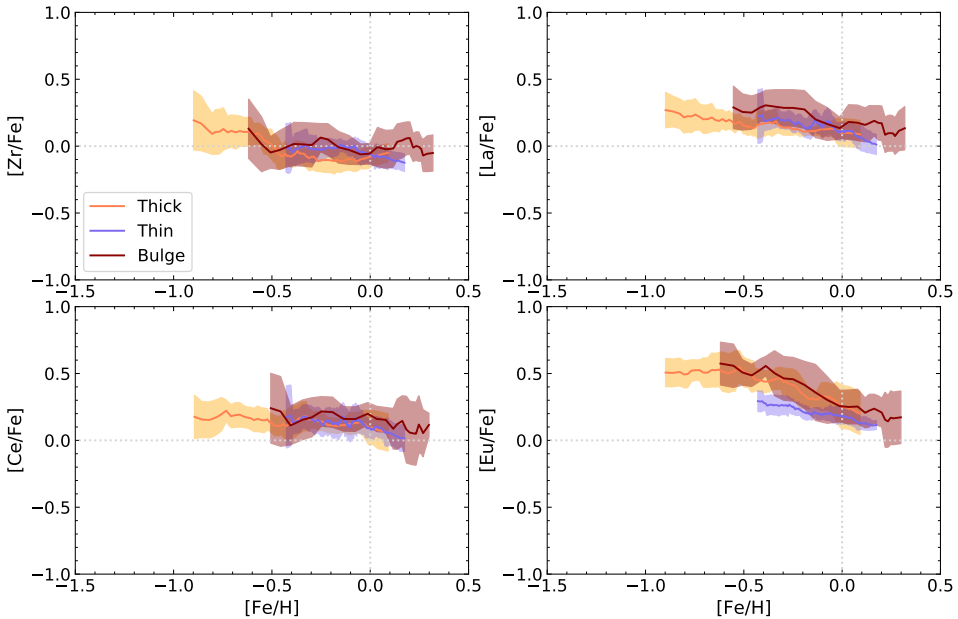

Fig. 7. Running mean for the bulge (red solid line) compared with the running mean of the thick disk (yellow solid line) and thin disk (blue solid line), with a 1σ scatter (shaded regions, same colours as solid lines).

the bulge sample extend to slightly higher values, pointing at a higher star formation rate of the bulge. Additionally, Matteucci et al. (2019) shows that implementing a Salpeter like initial mass function (IMF), which favours massive stars compared to typical IMFs for the disk, better reproduce bulge abundances.

For [Eu/Fe], the thick disk is enhanced as compared with the thin disk, reminding us of an α-element. The decreasing trend for metallicities larger than [Fe/H] $\gtrsim -0.4$ is a result of iron production by SN Ia after a time delay of roughly 100 Myr-1 Gyr (Matteucci & Brocato 1990; Ballero et al. 2007). The bulge traces the thick disk in the [Eu/Fe] abundance, suggesting the bulge has a similar star formation rate as that of the thick disk. A plateau, or a knee, can be seen around metallicities of approximately -0.4 for both the thick disk and the bulge. A knee at higher metallicities than in the solar vicinity was already predicted for the bulge by Matteucci & Brocato (1990) and in general for systems with higher star formation rates than in the solar vicinity.

In Fig. 8 we compare Eu with the well-determined α-element magnesium (from Jönsson et al. 2017b), by plotting [Eu/Mg], for the same stars. The resulting, mostly flat trend of all populations is already expected from the [Eu/Fe] trend, pointing at Eu having a contribution from progenitors of similar timescales to that of progenitors producing Mg (i.e. SNe II). It has indeed been shown by Travaglio et al. (1999) that SNe II progenitors with masses of 8–10 $M_\odot$ best reproduce the r-process enrichment in the Galaxy, and Cescutti et al. (2006) showed that to reproduce the ratio of typical s-process elements, such as [Ba/Fe], at low metallicities,

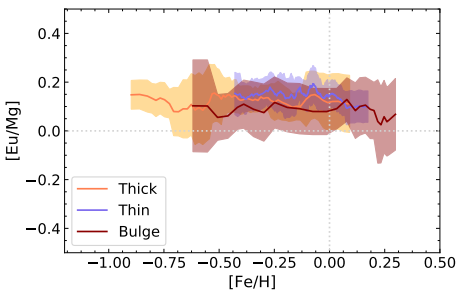

Fig. 8. [Eu/Mg] abundances against [Fe/H] as running mean with a 1σ scatter for the thin disk (blue), thick disk (yellow), and bulge (red).

an r-process production of these elements in stars with masses ranging from 8 to 30 $M_\odot$ should be assumed. Nonetheless, the origin of r-elements is, as mentioned earlier, still debated (see e.g. Sneden et al. 2000; Thielemann et al. 2011; Côté et al. 2019; Siegel et al. 2019; Kajino et al. 2019).

A way to disentangle the s- and r-process contribution throughout the evolution of the Galaxy is to compare an s-process-dominated element with an r-process-dominated one. We thus compare La, with an s-process contribution of 76%, to

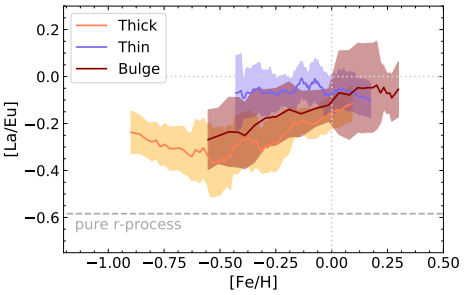

Fig. 9. [La/Eu] abundances against [Fe/H] as running mean with a 1σ scatter for the thin disk (blue), thick disk (yellow), and bulge (red). A pure r-process line is plotted, calculated using the values presented in Bisterzo et al. (2014).

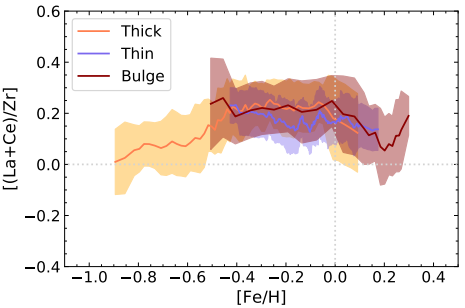

Fig. 10. Abundance ratio of the second-peak s-process elements (La, Ce) and the first-peak s-process element (Zr) against [Fe/H] as running mean with a 1σ scatter for the thin disk (blue), thick disk (yellow), and bulge (red).

that of Eu with an r-process contribution of 94% (Bisterzo et al. 2014), plotted as [La/Eu] in Fig. 9. A pure r-process line is added, using the values from Bisterzo et al. (2014). The value of the pure r-process line is calculated by subtracting the predicted s-process abundance from the solar system total values, that is, by treating the r-process as a residual (Bisterzo et al. 2014).

The trends in Fig. 9 show that the r-process increasingly dominates the production of neutron-capture elements with decreasing metallicity, reaching [La/Eu] = −0.25 for the bulge and [La/Eu] = −0.4 for the thick disk at [Fe/H] ∼ −0.5. With regard to the large scatter at supersolar metallicities, we refrain from making any further interpretations of the bulge abundances at these metallicities. At around [Fe/H] ∼ −0.6 the [La/Eu] thick disk trend levels off or even increases with lower metallicities. Whether this is significant or not is yet to be understood and observations of more stars in this metallicity range are needed. The generally higher [La/Eu] abundances of the bulge compared with those of the thick disk point at the bulge having either less r-process production (in turn, possibly a different amount of SNe II), or a higher s-process contribution (as seen previously in the [La/Fe]-trend) than that of the thick disk.

5.3. First- and second-peak s-process elements

In Fig. 10, the running mean of the ratio of the second-peak s-process elements (a mean of La and Ce) and the first-peak s-process element Zr are plotted against metallicity. The trend, elaborated on in the last paragraph of this section, can be explained by considering the stellar yields from Karakas & Lugaro (2016), where low-mass AGB stars have a higher relative production of second-peak elements compared to the production of first-peak elements.

The neutrons in the s-process come from two neutron sources: the $^{13}C(\alpha, n)^{16}O$- and the $^{22}Ne(\alpha, n)^{25}Mg$-reactions. The ^{13}C source has a lower neutron density of roughly 10^7 neutrons cm^{-3}, whereas the neutron density for the ^{22}Ne source is around 10^{15} neutrons cm^{-3}. However, due to the longer timescales of the ^{13}C reaction (∼10^3 yr compared to ∼10 yr), the time integrated neutron flux for this neutron source is much higher than for the ^{22}Ne source. Due to this, the ^{13}C reaction builds up the heavier s-process elements, such as the second- (and third-)peak elements, whilst the ^{22}Ne reaction is limited to producing the first-peak s-process elements (Karakas & Lattanzio 2014).

Furthermore, Bisterzo et al. (2017) elaborate on the importance of the size of the ^{13}C-pocket in the s-process production. The ^{22}Ne reaction takes place only in initially more massive (AGB) stars of >4 $M_\odot$, due to the higher temperatures of these stars (Karakas & Lattanzio 2014). This shrinks the ^{13}C-pocket, resulting in a smaller quantity of s-elements being expected, especially the heavier ones. In short, heavier AGB stars produce relatively fewer second-peak elements compared to low-mass AGB stars, and the latter have a longer time delay.

Another aspect to keep in mind is that at lower metallicities, the ratio of the number of neutrons to the number of available ^{56}Fe-seeds is higher, compared to higher metallicities, which enables the build-up of second-peak elements (Busso et al. 1999).

In Fig. 10 we first see an increasing trend in the thick disk for increasing metallicities, which turns over for solar metallicities and higher. Below solar metallicities (and above [Fe/H] ∼ −0.5), all trends show an enrichment of second-peak as compared to first-peak elements. This is therefore explained by the low-mass AGB stars which have not yet enriched the interstellar medium (ISM) at the time of the formation of the older thick disk stars, resulting in relatively low [(La+Ce)/Zr] abundances at early times.

At solar metallicities, the disk populations does not show any clear differences. As for the bulge, it follows the trend of the thick disk more closely than that of the thin disk at subsolar metallicities. At supersolar metallicities, the first-peak elements seem to increase in the bulge, possibly explained by a contribution of metal-rich AGB stars, producing a higher amount of first-peak elements (Karakas & Lugaro 2016).

6. Conclusions

In this work we determined abundances of the neutron-capture elements Zr, La, Ce, and Eu in 45 bulge giants and 291 local disk giants. The determination has been done using high-resolution spectra obtained with FLAMES/UVES (bulge sample) or either FIES or PolarBase (disk sample) and the analysis code SME.

All spectra are evaluated over the wavelength region 5800–6800 Å and the careful, manual definition of the continuum

surrounding the spectral lines of interest in the spectra has been crucial in order to get high-precision abundances. Hyperfine splitting (in the cases of La, Eu) has been taken into account, as well as isotopic shifts by manually scaling the log (gf)-values of the identified transitions in the line list (for the isotopes of Zr, Ce, Eu).

The stellar mass and metallicity are factors that contribute to, and affect, the s- and r-process production. Due to this, the enrichment of the ISM and the abundance of neutron-capture elements vary with time in the Galaxy, making them suitable probes for Galactic chemical evolution.

Our [Zr, La, Ce/Fe] bulge trends are in general flatter than those reported by previous studies, many of which are decreasing with higher metallicities. Such decreasing trends would suggest a higher r-process contribution to these elements in the bulge, while our flatter trends that have the same general shapes as our thick disk trends suggest more similar r/s-proportions in the creation of the neutron capture elements in the bulge and disks. The [La/Fe] bulge trend is ∼0.1 dex higher compared with the disk, possibly indicating a higher s-process contribution in the bulge, compared with that of the disk.

For [Eu/Fe], we see a decreasing trend with increasing metallicities for both the disk and the bulge, with a plateau at around [Fe/H] ~ -0.4. This is very similar to the typical α-element trend, and plotting [Eu/Mg] confirms this, suggesting that the r-process has a similar production rate as that of Mg (coming from SNe II).

For [La/Eu] we find that towards low metallicities, the abundances lay closer to the pure r-process line (reaching [La/Eu] −0.4 (disk) and −0.25 (bulge) at [Fe/H] ~ -0.5), indicating that the r-process was the dominating neutron-capture process at early times, both in the disk and the bulge. The results also point at either (a) a different amount of massive stars or (b) different contribution of the s-process in the local thick disk and the bulge, where the [La/Eu] abundances seem to be systematically higher in the bulge than in the thick disk. Since we compare abundances determined with the same method, and for stars at the same evolutionary stage, the difference between the disk and the bulge in [La/Fe] could likely be real.

When plotting the ratio of the second- and first-peak s-process elements, [(La+Ce)/Zr], against metallicity we see that the bulge and the thick disk trends follow each other closely. We also show that, according to theoretical predictions by Karakas & Lattanzio (2014), low-mass AGB stars are needed to explain the enhancement of second-peak s-process abundances compared to first-peak s-process abundances.

To conclude, in general, our findings for Zr, Ce and Eu suggest that the bulge experiences a similar chemical evolution to that of the local thick disk, with a similar star formation rate. On the other hand, our La trends for the bulge and the thick disk are offset by about 0.1: systematic effects could not be identified in our homogeneous analysis of the bulge and disk samples and further investigation is still required. Our results for the s-process elements differ substantially from previous studies: here we find flatter trends. More bulge data would be needed to decrease the scatter and put further constraints on bulge abundances. Additionally, it would be useful to adopt the abundances in Galactic Chemical Evolution models to put further constraints on the evolution of the Galaxy and its components.

Acknowledgements. We would like to thank the referee, Mathieu Van der Swaelmen, for very insightful comments and suggestions which helped to improve this paper in many ways. This research has been partly supported by the Lars Hierta Memorial Foundation, and the Royal Physiographic Society in Lund through Stiftelsen Walter Gyllenbergs fond and Märta och Erik Holmbergs donation. H.J. acknowledges support from the Crafoord Foundation, Stiftelsen Olle Engkvist Byggmästare, and Ruth och Nils-Erik Stenbäcks stiftelse. This work has made use of data from the European Space Agency (ESA) mission *Gaia* (`https://www.cosmos.esa.int/gaia`), processed by the *Gaia* Data Processing and Analysis Consortium (DPAC, `https://www.cosmos.esa.int/web/gaia/dpac/consortium`). Funding for the DPAC has been provided by national institutions, in particular the institutions participating in the *Gaia* Multilateral Agreement. This publication made use of the SIMBAD database, operated at CDS, Strasbourg, France; NASA's Astrophysics Data System; and the VALD database, operated at Uppsala University, the Institute of Astronomy RAS in Moscow, and the University of Vienna.

References

Abbott, B. P., Abbott, R., Abbott, T. D., et al. 2017, Phys. Rev. Lett., 119, 161101
Bailer-Jones, C. A. L., Rybizki, J., Fouesneau, M., Mantelet, G., & Andrae, R. 2018, AJ, 156, 58
Ballero, S. K., Matteucci, F., Origlia, L., & Rich, R. M. 2007, A&A, 467, 123
Barbuy, B., Chiappini, C., & Gerhard, O. 2018, ARA&A, 56, 223
Battistini, C., & Bensby, T. 2016, A&A, 586, A49
Bensby, T., Feltzing, S., & Oey, M. S. 2014, A&A, 562, A71
Biemont, E., Grevesse, N., Hannaford, P., & Lowe, R. M. 1981, ApJ, 248, 867
Bisterzo, S., Travaglio, C., Gallino, R., Wiescher, M., & Käppeler, F. 2014, ApJ, 787, 10
Bisterzo, S., Travaglio, C., Wiescher, M., Käppeler, F., & Gallino, R. 2017, ApJ, 835, 97
Brooke, J. S. A., Bernath, P. F., Schmidt, T. W., & Bacskay, G. B. 2013, J. Quant. Spectr. Rad. Transf., 124, 11
Buder, S., Asplund, M., Duong, L., et al. 2018, MNRAS, 478, 4513
Burbidge, E. M., Burbidge, G. R., Fowler, W. A., & Hoyle, F. 1957, Rev. Mod. Phys., 29, 547
Busso, M., Gallino, R., & Wasserburg, G. J. 1999, ARA&A, 37, 239
Cardelli, J. A., Clayton, G. C., & Mathis, J. S. 1989, ApJ, 345, 245
Cescutti, G., François, P., Matteucci, F., Cayrel, R., & Spite, M. 2006, A&A, 448, 557
Chang, T. L., Qian, Q.-Y., Zhao, M.-T., & Wang, J. 1994, Int. J. Mass Spectrom. Ion Process., 139, 95
Chang, T.-L., Qian, Q.-Y., Zhao, M.-T., Wang, J., & Lang, Q.-Y. 1995, Int. J. Mass Spectrom. Ion Process., 142, 125
Côté, B., Eichler, M., Arcones, A., et al. 2019, ApJ, 875, 106
Couch, R. G., Schmiedekamp, A. B., & Arnett, W. D. 1974, ApJ, 190, 95
Cristallo, S., Abia, C., Straniero, O., & Piersanti, L. 2015, ApJ, 801, 53
de Laeter, J. R., & Bukilic, N. 2005, Int. J. Mass Spectrom., 244, 91
Delgado Mena, E., Tsantaki, M., Adibekyan, V. Z., et al. 2017, A&A, 606, A94
Duong, L., Asplund, M., Nataf, D. M., Freeman, K. C., & Ness, M. 2019, MNRAS, 486, 5349
Gaia Collaboration (Prusti, T., et al.) 2016, A&A, 595, A1
Gaia Collaboration (Brown, A. G. A., et al.) 2018, A&A, 616, A1
Gonzalez, O. A., Rejkuba, M., Zoccali, M., et al. 2011, A&A, 530, A54
Gonzalez, O. A., Rejkuba, M., Zoccali, M., et al. 2012, A&A, 543, A13
Gonzalez, O. A., Zoccali, M., Vasquez, S., et al. 2015, A&A, 584, A46
Grevesse, N., Asplund, M., & Sauval, A. J. 2007, Space Sci. Rev., 130, 105
Grevesse, N., Scott, P., Asplund, M., & Sauval, A. J. 2015, A&A, 573, A27
Gruyters, P., Lind, K., Richard, O., et al. 2016, A&A, 589, A61
Guiglion, G., de Laverny, P., Recio-Blanco, A., & Prantzos, N. 2018, A&A, 619, A143
Gustafsson, B., Edvardsson, B., Eriksson, K., et al. 2008, A&A, 486, 951
Hayden, M. R., Bovy, J., Holtzman, J. A., et al. 2015, ApJ, 808, 132
Heiter, U., Lind, K., Asplund, M., et al. 2015, Phys. Scr, 90, 054010
Herwig, F. 2005, ARA&A, 43, 435
Hinkle, K., Wallace, L., Harmer, D., Ayres, T., & Valenti, J. 2000, IAU Joint Discuss., 24, 26
Immeli, A., Samland, M., Gerhard, O., & Westera, P. 2004, A&A, 413, 547
Jofré, P., Heiter, U., Soubiran, C., et al. 2015, A&A, 582, A81
Johnson, C. I., Rich, R. M., Kobayashi, C., & Fulbright, J. P. 2012, ApJ, 749, 175
Jönsson, H., Ryde, N., Nordlander, T., et al. 2017a, A&A, 598, A100
Jönsson, H., Ryde, N., Schultheis, M., & Zoccali, M. 2017b, A&A, 600, C2
Kajino, T., Aoki, W., Balantekin, A. B., et al. 2019, Prog. Part. Nucl. Phys., 107, 109
Karakas, A. I., & Lattanzio, J. C. 2014, PASA, 31, e030

Karakas, A. I., & Lugaro, M. 2016, ApJ, 825, 26
Korn, A. J., Grundahl, F., Richard, O., et al. 2007, ApJ, 671, 402
Kratz, K.-L., Farouqi, K., Pfeiffer, B., et al. 2007, ApJ, 662, 39
Lawler, J. E., Bonvallet, G., & Sneden, C. 2001a, ApJ, 556, 452
Lawler, J. E., Wickliffe, M. E., den Hartog, E. A., & Sneden, C. 2001b, ApJ, 563, 1075
Lawler, J. E., Sneden, C., Cowan, J. J., & Ivans, I. I., & Den Hartog E. A. 2009, ApJS, 182, 51
Lecureur, A., Hill, V., Zoccali, M., et al. 2007, A&A, 465, 799
Lind, K., Korn, A. J., Barklem, P. S., & Grundahl, F. 2008, A&A, 490, 777
Lind, K., Bergemann, M., & Asplund, M. 2012, MNRAS, 427, 50
Liu, F., Asplund, M., Yong, D., et al. 2019, A&A, 627, A117
Lomaeva, M., Jönsson, H., Ryde, N., Schultheis, M., & Thorsbro, B. 2019, A&A, 625, A141
Marquardt, D. W. 1963, J. Soc. Ind. Appl. Math., 11, 431
Mashonkina, L., & Gehren, T. 2000, A&A, 364, 249
Matteucci, F., & Brocato, E. 1990, ApJ, 365, 539
Matteucci, F., Grisoni, V., Spitoni, E., et al. 2019, MNRAS, 487, 5363
McMillan, P. J. 2018, Res. Notes AAS, 2, 51
McWilliam, A. 2016, PASA, 33, e040
Meléndez, J., Asplund, M., Alves-Brito, A., et al. 2008, A&A, 484, L21
Mishenina, T. V., Pignatari, M., Korotin, S. A., et al. 2013, A&A, 552, A128
Nomura, M., Kogure, K., & Okamoto, M. 1983, Int. J. Mass Spectrom. Ion Process., 50, 219
Nordlander, T., Korn, A. J., Richard, O., & Lind, K. 2012, ApJ, 753, 48
Pedregosa, F., Varoquaux, G., Gramfort, A., et al. 2011, J. Mach. Learn. Res., 12, 2825
Petit, P., Louge, T., Théado, S., et al. 2014, PASP, 126, 469
Piskunov, N., & Valenti, J. A. 2017, A&A, 597, A16
Portail, M., Gerhard, O., Wegg, C., & Ness, M. 2017, MNRAS, 465, 1621
Prochaska, J. X., & McWilliam, A. 2000, ApJ, 537, L57
Shen, J., & Li, Z.-Y. 2016, in Galactic Bulges, eds. E. Laurikainen, R. Peletier, & D. Gadotti (Berlin: Springer), 418, 233
Siegel, D. M., Barnes, J., & Metzger, B. D. 2019, Nature, 569, 241
Sneden, C., Cowan, J. J., Ivans, I. I., et al. 2000, ApJ, 533, L139
Sneden, C., Lucatello, S., Ram, R. S., Brooke, J. S. A., & Bernath, P. 2014, ApJS, 214, 26
Souto, D., Allende Prieto, C., Cunha, K., et al. 2019, ApJ, 874, 97
Telting, J. H., Avila, G., Buchhave, L., et al. 2014, Astron. Nachr., 335, 41
Thielemann, F.-K., Arcones, A., Käppeli, R., et al. 2011, Prog. Part. Nucl. Phys., 66, 346
Thielemann, F. K., Eichler, M., Panov, I. V., & Wehmeyer, B. 2017, Ann. Rev. Nucl. Part. Sci., 67, 253
Thielemann, F.-K., Isern, J., Perego, A., & von Ballmoos, P. 2018, Space Sci. Rev., 214, 62
Thorsbro, B., Ryde, N., Schultheis, M., et al. 2018, ApJ, 866, 52
Thygesen, A. O., Frandsen, S., Bruntt, H., et al. 2012, A&A, 543, A160
Travaglio, C., Galli, D., Gallino, R., et al. 1999, ApJ, 521, 691
Travaglio, C., Gallino, R., Arnone, E., et al. 2004, ApJ, 601, 864
Valenti, J. A., & Piskunov, N. 1996, A&AS, 118, 595
Van der Swaelmen, M., Barbuy, B., Hill, V., et al. 2016, A&A, 586, A1
Velichko, A. B., Mashonkina, L. I., & Nilsson, H. 2010, Astron. Lett., 36, 664
Wegg, C., Gerhard, O., & Portail, M. 2015, MNRAS, 450, 4050
Weiland, J. L., Arendt, R. G., Berriman, G. B., et al. 1994, ApJ, 425, L81
Zasowski, G., Schultheis, M., Hasselquist, S., et al. 2019, ApJ, 870, 138

Appendix A: Additional tables

Table A.1. Basic data for the observed bulge giants.

Star [(a)]	RA (J2000) (h:m:s)	Dec (J2000) (d:am:as)	V	S/N
SW-09	17:59:04.533	−29:10:36.53	16.153	16
SW-15	17:59:04.753	−29:12:14.77	16.326	15
SW-17	17:59:08.138	−29:11:20.10	16.388	11
SW-18	17:59:06.455	−29:10:30.53	16.410	14
SW-27	17:59:04.457	−29:10:20.67	16.484	13
SW-28	17:59:07.005	−29:13:11.35	16.485	16
SW-33	17:59:03.331	−29:10:25.60	16.549	14
SW-34	17:58:54.418	−29:11:19.82	16.559	12
SW-43	17:59:04.059	−29:13:30.26	16.606	16
SW-71	17:58:58.257	−29:12:56.97	16.892	14

Notes. The S/N per data point is measured by the IDL-routine `der_snr.pro`, see http://www.stecf.org/software/ASTROsoft/DER_SNR. [(a)]Using the same naming convention as Lecureur et al. (2007) for the B3-BW-B6-BL-stars. This is only an excerpt of the table to show its form and content. The complete table is available in electronic form at the CDS.

Table A.2. Basic data for the observed solar neighbourhood giants.

HIP/KIC/TYC	Alternative name	RA (J2000) (h:m:s)	Dec (J2000) (d:am:as)	V	$v_{\rm rad}$ km s^{-1}	S/N	Source
HIP1692	HD1690	00:21:13.32713	−08:16:52.1625	9.18	18.37	114	FIES-archive
HIP9884	alfAri	02:07:10.40570	+23:27:44.7032	2.01	−14.29	90	PolarBase
HIP10085	HD13189	02:09:40.17260	+32:18:59.1649	7.56	26.21	156	FIES-archive
HIP12247	81Cet	02:37:41.80105	−03:23:46.2201	5.66	9.34	176	FIES-archive
HIP28417	HD40460	06:00:06.03883	+27:16:19.8614	6.62	100.64	121	PolarBase
HIP33827	HR2581	07:01:21.41827	+70:48:29.8674	5.69	−17.99	79	PolarBase
HIP35759	HD57470	07:22:33.85798	+29:49:27.6626	7.67	−30.19	85	PolarBase
HIP37447	alfMon	07:41:14.83257	−09:33:04.0711	3.93	11.83	71	Thygesen et al. (2012)
HIP37826	betGem	07:45:18.94987	+28:01:34.3160	1.14	3.83	90	PolarBase
HIP43813	zetHya	08:55:23.62614	+05:56:44.0354	3.10	23.37	147	PolarBase

Notes. Coordinates and magnitudes are taken from the SIMBAD database, while the radial velocities are measured from the spectra. The S/N per data point is measured by the IDL-routine `der_snr.pro`, see http://www.stecf.org/software/ASTROsoft/DER_SNR. This is only an excerpt of the table to show its form and content. The complete table is available in electronic form at the CDS.

Table A.3. Stellar parameters and determined abundances for observed bulge giants.

Star	$T_{\rm eff}$	$\log g$	[Fe/H]	$v_{\rm micro}$	A(Zr)	A(La)	A(Ce)	A(Eu)
SW-09	4095	1.79	−0.15	1.32	2.79	1.09	1.72	0.75
SW-15	4741	1.96	−0.98	1.62	...	...	1.51	...
SW-17	4245	2.09	0.24	1.44	2.95	1.26	...	0.97
SW-18	4212	1.67	−0.13	1.49	2.30	0.84	1.86	0.86
SW-27	4423	2.34	0.11	1.60	2.73	1.22	2.09	1.05
SW-28	4254	2.36	−0.14	1.44	2.26	1.42	2.45	0.91
SW-33	4580	2.72	0.16	1.39	2.55	1.60	2.29	1.05
SW-34	4468	1.75	−0.45	1.63	2.34	1.04	...	...
SW-43	4892	2.34	−0.77	1.84	...	0.75	...	0.28
SW-71	4344	2.66	0.39	1.31	3.10	1.77	...	...

Notes. [Fe/H] is listed in the scale of Grevesse et al. (2015). This is only an excerpt of the table to show its form and content. The complete table is available in electronic form at the CDS.

Table A.4. Stellar parameters and determined abundances for observed solar neighbourhood giants.

HIP/KIC/TYC	$T_{\rm eff}$	$\log g$	[Fe/H]	$v_{\rm micro}$	A(Zr)	A(La)	A(Ce)	A(Eu)
HIP1692	4216	1.79	−0.26	1.55	2.20	0.97	1.41	0.51
HIP9884	4464	2.27	−0.21	1.34	2.34	1.08	1.55	0.53
HIP10085	4062	1.44	−0.32	1.63	2.32	1.03	1.48	0.51
HIP12247	4790	2.71	−0.04	1.40	2.57	1.28	1.74	0.63
HIP28417	4746	2.56	−0.25	1.40	2.24	1.02	1.39	0.52
HIP33827	4235	1.99	0.01	1.50	2.61	1.23	1.68	0.72
HIP35759	4606	2.47	−0.15	1.42	2.23	1.06	1.54	0.74
HIP37447	4758	2.73	−0.04	1.35	2.49	1.26	1.75	0.71
HIP37826	4835	2.93	0.07	1.24	2.68	1.33	1.79	0.73
HIP43813	4873	2.62	−0.07	1.51	2.61	1.35	1.83	0.63

Notes. [Fe/H] is listed in the scale of Grevesse et al. (2015). This is only an excerpt of the table to show its form and content. The complete table is available in electronic form at the CDS.

Paper II

A&A 666, A125 (2022)
https://doi.org/10.1051/0004-6361/202244013

Astronomy & Astrophysics

Abundances of disk and bulge giants from high-resolution optical spectra

V. Molybdenum: The p-process element⋆,⋆⋆

R. Forsberg[1], N. Ryde[1], H. Jönsson[2], R. M. Rich[3], and A. Johansen[1,4]

[1] Lund Observatory, Department of Astronomy and Theoretical Physics, Lund University, Box 43, 22100 Lund, Sweden
e-mail: rebecca@astro.lu.se
[2] Materials Science and Applied Mathematics, Malmö University, 205 06 Malmö, Sweden
[3] Department of Physics and Astronomy, ICLA, 430 Portola Plaza, Box 951547, Los Angeles, CA 90095-1547, USA
[4] Center for Star and Planet Formation, GLOBE Institute University of Copenhagen, Øster Voldgade 5–7, 1350 Copenhagen, Denmark

Received 10 May 2022 / Accepted 27 June 2022

ABSTRACT

Aims. In this work, we aim to make a differential comparison of the neutron-capture and p-process element molybdenum (Mo) in the stellar populations in the local disk(s) and the bulge, focusing on minimising possible systematic effects in the analysis.
Methods. The stellar sample consists of 45 bulge and 291 local disk K-giants observed with high-resolution optical spectra. The abundances are determined by fitting synthetic spectra using the Spectroscopy Made Easy (SME) code. The disk sample is separated into thin and thick disk components using a combination of abundances and kinematics. The cosmic origin of Mo is investigated and discussed by comparing with published abundances of Mo and the neutron-capture elements cerium (Ce) and europium (Eu).
Results. We determine reliable Mo abundances for 35 bulge and 282 disk giants with a typical uncertainty of [Mo/Fe] ∼ 0.2 and ∼0.1 dex for the bulge and disk, respectively.
Conclusions. We find that the bulge is possibly enhanced in [Mo/Fe] compared to the thick disk, which we do not observe in either [Ce/Fe] or [Eu/Fe]. This might suggest a higher past star-formation rate in the bulge; however, as we do not observe the bulge to be enhanced in [Eu/Fe], the origin of the molybdenum enhancement is yet to be constrained. Although the scatter is large, we may be observing evidence of the p-process contributing to the heavy element production in the chemical evolution of the bulge.

Key words. stars: abundances – Galaxy: abundances – Galaxy: bulge – Galaxy: disk – Galaxy: evolution – solar neighborhood

1. Introduction

Elemental abundances of stars have proven to be key both in tracing the chemical evolution of the Milky Way and to our understanding of the origin of the elements themselves. Stars carry a chemical fingerprint from the molecular cloud from which they formed, which can be measured in their photospheres. The Galaxy is enriched with elements over time, where they are formed in various processes, either internally in stars or in more explosive environments such as type Ia and II supernovae (SNe) and neutron star mergers (NSM).

By measuring the chemical abundances in stars of a range of metallicities, [Fe/H], we can trace the evolution of elements and, in turn, the stellar populations that make up the Milky Way. In this work, we focus on the disk components (thin and thick) and the bulge. The origin and evolution of the bulge have attracted much attention, and the bulge has been re-defined from a classical, spherical bulge to now being primarily classified as a pseudo-bulge with a box/peanut bar (e.g. Ness et al. 2012; Di Matteo et al. 2014; Shen & Zheng 2020). The connection of the bulge or bar to the disk structure remains central, and careful, detailed abundance studies reveal surprisingly small differences between the composition of the bulge and the thick disk (Jönsson et al. 2017b; Lomaeva et al. 2019; Forsberg et al. 2019). While it is agreed that the bulge metallicities reach values higher than those of the thick disk (Matteucci & Brocato 1990; McWilliam 2016), there remains no convincing difference in abundance trends (see e.g. Barbuy et al. 2018, and references therein). A careful differential comparison between the bulge and the disk is needed, and while many such studies are published, ours employs newly reduced and analysed high-quality data sets.

In this series of articles, (Jönsson et al. 2017a,b; Lomaeva et al. 2019; Forsberg et al. 2019, hereafter referred to as Paper I, Paper II, Paper III, Paper IV), the bulge chemistry is investigated by a differential comparison to a disk sample. The two

⋆ Full Tables A.1–A.4 are only available at the CDS via anonymous ftp to cdsarc.u-strasbg.fr (130.79.128.5) or via http://cdsarc.u-strasbg.fr/viz-bin/cat/J/A+A/666/A125

⋆⋆ Based on observations made with the Nordic Optical Telescope (programs 51-018 and 53-002) operated by the Nordic Optical Telescope Scientific Association at the Observatorio del Roque de los Muchachos, La Palma, Spain, of the Instituto de Astrofisica de Canarias, spectral data retrieved from PolarBase at Observatoire Midi Pyrénées, and observations collected at the European Southern Observatory, Chile (ESO programs 71.B-0617(A), 073.B-0074(A), and 085.B-0552(A)).

stellar populations have been analysed with the same method, atomic data, and set of spectral lines from high-resolution spectra of 291 disk giants and 45 bulge giants in order to minimise the systematic uncertainties in the analysis. In particular, using the same type of star removes the possible systematic difference in abundance between dwarf and giant stars (see e.g. Meléndez et al. 2008; Gonzalez & Gadotti 2016). In the previous papers of this series we present findings supporting that the bulge has a similar evolutionary history to the thick disk, although we cannot exclude possible relative enrichment in some elements, such as vanadium (V), cobalt (Co) (Paper III), and lanthanum (La) (Paper IV) in the bulge.

In Paper IV, we investigated the neutron-capture elements Zr, La, Ce, and Eu. These are produced through neutron-capture processes (Cameron 1957; Burbidge et al. 1957), which is the process responsible for creating more than two-thirds of the periodic table of elements. These can add an additional piece to the puzzle in Galactic archaeology, because these neutron-capture elements are different from both the α- and iron-peak elements which have primarily SNe type II and SNe type Ia origin.

The neutron-capture process involves two physical processes. The capture of a neutron onto a seed atom, creating a heavier isotope, and the possible subsequent β^- − decay, $n \rightarrow p + e^- + \nu_e$, creating a heavier element. As a consequence, the neutron-capture and β^- − decay outline two sub-processes, the *slow* s-process, and the *rapid* r-process.

While it is usual to refer to elements as primarily being either s- or r-process elements, in virtually all cases, both r- and s-processes contribute. An r-process element is an element with a dominant origin from the r-process in the Sun, and vice versa for s-process elements. However, it can be more informative to examine the origin of the (stable) isotopes that make up the element. For instance, europium (Eu, $Z = 63$) has two stable isotopes that each contribute roughly 50% to the solar Eu, ^{151}Eu, and ^{153}Eu (Bisterzo et al. 2014; Prantzos et al. 2020), where both of them have a dominating origin from the r-process, making Eu an r-process element. There are 35 stable isotopes that cannot be reached through either the s- or r-process and are instead formed in the so-called p-process (Cameron 1957; Burbidge et al. 1957); we discuss these in Sect. 5.

The element molybdenum[1] (Mo, $Z = 42$) has seven stable isotopes, namely ^{92,94,95,96,97,98,100}Mo and is an intriguing element because some of these isotopes are purely from the s-, r-, or p-processes. Both of the lightest ones, ^{92}Mo and ^{94}Mo, are p-isotopes, whereas ^{96}Mo is a pure s-isotope and ^{100}Mo is a pure r-isotope. Combined, the p-isotopes contribute roughly 20-25% of the solar Mo abundance, which is the highest contribution from the p-process seen in any element (as measured in the Sun, Prantzos et al. 2020). The second-highest contributing p-element is ruthenium (Ru, $Z = 44$) with roughly 7% of the solar ruthenium abundance (Prantzos et al. 2020). As such, Mo and its isotopes provide excellent benchmark examples for nuclear physics and astrophysics. Studying Mo from the perspective of Galactic chemical evolution can help to put constraints on the origin of this element, the origin of the p-process, and to constrain the evolution of the Galaxy itself.

The remaining contributions from the s- and r-process to Mo have varying values, where Bisterzo et al. (2014) report 39% of Mo production coming from the s-process, whereas Prantzos et al. (2020) instead give a 50% s-process and 27% r-process origin to Mo, at solar metallicities. However, it should be noted that the solar composition of molybdenum might not be representative of the Galactic composition often presented in Galactochemical evolution models. Measurements of meteorites show that the inner Solar System, especially the Earth, is relatively enriched in the s-process by high ^{96}Mo values compared to ^{92,94}Mo (p-process) and ^{95}Mo (r-process dominated; Burkhardt et al. 2011; Budde et al. 2016, 2019). This means that the Mo isotopic composition of Earth can be used to put constraints on the types of meteoric material that contributed to the formation of our planet. The meteoric isotopic composition has been suggested to be affected by the origin of the dust that makes up the meteorites (Lugaro et al. 2016; Ek et al. 2020). This makes Mo a particularly interesting target for study and means that putting further constraints on its cosmic origin could be of significant value.

Larger published samples of Mo abundances for stars in the disk and bulge are sparse. Mishenina et al. (2019) determined Mo abundances for roughly 200 dwarf disk stars, which complements previous abundances at metallicities of [Fe/H] < -1.2 dex (Peterson 2013; Roederer et al. 2014a; Hansen et al. 2014; Spite et al. 2018). However, in Galactic chemical evolution models, Mo has been consequently underestimated compared to observations (Mishenina et al. 2019). On the other hand, the models in Kobayashi et al. (2020), where ν-winds are included (which is a suggested production channel for p-isotopes), overproduce Mo, indicating that constraining this element is problematic without proper knowledge and modelling of the p-process. By presenting abundances for Mo in both giants in the local disk and in the bulge, we aim to put further constraints on both the Galactochemical evolution of the bulge and the origin of Mo.

This paper is structured as follows: in Sect. 2 we present the spectroscopic data used. In Sect. 3, we present the methodology for the analysis of the data, which follows closely that of previous papers in this series. In Sect. 4, we present the abundances, the estimated uncertainties and a comparison with previous studies. Finally, in Sects. 5 and 6 we discuss our results and outline our conclusions.

2. Data

In this section, we introduce the data used in this work, where we aim to have high-resolution and high-signal-to-noise (S/N) spectra for our bulge- and disk giants.

2.1. Bulge

Optical high-resolution spectra of bulge giants are fairly rare, because of the long integration times needed for observing these stars. Additionally, observing bulge giants in the optical wavelength regime is a challenge in itself, given the high amount of dust causing extinction. The spectra used here were therefore collected from low-extinction regions in the bulge, or its vicinity, which can be seen in Fig. 1.

The spectra for stars in the B3, BW, B6, and BL fields (using the naming convention in Lecureur et al. 2007) were obtained in 2003–2004 whilst the SW field was obtained in 2011 (ESO program 085.B-0552(A)). All spectra were obtained with the UVES/FLAMES spectrograph ($R \sim 47\,000$) mounted on the VLT and are limited to the wavelength regime of 5800–6800 Å.

[1] Molybdenum is an element both discovered and first time isolated by the Swedish chemists Carl Wilhelm Scheele and Peter Jacob Hjelm in the 18th century.

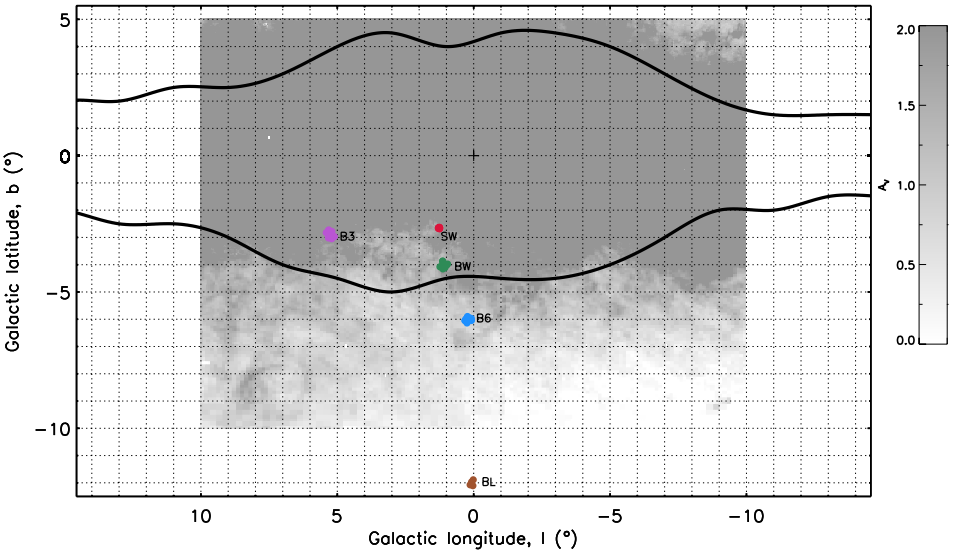

Fig. 1. Map of the Galactic bulge showing the five analysed fields, B3, BW, B6, BL (using the naming convention in Lecureur et al. 2007), and SW. The dust extinction towards the bulge is taken from Gonzalez et al. (2011, 2012) and scaled to optical extinction (Cardelli et al. 1989). The scale saturates at $A_V = 2$, which is the upper limit in the figure. The COBE/DIRBE contours of the Galactic bulge, in black, are from Weiland et al. (1994).

The S/N (see Paper I, for details of the S/N estimation) are generally around 50; see Table A.3 for details of all the bulge giants and their spectra.

The spectra from the B3, BW, B6, and BL fields were first used in Zoccali et al. (2006) and were reanalysed in several subsequent articles, such as Lecureur et al. (2007); Van der Swaelmen et al. (2016). In Papers II; III; IV, we reanalyse 27 of these bulge stars, plus the additional 18 stars in the low-extinction SW field, which brings the total number of bulge stars analysed in this paper to 45. The reader is referred to Paper II for further details of the bulge sample.

2.2. Disk

The disk sample consists of 291 giant local disk stars, 272 of which were observed by us using the FIbre-fed Echelle Spectrograph (FIES; Telting et al. 2014) mounted on the Nordic Optical Telescope, Roque de Los Muchachos, La Palma, and 19 spectra are downloaded from the PolarBase data base (Petit et al. 2014), in turn coming from the ESPaDOnS and NARVAL spectrographs (mounted on Canada–France–Hawaii Telescope and Telescope *Bernard Lyot*, respectively). The FIES and PolarBase spectrographs have similar resolutions of $R \sim 67\,000$ and $R \sim 65\,000$, respectively, and wavelength coverage of 3700–8300 Å and 3700–10 500 Å, respectively. However, we note that we only use the 5800–6800 Å wavelength regime, to match that of the bulge spectra and to only use the same spectral lines in the analysis. The FIES spectra have a S/N of around 80–120, whereas that of the PolarBase is lower, at around 30–50. All spectra are reduced using the standard automatic pipelines. See Table A.1 for details of all the disk giants and their spectra.

We plotted a telluric spectrum over the observed stellar spectra, namely the one in the Arcturus atlas (Hinkle et al. 1995), such that regions affected by telluric lines could be avoided on a star-by-star basis. Further details of the FIES observational programs and the disk spectra are found in Paper I.

3. Methodology

The methodology of the analysis in this work closely follows the methodology set out in the previous papers in this series: Paper I; Paper II; Paper III; Paper IV. In those previous papers, we obtain very tight abundance trends with metallicity, and we can see that a carefully chosen set of spectral lines is key to achieving these high-quality abundances. In this section, we go through the basic details of the analysis of the giant stars, especially focusing on the 6030 Å Mo I line.

3.1. Spectral analysis

The spectral analysis to obtain the stellar parameters and elemental abundances was carried out using the tool Spectroscopy Made Easy (Valenti & Piskunov 1996; Piskunov & Valenti 2017, SME, version 554). SME produces a synthetic spectrum using a χ^2-minimisation to fit the observed spectrum. To produce a synthetic spectrum, SME requires:

– A line list containing atomic- and/or molecular data. We use the *Gaia*-ESO line list version 6 as published in Heiter et al. (2021).

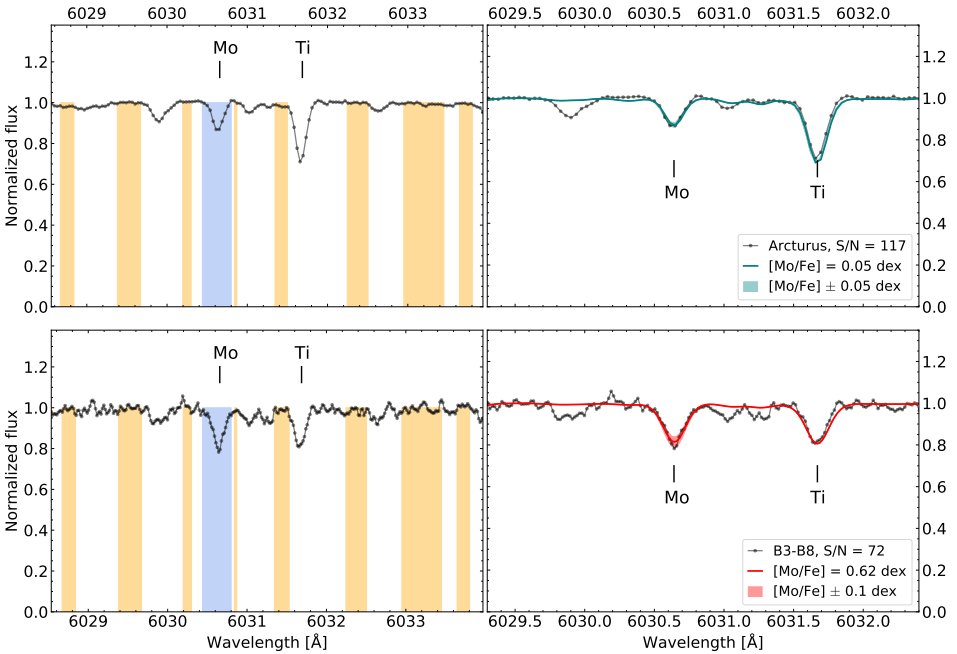

Fig. 2. Observed spectrum (black) for a disk star (*top*, Arcturus) and bulge star (*bottom*, B3–B8). *Left*: line mask placements for the Mo line marked in blue and the continuum placements in yellow. *Right*: synthetic spectra, either in teal (*top*, disk star Arcturus) or red (*bottom*, bulge star B3–B8). The estimated S/N of both spectra, 117 and 72 respectively, are indicated in the legend. We note that the wavelength region of the rightmost figures is zoomed in with respect to the leftmost figures.

– Model atmospheres; in this work use the grid of MARCS models[2] (Gustafsson et al. 2008). As our stellar sample consists of giant stars, we use the MARCS models with spherical symmetry for $\log(g) < 3.5$.

– Stellar parameters; the ones used in this work were derived by Papers I; II, where more details can be found. Briefly, we use a combination of iron (Fe) and calcium (Ca) lines, namely Fe I and Fe II, Ca I, and $\log g$ sensitive Ca I line wings. The Fe I lines suffers from deviations from Local Thermodynamic Equilibrium (LTE) and we adopt non-LTE (NLTE) corrections from Lind et al. (2012). In Papers I; II, we also estimate typical uncertainties and compare with *Gaia* benchmark stars (Heiter et al. 2015; Jofré et al. 2014, 2015). In general, the stellar parameters compare well with the benchmark parameters. However, the surface gravities are likely systematically high from the benchmark comparison with +0.10 dex. Furthermore, comparing with StarHorse (Queiroz et al. 2018) surface gravities derived from *Gaia* EDR3 (Gaia Collaboration 2016, 2021; Anders et al. 2022), the Paper I surface gravities are also systematically +0.10 dex too high. This could cause some overestimation of the abundances, but the main scope of this work is to make a differential comparison between the disk and bulge sample, which will be equally systematically affected.

– A defined spectral segment, within which the line of interest and local continuum is marked with a line mask, or continuum masks, respectively. By the manual placement of local continuum masks, the continuum is renormalised[3] more carefully to the local segment around the spectral line of interest. SME uses the continuum masks to fit a straight line in between, creating the local continua.

The line mask around the line of interest, the Mo I 6030 Åline in this case, is also defined manually. This manual placement of both line- and continuum masks has been shown to be crucial in order to get high-precision abundances (Paper I; Paper II; Paper III; Paper IV). The line mask and continuum masks can be seen in Fig. 2. We go into more details of the abundance determination below.

3.2. Abundance determination of Mo

In the abundance determination, we use the Mo I spectral line located at 6030 Å. The atomic data we use for this line come from the *Gaia*-ESO line list version 6 (Heiter et al. 2021); see Table 1. The spectral line is classified as a *Yes*/*Yes* line in the *Gaia*-ESO list, meaning that it has a high-quality $\log(gf)$-value

[2] Available at `marcs.astro.uu.se`

[3] A crude normalisation has already been done using the IRAF `continuum` tool.

Table 1. Atomic data for the Mo I atomic line.

Element	Air wavelength (Å) [(a)]	$\log(gf)$	$\chi_{\rm exc}^{\rm low}$ (eV)
Mo I	6030.644	−0.523	1.531

Notes. Data from Whaling & Brault (1988), as compiled in the *Gaia*-ESO. v.6 line list (Heiter et al. 2021). [(a)]The wavelength is the wavelength in air.

and is unblended. Furthermore, Heiter et al. (2021) report that this line should be avoided in abundance analyses of dwarf stars. As such, this line is a great example of a line that can only be reached in giant stars, where the lower surface gravities increase the line strength sufficiently for reliable abundances to be estimated.

Molybdenum does not have any hyperfine splitting (HFS) but has, as mentioned above, seven stable isotopes in the Sun. However, these are not included in the line list because the isotopic shift (IS) cannot be resolved, partly because of the Mo I lines being very weak. This means that we cannot measure the individual isotopic abundances, but rather the molybdenum abundance as a whole.

The observed and synthetic spectra close to the 6030 Å line can be seen in Fig. 2 for both a typical bright red giant disk star (Arcturus/α-Boo/HIP69673, in the top row) and one of the bulge stars (B3–B8, in the bottom row). Here, we also plot the line- and continuum segments used to produce the synthetic spectra. The same masks are used for all stars in the analysis for optimal coherence.

All synthetic spectra are examined by eye and the masks edited to return the best possible fit of the synthetic spectra to the observed spectrum. We were able to determine reliable synthetic spectra and, in turn, abundances for all stars where a line is detectable and above the noise. In instances where the spectral line is weaker than the noise, the line cannot be used to determine a reliable abundance. Nonetheless, using giant stars we are able to determine abundances for stars with a low molybdenum abundance because the line strengths typically increase with decreasing surface gravity. It should be noted that we determined all Mo abundances under the assumption of LTE. The 6030 Å line is a rather weak line, and forms in the deeper parts of the stellar atmosphere where collisions dominate, establishing LTE. As such, NLTE corrections for Mo should be small or negligible, which has been noted previously with smaller samples of stars (see e.g. Peterson 2011; Roederer et al. 2014b, 2022).

3.3. Population separation

The separation of the disk components has been done using chemical and kinematical properties. As described in more detail in Paper III, we use [Ti/Fe] and [Fe/H] (determined in Paper I) as a proxy for the chemical separation typically observed in α-abundances. Additionally, we use Galactic space velocities as calculated with `galpy` (Bovy 2015) using radial velocities (see Table A.1), distances (McMillan 2018), and proper motions (Gaia Collaboration 2016, 2018) as input and calculate the total velocities, $V_{\rm total}^2 = U^2 + V^2 + W^2$. As *Gaia* has a limit on brightness, some of our brightest stars are not observed with *Gaia*, and kinematic data were available for a total of 268 of the disk stars. We then use the clustering method called `Gaussian Mixture Model` (GMM) – found in the `scikit-learn` module in Python (Pedregosa et al. 2011) – to cluster the disk data into the two components. As we use a combination of chemistry and kinematics, we refer to the components as thin and thick disk, where the thick disk is typically more α-rich and kinematically hotter than the thin disk.

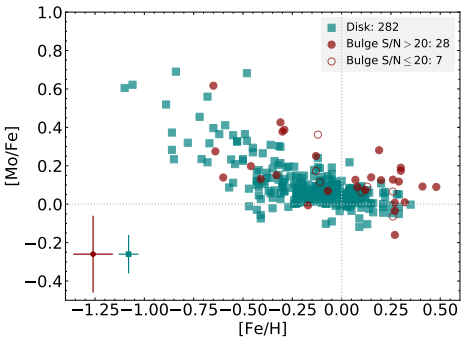

Fig. 3. [Mo/Fe] vs [Fe/H] for the disk (teal) and the bulge (red) in this study. The typical uncertainties, as described in Sect. 4.3 are indicated in the lower right corner. The grey dashed lines that go through [0, 0] indicate the solar value, which we have normalised to A(Fe) = 7.45 (Grevesse et al. 2007) and A(Mo) = 1.88 (Grevesse et al. 2015).

4. Results

In this section, we introduce the abundances that we determined in this study, show a comparative plot with abundances from previous studies, as well as introduce the uncertainty estimates for the abundances from this study.

4.1. Abundances from this study

After manual inspection of the synthetic spectra, we end up with 282 stars in the local disk and 35 in the bulge with reliably determined Mo abundances. The detailed abundances for the disk and bulge giants can be found in Tables A.2 and A.4, respectively. The abundance ratio [Mo/Fe] plotted against the metallicity [Fe/H] for the stellar samples can be seen in Fig. 3. For consistency with the previous papers in this series, we make a distinction between bulge spectra with S/Ns of above and below 20. Nonetheless, as can be seen in Fig. 3, the bulge stars with $S/N \leq 20$ are within the scatter of the overall bulge trend. The typical uncertainties are noted in the lower left corner of the plot. Our method of estimation of the uncertainties is described further in Sect. 4.3.

4.2. Abundances from previous studies

The separation of the disk components can be seen in Fig. 4, where we also compare with a disk sample from Mishenina et al. (2019). They published the first extended sample of Mo-abundances for stars in the Milky Way disk, which, together with halo observations (as described below), help to extend our knowledge of molybdenum. With our additional sample, we now extend the study of Mo even further, and provide a comparison giant sample to the disk abundances. The Mishenina et al. (2019) sample consists of 183 disk stars, where they identify 163 as thin and 20 as thick disk dwarf stars (determined using kinematics, Mishenina et al. 2013, 2019), whereas we identify 191 and 68 thin and thick disk giant stars. As such, we more than double

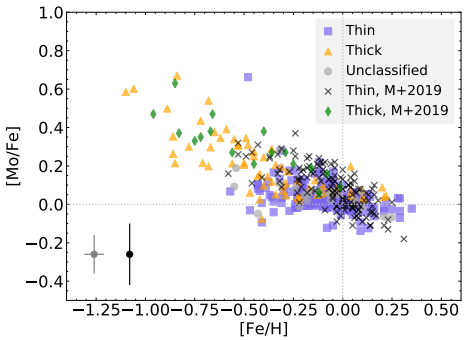

Fig. 4. Comparison of the [Mo/Fe] thin (blue squares) and thick (orange triangles) disk abundances determined in this work with the thin (black crosses) and thick (green diamonds) disk in Mishenina et al. (2019). It should be noted that the 23 stars that we do not have kinematical data for have not been classified as either thin or thick disk, and can be seen as grey circles. The typical uncertainties are indicated in the lower left corner (this work in grey, Mishenina et al. 2019 in black). The grey dashed lines that go through [0,0] indicate the solar value, which we have normalised to $A(\mathrm{Fe}) = 7.45$ (Grevesse et al. 2007) and $A(\mathrm{Mo}) = 1.88$ (Grevesse et al. 2015). The thin disk star at $[\mathrm{Fe/H}] = -0.55$ with high molybdenum abundance of $[\mathrm{Mo/Fe}] = 0.68$, HIP65028, is discussed at the end of Sect. 5.

and triple the thin and thick disk sample of Mo-abundances, respectively.

Mishenina et al. (2019) also have high-resolution spectra of $R > 42\,000$ and $S/N > 100$. In the abundance analysis of Mo I of their dwarf sample, they use the spectral lines at 5506 and 5533 Å. These two lines have relatively strong blends, which can make abundance determination difficult (Heiter et al. 2021). As these two lines are outside of the spectral range for our bulge stars, we have not included these in our analysis. Additionally, the 6030 Å line that is used in our study is not accessible in dwarf stars, where it is very weak (see Sect. 3.2).

In Fig. 5, we plot some additional previous work in the more metal-poor regime of $[\mathrm{Fe/H}] < -1.2$, which consists mainly of halo stars. Roederer et al. (2014a) uses the 3864 Å Mo I line to determine the Mo-abundances in both horizontal branch, main sequence, red giant, and subgiant stars. Altogether, they determine Mo in 279 low-metallicity stars (we note that the two metal-poor stars in Roederer et al. 2014b, are not included in Fig. 5). It is worth noting that even though the 3864 Å is not reachable in our sample, which is limited to 5800–6800 Å, the bluer wavelength regime would be very crowded with lines in giant stars at the metallicities of our stellar sample, making continuum placement extremely difficult.

In the work from Hansen et al. (2014) and Peterson (2013), the authors primarily also use the 3864 Å Mo I line to determine Mo abundances. While Peterson (2013) focuses on turnoff stars, Hansen et al. (2014) sample consists of dwarfs and giant stars, a total of 52. These latter authors have high-quality data with spectral resolution of $R \sim 40\,000$ and $S/N > 100$. We note that in Fig. 5, we only plot the 40 stars that have abundances marked as high quality, which are not affected by large uncertainties due to blends and continuum placement (see Table 4 in Hansen et al. 2014). Finally, we also plot the Mo abundances of the 11 stars in Spite et al. (2018), who also use the bluer 3864 Å line. It should be noted that the star identified at [Fe/H] −3.06 with [Mo/Fe] of −0.38 is a r-poor star, BD−18 5550, explaining the low abundance.

There are also published Mo abundances for barium stars (Ba-stars). These are stars enriched in s-process elements, as well as in carbon, but otherwise have nominal abundances. These stars have been enriched due to accretion of s-process elements from a companion AGB-star, resulting in these peculiar abundances (Allen & Barbuy 2006; Roriz et al. 2021). As such, we do not include Ba-stars in the comparison plot with previous Mo abundances. Furthermore, Mo has been measured in the globular clusters M22 (Roederer et al. 2011) and 47 Tucanae (Thygesen et al. 2014), in open clusters (see e.g. Overbeek et al. 2016; Mishenina et al. 2020, among others), and in the r-process enhanced bulge star 2MASS J18174532−3353235 in Johnson et al. (2013). We note that these are not included in Fig. 5, where we look at the overall disk (and halo) trend in molybdenum.

Lastly, in Figs. 6 and 7, we compare the Mo abundance with the abundances of Ce (s-process) and Eu (r-process) from Paper IV. We discuss these figures further in Sect. 5 below.

4.3. Uncertainties

The random uncertainties that arise because of line- and continuum placements are hard to estimate, which is also true for the possible uncertainties in the atomic data and the model atmosphere assumptions used for the spectral line synthesis. As such, the uncertainties for the abundances determined in this work are deemed to be mostly affected by the possible uncertainties in the stellar parameters.

The typical uncertainties for a local disk giant of the median $S/N \sim 100$ are estimated by Paper I to be on the order of $T_{\mathrm{eff}} \pm 50$ K, $\log g \pm 0.15$ dex, $[\mathrm{Fe/H}] \pm 0.05$ dex, and lastly ± 0.1 km s^{-1} for ξ_{micro}. As the bulge stars have a generally lower S/N, the uncertainties are estimated to be twice that of the disk stars (Paper II). These values can be seen in the leftmost column of Table 2, and are subsequently used to estimate the uncertainties for the Mo abundances.

To estimate the Mo abundances, we add the uncertainties from Paper I to two typical giant stars, Arcturus (also known as α−Boo or HIP69673) and Rasalas (μ−Leo or HIP48455). We do this step-wise, and determine the abundance with that new set of stellar parameters, for both stars.

The total abundance uncertainties coming from the uncertainties in the stellar parameters are then calculated as

$$\sigma[\mathrm{Mo/Fe}] = \sqrt{|\delta A_{T_{\mathrm{eff}}}|^2 + |\delta A_{\log(g)}|^2 + |\delta A_{[\mathrm{Fe/H}]}|^2 + |\delta A_{v_{\mathrm{micro}}}|^2}, \quad (1)$$

where for possible non-symmetrical abundance changes, the mean value is used in the squared sums. Taking the average of the $\delta A(\mathrm{Mo})_{\alpha-\mathrm{Boo}}$ and $\delta A(\mathrm{Mo})_{\mu-\mathrm{Leo}}$ as calculated from Eq. (1) we get a typical abundance uncertainty of 0.1 dex in the disk and 0.2 dex in the bulge. We list the total uncertainties in Table 2.

Stellar parameters in reality are coupled and change as a function of one another, and the method of determining the uncertainties used here is a simplified approach. From Monte Carlo estimations of the uncertainties (Paper III; Paper IV), we find the uncertainties determined in this simplified way to yield very similar values. Additionally, considering the tight abundance trends we produce, the uncertainties can in general be considered to be upper limits.

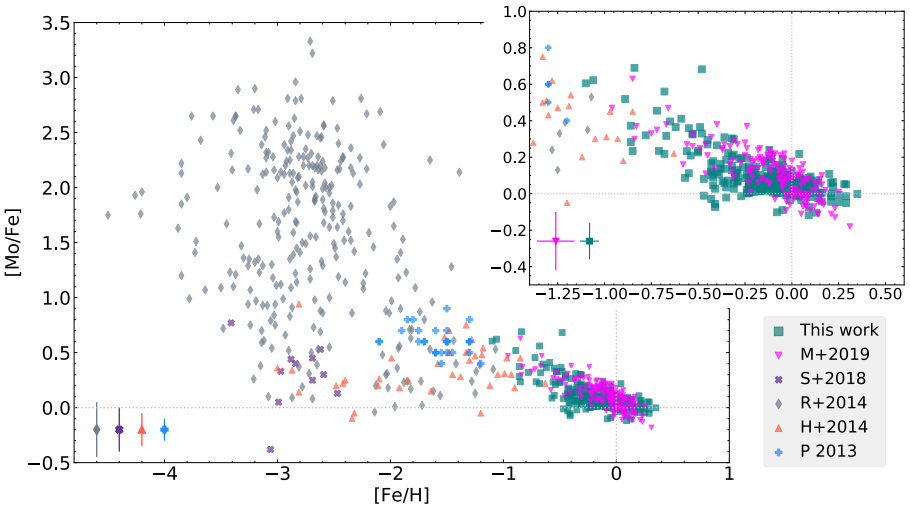

Fig. 5. Comparing the [Mo/Fe] disk abundances determined in this work (teal squares, as in Fig. 3) to those in previous studies in the disk (Mishenina et al. 2019, magenta downward pointing triangles) and the halo (Peterson 2013; Roederer et al. 2014a; Hansen et al. 2014; Spite et al. 2018, blue pluses, grey diamonds, coral triangles, purple crosses, respectively). This is also indicated in the lower right legend. The smaller upper rightmost plot shows a zoomed in portion of the higher metallicity region in the larger leftmost plot. The typical uncertainties reported in the studies are indicated in the lower left corner of both plots. The grey dashed lines that go through [0, 0] indicate the solar value, which we have normalised to A(Fe) = 7.45 (Grevesse et al. 2007) and A(Mo) = 1.88 (Grevesse et al. 2015).

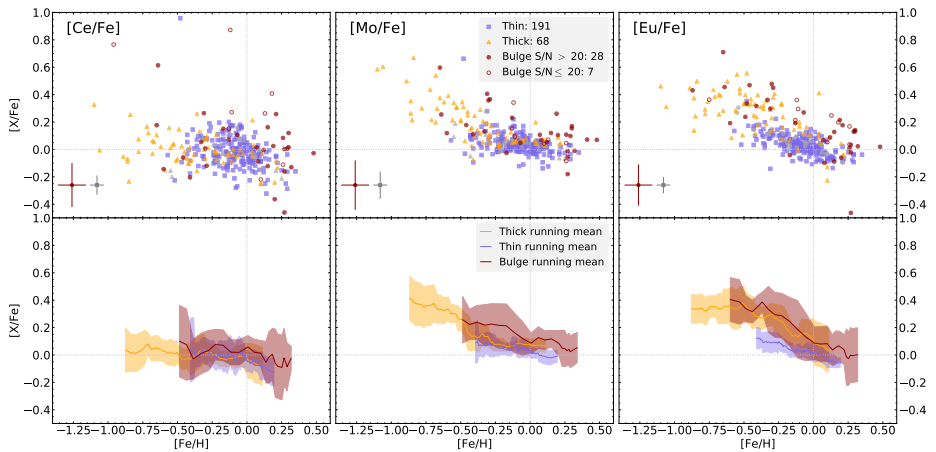

Fig. 6. [Mo/Fe] over [Fe/H] for the thick disk (yellow), thin disk (blue), and bulge (red) stars seen in the middle panels. The number of stars in each population is marked in the legend of the scatter plot (*upper*). The running mean (*lower*) is calculated using a box size of 10 (thick), 20 (thin), and 7 (bulge) stars and plotted with a 1σ deviation. We note that for the bulge, we only use stars with a spectra of >20 S/N to produce the running mean. We compare this to the s-process element Ce (*left*) and r-process element Eu (*right*) from Forsberg et al. (2019). The typical uncertainties are indicated in the lower right corner of the plots (red for bulge, grey for disk). The grey dashed lines that go through [0, 0] indicate the solar value, which we have normalised to A(Fe) = 7.45, A(Ce) = 1.70 (Grevesse et al. 2007), A(Mo) = 1.88, A(Eu) = 0.52 (Grevesse et al. 2015). The [Eu/Fe] values in Forsberg et al. (2019) are reported to likely be systematically too high, possibly originating from the systematic uncertainties in log(g) as reported in Paper I. Due to this, we lower the [Eu/Fe] abundances by 0.10 dex in this figure, such that the thin disk in [Eu/Fe] goes through the solar value.

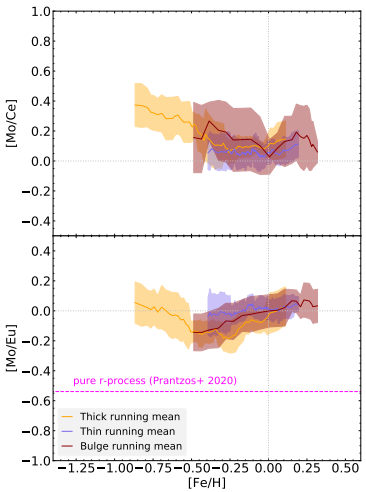

Fig. 7. Comparison of Mo with the s-process element Ce (*top*) and the r-process element Eu (*bottom*), for the running means of the populations, similarly to Fig. 6. We also plot the pure r-process line using the values in Prantzos et al. (2020; magenta).

Table 2. Estimated uncertainties for Mo using the typical giant stars $\alpha-$Boo and $\mu-$Leo.

Uncertainty [a]	δ[Mo/Fe]$_{\alpha-\mathrm{Boo}}$	δ[Mo/Fe]$_{\mu-\mathrm{Leo}}$
$\delta\, T_{\rm eff}$ = −50 K	−0.05	−0.05
$\delta\, T_{\rm eff}$ = +50 K	+0.05	+0.05
δ log(g) = −0.15	−0.02	−0.03
δ log(g) = +0.15	+0.03	+0.03
δ [Fe/H] = −0.05	−0.04	+0.04
δ [Fe/H] = +0.05	+0.04	−0.04
$\delta\, \xi_{\rm mic}$ = −0.10	0.00	0.00
$\delta\, \xi_{\rm mic}$ = +0.10	0.00	0.00
δ[Mo/Fe]$_{\rm total}$ disk	0.11 dex	0.10 dex
$\delta\, T_{\rm eff}$ = −100 K	−0.10	+0.09
$\delta\, T_{\rm eff}$ = +100 K	+0.11	+0.10
δ log(g) = −0.30	0.00	−0.05
δ log(g) = +0.30	+0.06	+0.05
δ [Fe/H] = −0.10	−0.08	+0.08
δ [Fe/H] = +0.10	+0.09	−0.08
$\delta\, \xi_{\rm mic}$ = −0.20	+0.01	+0.01
$\delta\, \xi_{\rm mic}$ = +0.20	0.00	−0.01
δ[Mo/Fe]$_{\rm total}$ Bulge	0.20 dex	0.20 dex

Notes. The upper half of the table shows the typical uncertainties for a disk star, and the lower half for a typical bulge star. The total uncertainty, δ[Mo/Fe]$_{\rm total}$, is calculated using Eq. (1). [a]The uncertainties in the stellar parameters are estimated in Paper I.

5. Discussion

Here, we first discuss the astrophysical sites for the s-, r-, and p-processes. We then compare with previous data of molybdenum, and end with a discussion of molybdenum as compared with other neutron-capture elements. Lastly, we briefly comment on the star HIP65028.

5.1. The neutron-capture and p-processes

As mentioned in Sect. 1, the origins of Mo are diverse, with stable isotopes originating from the s-, r-, and p-processes, or a combination of these. As for the two neutron-capture processes, the sites where these take place are constrained via the required neutron flux.

The s-process can be divided into two subprocesses, the main s-process and the weak s-process. The main s-process takes place in the interior of low- and intermediate asymptotic giant branch (AGB) stars in a ^{13}C-pocket during the third dredge-up (see Karakas & Lattanzio 2014; Bisterzo et al. 2017, and references therein). This process is the main s-process producer of elements with $A \gtrsim 90$, such as cerium, which we compare our Mo abundances to. We refer the reader to Paper IV for a more in-depth description of the main s-process and its components.

The weak s-process requires higher temperatures and has the ^{22}Ne(α, n)^{25}Mg-reaction as a neutron source. As such, it takes place in the interior of massive stars with mass $\gtrsim 8\, M_{\odot}$. The weak s-process can produce trans-iron elements of $60 \lesssim A \lesssim 90$, making its affect on the production of molybdenum-isotopes likely very small and close to negligible (Johnson & Bolte 2002; Pignatari et al. 2010; Prantzos et al. 2020).

However, some studies (e.g. Travaglio et al. 2004; Bisterzo et al. 2014, 2017) find that an additional process, Light Element Primary Process (LEPP), which is different from both the main s-process and the weak s-process, would be necessary to explain the abundances of Sr, Y, and Zr, as well as the s-only isotopes ^{96}Mo and ^{130}Xe. Nonetheless, the s-process has proven difficult to model, because of its dependence on a wide range of physical parameters, and the uncertainties on the yields (Cescutti & Matteucci 2022). The necessity for LEPP has also been questioned (see e.g. Cristallo et al. 2011, 2015; Trippella et al. 2016; Prantzos et al. 2020; Kobayashi et al. 2020); indeed it was deemed unnecessary when modifying parameters of Galactic chemical evolution models, such as the star formation rate, stellar yields, and varying the size of the ^{13}C-pocket. Additionally, the rotation of massive stars has also been shown to have an affect on the amounts of s-process elements of $A \lesssim 90$ being produced at low metallicities (Cescutti et al. 2013; Frischknecht et al. 2016; Limongi & Chieffi 2018). Therefore, the s-process contribution to molybdenum is believed to mainly come from the main s-process in AGB stars.

Given the AGB origin of main s-process elements, we expect these to have a trailing end at lower metallicities in abundance plots caused by the natural delay-time of AGB-stars. As AGB stars start to enrich the interstellar medium (ISM) with s-process elements, the abundance of these elements increases in newly formed stars, resulting in an increase in [s/Fe] before SNe type Ia start to enrich the ISM with iron, bringing the abundance trend down again (see e.g. observations in Mishenina et al. 2013; Battistini & Bensby 2016; Delgado Mena et al. 2017; Forsberg et al. 2019).

The r-process produces elements such as Eu, which we also compare with Mo. Given the high neutron flux required for the r-process, this is a production channel that works on very short timescales. The proposed production sites for the r-process are various SNe such as core-collapse, magneto-rotational, electron capture (CC, MR, EC, Woosley et al. 1994; Nishimura et al. 2006; Kobayashi et al. 2020; Wanajo et al. 2011) and neutron star mergers (NSMs; Freiburghaus et al. 1999;

Matteucci et al. 2014). R-process ejecta was detected in observations of the electromagnetic signature from the NSM GW170817 (Abbott et al. 2017a,b; Kasen et al. 2017). However, Kobayashi et al. (2020) uses Galactochemical evolution models to show that NSMs are more or less negligible in the production of r-process elements, and point to MRSNe as the major contributor. Côté et al. (2019) and Skúladóttir & Salvadori (2020) point out the necessity for a combination of two sources with different delay-times in order to reproduce observed abundance trends – which is very similar to that of α-elements – in the Milky Way and some of the dwarf galaxies. In conclusion, there are still uncertainties as to the relative contributions from different sources. To determine the contribution from the suggested production sites is an active area of research, and having high-quality observational data for comparison with models is key in this continued effort.

The site of the p-process is even less well understood. Cameron (1957); Burbidge et al. (1957) suggested that it may take place in hydrogen-rich layers of SNe type II. The name 'p-process' refers to proton capture, but this is not necessarily always the case and there are several mechanisms and sites suggested as the cosmic origin for the p-isotopes, which we outline here (see also the review of Rauscher et al. 2013).

The γ-process is the photo-disintegration of heavy, neutron-rich isotopes that have already been created by means of neutron-capture processes, caused by highly energetic gamma-photons. (Woosley & Howard 1978; Arnould & Goriely 2003; Hayakawa et al. 2004; Pignatari et al. 2016). It has been proposed that the γ-process takes place in the explosive O/Ne-shell-burning stages of core-collapse SNe (Hoffman et al. 1994; Rayet et al. 1995; Pignatari et al. 2016; Nishimura et al. 2018; Travaglio et al. 2018), in pre-SNe stages (Ritter et al. 2018), or in type Ia SNe (Howard et al. 1991; Travaglio et al. 2011, 2015). As such, we expect the signature from these processes to be similar to the signatures for α- and iron-peak elements, which also originate from core-collapse SNe and type Ia SNe, respectively.

The ν-process, which takes place during core-collapse SNe, could also be responsible for the production of p-isotopes. This process has been favoured among those put forward as giving rise to some of the lightest p-isotopes, including ^{92,94}Mo (Woosley et al. 1990; Fröhlich et al. 2006).

The rapid proton-capture processes can be divided into three different processes, the rp-, pn-, and νp-process. The rapid proton capture takes place in proton-rich environments through (p,γ)-reactions (Schatz et al. 1998).

The rp-process is usually halted at isotopes with a combination of long half-lives and small proton-capture cross sections, causing 'waiting points' (Schatz et al. 2001). The rp-process has been suggested to be linked to the explosive hydrogen- and helium-burning on the surface of mass-accreting neutron stars (Schatz et al. 1998; Koike et al. 2004). These waiting points that halt the rp-process can be crossed either by the pn- or the νp-process. If there is a high density of neutrons, (n,p)-reactions can cross the waiting points, which is the pn-process. Otherwise, neutrons can be created through anti-neutrino interactions with protons, in $\overline{\nu}_e(p, e^+)$n-reactions, which is the νp-process (Fröhlich et al. 2006).

The pn-process has been suggested to take place in a subclass of type Ia SNe which is the result of disruption of a sub-Chandrasekhar CO-white dwarf (WD) due to a thermonuclear runaway in He-rich accretion layers (Goriely et al. 2002). The site for the νp-process is thought to be either core-collapse SNe explosions or at accretion disks around compact objects (Fröhlich et al. 2006, 2017; Eichler et al. 2018).

In conclusion, there is a plethora of different mechanisms and sites that could produce the p-isotopes. By comparing to neutron-capture elements that dominate in the s- and r-process, the p-process might be disentangled from these.

5.2. Comparison with previous work on molybdenum

As noted earlier, the disk [Mo/Fe]-trend in Mishenina et al. (2019) decreases at higher metallicities, whereas our disk trend decreases to a lesser degree. Furthermore, considering the separation of the thin and thick disk in Fig. 4, we see that the solar–[Mo/Fe] found at around [Fe/H] ~ -0.4 in our data, corresponds to the thin disk, which is not observed in Mishenina et al. (2019). As such, our [Mo/Fe] trend with metallicity for the thin disk shows more of a trailing end at lower metallicities, which is typical for an s-process element that has a dominating enrichment from AGB stars at [Fe/H] $\gtrsim -0.5$, as discussed above.

As can be seen in Fig. 5, the cosmic scatter at [Fe/H] < -1.5 is extremely large, mostly based on the data from Roederer et al. (2014a). A similarly large spread at low metallicities is also seen for other neutron-capture elements, such as Eu (François et al. 2007; Frebel 2010; Cescutti et al. 2015) and ytterbium (Yb, $Z = 70$, also as published in Roederer et al. 2014a), whereas tighter trends are observed at higher metallicities (see e.g. Montelius et al. 2022, for Yb). The stochastic Galactochemical evolution models from Cescutti et al. (2015) can reproduce these observations and show that neutron-capture elements indeed have a large spread at lower metallicities. This is explained by the fact that at low metallicities, all neutron-capture elements in fact have an r-process origin, because the onset of s-process production of AGB has not yet taken place. The spread could be a signature of local r-process production, such as NSM, as discussed in Cescutti et al. (2015). This, in combination with the Galaxy not being well mixed, and indeed very low in Fe, could give rise to locally high [r-process/Fe], which is observed for [Mo/Fe].

It should be noted that the scatter at the lower metallicities, spanning the range [Mo/Fe] $\sim 0-3.3$ dex, mostly originates from the data of Roederer et al. (2014a), whereas the abundances of Peterson (2013); Hansen et al. (2014); Spite et al. (2018) are found within [Mo/Fe] $\sim 0-1$ dex. More abundances for these low-metallicity stars would be needed to further constrain the physical origin of this scatter for the r-process.

5.3. Comparison with other neutron-capture elements

We investigate the origin of Mo by comparing it to Ce which has a roughly 85% contribution from the s-process (Bisterzo et al. 2014; Prantzos et al. 2020) and to Eu which has a roughly 95% contribution from the r-process (Bisterzo et al. 2014; Prantzos et al. 2020), making these elements key representatives of these processes in the Galactic stellar populations. The abundance data for Ce and Eu in the disk and bulge come from Paper IV, and can be seen in Fig. 6, which reveals that the down-turning trailing end at lower metallicities is more prominent in [Ce/Fe] than in [Mo/Fe], which is expected from the theoretical origins of these elements. Moreover, both the thick disk and the bulge show decreasing [Mo/Fe]-trends with increasing metallicity – which is typical for an r-process element – due to the fast enrichment (see the models in Matteucci et al. 2014; Grisoni et al. 2020).

In [Eu/Fe], we observe a 'knee' or plateau in the thick disk at [Fe/H] ≤ -0.5, which is not observed for [Mo/Fe]. Indeed, [Mo/Fe] does not seem to plateau at all. However, more abundances at these metallicites are needed to further constrain this.

With the combined data from Peterson (2013); Hansen et al. (2014); Roederer et al. (2014a) it does seem like [Mo/Fe] has a knee around [Fe/H] ∼ −0.75 before the previously discussed increased scatter at low metallicities.

As previously stated in Paper IV, the general similarity between the thick disk and the bulge is high in [Ce, Eu/Fe], as seen in the running means of the abundances in the second row of Fig. 6, pointing to a similar star formation history of the populations. The [Ce,Eu/Fe] abundances in the running means are at some metallicities ∼0.1 dex higher in the bulge than in the thick disk, however as the scatter is large in the bulge, we are unable to draw any robust conclusions.

It seems like the bulge is possibly enriched in [Mo/Fe] compared to the thick disk, especially at $-0.5 < [Fe/H] < 0$. However, we do note that the scatter is large for the bulge, and the following discussion is speculative based on the possible enrichment. As we do not see any difference between the stellar populations in either [Ce/Fe] or [Eu/Fe], the high [Mo/Fe] in the bulge could be linked to the p-process. In our previous studies, we found a possible enrichment in [V, Co, La/Fe] for the bulge, but these differences are not consistent with a single nucleosynthetic origin, meaning that, all elements considered, we cannot with confidence say that the bulge is distinguishable from the thick disk in the amount and rate of SNe type I and II. In turn, this means that the p-process sites linked to SNe type II and WD sources likely cannot produce the possible difference in the thick disk and bulge [Mo/Fe]. Of the suggested p-process sites, the one remaining is the rp-process, which is linked to burning on mass-accreting neutron stars (as discussed above, Schatz et al. 1998; Koike et al. 2004). However, there is no obvious reason why such events would be more common in the bulge, because either a high star formation rate or top-heavy initial mass function would make the bulge stand out in α-elements.

In order to further investigate the s- and r-process contribution to the origin of molybdenum, we also consider the abundance ratios of [Mo/Ce] and [Mo/Eu] over metallicity in Fig. 7. Here we only plot the running means so as to help with the interpretation of the trends. We also plot the so-called pure r-process line in the [Mo/Eu]-plot, which is calculated using the solar r-process contributions of the elements. The pure r-process is then the value of the r-process contribution in both elements, [r-process(Mo)/r-process(Eu)]. The closer the ratio is to the pure-r-process line, the more of the elements have a joint origin from the r-process (or rather are enriched by a source with similar time- and enrichment rate).

As all neutron-capture elements are produced by the r-process at lower metallicities, we can see that a greater proportion of Mo is produced by the r-process compared to Ce at low metallicities ≤ -0.5. At $[Fe/H] = -0.5$, AGB stars (originating from low- to intermediate-mass stars) start to enrich the Galactic ISM with s-process elements, producing a higher fraction of Mo and Ce than the r-process. As a result, the [Mo/Ce] trend flattens out. Considering [Mo/Eu] in Fig. 7, we see an increase with increasing metallicities – again at $[Fe/H] = -0.5$ – due to the AGB enrichment, pointing at the s-process contribution to Mo. Below those metallicities, we observe a relative increase in Mo over Eu, which is linked to the lack of knee or plateau in Mo at these metallicities.

5.4. Comment on HIP65028

The star HIP65028 stands out as a Mo-enriched star in the thin disk, with [Mo/Fe] = 0.68. Considering the values for other neutron-capture elements, [La/Fe] = 1.04, [Ce/Fe] = 0.96, [Eu/Fe] = 0.37 (Paper IV), we can conclude that this is a star enriched in s-process elements rather than r-process elements. This makes it a candidate Barium star, which could be investigated further by determining its C-abundance (which is usually high in Ba-stars) or by determining whether or not it has a strong variance in radial velocity measurements, which would indicate a binary companion. Usually these companions are WDs and stripped AGB-stars from where the carbon and s-process elements originate, and are too faint to be directly observed. Nonetheless, this also shows the high contribution from the s-process in creating Mo (∼40 to 50% in Bisterzo et al. 2014; Prantzos et al. 2020, respectively) even at the low metallicities of [Fe/H] ∼ −0.5 dex.

6. Conclusions

With this study, we continue our series of papers, determining high-quality abundances of bulge and disk stars using high-resolution optical spectra with the aim of making a differential comparison between the stellar populations. We use the same type of stars (K-giants), the same spectral lines and atomic data, and the same method for analysing and determining the Mo abundances. By using the same set of spectral lines for all stars, we minimise the possible systematic uncertainties in the comparison of the bulge and the disk.

We determine Mo abundances for 35 bulge stars, which to the best of our knowledge is the largest sample of Mo abundances in bulge stars. We also determine Mo for 282 disk stars. With the previous sample of 183 disk stars from Mishenina et al. (2019), our sample significantly increases the Mo abundances determined at $[Fe/H] \gtrsim -1.2$. This allows us to both compare the bulge and disk stellar populations and investigate the cosmic origin of Mo.

Molybdenum has an interesting cosmic origin, being composed of a combination of seven stable isotopes, all with s-, r-, or p-process origin or a combination of these. We cannot determine the abundance of specific isotopes, but simply the overall abundance of Mo in our stellar populations. In comparison with other neutron-capture elements, such as Ce and Eu, we cannot exclude that Mo stands out in the bulge as compared to the thick disk. This could possibly be explained by the roughly 25% p-process origin of Mo (at solar metallicities). As such, the explanation to this possible difference between the bulge and thick disk could lie in understanding how and where these p-isotopes, namely ^{92,94}Mo, form. The production site of p-isotopes is yet to be fully constrained, and although the scatter in our bulge sample is large, we speculate that an origin through mass-accreting neutron stars could possibly explain the seemingly high bulge abundances.

Acknowledgements. We thank Ross Church for insightful discussions about neutron-capture elements. We thank Lennart Lindegren for his expertise help in statistics. We also thank the anonymous referee for insightful comments that helped to improve this paper. R. F. and N. R. acknowledge support from the Royal Physiographic Society in Lund through the Stiftelse Walter Gyllenbergs fond and Märta och Erik Holmbergs donation. R. F.'s and A. J.'s research is supported by the Göran Gustafsson Foundation for Research in Natural Sciences and Medicine. A. J. acknowledges funding from the European Research Foundation (ERC Consolidator Grant 724687-PLANETESYS), the Knut and Alice Wallenberg Foundation (Wallenberg Academy Fellow Grant 2017.0287) and the Swedish Research Council (Project Grant 2018-04867). This work has made use of data from the European Space Agency (ESA) mission *Gaia* (`https://www.cosmos.esa.int/gaia`), processed by the *Gaia* Data Processing and Analysis Consortium (DPAC, `https://www.cosmos.esa.int/web/gaia/dpac/consortium`). Funding for the DPAC has been provided by national institutions, in particular the institutions participating in the *Gaia* Multilateral Agreement. *Software:* `matplotlib` (Hunter 2007), `galpy` (`http://github.com/jobovy/galpy`, Bovy 2015), `astropy` (Astropy Collaboration 2013).

References

Abbott, B. P., Abbott, R., Abbott, T. D., et al. 2017a, Phys. Rev. Lett., 119, 161101
Abbott, B. P., Abbott, R., Abbott, T. D., et al. 2017b, ApJ, 848, L12
Allen, D. M., & Barbuy, B. 2006, A&A, 454, 917
Anders, F., Khalatyan, A., Queiroz, A. B. A., et al. 2022, A&A, 658, A91
Arnould, M., & Goriely, S. 2003, Phys. Rep., 384, 1
Astropy Collaboration (Robitaille, T. P., et al.) 2013, A&A, 558, A33
Barbuy, B., Chiappini, C., & Gerhard, O. 2018, ARA&A, 56, 223
Battistini, C., & Bensby, T. 2016, A&A, 586, A49
Bisterzo, S., Travaglio, C., Gallino, R., Wiescher, M., & Käppeler, F. 2014, ApJ, 787, 10
Bisterzo, S., Travaglio, C., Wiescher, M., Käppeler, F., & Gallino, R. 2017, ApJ, 835, 97
Bovy, J. 2015, ApJS, 216, 29
Budde, G., Burkhardt, C., Brennecka, G. A., et al. 2016, Earth Planet. Sci. Lett., 454, 293
Budde, G., Burkhardt, C., & Kleine, T. 2019, Nat. Astron., 3, 736
Burbidge, E. M., Burbidge, G. R., Fowler, W. A., & Hoyle, F. 1957, Rev. Mod. Phys., 29, 547
Burkhardt, C., Kleine, T., Oberli, F., et al. 2011, Earth Planet. Sci. Lett., 312, 390
Cameron, A. G. W. 1957, PASP, 69, 201
Cardelli, J. A., Clayton, G. C., & Mathis, J. S. 1989, ApJ, 345, 245
Cescutti, G., & Matteucci, F. 2022, Universe, 8, 173
Cescutti, G., Chiappini, C., Hirschi, R., Meynet, G., & Frischknecht, U. 2013, A&A, 553, A51
Cescutti, G., Romano, D., Matteucci, F., Chiappini, C., & Hirschi, R. 2015, A&A, 577, A139
Côté, B., Eichler, M., Arcones, A., et al. 2019, ApJ, 875, 106
Cristallo, S., Piersanti, L., Straniero, O., et al. 2011, ApJS, 197, 17
Cristallo, S., Straniero, O., Piersanti, L., & Gobrecht, D. 2015, ApJS, 219, 40
Delgado Mena, E., Tsantaki, M., Adibekyan, V. Z., et al. 2017, A&A, 606, A94
Di Matteo, P., Haywood, M., Gómez, A., et al. 2014, A&A, 567, A122
Eichler, M., Nakamura, K., Takiwaki, T., et al. 2018, J. Phys. G Nucl. Phys., 45, 014001
Ek, M., Hunt, A. C., Lugaro, M., & Schönbächler, M. 2020, Nat. Astron., 4, 273
Forsberg, R., Jönsson, H., Ryde, N., & Matteucci, F. 2019, A&A, 631, A113
François, P., Depagne, E., Hill, V., et al. 2007, A&A, 476, 935
Frebel, A. 2010, Astron. Nachr., 331, 474
Freiburghaus, C., Rosswog, S., & Thielemann, F. K. 1999, ApJ, 525, L121
Frischknecht, U., Hirschi, R., Pignatari, M., et al. 2016, MNRAS, 456, 1803
Fröhlich, C., Martínez-Pinedo, G., Liebendörfer, M., et al. 2006, Phys. Rev. Lett., 96, 142502
Fröhlich, C., Hatcher, D., Perdikakis, G., & Nikas, S. 2017, in 14th International Symposium on Nuclei in the Cosmos (NIC2016), eds. S. Kubono, T. Kajino, S. Nishimura, T. Isobe, S. Nagataki, T. Shima, & Y. Takeda, 010505
Gaia Collaboration (Prusti, T., et al.) 2016, A&A, 595, A1
Gaia Collaboration (Brown, A. G. A., et al.) 2018, A&A, 616, A1
Gaia Collaboration (Brown, A. G. A., et al.) 2021, A&A, 649, A1
Gonzalez, O. A., & Gadotti, D. 2016, in Astrophysics and Space Science Library, Galactic Bulges, eds. E. Laurikainen, R. Peletier, & D. Gadotti, 418, 199
Gonzalez, O. A., Rejkuba, M., Zoccali, M., et al. 2011, A&A, 530, A54
Gonzalez, O. A., Rejkuba, M., Zoccali, M., et al. 2012, A&A, 543, A13
Goriely, S., José, J., Hernanz, M., Rayet, M., & Arnould, M. 2002, A&A, 383, L27
Grevesse, N., Asplund, M., & Sauval, A. J. 2007, Space Sci. Rev., 130, 105
Grevesse, N., Scott, P., Asplund, M., & Sauval, A. J. 2015, A&A, 573, A27
Grisoni, V., Cescutti, G., Matteucci, F., et al. 2020, MNRAS, 492, 2828
Gustafsson, B., Edvardsson, B., Eriksson, K., et al. 2008, A&A, 486, 951
Hansen, C. J., Andersen, A. C., & Christlieb, N. 2014, A&A, 568, A47
Hayakawa, T., Iwamoto, N., Shizuma, T., et al. 2004, Phys. Rev. Lett., 93, 161102
Heiter, U., Jofré, P., Gustafsson, B., et al. 2015, A&A, 582, A49
Heiter, U., Lind, K., Bergemann, M., et al. 2021, A&A, 645, A106
Hinkle, K., Wallace, L., & Livingston, W. 1995, PASP, 107, 1042
Hoffman, R. D., Woosley, S. E., Fuller, G. M., & Meyer, B. S. 1994, in American Astronomical Society Meeting Abstracts, 185, 33.09
Howard, W. M., Meyer, B. S., & Woosley, S. E. 1991, ApJ, 373, L5
Hunter, J. D. 2007, Comput. Sci. Eng., 9, 90
Jofré, P., Heiter, U., Soubiran, C., et al. 2014, A&A, 564, A133
Jofré, P., Heiter, U., Soubiran, C., et al. 2015, A&A, 582, A81
Johnson, J. A., & Bolte, M. 2002, ApJ, 579, 616
Johnson, C. I., McWilliam, A., & Rich, R. M. 2013, ApJ, 775, L27
Jönsson, H., Ryde, N., Nordlander, T., et al. 2017a, A&A, 598, A100
Jönsson, H., Ryde, N., Schultheis, M., & Zoccali, M. 2017b, A&A, 600, A2
Karakas, A. I., & Lattanzio, J. C. 2014, PASA, 31, e030
Kasen, D., Metzger, B., Barnes, J., Quataert, E., & Ramirez-Ruiz, E. 2017, Nature, 551, 80
Kobayashi, C., Karakas, A. I., & Lugaro, M. 2020, ApJ, 900, 179
Koike, O., Hashimoto, M.-a., Kuromizu, R., & Fujimoto, S.-I. 2004, ApJ, 603, 242
Lecureur, A., Hill, V., Zoccali, M., et al. 2007, A&A, 465, 799
Limongi, M., & Chieffi, A. 2018, ApJS, 237, 13
Lind, K., Bergemann, M., & Asplund, M. 2012, MNRAS, 427, 50
Lomaeva, M., Jönsson, H., Ryde, N., Schultheis, M., & Thorsbro, B. 2019, A&A, 625, A141
Lugaro, M., Pignatari, M., Ott, U., et al. 2016, Proc. Natl. Acad. Sci. U.S.A., 113, 907
Matteucci, F., & Brocato, E. 1990, ApJ, 365, 539
Matteucci, F., Romano, D., Arcones, A., Korobkin, O., & Rosswog, S. 2014, MNRAS, 438, 2177
McMillan, P. J. 2018, RNAAS, 2, 51
McWilliam, A. 2016, PASA, 33, e040
Meléndez, J., Asplund, M., Alves-Brito, A., et al. 2008, A&A, 484, L21
Mishenina, T. V., Pignatari, M., Korotin, S. A., et al. 2013, A&A, 552, A128
Mishenina, T., Pignatari, M., Gorbaneva, T., et al. 2019, MNRAS, 489, 1697
Mishenina, T., Shereta, E., Pignatari, M et al. 2020, J. Phys. Stud., 24, N3
Montelius, M., Forsberg, R., Ryde, N., et al. 2022, A&A, 665, A135
Ness, M., Freeman, K., Athanassoula, E., et al. 2012, ApJ, 756, 22
Nishimura, S., Kotake, K., Hashimoto, M.-A., et al. 2006, ApJ, 642, 410
Nishimura, N., Rauscher, T., Hirschi, R., et al. 2018, MNRAS, 474, 3133
Overbeek, J. C., Friel, E. D., & Jacobson, H. R. 2016, ApJ, 824, 75
Pedregosa, F., Varoquaux, G., Gramfort, A., et al. 2011, J. Mach. Learn. Res., 12, 2825
Peterson, R. C. 2011, ApJ, 742, 21
Peterson, R. C. 2013, ApJ, 768, L13
Petit, P., Louge, T., Théado, S., et al. 2014, PASP, 126, 469
Pignatari, M., Gallino, R., Heil, M., et al. 2010, ApJ, 710, 1557
Pignatari, M., Göbel, K., Reifarth, R., & Travaglio, C. 2016, Int. J. Mod. Phys. E, 25, 1630003
Piskunov, N., & Valenti, J. A. 2017, A&A, 597, A16
Prantzos, N., Abia, C., Cristallo, S., Limongi, M., & Chieffi, A. 2020, MNRAS, 491, 1832
Queiroz, A. B. A., Anders, F., Santiago, B. X., et al. 2018, MNRAS, 476, 2556
Rauscher, T., Dauphas, N., Dillmann, I., et al. 2013, Rep. Progr. Phys., 76, 066201
Rayet, M., Arnould, M., Hashimoto, M., Prantzos, N., & Nomoto, K. 1995, A&A, 298, 517
Ritter, C., Andrassy, R., Côté, B., et al. 2018, MNRAS, 474, L1
Roederer, I. U., Marino, A. F., & Sneden, C. 2011, ApJ, 742, 37
Roederer, I. U., Preston, G. W., Thompson, I. B., et al. 2014a, AJ, 147, 136
Roederer, I. U., Schatz, H., Lawler, J. E., et al. 2014b, ApJ, 791, 32
Roederer, I. U., Lawler, J. E., Den Hartog, E. A., et al. 2022, ApJS, 260, 27
Roriz, M. P., Lugaro, M., Pereira, C. B., et al. 2021, MNRAS, 507, 1956
Schatz, H., Aprahamian, A., Goerres, J., et al. 1998, Phys. Rep., 294, 167
Schatz, H., Aprahamian, A., Barnard, V., et al. 2001, Phys. Rev. Lett., 86, 3471
Shen, J., & Zheng, X.-W. 2020, Res. Astron. Astrophys., 20, 159
Skúladóttir, Á., & Salvadori, S. 2020, A&A, 634, A2
Spite, F., Spite, M., Barbuy, B., et al. 2018, A&A, 611, A30
Telting, J. H., Avila, G., Buchhave, L., et al. 2014, Astron. Nachr., 335, 41
Thygesen, A. O., Sbordone, L., Andrievsky, S., et al. 2014, A&A, 572, A108
Travaglio, C., Gallino, R., Arnone, E., et al. 2004, ApJ, 601, 864
Travaglio, C., Röpke, F. K., Gallino, R., & Hillebrandt, W. 2011, ApJ, 739, 93
Travaglio, C., Gallino, R., Rauscher, T., Röpke, F. K., & Hillebrandt, W. 2015, ApJ, 799, 54
Travaglio, C., Rauscher, T., Heger, A., Pignatari, M., & West, C. 2018, ApJ, 854, 18
Trippella, O., Busso, M., Palmerini, S., Maiorca, E., & Nucci, M. C. 2016, ApJ, 818, 125
Valenti, J. A., & Piskunov, N. 1996, A&AS, 118, 595
Van der Swaelmen, M., Barbuy, B., Hill, V., et al. 2016, A&A, 586, A1
Wanajo, S., Janka, H.-T., & Müller, B. 2011, ApJ, 726, L15
Weiland, J. L., Arendt, R. G., Berriman, G. B., et al. 1994, ApJ, 425, L81
Whaling, W., & Brault, J. W. 1988, Phys. Scr, 38, 707
Woosley, S. E., & Howard, W. M. 1978, ApJS, 36, 285
Woosley, S. E., Hartmann, D. H., Hoffman, R. D., & Haxton, W. C. 1990, ApJ, 356, 272
Woosley, S. E., Wilson, J. R., Mathews, G. J., Hoffman, R. D., & Meyer, B. S. 1994, ApJ, 433, 229
Zoccali, M., Lecureur, A., Barbuy, B., et al. 2006, A&A, 457, L1

Appendix A: Supplementary data

Table A.1. Basic data for the observed solar neighbourhood giants. Coordinates and magnitudes are taken from the SIMBAD database, while the radial velocities are measured from the spectra.

HIP/KIC/TYC	Alternative name	RA (J2000) (h:m:s)	Dec (J2000) (d:am:as)	V	v_{rad} km/s	S/N[a]	Source
HIP1692	HD1690	00:21:13.32713	−08:16:52.1625	9.18	18.37	114	FIES-archive
HIP9884	alfAri	02:07:10.40570	+23:27:44.7032	2.01	−14.29	90	PolarBase
HIP10085	HD13189	02:09:40.17260	+32:18:59.1649	7.56	26.21	156	FIES-archive
HIP12247	81Cet	02:37:41.80105	−03:23:46.2201	5.66	9.34	176	FIES-archive
HIP28417	HD40460	06:00:06.03883	+27:16:19.8614	6.62	100.64	121	PolarBase
HIP33827	HR2581	07:01:21.41827	+70:48:29.8674	5.69	−17.99	79	PolarBase
HIP35759	HD57470	07:22:33.85798	+29:49:27.6626	7.67	−30.19	85	PolarBase
HIP37447	alfMon	07:41:14.83257	−09:33:04.0711	3.93	11.83	71	Thygesen et al. (2012)
HIP37826	betGem	07:45:18.94987	+28:01:34.3160	1.14	3.83	90	PolarBase
HIP43813	zetHya	08:55:23.62614	+05:56:44.0354	3.10	23.37	147	PolarBase

Notes. This is only an excerpt of the table to show its form and content. The complete table is available in electronic form at the CDS.
[a] The S/N per data point is measured by the IDL-routine `der_snr.pro`, see http://www.stecf.org/software/ASTROsoft/DER_SNR.

Table A.2. Stellar parameters and determined abundances for observed solar neighbourhood giants.

HIP/KIC/TYC	T_{eff}	$\log g$	[Fe/H]	v_{micro}	A(Mo)
HIP1692	4216	1.79	−0.26	1.55	1.64
HIP9884	4464	2.27	−0.21	1.34	1.74
HIP10085	4062	1.44	−0.32	1.63	1.65
HIP12247	4790	2.71	−0.04	1.40	1.94
HIP28417	4746	2.56	−0.25	1.40	1.64
HIP33827	4235	1.99	0.01	1.50	1.95
HIP35759	4606	2.47	−0.15	1.42	1.80
HIP37447	4758	2.73	−0.04	1.35	1.91
HIP37826	4835	2.93	0.07	1.24	2.04
HIP43813	4873	2.62	−0.07	1.51	2.00

Notes. This is only an excerpt of the table to show its form and content. The complete table is available in electronic form at the CDS. [Fe/H] is listed in the scale of Grevesse et al. (2007)..

Table A.3. Basic data for the observed bulge giants.

Star[a]	RA (J2000) (h:m:s)	Dec (J2000) (d:am:as)	V	S/N[b]
SW-09	17:59:04.533	−29:10:36.53	16.153	16
SW-15	17:59:04.753	−29:12:14.77	16.326	15
SW-17	17:59:08.138	−29:11:20.10	16.388	11
SW-18	17:59:06.455	−29:10:30.53	16.410	14
SW-27	17:59:04.457	−29:10:20.67	16.484	13
SW-28	17:59:07.005	−29:13:11.35	16.485	16
SW-33	17:59:03.331	−29:10:25.60	16.549	14
SW-34	17:58:54.418	−29:11:19.82	16.559	12
SW-43	17:59:04.059	−29:13:30.26	16.606	16
SW-71	17:58:58.257	−29:12:56.97	16.892	14

Notes. This is only an excerpt of the table to show its form and content. The complete table is available in electronic form at the CDS.
[a] Using the same naming convention as Lecureur et al. (2007) for the B3-BW-B6-BL-stars.
[b] The S/N per data point is measured by the IDL-routine `der_snr.pro`, see http://www.stecf.org/software/ASTROsoft/DER_SNR.

Table A.4. Stellar parameters and determined abundances for observed bulge giants.

Star	T_{eff}	$\log g$	[Fe/H]	v_{micro}	A(Mo)
SW-09	4095	1.79	−0.15	1.32	1.90
SW-15	4741	1.96	−0.98	1.62	...
SW-17	4245	2.09	0.24	1.44	2.06
SW-18	4212	1.67	−0.13	1.49	1.86
SW-27	4423	2.34	0.11	1.60	2.08
SW-28	4254	2.36	−0.14	1.44	2.10
SW-33	4580	2.72	0.16	1.39	...
SW-34	4468	1.75	−0.45	1.63	...
SW-43	4892	2.34	−0.77	1.84	...
SW-71	4344	2.66	0.39	1.31	2.36

Notes. This is only an excerpt of the table to show its form and content. The complete table is available in electronic form at the CDS. [Fe/H] is listed in the scale of Grevesse et al. (2007).

Paper III

A&A 669, A17 (2023)
https://doi.org/10.1051/0004-6361/202244305

Astronomy & Astrophysics

First *r*-process enhanced star confirmed as a member of the Galactic bulge

R. Forsberg[1], R. M. Rich[2,3], N. Nieuwmunster[1,3], H. Jönsson[4], M. Schultheis[3], N. Ryde[1], and B. Thorsbro[1,5]

[1] Lund Observatory, Department of Astronomy and Theoretical Physics, Lund University, Box 43, 22100 Lund, Sweden
e-mail: rebecca@astro.lu.se
[2] Department of Physics and Astronomy, ICLA, 430 Portola Plaza, Box 951547, Los Angeles, CA 90095-1547, USA
[3] Université Côte-d'Azur, Observatoire de la Côte d'Azur, Laboratoire Lagrange, CNRS, Blvd de l'Observatoire, 06304 Nice, France
[4] Materials Science and Applied Mathematics, Malmö University, 205 06 Malmö, Sweden
[5] Department of Astronomy, School of Science, The University of Tokyo, 7-3-1 Hongo, Bunkyo-ku, Tokyo 113-0033, Japan

Received 20 June 2022 / Accepted 10 October 2022

ABSTRACT

Aims. Stars with strong enhancements of *r*-process elements are rare and tend to be metal-poor, generally with [Fe/H] < -2 dex, and located in the halo. In this work, we aim to investigate a candidate *r*-process enriched bulge star with a relatively high metallicity of [Fe/H] ~ -0.65 dex and to compare it with a previously published r-rich candidate star in the bulge.
Methods. We reconsidered the abundance analysis of a high-resolution optical spectrum of the red-giant star 2MASS J18082459-2548444 and determined its europium (Eu) and molybdenum (Mo) abundance, using stellar parameters from five different previous studies. Applying 2MASS photometry, *Gaia* astrometry, and kinematics, we estimated the distance, orbits, and population membership of 2MASS J18082459-2548444 and a previously reported r-enriched star 2MASS J18174532–3353235.
Results. We find that 2MASS J18082459-2548444 is a relatively metal-rich, enriched *r*-process star that is enhanced in Eu and Mo, but not substantially enhanced in *s*-process elements. There is a high probability that it has a Galactic bulge membership, based on its distance and orbit. We find that both stars show *r*-process enhancement with elevated [Eu/Fe]-values, even though 2MASS J18174532–3353235 is 1 dex lower in metallicity. Additionally, we find that the plausible origins of 2MASS J18174532–3353235 to be either that of the halo or the thick disc.
Conclusions. We conclude that 2MASS J18082459-2548444 represents the first example of a confirmed *r*-process enhanced star confined to the inner bulge. We assume it is possibly a relic from a period of enrichment associated with the formation of the bar.

Key words. stars: abundances – stars: chemically peculiar – Galaxy: bulge – Galaxy: evolution

1. Introduction

The composition of stars presents a record of the formation and chemical enrichment of the Milky Way. Stars form from molecular clouds and can potentially carry a chemical fingerprint of their birth cloud that may include pollution from earlier events. The Galactic interstellar medium is chemically enriched over time, through nucleosynthetic processes occurring either in stars or in explosive environment such as supernovae (SNe) and neutron star mergers.

The Galactic bulge is of great interest because of its age and high metallicity, which are consistent with early, rapid enrichment. The modern era of study gave observations of high iron abundance and α-enhancements (Rich 1988; McWilliam & Rich 1994) paired with old age (Ortolani et al. 1995) have substantiated this picture of rapid enrichment via Type II SNe (Matteucci & Brocato 1990). The actual picture may be more nuanced. Deep studies of the main sequence in fields imaged by the ESA/NASA *Hubble* Space Telescope largely support a predominant older age (Clarkson et al. 2008; Renzini et al. 2018), while Bensby et al. (2017) have argued for a far greater dispersion in age, based on the analysis of microlensed bulge dwarfs. A recent study by Joyce et al. (2022) confirms that the most metal-rich stars may be younger than 10 Gyr, with a 5 Gyr age dispersion.

Stars with [Fe/H] > -0.5 dex are predominantly in a bar (Ness et al. 2012, 2013) that appears to have formed via the buckling of a pre-existing disc (Shen et al. 2010; Di Matteo et al. 2014). Overall, in the present day, a tension is apparent between seemingly robust evidence for early rapid enrichment from analyses of color-magnitude diagrams and luminosity functions, with the study of the microlensed dwarfs providing a counterpoint of possibly extended formation. The progressive flattening of the metal-rich population (Johnson et al. 2020) offers some support for the extended formation scenario.

This tension between evidence of early enrichment in the bulge versus a potentially extended formation history for the most metal-rich bulge populations is an intriguing area or research where still much can be learnt. One characteristic of the ancient Galactic halo is the presence of neutron-capture (Burbidge et al. 1957) enhanced stars, especially those with high amount of *r*-process elements. The discovery of a bulge or inner halo candidate displaying the full *r*-process pattern (Johnson et al. 2013) raises the possibility that such stars also formed early in the history of the bulge or inner halo.

These types of r-enhanced stars remain rare, but are of sufficient interest that they have been catalogued and studied across Galactic populations, with more than 300 known at this time (see the R-process Alliance, Holmbeck et al. 2020).

Whilst the origins of such enhancements remain an open matter of discussion to date, and it is possible that the primary source has changed over time (Sneden et al. 2008), they are proposed to offer clear signatures of *r*-process events. Such events could be neutron star mergers (NSM, Matteucci et al. 2014) and/or magneto-rotational driven SNe (MRSNe, Nishimura et al. 2006; Kobayashi et al. 2020) which can provide the neutron-rich conditions that favour the nucleogenesis of these heavy elements.

In general, stars showing *r*-process enhancements are metal poor, with [Fe/H] < -2 dex (McWilliam et al. 1995; Sneden et al. 2003, 2008; Holmbeck et al. 2020), appearing in the Milky Way halo and in dwarf galaxies (Hirai et al. 2015; Matsuno et al. 2021; Jeon et al. 2021). These are classified into two groups, *r*-I and *r*-II, depending on the level of *r*-process enrichment. The discrepancy of *r*-I and *r*-II stars has been given by $0.3 <$ [Eu/Fe] ≤ 1.0 dex and [Eu/Fe] > 1.0 dex, respectively, with [Ba/Eu] < 0 dex for the *r*-II stars (Christlieb et al. 2004). In the R-process Alliance, they listed 232 r-I and 72 *r*-II stars, whilst proposing a new demarcation between these two groups at [Eu/Fe] = 0.7 dex (Holmbeck et al. 2020). As the astrophysical site(s) of the *r*-process remains a matter of vigorous debate (see e.g. Côté et al. 2019), it continues to be important to document such stars in a range of stellar populations as their presence potentially gives insight into the early enrichment history of a population.

One interesting set of spectra was first used in Zoccali et al. (2006) and later reanalysed in several subsequent studies (Lecureur et al. 2007; Ryde et al. 2010; Van der Swaelmen et al. 2016; Jönsson et al. 2017b; Lomaeva et al. 2019; Forsberg et al. 2019, 2022). A star found in the set, the K-giant 2MASS J18082459-2548444 (hereafter, the Z06-star), has recently been shown to be high in [Eu/Fe] (Van der Swaelmen et al. 2016; Forsberg et al. 2019) and [Mo/Fe] (Forsberg et al. 2022). At [Fe/H] ~ -0.65 dex (Lecureur et al. 2007; Zoccali et al. 2008; Ryde et al. 2010; Johnson et al. 2014; Jönsson et al. 2017b), this star is remarkably high in metallicity for a potentially *r*-process enhanced star. Whilst at present we focus our reporting only on this star, the discovery of it makes emphatic the importance of searching for other stars with unusual enhancements of heavy elements that are also found in the Galactic bulge.

Indeed, Johnson et al. (2013) published the first r-enriched candidate in the Galactic bulge, 2MASS J18174532–3353235, located at $(l, b) = (-1, -8)^\circ$. The star is reported to have a relatively high metallicity (relative the halo r-enhanced population) of [Fe/H] $= -1.67$ dex and an r-enrichment as traced by europium of [Eu/Fe] = 1.0 dex and molybdenum of [Mo/Fe] = 0.72 dex. It should be noted that Johnson et al. (2013) did not rule out a halo origin for 2MASS J18174532–3353235 (hereafter, the J13-star) and noted that with more precise proper motions, the kinematics of the star would be constrained with a greater certainty.

In this work, we re-analyse the optical spectrum of the Z06-star, as described in Sect. 2. We use the stellar parameters from the earlier studies (Zoccali et al. 2006; Lecureur et al. 2007; Ryde et al. 2010; Van der Swaelmen et al. 2016; Jönsson et al. 2017b) to determine the abundances of the *r*-process elements europium and molybdenum, as described in Sect. 3. We compare the results with studies from Forsberg et al. (2019, 2022). In Sect. 4, we investigate the bulge membership of the two r-enhanced stars, the Z06-star, 2MASS J18082459-2548444, and the J13-star, 2MASS J18174532–3353235. With the data from *Gaia* Early Data Release 3 (*Gaia* EDR3, Gaia Collaboration 2021), we now have access to a highly precise value for the proper motion of these stars, allowing us to calculate their orbits.

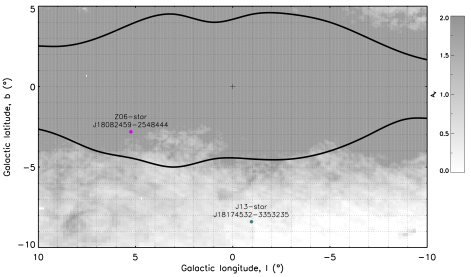

Fig. 1. Map of the Galactic bulge, showing the position of the Z06-star, 2MASS J18082459-2548444 (magenta), and the J13-star, 2MASS J18174532–3353235 (teal), presented in this work. The dust extinction towards the bulge is taken from Gonzalez et al. (2011, 2012) and scaled to optical extinction (Cardelli et al. 1989). The scale saturates at $A_V = 2$, setting the upper limit. We also plot the COBE/DIRBE outlines of the Galactic bulge (Weiland et al. 1994).

2. Observational data

The spectrum of the Z06-star is part of the Zoccali et al. (2006) data set and has been observed with the FLAMES-UVES ($R \sim 47\,000$) at the European Southern Observatory's Very Large Telescope (ESO's VLT). The spectral wavelength is limited to 5800–6800 Å. The star is located at $(l, b) = (5.2^\circ, -2.8^\circ)$, placing it in the line of sight within the bulge as outlined from COBE/DIRBE (Weiland et al. 1994), as seen in Fig. 1.

The stellar parameters of the Z06-star were determined in Lecureur et al. (2007); Zoccali et al. (2008); Ryde et al. (2010); Johnson et al. (2014); Jönsson et al. (2017b). We provide more details in Table 1. With an effective temperature of ∼4400 K and $\log(g)$ of ∼1.75, it is a typical red-giant star. With the combined works of Lecureur et al. (2007); Ryde et al. (2010); Johnson et al. (2014); Van der Swaelmen et al. (2016); Jönsson et al. (2017b); Lomaeva et al. (2019); Forsberg et al. (2019, 2022), the known chemical fingerprint of the Z06-star consists of 21 abundances (see Table 2).

The J13-star, placed at $(l, b) = (1^\circ, -8^\circ)$, is also marked in Fig. 1 and is found within the bulge Plaut field. The spectrum of the J13-star, analysed in Johnson et al. (2013), has been observed with the Magellan Inamori Kyocera Echelle (MIKE) spectrograph on the 6.5 m Magellan Clay telescope ($R \sim 30\,000$).

3. Analysis of the spectrum

In this section, we give a brief discussion of the analysis of the spectrum of the Z06-star, where we follow the methodology as outlined in the Jönsson-series (Jönsson et al. 2017a,b; Lomaeva et al. 2019; Forsberg et al. 2019, 2022). We re-determine the Mo and Eu abundances using the stellar parameters presented in Lecureur et al. (2007); Zoccali et al. (2008); Ryde et al. (2010); Johnson et al. (2014) to confirm the high abundances determined in previous papers. We refer to these papers for a more detailed description of the stellar parameters and details of the elemental abundance determination for the other elements presented in Table 2.

The analysis of the spectra is done using the tool Spectroscopy Made Easy (SME, version 554 Valenti & Piskunov 1996; Piskunov & Valenti 2017). This tool uses a grid of MARCS

Table 1. Comparison of the stellar parameters (Cols. 2–5) for the Z06-star from five different spectroscopic studies (Col. 1).

Reference	$T_{\rm eff}$ (K)	log(g) (dex)	[Fe/H] (dex)	$\xi_{\rm mic}$ (km s^{-1})	[Mo/Fe] (dex)	[Eu/Fe] (dex)
Lecureur et al. (2007)	4400	1.8	–0.62	1.4	0.73	0.85
Zoccali et al. (2008)	4350	1.7	–0.65	1.4	0.68	0.83
Ryde et al. (2010)	4250	1.5	–0.69	1.4	0.58	0.81
Johnson et al. (2014)	4425	1.65	–0.58	1.70	0.68	0.74
Jönsson et al. (2017b)	4287	1.79	–0.67	1.46	0.62	0.78

Notes. Note that the Ryde et al. (2010) stellar parameters are determined from an infrared, H-band spectrum of the Z06-star. We calculate the [Mo/Fe] and [Eu/Fe] (Cols. 6–7) using the methodology as described in Sect. 3, and use $A(\rm Mo)_\odot$ = 1.88 and $A(\rm Eu)_\odot$ = 0.52 from Grevesse et al. (2015). Eu has been decreased by 0.10 dex, since Forsberg et al. (2019) report possible [Eu/Fe] to possibly be systematically too high due to systematics in the stellar parameters. We lower it such that their overall thin disc, as seen in Fig. 2, goes through the solar value, also as described in Sect. 3.1.

Table 2. Determined absolute abundances A(X) and solar- and metallicity-normalised abundances [X/Fe] of the Z06-star.

Species	A(X)	[X/Fe]	Reference
C	7.63	–0.10	Ryde et al. (2010)
N	7.34	0.21	Ryde et al. (2010)
O I	8.47	0.48	Jönsson et al. (2017b)
Na I	5.67	–0.08	Johnson et al. (2014)
Mg I	7.27	0.47	Jönsson et al. (2017b)
Al I	6.16	0.27	Johnson et al. (2014)
Si I	7.21	0.24	Johnson et al. (2014)
Ca I	5.88	0.25	Jönsson et al. (2017b)
Sc II	2.57	0.08	Lomaeva et al. (2019)
Ti I	4.43	0.19	Jönsson et al. (2017b)
V I	3.34	0.12	Lomaeva et al. (2019)
Cr I	4.48	–0.11	Lomaeva et al. (2019)
Co I	4.40	0.14	Lomaeva et al. (2019)
Ni I	5.57	0.04	Lomaeva et al. (2019)
Zr I	2.35	0.43	Forsberg et al. (2019)
Mo I	1.87	0.62	Forsberg et al. (2022)
Ba II	2.33	0.78	Van der Swaelmen et al. (2016)
La II	0.93	0.42*	Forsberg et al. (2019)
Ce II	1.11	0.22*	Forsberg et al. (2019)
Nd II	1.15	0.32	Van der Swaelmen et al. (2016)
Eu II	0.73	0.78*	Forsberg et al. (2019)

Notes. The Jönsson series, Jönsson et al. (2017b); Lomaeva et al. (2019); Forsberg et al. (2019, 2022) uses the solar values in the series of Scott et al. (2015a,b); Grevesse et al. (2015). For elements not determined in that series, we complement with values from Ryde et al. (2010); Johnson et al. (2014); Van der Swaelmen et al. (2016). The C and N abundances are from molecular CO and CN (Ryde et al. 2010). La, Ce, and Eu have been decreased by 0.05, 0.01, and 0.10 dex, as described in Sect. 3.1.

models[1] (Gustafsson et al. 2008), with spherical symmetry for log(g) $<$3.5, which is applicable to the Z06-star and the bulge stars analysed in the Jönsson-series. The atomic data comes from the *Gaia*-ESO line list version 6 (Heiter et al. 2021).

In order for SME to produce a synthetic spectrum, it requires a line list, model atmospheres, and defined spectral segments, as well as spectral line and continuum masks. The masks are defined manually around the spectral line of interest, which in Jönsson et al. (2017a,b); Lomaeva et al. (2019); Forsberg et al. (2019, 2022) was shown to be crucial for obtaining the high-precision abundances they report.

[1] Available at `https://marcs.astro.uu.se`.

3.1. Europium

For europium (Eu, Z = 63), we used the Eu II 6645 Å spectral line for the abundance determination, with the atomic data from the *Gaia*-ESO (GES) line list version 6 (Heiter et al. 2021). They classified the 6645 Å line as 'yes/uncertain', indicating that the log(gf)-value was of high quality, however that there could be some uncertain blends in the line. They recommended the line to be used only for giant stars with high S/N spectra, which is the case for the Zoccali et al. (2006) – spectrum of the Z06-star used here. Europium has both hyperfine structure and two stable isotopes in the Sun. The hyperfine splitting is included in the GES line list, whereas the isotopic shift cannot be resolved and is not included.

This line has been used with the same analysis as described here to determine the Eu abundance for close to 300 disc K-giants in Forsberg et al. (2019). Their abundance trend is tightly correlated with [Fe/H], giving confidence in the quality of our analysis presented here. However, we do note that the [Eu/Fe] abundances seems to be systematically too high in the disc stars in Forsberg et al. (2019), which might be explained by the possible systematic uncertainty in their log(g) as reported in Jönsson et al. (2017a,b) when compared to *Gaia* Benchmark stars (in Jofré et al. 2014, 2015; Heiter et al. 2015). Therefore, we systematically lowered the overall disc abundances with 0.10 dex, such that the thin disc trend passes through the Solar value, as can be seen in Fig. 2. For the same reasons, the [La,Ce/Fe] values are also systematically lowered, as shown in Table 2.

Nonetheless, the [Eu/Fe] value for the Z06-starfrom their study remains high, which is confirmed by determining the abundance using the Lecureur et al. (2007); Zoccali et al. (2008); Ryde et al. (2010); Johnson et al. (2014) stellar parameters as well, which do not report any systematics in their parameters, indicating the Eu-content to indeed be high in the Z06-star.

3.2. Molybdenum

For molybdenum (Mo, Z = 42), we used the Mo I 6030 Å spectral line for the abundance determination, which is very weak in dwarf stars but usable in giant stars (Forsberg et al. 2022). In Heiter et al. (2021) the line is reported to be Yes/Yes, having well-known atomic data and being unblended. Mo does not have hyperfine structure, but it has seven stable isotopes in the Sun. Similarly to Eu, this isotopic splitting is not included in the linelist and we determine the abundance using the five sets of stellar parameters given in Table 1. The manually defined line- and continuum masks can be seen in Fig. 3. Both the spectrum

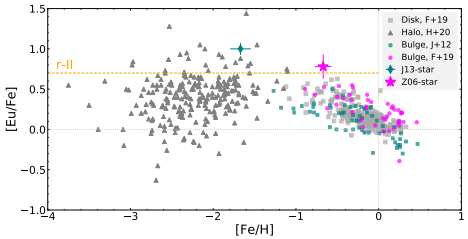

Fig. 2. [Eu/Fe] over [Fe/H] for the Z06-star (magenta star) and the J13-star (teal diamond). For reference, we plot the bulge (magenta circles) and disc stars (grey squares) from Forsberg et al. (2019) as well as the bulge stars from Johnson et al. (2012). The abundances of the halo stars come from the *r*-process alliance sample (dark grey triangles Holmbeck et al. 2020). The orange line indicates the '*r*-II' limit as defined in the *r*-process alliance (Holmbeck et al. 2020). We note that the abundances from Forsberg et al. (2019) have been systematically lowered with 0.10 dex, as described in Sect. 3.1.

of the Z06-star and the synthetic spectrum can be seen in Fig. 4, with a ±0.1 dex uncertainty.

4. Bulge membership

A majority of the *r*-process enriched stars are metal-poor, [Fe/H] ≤ −1.5 dex, and confined to the Galactic halo (Holmbeck et al. 2020). In order to investigate whether the Z06-star and the J13-star are likely to be confined to the Galactic bulge or visiting halo-stars, we estimated their line-of-sight distances and, using their proper motions (from *Gaia* EDR3, Gaia Collaboration 2016, 2021), we estimated their orbits using `galpy` (Bovy 2015). The line-of-sight positions of both stars can be seen in Fig. 1, where the Z06-star is closer to the Galactic plane, compared to the J13-star.

4.1. Distance estimates

We calculated the spectrophotometric distances for the two stars for which we incorporated the stellar properties $T_{\rm eff}$, log(g), [Fe/H], and the 2MASS *JHKs* photometry into the spectrophotometric method described in Rojas-Arriagada et al. (2017). For the stellar parameters, we used the Jönsson et al. (2017b) parameters for the Z06-star, and Johnson et al. (2013) parameters for the J13-star. Each parameter point in the parameter space $T_{\rm eff}$, log(g), [Fe/H] is compared to a set of theoretical isochrones for each star. We use the PARSEC isochrones (Bressan et al. 2012; Marigo et al. 2017) spanning ages from 1 to 13 Gyr in steps of 1 Gyr and metallicities from –2.2 to +0.5 in steps of 0.1 dex. We note that the PARSEC isochrones do not take α-elements into account.

A number of extra multiplicative weights are defined to account for the evolutionary speed of the points along the isochrones and for the initial mass function. Using these weights, the most likely absolute magnitudes (MJ, MH, MKs) of the observed stars can be computed as the weighted mean or median of the theoretical values of the whole set of isochrone points. The computed absolute magnitudes are then compared to the observed photometry, allowing us to estimate the line-of-sight reddening and distance modulus. These distances were extensively tested and used within the APOGEE survey (Majewski et al. 2017; see e.g. Rojas-Arriagada et al. 2020; Zasowski et al. 2019).

For the Z06-star we derive a heliocentric distance of 7.2 ± 0.3 kpc and for the J13-star 11.8 ± 1.0 kpc. The uncertainties for the distances are estimated using the reported uncertainties of the photometry and stellar parameters. These distances indicate that the Z06-star belongs to the Galactic bulge, while the large distance of the J13-star suggests, together with its low metallicity of [Fe/H] = −1.69 dex, that it originates from either the Galactic halo or thick disc. This hypothesis was indeed already suggested by Johnson et al. (2013).

In addition, we calculated the distances using the *Gaia* DR3 photometry in the *G*-band (Kordopatis et al. 2022) for these two stars in order to check the consistency. A distance of 7.4 ± 1.0 kpc has been obtained for the Z06-star and of 12.2 ± 1.5 kpc for the J13-star, respectively. This strengthen our argument that indeed the J13-star is a visiting halo or inner halo or a thick disc star, while the Z06-star belongs to the Galactic bulge.

4.2. Modelling of orbits

To further investigate the bulge membership, we explored possible orbits of the stars using `GalPy` (Bovy 2015). We adopted the Milky Way like `MWPotential2014`-potential (Bovy 2015), which includes an axisymmetric disc, a halo, and a spherical bulge. To that, we added the Dehnen (2000)-bar potential (which in `GalPy` has been generalised to 3D following Monari et al. 2016).

We integrate the orbits up to 10 Gyr for both stars, using positions in RA+Dec; proper motions (Gaia Collaboration 2021); distances as derived above; and radial velocities determined in Johnson et al. (2013); Jönsson et al. (2017b). We also calculated the orbits using the uncertainties for distances and proper motions to check whether the orbits remain similar. The data used can be seen in Table 3. As a sanity check, we also calculated the orbits using the `AGAMA` code (Vasiliev 2019), where we implement a combined `MWPotential2014` and Launhardt et al. (2002) – inner bulge potential. The code gives similar results as the ones presented for `GalPy`.

5. Results and discussion

We present the abundances of the Z06-star and compare with both the J13-star and the overall bulge sample as determined in our series of papers. We show and discuss the orbits as well as the distances, and we consider the implications for the formation history of the bulge.

5.1. Abundances

We re-analysed the spectrum of the Z06-star and determine both the [Eu/Fe] and [Mo/Fe] abundance using the stellar parameters reported in Lecureur et al. (2007); Zoccali et al. (2008); Ryde et al. (2010); Johnson et al. (2014); Jönsson et al. (2017b), which can be seen in Table 1.

From these, we find that the Z06-star has a mean [Eu/Fe] = 0.80 dex, based on the five different stellar parameter determinations, pointing at the Eu-content being high in the Z06-star, independently on the stellar parameters. All of the values are [Eu/Fe] ≥ +0.74 dex, which classifies it as a, relatively metal-rich, *r*-II star (following the classification in the R-process Alliance, Holmbeck et al. 2020). In Fig. 2 we show [Eu/Fe] vs. [Fe/H] for the bulge stars in Forsberg et al. (2019) and Johnson et al. (2012), which both include the Z06-star and the J13-star, respectively. We also plot the typical local disc abundances (Forsberg et al. 2019) and stars from the R-process

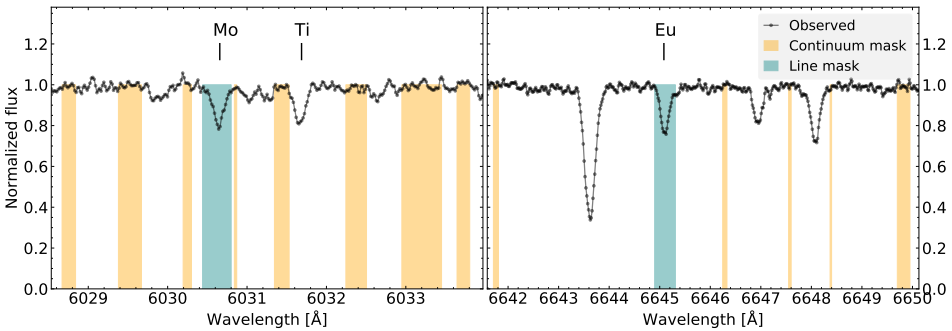

Fig. 3. Observed spectrum of the Z06-star in black with a SNR of 65. The line mask placements for the Mo (left) and Eu (right) line can be seen in turquoise and the continuum placements in yellow.

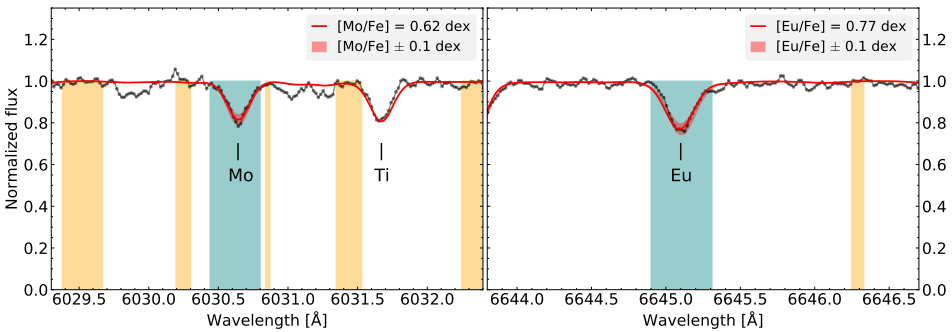

Fig. 4. As Fig. 3, the observed spectrum of the Z06-star can be seen in black. The line mask placements for the Mo (left) and Eu (right) line can be seen in turquoise and the continuum placements in yellow. The best fit to the synthetic spectrum is shown with a solid red line and the ±0.1 dex with a shaded red. Note that the wavelength region is zoomed in compared to Fig. 3 to better show the fit of the synthetic spectrum.

Alliance (Holmbeck et al. 2020). We note that even though the [Eu/Fe]-abundances from Forsberg et al. (2019) has been systematically lowered with 0.10 dex, as described in Sect. 3.1, both the Z06-star and the J13-star lie above the Holmbeck et al. (2020) – classification boundary for an *r*-II star, and are high in [Eu/Fe] as compared to the bulge samples.

The [Mo/Fe] abundance for the Z06-star is high with 0.62 dex from the Forsberg et al. (2022) study, and an average of 0.66 dex when determined using the five different stellar parameter studies (Table 1). In Fig. 5, we show the [Mo/Fe] abundances for the local disc and the bulge (Forsberg et al. 2022), including the Z06-star. We have also added the J13-star and molybdenum abundances from disc and halo studies (Peterson 2013; Hansen et al. 2014; Roederer et al. 2014; Mishenina et al. 2013).

In order to make a comparison amongst the stars, in Fig. 6, we compared their [X/Fe] in with the overall bulge abundances as measured from the Jönsson-series (Jönsson et al. 2017b; Lomaeva et al. 2019; Forsberg et al. 2019, 2022). We see that both the Z06-star and the J13-star are enhanced in [Mo/Fe] and [Eu/Fe]. Additionally, both stars are on the higher side in the *s*-process elements [Zr,La/Fe]. This pattern of high abundance in heavier elements is similar to that of the prototypical *r*-process enhanced metal-poor halo stars BD +17°3248

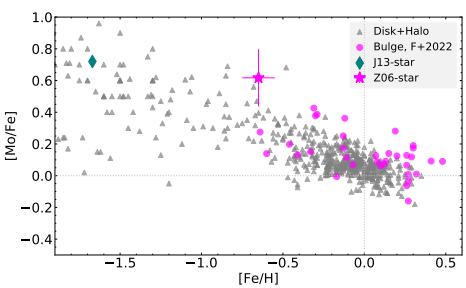

Fig. 5. [Mo/Fe] over [Fe/H] for the Z06-star (magenta star) and J13-star (teal diamond). We also show the bulge in [Mo/Fe] from Forsberg et al. (2022, magenta circles). The disc and halo with grey triangles are from (Peterson 2013; Hansen et al. 2014; Roederer et al. 2014; Mishenina et al. 2019; Forsberg et al. 2022).

(Cowan et al. 2002), CS 22892-052 (Sneden et al. 2003) and HD 222925 (Roederer et al. 2022).

Table 3. RA+Dec and proper motions from *Gaia* EDR3, (Gaia Collaboration 2016,2021).

Properties	J13-star	Z06-star
(l, b) (deg)	(–1.0, –8.4)	(5.2, –2.8)
RA (deg)	274.438	272.10
Dec (deg)	–33.890	–25.812
J mag	11.686	12.255
H mag	11.034	11.395
K mag	10.955	11.130
Distance (kpc)	11.8 ± 1.0	7.2 ± 0.3
pm(ra) (mas yr^{-1})	–3.734 ± 0.023	–0.304 ± 0.052
pm(dec) (mas yr^{-1})	–9.512 ± 0.018	–2.601 ± 0.036
RV (km s^{-1})	–16	–36

Notes. Distance estimates, as described in Sect. 4.1. The JHK photometry comes from 2MASS (Cutri et al. 2003). The radial velocities comes from Johnson et al. (2011) and Jönsson et al. (2017b), respectively for the J13-star and Z06-star.

Europium has a close to pure *r*-process origin with 96% *r*-process contribution at solar metallicites. Molybdenum has a more complex cosmic origin, as is composed of seven stable isotopes, with either an *s*-, *r*-, and *p*-process origin, or a combination of them. The *r*-process contribution varies a bit in the literature, from 27% to 36% at solar metallicities (Prantzos et al. 2020; Bisterzo et al. 2014, respectively). Mo has a roughly 25% origin from the p-process, a process which have several suggested cosmic sites and mechanisms behind it. It is likely to take place in proton-dense and/or explosive environments, which points toward fast timescales, such as core-collapse SNe, events linked to SNe type Ia, or mass-accreting neutron stars (see e.g. Rauscher et al. 2013; Forsberg et al. 2022). At the low metallicites of −0.65 and −1.67 dex for the stars, the *s*-process, taking place in AGB-stars, is less likely to contribute to the production the Mo (Karakas & Lattanzio 2014; Cescutti et al. 2015; Cescutti & Matteucci 2022). As such, at low metallicities Mo is effectively an *r*-process and *p*-process element. The same applies to Zr and La, which at lower metallicities have a dominating production from the *r*-process.

To decipher if the high neutron-capture abundances have an *r*- or *s*-process origin, we considered the [s/r]-ratio. Both the Z06-star and the J13-star have rather low [La/Eu]-ratio of −0.36 and −0.44 dex, respectively. Additionally, the [Ce/Eu]-ratio[2] is –0.56 and −0.62 dex, respectively, for the Z06-star and J13-star. This supports a significant contribution from the *r*-process in the enrichment of these two stars, and less significant contribution from the *s*-process (which is, indeed, the case for many bulge stars; see e.g. McWilliam 2016).

Although many stars with high *r*-process enhancements are known (Cowan et al. 2002; Sneden et al. 2003, 2008; Christlieb et al. 2004; Holmbeck et al. 2020), it is rare to find one at the comparatively high metallicities of the J13-star and the Z06-star. It should be noted that the metallicity distribution in the bulge varies with latitude, where the metallicity is higher towards the plane (see e.g. Johnson et al. 2020). As such, the Z06-star is metal-poor relative to its neighbouring stars. The same applies for the J13-star, where at the latitudes of $b = -8°$, lower metallicity stars are more common. Nonetheless, the relatively high metallicities of the stars (for being r-enriched stars) may likely be explained by a combination of iron-producing SNe driving the metallicity up, with multiple *r*-process events (NSM, MRSNe, Matteucci et al. 2014; Kobayashi et al. 2020) and Galactic mixing that inhibits otherwise high [*X*/Fe]-abundances. A more robust interpretation awaits surveys where we might answer whether the Z06-star is indeed unusual or whether more *r*-enhanced bulge giants are found near [Fe/H] ∼ −0.5 dex, perhaps relics of an early formation epoch in the bar.

[2] La and Ce has a roughly 75% and 85% origin from the *s*-process at solar metallicities, respectively (Bisterzo et al. 2014; Prantzos et al. 2020).

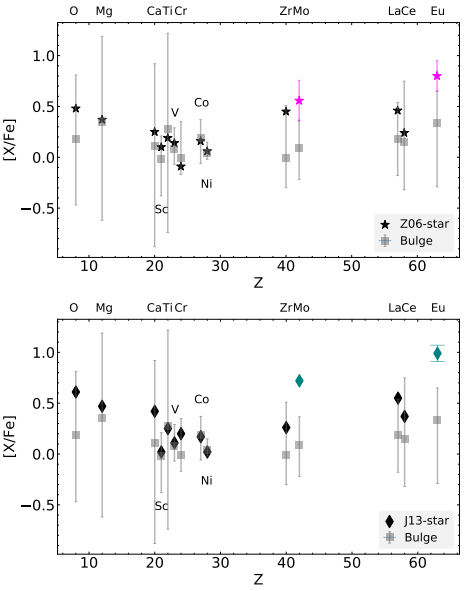

Fig. 6. [*X*/Fe] over Z for the bulge abundances (grey) presented in the Jönsson-series (Jönsson et al. 2017b; Lomaeva et al. 2019; Forsberg et al. 2019, 2022) for the Z06-star (upper plot, indicated with a star-symbol and the estimated uncertainties) and Johnson et al. (2013)-star (lower plot, indicated with a diamond). The bulge abundances are indicated by the mean (grey box) with the highest and lowest value (the Z06-star excluded) indicated by the bar, showing the spread in abundance in the bulge sample. To facilitate the reading of the plot, the element corresponding to a certain Z has been indicated. The *r*-process elements Mo and Eu has been indicated using magenta (Z06-star) and teal (J13-star).

5.2. The orbits

In Fig. 7 we show the orbits for both stars. The J13-star makes clear deviations to both high $|z| > 5$ kpc and even passes outside of the Sun's orbit in x–y plane. We also estimate the orbital parameters taking into account the derived uncertainties in distance and proper motion, and find that the distance is the parameter that makes the largest difference, and the proper motion is less important when the uncertainty in the distance is large. In Fig. 8, we show the orbits with the low and high distance estimates (as taken from Table 3) using the nominal proper motions. The Z06-star always remains in the bulge, given its smaller uncertainty in distance, whereas the J13-star is heavily

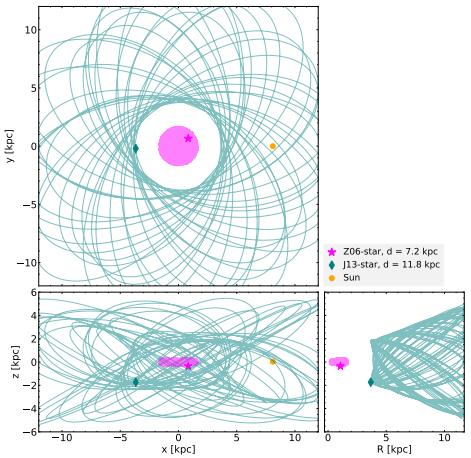

Fig. 7. Orbit for the J13-star (teal) and the Z06-star (magenta) plotted in *x*–*y* (top), *x*–*z* (*bottom left*) and R-z (*bottom right*) plane. The orbits are integrated over 10 Gyr and the position of the stars in their orbits are indicated, as well as the position of the Sun (yellow dot). This is the nominal case for the distances ("*d*"), which are indicated in the legend, and seen in Table 3.

affected by its distance. For the lower distance of the J13-star, it extends to $|z| \sim 3$ kpc, and seems to trace the bar potential adopted in the `GalPy`-setup (see Sect. 4.2).

As for the distances of the stars, we do note that both stars have distance estimates in Bailer-Jones et al. (2021), which uses a Bayesian approach and a prior model of the Galaxy. The distances are estimated to 7409^{+1369}_{-972} pc and 6839^{+2375}_{-1252} pc for the J13-star and the Z06-star, respectively[3]. We refer to Bailer-Jones et al. (2021) for more details on the distance measurements.

Similarly, the StarHorse code (SH, Queiroz et al. 2018), which also uses a Galactic prior, has distance estimates and stellar parameters to the stars using *Gaia* EDR3 and photometric catalogues in Anders et al. (2022). They give the distances to 6.1 kpc and 7.4 kpc, respectively, for the J13-star and the Z06-star.

These distance measurements puts the J13-star within the bulge, however, we also do note that the metallicity output from SH is very high, −0.38 dex, compared to −1.67 dex from the spectroscopic measurements (Johnson et al. 2013). Similarly, they estimated a 0.18 dex metallicity for the Z06-star, indicating large uncertainties when determining metallicities for very distant stars, which propagate to the estimated distances. Additionally, the parallax error in *Gaia* EDR3 for this star is as high as a quarter of the parallax (`parallax_over_error` of 3.9), implying that the parallax, used in Bailer-Jones et al. (2021), is unreliable. In conclusion, given the low metallicity and considering our distance- and orbital estimates of the J13-star, it seems likely that it has its origin in the Galactic halo or thick disc.

[3] Note: this is the geometric distance as measured by Bailer-Jones et al. (2021), the photogeometric, which combines the geometric with G-magnitude and BP-RP colours, gives 6316^{+1257}_{-747} pc and 6559^{+1781}_{-1372} pc, respectively, for J13-star and Z06-star. In general, the photogeometric distance extend to larger distances and tend to have smaller uncertainties.

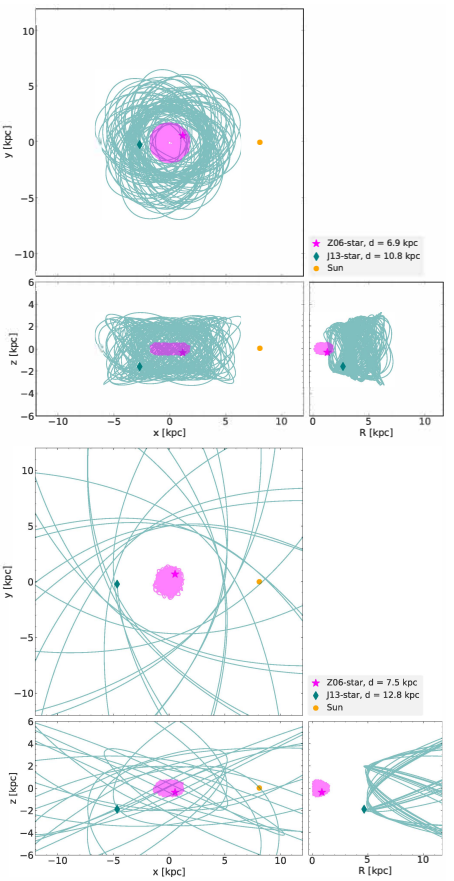

Fig. 8. Orbits for the J13-star (teal) and the Z06-star (magenta) plotted in *x*–*y*, *x*–*z* and *R*–*z* plane (as in Fig. 7). The position of the stars in their orbits are indicated, as well as the position of the Sun (yellow dot). The top figure show the orbits computed with the low distance estimate ("*d*"), and the bottom one with the high distance estimate, as indicated in the legend. Similarly as the nominal case, we integrate the orbits for 10 Gyr.

6. Conclusions

In this work, we present an *r*-process enriched bulge star, 2MASS J18082459-2548444 (the Z06-star). We show that it is high in both molybdenum with [Mo/Fe] = 0.62 dex and europium with [Eu/Fe] = 0.78 dex, whilst having otherwise overall

bulge-like abundances for other heavy trans-iron elements. Furthermore, the low [Ce,La/Eu] ratio suggests that the heavier trans-iron elements in the Z06-star were predominantly produced by the *r*-process, rather than the *s*-process.

We compared the star to the previously published r-enriched star in the bulge, MASS J18174532–3353235 (the J13-star), and estimated both stars' distances and orbits. We find that the Z06-star likely is confined and has an origin in the bulge, whilst the J13-star is more probable to have a halo or thick disc origin. Nonetheless, we cannot firmly exclude that it resides in the bulge or that it has bulge origin, since distance measurements of stars at these distances in general come with large uncertainties.

It would be beneficial to measure the ruthenium (Ru, Z = 44) abundance of the Z06-star, which has a 7% p-process and 59% contribution from the *r*-process at solar metallicities. The J13-star is extremely high in Ru, [Ru/Fe] = 1.58 dex, which could suggests that intermediate mass elements such as Ru and Mo are produced in a distinct way (possibly the p-process in the case for Ru and Mo). However, all Ru-lines in the optical, such as the 5309 Å and 5699 Å line used in Johnson et al. (2013), lie outside of the spectrum range of 5800–6800 Å for the Z06-star, and new high-resolution spectra covering the whole optical region would be beneficial to be able to determine more trans-iron elements. The use of high-resolution, high S/N optical spectra is key in the search for these *r*-process enhanced stars; the *r*-process signatures are difficult to infer in the infrared (so far, only the *r*-process element ytterbium has had successful abundance determination in the infrared from high-resolution IGRINS spectra, as, for instance, in Montelius et al. 2022).

The discovery of one *r*-process enhanced star that is a member of the bulge does not independently provide insight into the bulge formation process. What this does is demonstrate, despite the significantly higher metallicities and implied greater rate of enrichment that it has been possible for sufficient *r*-process elements to be produced for a star such as the Z06-star could be discovered in the inner bulge. It is interesting to consider whether the tail of stars toward [Fe/H] ~ -1 dex reflects an early period of enrichment in the history of the inner bulge and bar – and, as such, whether other signatures of stochastic production of elements in the early bulge might be found with subsequent studies.

We do have evidence to support that the inner halo at $b = -11°$ (Koch et al. 2006) is interesting in this regard and that even small surveys find stars with unusual composition, including *s*- and *p*-process enhancements (Koch et al. 2016, 2019). However, it is important to emphasise that these stars, along with other recent surveys that emphasise the discovery of stars with [Fe/H] < -2 dex (e.g. EMBLA and Pristine Inner Galaxy Survey, Howes et al. 2016; Arentsen et al. 2020, respectively) explore a different potential discovery space, namely, that of the early inner halo. The importance of the Z06-star is rooted in strong evidence supporting its presence in the inner bulge and its [Fe/H] > -1 dex. The discovery of other stars similar to it, and residing in the tail toward -1 dex of the primary bulge metallicity distribution, might preserve the history of the enrichment event that gave rise to the chemical fingerprint associated with the formation of the bar. Alternatively, the low metallicity tail might preserve the record of an early merger. The discovery of additional similar stars and the detailed exploration of this population might provide new insights into the early formation history of the bulge.

Acknowledgements. We thank the anonymous referees for comments and suggestions that helped improve the manuscript. We thank Paul McMillan for discussions on Galactic potentials and distance estimates. R.F.'s research is supported by the Göran Gustafsson Foundation for Research in Natural Sciences and Medicine. R.F. and N.R. acknowledge support from the Royal Physiographic Society in Lund through the Stiftelse Walter Gyllenbergs fond and Märta och Erik Holmbergs donation. N.N. and M.S. acknowledge the funding of the BQR Lagrange. R.M.R. acknowledges the financial support and hospitality of the Observatoire de Côte d'Azur. B.T. acknowledges the financial support from the Japan Society for the Promotion of Science as a JSPS International Research Fellow. This work has made use of data from the European Southern Observatory (ESO) and the European Space Agency's (ESA) *Gaia* mission (`https://www.cosmos.esa.int/gaia`), processed by the *Gaia* Data Processing and Analysis Consortium (DPAC, `https://www.cosmos.esa.int/web/gaia/dpac/consortium`). Funding for the DPAC has been provided by national institutions, in particular the institutions participating in the *Gaia* Multilateral Agreement. *Software:* `NumPy` (Harris et al. 2020), `Matplotlib` (Hunter 2007), `GalPy` (`http://github.com/jobovy/galpy`, Bovy 2015), `AstroPy` (Astropy Collaboration 2013).

References

Anders, F., Khalatyan, A., Queiroz, A. B. A., et al. 2022, A&A, 658, A91
Arentsen, A., Starkenburg, E., Martin, N. F., et al. 2020, MNRAS, 496, 4964
Astropy Collaboration (Robitaille, T. P., et al.) 2013, A&A, 558, A33
Bailer-Jones, C. A. L., Rybizki, J., Fouesneau, M., Demleitner, M., & Andrae, R. 2021, AJ, 161, 147
Bensby, T., Feltzing, S., Gould, A., et al. 2017, A&A, 605, A89
Bisterzo, S., Travaglio, C., Gallino, R., Wiescher, M., & Käppeler, F. 2014, ApJ, 787, 10
Bovy, J. 2015, ApJS, 216, 29
Bressan, A., Marigo, P., Girardi, L., et al. 2012, MNRAS, 427, 127
Burbidge, E. M., Burbidge, G. R., Fowler, W. A., & Hoyle, F. 1957, Rev. Mod. Phys., 29, 547
Cardelli, J. A., Clayton, G. C., & Mathis, J. S. 1989, ApJ, 345, 245
Cescutti, G., & Matteucci, F. 2022, Universe, 8, 173
Cescutti, G., Romano, D., Matteucci, F., Chiappini, C., & Hirschi, R. 2015, A&A, 577, A139
Christlieb, N., Beers, T. C., Barklem, P. S., et al. 2004, A&A, 428, 1027
Clarkson, W., Sahu, K., Anderson, J., et al. 2008, ApJ, 684, 1110
Côté, B., Eichler, M., Arcones, A., et al. 2019, ApJ, 875, 106
Cowan, J. J., Sneden, C., Burles, S., et al. 2002, ApJ, 572, 861
Cutri, R. M., Skrutskie, M. F., van Dyk, S., et al. 2003, VizieR Online Data Catalog: II/246
Dehnen, W. 2000, AJ, 119, 800
Di Matteo, P., Haywood, M., Gómez, A., et al. 2014, A&A, 567, A122
Forsberg, R., Jönsson, H., Ryde, N., & Matteucci, F. 2019, A&A, 631, A113
Forsberg, R., Ryde, N., Jönsson, H., Rich, R. M., & Johansen, A. 2022, A&A, 666, A125
Gaia Collaboration (Prusti, T., et al.) 2016, A&A, 595, A1
Gaia Collaboration (Brown, A. G. A., et al.) 2021, A&A, 649, A1
Gonzalez, O. A., Rejkuba, M., Zoccali, M., et al. 2011, A&A, 530, A54
Gonzalez, O. A., Rejkuba, M., Zoccali, M., et al. 2012, A&A, 543, A13
Grevesse, N., Scott, P., Asplund, M., & Sauval, A. J. 2015, A&A, 573, A27
Gustafsson, B., Edvardsson, B., Eriksson, K., et al. 2008, A&A, 486, 951
Hansen, C. J., Andersen, A. C., & Christlieb, N. 2014, A&A, 568, A47
Harris, C. R., Millman, K. J., van der Walt, S. J., et al. 2020, Nature, 585, 357
Heiter, U., Jofré, P., Gustafsson, B., et al. 2015, A&A, 582, A49
Heiter, U., Lind, K., Bergemann, M., et al. 2021, A&A, 645, A106
Hirai, Y., Ishimaru, Y., Saitoh, T. R., et al. 2015, ApJ, 814, 41
Holmbeck, E. M., Hansen, T. T., Beers, T. C., et al. 2020, ApJS, 249, 30
Howes, L. M., Asplund, M., Keller, S. C., et al. 2016, MNRAS, 460, 884
Hunter, J. D. 2007, Comput. Sci. Eng., 9, 90
Jeon, M., Besla, G., & Bromm, V. 2021, MNRAS, 506, 1850
Jofré, P., Heiter, U., Soubiran, C., et al. 2014, A&A, 564, A133
Jofré, P., Heiter, U., Soubiran, C., et al. 2015, A&A, 582, A81
Johnson, C. I., Rich, R. M., Fulbright, J. P., Valenti, E., & McWilliam, A. 2011, ApJ, 732, 108
Johnson, C. I., Rich, R. M., Kobayashi, C., & Fulbright, J. P. 2012, ApJ, 749, 175
Johnson, C. I., McWilliam, A., & Rich, R. M. 2013, ApJ, 775, L27
Johnson, C. I., Rich, R. M., Kobayashi, C., Kunder, A., & Koch, A. 2014, AJ, 148, 67
Johnson, C. I., Rich, R. M., Young, M. D., et al. 2020, MNRAS, 499, 2357
Jönsson, H., Ryde, N., Nordlander, T., et al. 2017a, A&A, 598, A100
Jönsson, H., Ryde, N., Schultheis, M., & Zoccali, M. 2017b, A&A, 600, C2
Joyce, M., Johnson, C. I., Marchetti, T., et al. 2022, ApJ, submitted [arXiv:2205.07964]

Karakas, A. I., & Lattanzio, J. C. 2014, PASA, 31, e030
Kobayashi, C., Karakas, A. I., & Lugaro, M. 2020, ApJ, 900, 179
Koch, A., Grebel, E. K., Wyse, R. F. G., et al. 2006, AJ, 131, 895
Koch, A., McWilliam, A., Preston, G. W., & Thompson, I. B. 2016, A&A, 587, A124
Koch, A., Reichert, M., Hansen, C. J., et al. 2019, A&A, 622, A159
Kordopatis, G., Schultheis, M., McMillan, P. J., et al. 2022, A&A, in press, [arXiv.2206.07937]
Launhardt, R., Zylka, R., & Mezger, P. G. 2002, A&A, 384, 112
Lecureur, A., Hill, V., Zoccali, M., et al. 2007, A&A, 465, 799
Lomaeva, M., Jönsson, H., Ryde, N., Schultheis, M., & Thorsbro, B. 2019, A&A, 625, A141
Majewski, S. R., Schiavon, R. P., Frinchaboy, P. M., et al. 2017, AJ, 154, 94
Marigo, P., Girardi, L., Bressan, A., et al. 2017, ApJ, 835, 77
Matsuno, T., Hirai, Y., Tarumi, Y., et al. 2021, A&A, 650, A110
Matteucci, F., & Brocato, E. 1990, ApJ, 365, 539
Matteucci, F., Romano, D., Arcones, A., Korobkin, O., & Rosswog, S. 2014, MNRAS, 438, 2177
McWilliam, A. 2016, PASA, 33, e040
McWilliam, A., & Rich, R. M. 1994, ApJS, 91, 749
McWilliam, A., Preston, G. W., Sneden, C., & Searle, L. 1995, AJ, 109, 2757
Mishenina, T. V., Pignatari, M., Korotin, S. A., et al. 2013, A&A, 552, A128
Mishenina, T., Pignatari, M., Gorbaneva, T., et al. 2019, MNRAS, 489, 1697
Monari, G., Famaey, B., Siebert, A., et al. 2016, MNRAS, 461, 3835
Montelius, M., Forsberg, R., Ryde, N., et al. 2022, A&A, 665, A135
Ness, M., Freeman, K., Athanassoula, E., et al. 2012, ApJ, 756, 22
Ness, M., Freeman, K., Athanassoula, E., et al. 2013, MNRAS, 430, 836
Nishimura, S., Kotake, K., Hashimoto, M.-a., et al. 2006, ApJ, 642, 410
Ortolani, S., Renzini, A., Gilmozzi, R., et al. 1995, Nature, 377, 701
Peterson, R. C. 2013, ApJ, 768, L13
Piskunov, N., & Valenti, J. A., 2017, A&A, 597, A16
Prantzos, N., Abia, C., Cristallo, S., Limongi, M., & Chieffi, A. 2020, MNRAS, 491, 1832
Queiroz, A. B. A., Anders, F., Santiago, B. X., et al. 2018, MNRAS, 476, 2556
Rauscher, T., Dauphas, N., Dillmann, I., et al. 2013, Rep. Progr. Phys., 76, 066201
Renzini, A., Gennaro, M., Zoccali, M., et al. 2018, ApJ, 863, 16
Rich, R. M. 1988, AJ, 95, 828
Roederer, I. U., Preston, G. W., Thompson, I. B., et al. 2014, AJ, 147, 136
Roederer, I. U., Lawler, J. E., Den Hartog, E. A., et al. 2022, ApJS, 260, 27
Rojas-Arriagada, A., Recio-Blanco, A., de Laverny, P., et al. 2017, A&A, 601, A140
Rojas-Arriagada, A., Zasowski, G., Schultheis, M., et al. 2020, MNRAS, 499, 1037
Ryde, N., Gustafsson, B., Edvardsson, B., et al. 2010, A&A, 509, A20
Scott, P., Asplund, M., Grevesse, N., Bergemann, M., & Sauval, A. J. 2015a, A&A, 573, A26
Scott, P., Grevesse, N., Asplund, M., et al. 2015b, A&A, 573, A25
Shen, J., Rich, R. M., Kormendy, J., et al. 2010, ApJ, 720, L72
Sneden, C., Cowan, J. J., Lawler, J. E., et al. 2003, ApJ, 591, 936
Sneden, C., Cowan, J. J., & Gallino, R. 2008, ARA&A, 46, 241
Valenti, J. A. & Piskunov, N. 1996, A&AS, 118, 595
Van der Swaelmen, M., Barbuy, B., Hill, V., et al. 2016, A&A, 586, A1
Vasiliev, E. 2019, MNRAS, 482, 1525
Weiland, J. L., Arendt, R. G., Berriman, G. B., et al. 1994, ApJ, 425, L81
Zasowski, G., Schultheis, M., Hasselquist, S., et al. 2019, ApJ, 870, 138
Zoccali, M., Lecureur, A., Barbuy, B., et al. 2006, A&A, 457, L1
Zoccali, M., Hill, V., Lecureur, A., et al. 2008, A&A, 486, 177

Paper IV

A&A 665, A135 (2022)
https://doi.org/10.1051/0004-6361/202243140

Astronomy & Astrophysics

Chemical evolution of ytterbium in the Galactic disk*

M. Montelius[1,2], R. Forsberg[2], N. Ryde[2], H. Jönsson[3], M. Afşar[4,8], A. Johansen[2,5], K. F. Kaplan[6], H. Kim[7], G. Mace[8], C. Sneden[8], and B. Thorsbro[2]

[1] Kapteyn Astronomical Institute, University of Groningen, Landleven 12, 9747 AD Groningen, The Netherlands
e-mail: montelius@astro.rug.nl
[2] Lund Observatory, Department of Astronomy and Theoretical Physics, Lund University, Box 43, 22100 Lund, Sweden
[3] Materials Science and Applied Mathematics, Malmö University, 205 06 Malmö, Sweden
[4] Department of Astronomy and Space Sciences, Ege University, 35100 Bornova, İzmir, Turkey
[5] Center for Star and Planet Formation, GLOBE Institute University of Copenhagen, Øster Voldgade 5-7, 1350 Copenhagen, Denmark
[6] SOFIA Science Center – USRA, NASA Ames Research Center, Moffett Field, CA 94035, USA
[7] Gemini Observatory/NOIRLab, Casilla 603, La Serena, Chile
[8] Department of Astronomy and McDonald Observatory, The University of Texas, Austin, TX 78712, USA

Received 17 January 2022 / Accepted 31 January 2022

ABSTRACT

Context. Measuring the abundances of neutron-capture elements in Galactic disk stars is an important part of understanding key stellar and galactic processes. In the optical wavelength regime a number of different neutron-capture elements have been measured; however, only the *s*-process-dominated element cerium has been accurately measured for a large sample of disk stars from the infrared *H* band. The more *r*-process dominated element ytterbium has only been measured in a small subset of stars so far.

Aims. In this study we aim to measure the ytterbium (Yb) abundance of local disk giants using the Yb II line at $\lambda_{\rm air}$ = 16 498 Å. We also compare the resulting abundance trend with cerium and europium abundances for the same stars to analyse the *s*- and *r*-process contributions.

Methods. We analyse 30 K giants with high-resolution *H* band spectra using spectral synthesis. The very same stars have already been analysed using high-resolution optical spectra via the same method, but it was not possible to determine the abundance of Yb from those spectra due to blending issues for stars with [Fe/H] > −1. In the present analysis, we utilise the stellar parameters determined from the optical analysis.

Results. We determined the Yb abundances with an estimated uncertainty for [Yb/Fe] of 0.1 dex. By comparison, we found that the [Yb/Fe] trend closely follows the [Eu/Fe] trend and has clear *s*-process enrichment in identified s-rich stars. This comparison confirms both that the validity of the Yb abundances is ensured and that the theoretical prediction that the *s*-/*r*-process contribution to the origin of Yb of roughly 40/60 is supported.

Conclusions. These results show that, with a careful and detailed analysis of infrared spectra, reliable Yb abundances can be derived for a wider sample of cooler giants in the range −1.1 < [Fe/H] < 0.3. This is promising for further studies of the production of Yb and for the *r*-process channel, key for galactochemical evolution, in the infrared.

Key words. stars: abundances – stars: late-type – Galaxy: abundances – Galaxy: disk – Galaxy: evolution – infrared: stars

1. Introduction

Stellar elemental abundances play a key role in deciphering Galactic chemical evolution. The photosphere of stars carries a chemical imprint of the molecular cloud from which they formed, making them time stamps of the Galactic environment at that epoch. By measuring the stellar abundances from stars originating from different Galactic epochs, the chemical enrichment in the Galaxy can be traced (see e.g. Bland-Hawthorn & Gerhard 2016, and references therein). The field of Galactic research is increasingly moving to the infrared spectral range, with a different set of spectral lines compared to those available in the optical range. With this comes the possibility of expanding the study of the chemical evolution of the galaxy, in particular to dust-covered regions. Different elements can give us different angles on Galactic formation and evolution, and in this study we consider the heavy element ytterbium.

The production of elements through fusion becomes endothermic above iron, which means that the remaining two-thirds of the elements in the periodic table need another production channel. The idea that heavier elements are created by neutron-capture processes was introduced by Burbidge et al. (1957), who gave these elements the name 'neutron-capture elements'.

As an atomic nucleus captures a neutron, a heavier isotope of that element is created. If this isotope is unstable, a neutron will convert to a proton through β^- decay and create a heavier element. If the isotope is stable, it can capture further neutrons until eventually β^--decaying. This outlines two processes, one where the β^- decay is slower than the neutron-capture and one where the β^- decay is more rapid than the neutron-capture. These are called the *s*- and *r*-processes, and together they produce the heavier elements. Indeed, they produce a majority of the isotopes for elements with Z > 30. An example of elements formed through neutron-capture processes are the lanthanides, some of which are studied in this paper: cerium (Ce; Z = 58), europium (Eu; Z = 63), and ytterbium (Yb; Z = 70).

* Tables 1 and 3 are also available at the CDS via anonymous ftp to cdsarc.u-strasbg.fr (130.79.128.5) or via http://cdsarc.u-strasbg.fr/viz-bin/cat/J/A+A/665/A135

The neutron-capture rate is not constant but depends on both (i) the local neutron density and (ii) the neutron absorption cross-section of the isotope. This allows some constraints to be put on the environment where they occur. The *s*-process requires a neutron density of $\leq 10^{11}$ cm^{-3} (Busso et al. 1999) and has been shown to take place in the interior of low-mass asymptotic giant branch (AGB) stars (see Karakas & Lattanzio 2014, and references therein). The *r*-process requires a neutron density of around 10^{24}–10^{28} cm^{-3} (see e.g. Kratz et al. 2007), which confines it to extremely neutron-dense environments, such as various supernovae (SNe) and mergers of neutron stars. The first observed neutron-star merger GW170817 (Abbott et al. 2017) indeed contained traces of *r*-process element production (Tanvir et al. 2017; Drout et al. 2017). In contrast, Kobayashi et al. (2020) found from comparing theoretical models to observations that core-collapse SNe, especially magneto-rotational supernovae (MRSNe), may be the predominant source of *r*-process production for most neutron-capture elements (see Fig. 39 in Kobayashi et al. 2020).

Most neutron-capture elements are produced by a combination of the s- and the *r*-processes. In the case of Ce, the *s*-process contributed approximately 85% and the *r*-process contributed the remaining 15% for stars with solar metallicities (Bisterzo et al. 2014; Prantzos et al. 2020). As such, it is usually referred to as 'an *s*-process element' since the dominating production channel is from this process. As a comparison, Eu is referred to as 'an *r*-process element', with only a 5% contribution from the *s*-process and the remaining from the *r*-process (Prantzos et al. 2020).

Yb[1], which is the focus of this study, is the second heaviest of the lanthanides and lies at the very end of the series in the periodic table. As such, it is a heavy neutron-capture element that lies between Ce and Eu, with approximately a 40/60–50/50 predicted contribution from the *s*- and *r*-processes, respectively (Bisterzo et al. 2014; Kobayashi et al. 2020; Prantzos et al. 2020). Nonetheless, the precise nature of its cosmic origin and abundance trend in the Galactic disk has not been well constrained, mainly due to the sparsely available observed abundance data.

Spectroscopically, however, Yb is relatively well studied, partially due to the interest in studying Ap stars (Cowley 1984) and ion traps (Olmschenk et al. 2009). The Yb II ion has a hydrogenic electron configuration, with an unpaired 6s valence electron. A consequence of this is that the strongest Yb II lines are the resonance lines, located at 3289.4 and 3694.2 Å[2], while the other spectral lines are significantly weaker. While both resonance lines have issues with blending, the line at 3694.2 Å has been preferred for abundance determination and has been used in a number of studies of low-metallicity stars, such as Honda et al. (2004); Johnson (2002); François et al. (2007); Roederer et al. (2014a,b); Sneden et al. (2009). The analysis is more difficult for stars with higher metallicities due to a larger impact of blending lines and the difficulty of defining the continuum of the spectrum in the bluer part of the optical regime. As a consequence, these lines have not been used for stars with metallicities[3] of [Fe/H] $\gtrsim -1.5$.

[1] The name ytterbium originates from the small Ytterby mine north-east of Stockholm, Sweden, and the element is one of seven discovered from the minerals found there during the 18th and 19th centuries.

[2] All wavelengths in this study are wavelengths in air.

[3] The metallicity and other abundances are defined using the notation $[A/B] = \log(N_A/N_B)_* - \log(N_A/N_B)_\odot$, where N_A and N_B are the number densities of the elements A and B, respectively. The solar abundances used in this study are from Grevesse et al. (2007), unless another reference is given.

Attempts have been made to fill this gap in metallicity by using the infrared Yb II line in the *H* band at 16498 Å. This line is the strongest of the infrared Yb lines and was first measured in the laboratory by Humphreys & Paul (1959). The APOGEE survey ($R = \lambda/\Delta\lambda \sim 22500$; Majewski et al. 2017) has investigated the utility of this line in their spectra (Smith et al. 2021), but do not consider the determined stellar Yb abundances reliable enough to be included in the final data release (DR17; Abdurro'uf et al. 2021; J. Holtzman et al., in prep.). In a reanalysis of APOGEE spectra in the Kepler field, Hawkins et al. (2016) attempted to use the same line, deriving upper limits for the Yb abundance, but did not publish abundances or further analyses.

Böcek Topcu et al. (2019, 2020) managed to determine Yb abundances for 11 and 10 stars in the open clusters NGC 6940 and NGC 752, respectively, by using the 16 498 Å Yb II line. The temperatures of the stars in these samples are around 5000 K, making a CO blend in the Yb II line close to negligible. Furthermore, Yb abundances of three horizontal-branch stars were determined in Afşar et al. (2018), who used the very same line, again for stars of $T_{\rm eff} \sim 5100$ K.

In this article we also attempt to use the Yb II line at 16 498 Å, and we succeed in deriving reliable Yb abundances for 30 K giants in the Milky Way disk, using high-resolution infrared spectra in the *H* band observed with the Immersion Grating INfrared Spectrometer (IGRINS). The spectral resolution it provides, $R \sim 45\,000$, is higher than that of APOGEE ($R \sim 22\,500$), which is important since the Yb II line is both weak and heavily blended with a CO molecular line. We investigate the *s*- and *r*-process contributions to the cosmic budget of Yb by comparing the Yb abundances to the abundances of the s-element Ce and the r-element Eu, which have been determined for the very same stars. The Ce abundances are determined from the *H* band spectra, while the Eu abundances are taken from Forsberg et al. (2019), where they were determined from optical spectra.

We succeed in measuring reliable Yb abundances from the 16 498 Å line for our sample of 30 disk stars. This demonstrates the possibility of larger studies of the *r*-process channel in the infrared $\bar{\imath}$ band, as well as the possibility of measuring Yb abundances for stars with metallicities of [Fe/H] $\gtrsim$ 1 dex. Knowing how to properly determine Yb abundances from the 16 498 Å line is a useful step towards deciphering the formation history and evolution of dust-covered regions in the Galaxy, such as the bulge.

In Sect. 2 we go through the observations and the data used. In Sect. 3 we go through the analysis, including uncertainty estimations. In Sect. 4 we present and discuss the results before concluding in Sect. 5.

2. Observations

For the present work, we observed 30 K giants, recording high-resolution spectra in the infrared (IGRINS). These stars were selected from a set of about 500 local disk giants, which have accurate stellar parameters determined through a careful optical spectroscopic analysis (FIES; H. Jönsson et al., in prep.) (see our Sect. 3.1).

2.1. IGRINS

The infrared spectra were observed with the IGRINS spectrograph (Yuk et al. 2010; Park et al. 2014) on the 4.3-metre Discovery Channel Telescope (DCT; now called the Lowell Discovery Telescope) at Lowell Observatory (Mace et al. 2018) and on the 2.7-metre Harlan J. Smith Telescope at McDonald

Table 1. IGRINS observing log, sorted to match Table 3.

Star	2MASS star name	H_{2MASS} (mag)	K_{2MASS} (mag)	Civil date	Telescope	Exposure (s)
α Boo	J14153968+1910558	−2.8	−2.9	2015 April 11	HJST	60
μ Leo	J09524585+2600248	1.3	1.2	2016 Jan. 31	HJST	26
ϵ Vir	J13021059+1057329	0.9	0.8	2016 Feb. 2	HJST	26
β Gem	J07451891+2801340	−1.0	−1.1	2016 Jan. 30	HJST	23
HD 102328	J11465561+5537416	2.9	2.6	2016 Feb. 2	HJST	32
HD 102328 [(a)]	J11465561+5537416	2.9	2.6	2016 Feb. 27	HJST	20
HIP 50583	J10195836+1950290	−0.8	−0.8	2016 June 20	HJST	29
HIP 63432	J12595500+6635502	2.4	2.1	2016 May 29	HJST	180
HIP 72012	J14434444+4027333	2.6	2.4	2016 June 16	HJST	120
HIP 90344	J18255915+6533486	2.2	2.1	2016 June 15	HJST	120
HIP 96014	J19311935+5018240	2.9	2.5	2016 June 15	HJST	120
HIP 102488	J20461266+3358128	0.2	0.1	2016 June 19	HJST	26
2M17215666	J17215666+4301408	7.6	7.5	2016 July 25	HJST	1080
KIC 3748585	J19272877+3848096	6.4	6.3	2016 Nov. 17	DCT	240
KIC 3955590	J19272677+3900456	7.8	7.7	2016 Nov. 23	DCT	480
KIC 4177025	J19434309+3917436	7.6	7.5	2016 Nov. 22	DCT	360
KIC 5113910	J19421943+4016074	8.2	8.0	2016 Nov. 22	DCT	720
KIC 5709564	J19321853+4058217	7.6	7.5	2016 Nov. 23	DCT	480
KIC 5779724	J19123427+4105257	8.0	7.8	2016 Dec. 09	DCT	600
KIC 5859492	J19021718+4107236	7.9	7.8	2016 Nov. 23	DCT	480
KIC 5900096	J19515137+4106378	6.0	5.8	2016 Nov. 22	DCT	120
KIC 6465075	J19512404+4149284	8.0	7.9	2016 Nov. 23	DCT	480
KIC 6547007	J19525719+4158129	8.3	8.2	2016 Dec. 9	DCT	600
KIC 6837256	J18464309+4223144	8.8	8.7	2016 Nov. 23	DCT	720
KIC 11045542	J19530590+4833180	8.4	8.2	2016 Dec. 11	DCT	2000
KIC 11342694	J19110062+4906529	7.6	7.4	2016 Nov. 17	DCT	480
KIC 11444313	J19014380+4923062	9.1	9.0	2016 Nov. 23	DCT	720
KIC 11569659	J19464387+4934210	9.4	9.3	2016 Dec. 9	DCT	2400
KIC 11657684	J19175551+4946243	9.6	9.5	2016 Dec. 11	DCT	3000
2M14231899	J14231899+0540079	8.0	7.8	2016 June 19	HJST	1200
HD 142091 [(a)]	J15511394+3539264	2.6	2.5	2016 Feb. 29	HJST	44

Notes. DCT: the Discovery Channel Telescope, a 4.3 m telescope at Lowell Observatory, Arizona. HJST: the Harlan J Smith Telescope, a 2.7 m telescope at McDonald Observatory, Texas. [(a)]Data from the IGRINS Spectral Library (Park et al. 2018).

Observatory (Mace et al. 2016) on the civil dates listed in Table 1.

IGRINS provides a spectral resolving power of $R \sim 45\,000$ and spans the full H and K bands (1.45−2.5 μm), which are recorded in one exposure. However, for this paper we are mainly interested in the Yb II line at 16 498 Å. The stars were observed in an ABBA nod sequence along the slit to permit sky background subtraction. We aimed for signal-to-noise ratios (S/N) of at least 100, leading to exposure times for these bright objects in the range of 30–3000 s (see Table 1). In conjunction with the science targets, telluric standard stars (typically rapidly rotating, late B to early A dwarfs) were observed at similar air masses. All the spectra were optimally extracted (thus, not a simple sum extraction) using the IGRINS reduction pipeline (Lee et al. 2017). The pipeline extracts wavelength-calibrated spectra after flat-field correction and A-B frame subtraction. Obvious cosmic-ray signatures in the spectra, being in emission or very strong one-pixel features in absorption, which are not taken care of by the pipeline, were carefully eliminated.

In order to divide out the telluric lines, the observed spectra were divided by the spectra of the telluric standard stars. Every order of the divided spectra was continuum-normalised with the IRAF task `continuum` (Tody 1993) and then combined with the task `scombine`, allowing the addition of overlapping regions of subsequent orders. The parts of the edges of the overlapping regions with no traceable continuum and spurious edge effects were omitted. This resulted in one normalised and stitched spectrum across the entire infrared H and K bands for each star. One of the stars, HD102328, was observed twice, and the two reduced spectra were analysed independently.

2.2. FIES

As already mentioned, the 30 stars in our infrared IGRINS sample are a sub-sample of some 500 local disk giants. This larger sample of stars was observed with the high-resolution spectrograph FIES (Telting et al. 2014), mounted on the Nordic Optical Telescope (NOT) in La Palma, Spain. FIES has a resolution of $R \sim 67\,000$, with a wavelength range of 3700–8300 Å. The S/N of these spectra is generally high, often around 200. More about these spectra and observations can be found in Jönsson et al. (2017).

3. Analysis

In this section we go through the stellar parameters determined from optical spectra in Sect. 3.1. Supporting abundances determined from either optical or IGRINS spectra are described

in Sect. 3.2. We cover the method and atomic data used in Sects. 3.3 and 3.4. Details of the Yb abundance and handling of the CO blend are described in Sect. 3.5, and the uncertainties are covered in Sect. 3.6.

3.1. Stellar parameters

Our sample of stars has accurate stellar parameters determined through a careful spectroscopic analysis of the optical FIES data. This analysis will be described in Jönsson et al. (in prep.) and builds upon and improves the analysis described in Jönsson et al. (2017). The main difference between the determination of stellar parameters in Jönsson et al. (2017) and in Jönsson et al. (in prep.) is that the latter use the entire wavelength region available in the FIES spectra, which was restricted to 5800–6800 Å in the former. This of course leads to more available Fe I and, in particular, Fe II lines, improving the accuracy of the determined stellar parameters in general. It also removes the systematic difference of 0.1 dex in $\log(g)$ when comparing to asteroseismic values found in the 2017 analysis. The uncertainties of the stellar parameters from the optical analysis are estimated to typically be 50 K in $T_{\rm eff}$, 0.1 dex in $\log(g)$, 0.05 dex in [Fe/H], and 0.1 km s^{-1} in $\xi_{\rm micro}$.

Macroturbulence, $\xi_{\rm macro}$, depends on large-scale motion in the stellar atmosphere and the instrumental profile of the spectrograph. As such, it cannot be adopted from the optical data and is instead determined from a set of Fe I lines in the infrared, with accurate van der Waals broadening parameters supplied by P. Barklem (2018, priv. comm.).

3.2. Other elemental abundances

In this paper we also make use of some of the stellar abundances derived from the optical spectra, in particular C, N, and O, for modelling the ubiquitous molecular lines in the IGRINS spectra. The C, N, and O abundances are derived from the forbidden O I doublet at 6300 and 6364 Å and selected CN and C_2 molecular lines. The general uncertainties of these abundances are estimated to be of the order of 0.05 dex. To ensure the highest accuracy in modelling the blending CO line, the C abundances for some of the stars were supplemented with measurements from C I lines in the IGRINS spectra.

In the discussion in Sect. 4, the star's abundances of the neutron-capture elements Ce and Eu are used. The Ce abundances were determined using the Ce II lines at 16 595.18 Å and 17 058.88 Å. The two lines have minor blends, Mg I and Fe I respectively, which do not appear to affect the measurements significantly. The derived abundances agree well with the optical measurements from Jönsson et al. (in prep.). The Eu abundances are taken from Forsberg et al. (2019), who used the same FIES spectra as Jönsson et al. (in prep.) but with the stellar parameters from Jönsson et al. (2017).

Within the Jönsson et al. (in prep.) analysis, several stars with unexpectedly high abundances of s-elements were found. On the other hand, these stars have 'normal' abundances of the other elements, following the general [X/Fe] versus [Fe/H] trend. This indicates both the precision of these optical measurements and the high confidence we can have in the determined s-element enhancement. Three of these stars are among the presently analysed sample of stars and stand out in terms of their *s*-process element Ce abundances (see Sect. 4). This is useful when discussing our Yb measurements.

All stellar parameters and abundances for the IGRINS sample of stars are provided in Sect. 4. The s-enriched stars are indicated, as is a classification of the stars into different stellar populations, the thin disk, the thick disk, or the halo. This division into stellar populations was made using a combination of high- and low-α abundances ([Mg/Fe]) combined with kinematics in a scheme similar to the method used in Lomaeva et al. (2019) and Forsberg et al. (2019).

3.3. Spectral synthesis

We determined the abundances using the spectral synthesis code Spectroscopy Made Easy (SME; Valenti & Piskunov 1996; Piskunov & Valenti 2017). This code interpolates a model atmosphere from a grid of spherically symmetric 1D MARCS models (Gustafsson et al. 2008), computed using local thermodynamic equilibrium (LTE). The abundance is determined by finding a best fit to the observed spectrum using χ^2 minimisation of the synthetic spectrum from the model atmosphere grid.

In order to synthesise a spectrum, SME requires, in addition to a line list with atomic data and a model atmosphere, a segment within which the line mask and several continuum masks are defined. We defined the line and continuum masks manually and examined all synthetic spectra by eye to ensure a good fit to the observed spectra. In the cases where the final spectra still had some modulation in their continuum levels, this was taken care of by defining specific local continua around the spectral line in those stars.

3.4. Atomic data

The basis of the line list used in this study is an extraction of atomic lines from the VALD3 database (Ryabchikova et al. 2015). As a number of the lines in the studied wavelength range lack reliable measurements of their log (gf) values, these values were shifted to match the solar spectra, most notably the Fe I and Zn I lines in the vicinity of the Yb II line. Additionally, we adjusted the log gf value of a nearby Ni I line to fit the spectrum of μ Leo using a $[{\rm Ni/Fe}]_{\mu\ {\rm Leo}} = 0.07$ since it presented a blending problem for super-solar metallicity stars while not being visible in the Sun.

For molecular lines, a number of additional sources were used: $^{12}C^{14}N$ and $^{13}C^{14}N$ from Sneden et al. (2014); $^{12}C^{16}O$ and $^{13}C^{16}O$ from Li et al. (2015); and ^{16}OH from Brooke et al. (2016). H_2O lines are present in the *H* band, but for the stars in this paper the impact on the spectra around the Yb II line is below 0.1% of the continuum level. As this is far below the noise level, the H_2O lines are not included. No other molecules are expected to show significant lines in *K*-giant *H* band spectra.

For the 16 498 Å line of Yb II used in this study, the atomic data were sourced from Biémont et al. (1998), which presents log (gf) values calculated using the Hartree-Fock approximation (Cowan 1981). The data for the line are given in Table 2 together with the most prominent blends.

The Ce II lines used to determine Ce abundances for the stars have wavelengths and excitation energies from Corliss (1973), but there are no laboratory measurements of the log(gf) values. They were instead determined astrophysically, by adjusting log(gf) line by line such that the mean abundances agree with the measurements of the same stars in Jönsson et al. (in prep.).

3.5. Ytterbium determination

The Yb II 16 498 Å line is rather weak, although detectable in high-resolution spectra with high S/N. The main difficulty in analysing the line comes from the molecular lines that blend it. Primarily, this blend is made up of a CO line, but with a

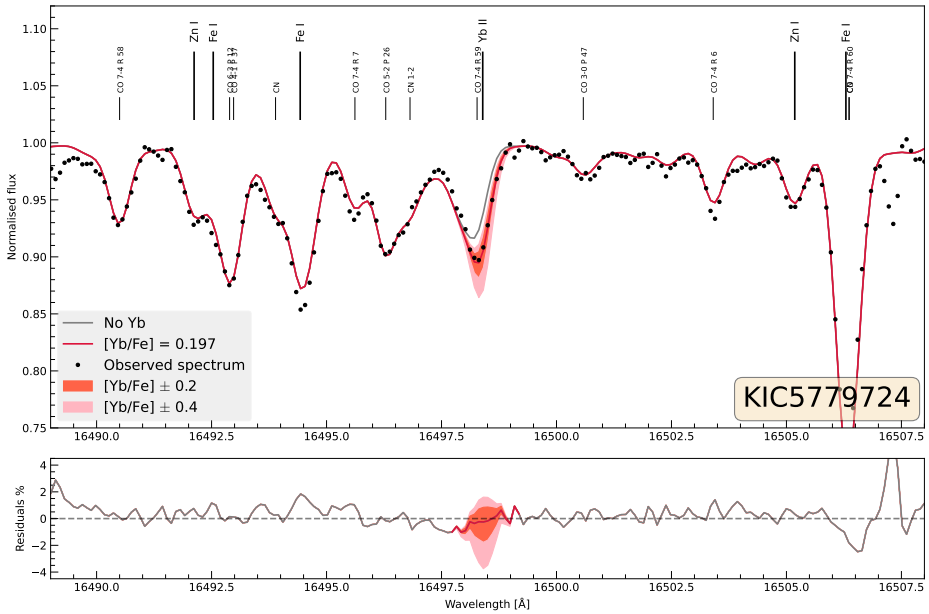

Fig. 1. Comparison between the observed and the synthesised spectrum for KIC 5779724 around the Yb II line at λ_{air} = 16 498.42 Å, with the residuals plotted below. Additional curves show the impact of increasing and decreasing the Yb abundance by 0.2 and 0.4 dex, respectively.

Table 2. Spectral line data for the line used to determine Yb abundances and nearby molecular lines, as well as the Ce II lines used to measure Ce.

	λ_{air} (Å)	log(gf)	E_{low} (eV)	Reference
CN	16 496.815	−1.584	1.307	S14
OH	16 497.737	−5.448	1.266	B16
OH	16 497.979	−5.448	1.266	B16
CO	16 498.273	−5.606	1.847	L15
Yb II	16 498.420	−0.640	3.017	B98
Ni I	16 499.131	−1.363	6.257	K08
Ce II	16 595.180	−2.114	0.122	C73
Ce II	17 058.880	−1.425	0.318	C73

Notes. The log (gf) values for the Ni I and Ce II lines are the ones measured in this study. The Ce II line at 16 595 Å was also measured astrophysically by Cunha et al. (2017), the $\Delta \log(gf) = 0.076$.
References. S14: Sneden et al. (2014), B16: Brooke et al. (2016), L15: Li et al. (2015), B98: Biémont et al. (1998), K08: Kurucz (2008), C73: Corliss (1973).

significant contribution from an OH doublet for cooler, low-metallicity stars.

The strength of the CO blend presents the largest obstacle to measuring the Yb abundance in our stars. To make sure that the CO lines are properly modelled, the fit of nearby CO lines was inspected. From this inspection, it became evident that the fit between the observed and the synthesised spectra is dependent not only on the species of the lines, but also on the vibrational and rotational state of the CO molecule. The CO line at 16 498 Å is caused by a 7-4 vibrational, R 59 rotational transition. Several other lines from this vibrational state can be seen in Fig. 1. Lines from lower rotational transitions, such as the 7-4 R 6 line at 16 503.4 Å, appear to be too weak, while the more highly excited 7-4 R 58 line at 16 490.5 Å appears to fit the observed spectra well. The reason for this discrepancy is likely related to the atmospheric depth where the lines form: lines with lower excitation energies form farther out, where the modelling of the atmosphere is less certain and 3D and non-LTE effects may play a large role.

Figure 2 shows CO lines from vibrational-rotational transitions similar to the CO line blending the Yb II line. As these lines should form in a similar way and the line-to-line strength differences are very accurately understood, the fit between them and the spectra should act as a proxy for evaluating the modelling of the Yb-blending CO line. Because of issues with blending, the quality of the fit is not always clear, although the lack of major discrepancies reassures us that the CO line of interest should not spoil the measurement of Yb.

The OH lines are less disruptive for the majority of the stars as the lines are generally weaker and farther to the blue side of the Yb II line. The low excitation energies of the lines make their strengths inversely dependent on temperature and move their formation farther out into the atmosphere, increasing the risk of modelling errors due to, for example, 3D effects. The strong oxygen enhancement for metal-poor stars further increases their strength relative to other lines, which in combination with a low

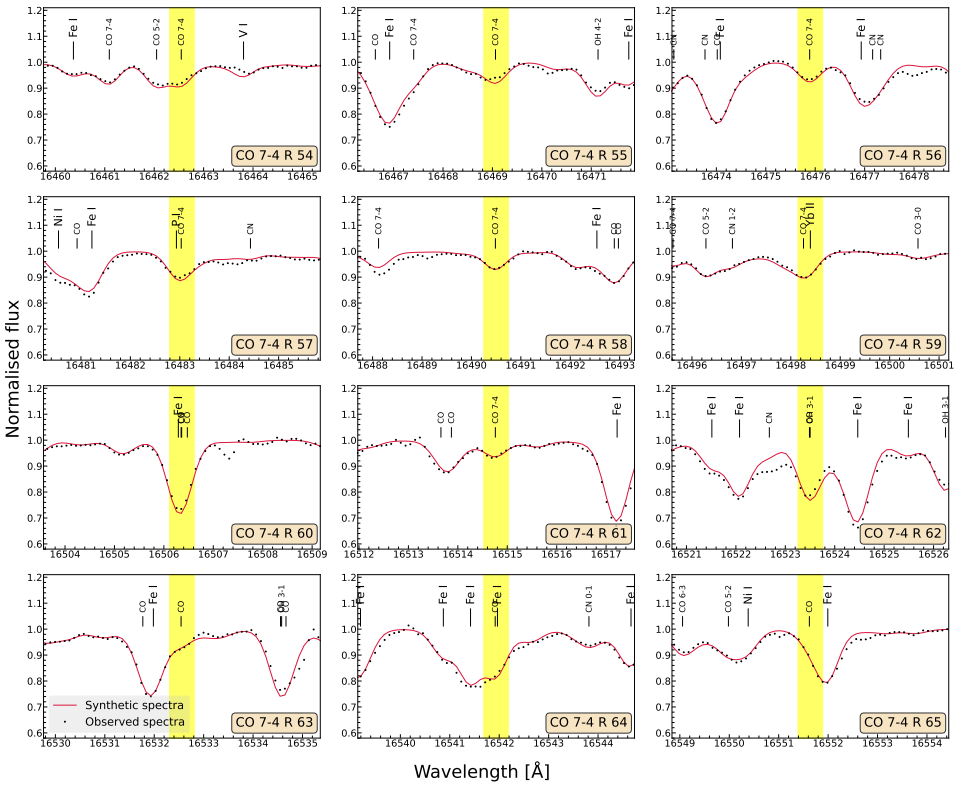

Fig. 2. Comparison between the observed and the synthesised spectra for the star KIC 5779724 around the CO 7-4 lines with rotational transitions between R 54 and R 65. The line blending the Yb II line is from the CO 7-4 R 59 transition. Details of the observation are listed in Table 1, and the parameters and stellar abundances are listed in Table 3.

$T_{\rm eff}$ can make the OH lines equal to the CO line in strength and significantly disrupt the Yb II line. The placement of the line mask and the visual inspection of the fit are therefore critical for measuring Yb in metal-poor stars with $T_{\rm eff} < 4300$ K. A nearby CN line at 16 496.8 Å may be a blending factor at lower resolutions but does not influence the Yb II line in the spectra studied in this paper.

3.6. Uncertainty analysis

3.6.1. Systematic uncertainties

The main sources of systematic uncertainty in abundance measurements are errors in stellar parameters and atomic data as well as assumptions made in the model atmosphere. As described in Sect. 3.1, the stellar parameters derived by Jönsson et al. (in prep.) are believed to be both precise and accurate, based on comparisons to benchmark values for $T_{\rm eff}$ and $\log(g)$ from angular diameter and asteroseismological measurements. Assessing whether there is a bias in the elemental abundances due to stellar parameters is sometimes done by plotting them against one another. This validation cannot be performed for this study, as there is an observational bias in our sample. Low-metallicity stars are often farther away; when such stars are observed with the optical 2.5 m NOT/FIES telescope/high resolution spectrograph combination, the metal-poor targets tend to have lower surface gravities and temperatures.

Non-LTE corrections have not been computed for Yb, and as such their impact cannot be quantified. As all stars have similar temperatures and surface gravities ($T_{\rm eff\,mean} = 4520 \pm 250$ K, $\log(g)_{\rm mean} = 2.2 \pm 0.5$), we would expect possible non-LTE effects to have a small impact on the shape of the [Yb/Fe] versus [Fe/H] trend.

There are seven stable isotopes of Yb, two of which have hyperfine structure splitting. Both the isotope shifts and the hyperfine structure splitting have been assessed for the resonance lines of Yb (e.g. Mårtensson-Pendrill et al. 1994), but no information is available for the 16 498 Å line. No sign of additional broadening from such factors has been seen in the spectra.

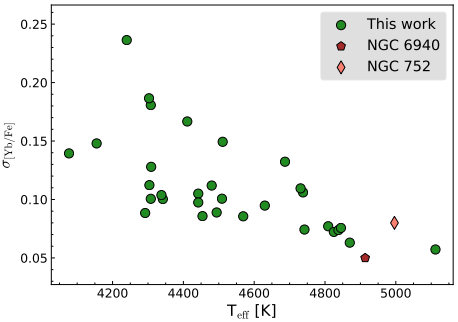

Fig. 3. Random uncertainties calculated as described in Sect. 3.6.2 plotted against the $T_{\rm eff}$ of the stars. The mean temperature and spread in Yb abundance for NGC 6940 and NGC 752 (Böcek Topcu et al. 2019, 2020) are also marked as a comparison.

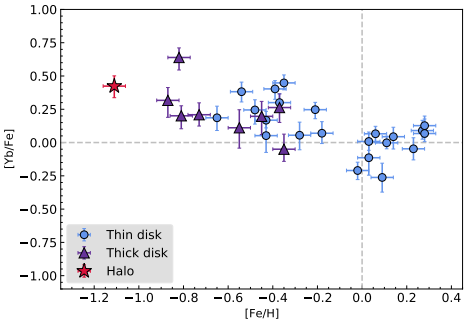

Fig. 4. Ytterbium abundances derived in this work. A division into thin disk, thick disk, and halo stars has been made based on [Mg/Fe] abundances and the kinematics of the stars (see text). The error bars reflect the first and third quartiles from the Monte Carlo uncertainty estimates presented in Sect. 3.6 along with a 0.05 dex uncertainty in [Fe/H].

3.6.2. Random uncertainties

To estimate the uncertainties in the abundance measurements stemming from random uncertainties in the stellar parameters, a Monte Carlo technique was used. For each star, the spectra were reanalysed 500 times using parameters drawn from normal distributions, with the adopted values of $T_{\rm eff}$, log(g), [Fe/H], $\xi_{\rm micro}$, and [C/Fe] taken as the mean of the distribution and the measurement uncertainty used as the standard deviation. The adapted uncertainties are 50 K in $T_{\rm eff}$, 0.1 dex in log(g), 0.05 dex in [Fe/H], 0.1 km s^{-1} in $\xi_{\rm micro}$, and 0.05 dex in [C/Fe]. Varying these parameters gives a good measure of the uncertainty in the analysis of the Yb II line itself as well as the uncertainty introduced by the blending lines. The mean average deviation of the Yb measurements performed with the varied stellar parameters was then adopted as the uncertainty in [Yb/Fe]. In Sect. 4 the upper and lower quantiles are used to create error bars for the measurement of each star.

The mean random uncertainty for our entire sample is 0.11 dex, which is slightly larger than the spread in Yb abundance measured for the open clusters NGC 6940 and NGC 752 of 0.05–0.08 dex (Böcek Topcu et al. 2019, 2020). The larger uncertainty in our study is possibly caused by a lower mean temperature in the stars studied here, increasing the influence of the molecular blends. Figure 3 provides support for this view, showing the calculated uncertainties for Yb plotted against $T_{\rm eff}$. A clear trend can be seen with large uncertainties for cooler stars and smaller values for the hotter stars, matching the results for the open clusters.

The star HD 102328 has been observed twice, allowing us to estimate the effect of random errors unrelated to stellar parameters, such as S/N and continuum determination. The difference in [Yb/Fe] between the two spectra is 0.06 dex, which matches the spread of 0.05–0.08 from Böcek Topcu et al. (2019, 2020) well. It should be noted that the difference in S/N between the spectra is sizeable (125 and 250) and likely contributes a significant part to the difference between the measurements.

4. Results and discussion

The Yb abundances derived in this work are presented in Table 3 and are shown in Fig. 4 as [Yb/Fe] versus [Fe/H]. In the figure the error bars are based on the first and third quartiles in the uncertainty calculations described in Sect. 3.6.2.

The spread in abundance that we see in our study is more likely to be the result of uncertainties in the analysis rather than a large cosmic spread in Yb abundances. The error bars represent the uncertainty from stellar parameters only, with factors such as continuum determination and errors in molecular line modelling not included.

To put these results in context, Fig. 5 shows our results together with previously published Yb measurements. The lack of a larger sample of measurements for [Fe/H] > -1 illustrates the historic difficulty in determining Yb abundances for higher-metallicity stars using the resonance lines in the UV. Validating that similar abundances are obtained with the infrared line used here and the resonance lines is not trivial, since the line we use is weak and thus ill-suited for studying metal-poor stars.

It may be possible to observe both lines for a portion of the sample in Fig. 5, the very metal-poor stars with [Fe/H] < -2 and [Yb/Fe] > 1. The low metallicity would reduce the blending in the near-UV while the high [Yb/Fe] enhancement would strengthen the H band line enough to be observable. Such stars typically have a high enhancement in carbon, which, depending on the $T_{\rm eff}$, may cause blending issues in the infrared, even for such metal-poor stars. A high resolution and S/N would be required to resolve the line, similar to in this study.

The high scatter at lower metallicities, below [Fe/H] < -2, in Fig. 5 does not solely originate from the uncertainties, which, according to the sources, span from 0.1 to 0.25 dex. It is instead a physical result of inhomogeneities in the Galactic interstellar medium at low metallicity combined with the fact that neutron-star mergers and the types of SNe (likely MRSNe; Kobayashi et al. 2020) that host the r-process are rare, which creates isolated stellar groups of high and low r-process element abundances (see Sneden et al. 2008, and references therein). This behaviour of an r-process-dominated element at low metallicities has been reproduced in the stochastic chemical evolution models in Cescutti et al. (2015), which take inhomogeneous mixing into account. As we can see in this work in Fig. 5, the scatter decreases substantially at higher metallicities, a result of a more homogeneous stellar disk and regular enrichment.

Table 3. Programme stars observed with IGRINS.

Star	$T_{\rm eff}$ (K)	log(g) (dex)	[Fe/H] (dex)	$\xi_{\rm micro}$ (km s^{-1})	Distance (pc)	Stellar pop.	S/N	[Yb/Fe] (dex)	[Eu/Fe] [b] (dex)	[Ce/Fe] (dex)
α Boo	4308	1.7	−0.56	1.8	...	Thick	155	0.111	0.317	−0.293
μ Leo	4494	2.5	0.29	1.5	...	Thin	169	0.090	0.034	−0.283
ϵ Vir	5112	3.0	0.15	1.6	...	Thin	299	−0.002	...	0.012
β Gem	4809	2.8	0.00	1.4	...	Thin	336	−0.210	0.016	−0.101
HD 102328	4442	2.5	0.30	1.5	70 ± 1	Thin	250	0.068	−0.027	−0.218
HD 102328 [a]	4442	2.5	0.28	1.5	68 ± 1	Thin	125	0.127	−0.027	−0.223
HIP 50583	4292	1.7	−0.49	1.7	...	Thin	86	0.382	0.193	0.020
HIP 63432	4155	1.3	−0.65	1.9	199 ± 4	Thick	275	0.317	0.292	−0.039
HIP 72012	4077	1.4	−0.19	1.5	196 ± 3	Thin	286	0.055	0.182	−0.123
HIP 90344	4454	2.2	−0.37	1.4	91 ± 1	Thin	283	0.403	0.223	0.013
HIP 96014	4240	1.6	−0.35	1.7	139 ± 2	Thin	414	0.052	0.086	−0.149
HIP 102488	4742	2.5	−0.16	1.6	...	Thin	343	0.247	0.137	−0.100
2M17215666	4342	1.6	−1.10	1.7	1900 ± 200	Halo, s−rich	165	0.424	0.511	0.207
KIC 3748585	4569	2.6	0.08	1.3	360 ± 10	Thin	205	0.008	−0.037	−0.105
KIC 3955590	4411	2.2	0.06	1.6	950 ± 50	Thin	140	−0.114	−0.079	−0.232
KIC 4177025	4309	1.7	−0.43	1.6	1200 ± 80	Thick	185	0.263	0.607	−0.254
KIC 5113910	4338	1.7	−0.37	1.6	1900 ± 200	Thin	183	0.245	0.122	−0.040
KIC 5709564	4687	2.2	−0.35	1.7	640 ± 20	Thick	137	−0.050	0.406	−0.330
KIC 5779724	4303	1.6	−0.48	1.7	1500 ± 100	Thick	215	0.197	0.417	−0.225
KIC 5859492	4511	2.4	0.14	1.5	780 ± 30	Thin	181	−0.262	0.030	−0.288
KIC 5900096	4480	2.5	0.22	1.5	313 ± 6	Thin	179	−0.047	0.071	−0.210
KIC 6465075	4825	2.8	−0.28	1.3	550 ± 20	Thin	146	0.300	0.169	0.071
KIC 6547007	4738	2.4	−0.72	1.4	750 ± 30	Thick	281	0.201	0.397	−0.149
KIC 6837256	4731	2.3	−0.68	1.5	1250 ± 60	Thick	148	0.209	0.306	−0.226
KIC 11045542	4304	1.6	−0.52	1.5	1900 ± 200	Thin	294	0.186	0.085	−0.201
KIC 11342694	4509	2.8	0.21	1.3	440 ± 10	Thin	139	0.044	0.044	−0.118
KIC 11444313	4630	2.3	−0.09	1.5	1400 ± 80	Thin	160	0.070	0.146	−0.144
KIC 11569659	4838	2.4	−0.33	1.6	1510 ± 80	Thin	246	0.168	0.162	−0.061
KIC 11657684	4870	2.6	−0.26	1.5	1700 ± 100	Thin, s-rich	184	0.448	0.096	0.351
2M14231899	4308	1.8	−0.77	1.6	1900 ± 300	Thick, s-rich	284	0.639	0.547	0.179
HD 142091 [a]	4845	3.3	0.06	1.2	30 ± 0.1	Thin	223	0.066	...	−0.217

Notes. The [Yb/Fe] and [Ce/Fe] abundances were determined in this work, whilst the [Eu/Fe] abundances are the ones from Forsberg et al. (2019). The distances are from McMillan (2018). The stellar parameters and classification into different stellar populations are determined in Jönsson et al. (in prep.) (see our Sects. 3.1 and 3.2). The S/N is determined using the code DER_SNR (Stoehr et al. 2008) applied to a set of continuum regions in the H band. We use A(Fe)$_\odot$ = 7.45, A(Yb)$_\odot$ = 1.08 (Grevesse et al. 2007) and A(Ce)$_\odot$ = 1.58, A(Eu)$_\odot$ = 0.52 (Grevesse et al. 2015). [a]Data from the IGRINS Spectral Library (Park et al. 2018) [b]The [Eu/Fe] values in Forsberg et al. (2019) are reported to be systematically too high, possibly originating from systematic uncertainties in log(g) as reported in Jönsson et al. (2017). We lower all these abundances by 0.10 dex both in this table and in subsequent figures, such that the overall thin disk in [Eu/Fe] goes through the solar value, as seen in Fig. 6.

The [Yb/Fe] trend with metallicity shows an enhancement in [Yb/Fe] for stars of subsolar metallicity, decreasing to solar values around solar metallicity, similar to elements produced in type II SNe (for example, the α elements), MRSNe, and likely neutron-star mergers (r-process; Cescutti et al. 2015; Grisoni et al. 2020; Kobayashi et al. 2020). The similarity of α- and r-process elemental trends originates from the timescales related to their formation, being a rapid and early onset of the enrichment of these elements in the Galaxy.

At super-solar metallicity the trend appears to flatten, with the exception of the highest-metallicity stars. The systematic uncertainties involved in determining abundances for these stars are likely to be high, so we draw no conclusions on the precise slope of the super-solar trend.

To ensure that the Yb abundances are in line with what is expected for neutron-capture elements and to examine the contribution from different production channels, we compared the [Yb/Fe] trend with those of [Ce/Fe] and [Eu/Fe] for the same stars. The Ce abundances were determined from the IGRINS spectra, as described in Sect. 3.2, while the Eu abundances are from the optical work in Forsberg et al. (2019), which has a 28 stellar overlap with our sample. The very tight abundance trend for Eu indicates a high precision in the analysis. The Eu abundances were determined using a similar method, although not the exact same stellar parameters. Nevertheless, this should limit systematic uncertainties in the comparison.

Since Yb is reported to have a contribution of somewhere between 40/60 and 50/50% from the s- and r-processes, respectively (e.g. Bisterzo et al. 2014; Kobayashi et al. 2020; Prantzos et al. 2020), the [Yb/Fe] trend should fit in between the s- and r-process trends of [Ce/Fe] and [Eu/Fe]. In Fig. 6, we plot running means of the full sample, the components of the disk and the s-enhanced stars for the neutron-capture elements. As can be seen, Yb indeed falls nicely in between the two comparison elements.

In Fig. 6 we see that the [Yb/Fe] trend with metallicity has a similar slope as [Eu/Fe], indicating an early enrichment from

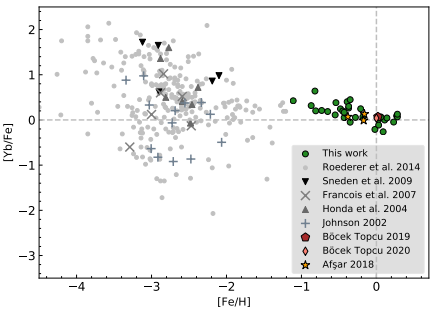

Fig. 5. [Yb/Fe] abundances determined in this work (green) compared to previous work. The studies of halo stars are indicated in various shades of grey: Honda et al. (2004), Johnson (2002), François et al. (2007), Roederer et al. (2014a,b), and Sneden et al. (2009). The uncertainties for these works are typically 0.10–0.25 dex. The two open clusters in Böcek Topcu et al. (2019, 2020), namely NGC 752 and NGC 6940, are indicated in red and pink using their mean abundance and consist of 10 and 11 stars, respectively. The measured spread in [Yb/Fe] for these clusters is 0.05 and 0.08. The horizontal-branch stars in Afşar et al. (2018) are indicted in yellow.

processes with short timescales. This is indicative of type II SNe, MRSNe, and possibly neutron-star mergers (Cescutti et al. 2015; Grisoni et al. 2020; Kobayashi et al. 2020)[4].

The [Ce/Fe] trend is much flatter than the [Yb/Fe] trend, although the thick disk s-enhanced star, marked with a yellow triangle in Fig. 6, clearly stands out in [Yb/Fe]. The other two s-enhanced stars (halo and thin disk, yellow star and filled circle, respectively) stand out too, but not to the same extent. This is expected since these two do not stand out as much in [Eu/Fe] either, once more highlighting the similarity between these two *r*-process-dominated elements. However, the fact that the s-enriched stars also show a similar pattern in [Yb/Fe] compared to [Ce,Eu/Fe] is a consequence of the precision in the determination of the Yb abundances and, to a lesser extent, of the *s*-process contribution to this element.

We can also consider the relative positions of the abundance ratios of the thin- and thick-disk stars in Fig. 6. The thick-disk stars (purple triangles) have lower [Ce/Fe] abundance ratios and higher [Eu/Fe] than what is typical for thin-disk stars (blue filled circles), as expected for *s*- and *r*-process-dominated elements (Forsberg et al. 2019). The [Yb/Fe] abundance ratios of the thick-disk stars are also found to be lower, although only slightly, than those of the thin-disk stars. This is a clear indication of the *s*-process contribution to this element. At the same time, the shape of the overall [Yb/Fe] trend, seen from the running mean, gives a clear indication of the *r*-process contribution, as expected from Galactic chemical evolution models of this ratio. Nonetheless, Kobayashi et al. (2020) report that the *s*-process has a significant contribution in producing Yb.

To further investigate the contribution from the *s*- and *r*-processes, we plotted [Yb/Ce] and [Yb/Eu] versus metallicity (see Fig. 7). A flat trend in these types of plots indicates a similar production rate of the two elements, whereas a decrease or increase indicates discrepancies.

[4] However, also see the discussion in Skúladóttir & Salvadori (2020) on the twofold timescales of the *r*-process originating from a joint contribution from SNe and neutron-star mergers.

The so-called pure *r*-process line is also indicated in the plot, which is calculated using the solar *r*-process contributions of the elements. As such, the pure *r*-process is the value of the *r*-process contribution in both elements, for instance [*r*-process(Yb)/*r*-process(Ce)]. The closer to the pure-*r*-process line, the more of the elements originate from the *r*-process.

Considering [Yb/Ce] in Fig. 7, it becomes clear that the *r*-process component is stronger in Yb than in Ce. The *r*-process dominates the production of neutron-capture elements at lower metallicities, also producing the *s*-process-dominated elements, such as Ce and, to a greater extent, Yb. The onset of s-production in AGB stars, originating from low- to intermediate-mass stars, has a time delay in enriching the Galactic interstellar medium. This can be seen at around [Fe/H] approximately −0.3, where the [Yb/Ce] trend starts decreasing due to an increase in *s*-process production and a higher Ce enrichment compared to Yb.

The [Yb/Eu] trend clearly indicates a significant contribution from the *r*-process in the production of Yb, similar to what is seen when comparing the trends in Fig. 6. We also note that the thick-disk stars tend to all lie around the pure *r*-process line, indicating a large *r*-process contribution in the thick disk.

Because of potential issues with finding local continuum points and the risk of stronger molecular blends for super-solar metallicities, we refrain from drawing any conclusion about the possible upturns we see in this metallicity region. Hotter stars with less significant molecular blends could possibly clarify the trend for these metallicities.

The above comparisons with other neutron-capture elements strengthen the validity of the Yb abundances presented in this work and assure us that we can correctly model the CO blend in the Yb II line.

5. Conclusions

In this work we have presented Yb abundances for 30 K giants, with metallicities in the $-1.1 < [Fe/H] < 0.3$ range, which, to the best of our knowledge, is the largest disk sample with Yb abundances to date. Our typical (random) uncertainties in [Yb/Fe] are approximately 0.1 dex.

The derived abundances align well with previous studies of low-metallicity stars. Although the Yb II line is not useful in the solar spectrum at this resolution, the measured trend obtained from abundance determinations in our K giants passes through the solar value at [0,0], which is reassuring. Via comparisons with the abundances of two other neutron-capture elements, namely Ce and Eu, we find the cosmic origin of Yb to be dominated by the *r*-process, which is supported by the [Yb/Eu] comparison. It is, however, clear from the s-enhanced stars and the precise alignment between the thin and thick disk that the *s*-process plays a part in producing Yb, as expected from theoretical models. Additionally, we find the Yb abundances to be of high quality since they reproduce the s-enhancement previously observed for the same stars in optical spectra, confirming that the CO blend in the Yb II line is modelled properly.

Previous measurements of neutron-capture elements in stars from the infrared *H* and *K* bands are dominated by Ce, which has a number of usable lines (Cunha et al. 2017). Two other elements have been measured in small samples, Yb and Nd (Hasselquist et al. 2016). Like Ce, Nd is thought to be produced predominately in the *s*-process for stars of solar metallicity (see e.g. Kobayashi et al. 2020), but at a higher uncertainty (Böcek Topcu et al. 2019, 2020).

Elements created in the *r*-process offer clear signatures of events that led to element formation on short timescales, such

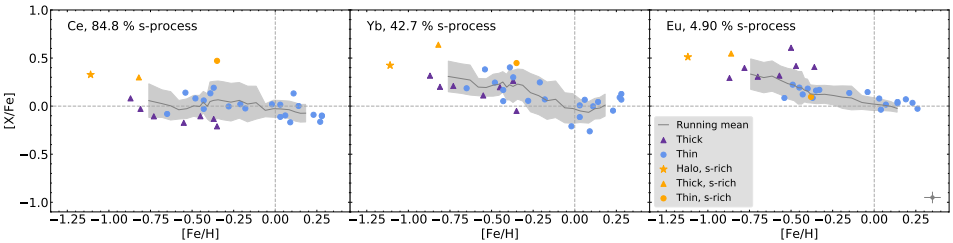

Fig. 6. Comparison between the [Ce/Fe] (*left*) and [Yb/Fe] abundances (*middle*) derived in this work and [Eu/Fe] abundances (*right*) from Forsberg et al. (2019). The stellar populations are indicated by colour and shape (see the legend), with the *s*-process-enhanced stars in yellow. The percentage of contribution from the *s*-process from Prantzos et al. (2020) is indicated in the top-left corner of each plot. The running mean with a 1σ error (grey) has a running box with a size of eight stars, roughly 25% of the sample size. In the lower-right corner of the [Eu/Fe] plot, the typical uncertainty from Forsberg et al. (2019) is indicated. Dashed grey lines going through [0,0] indicate the solar value.

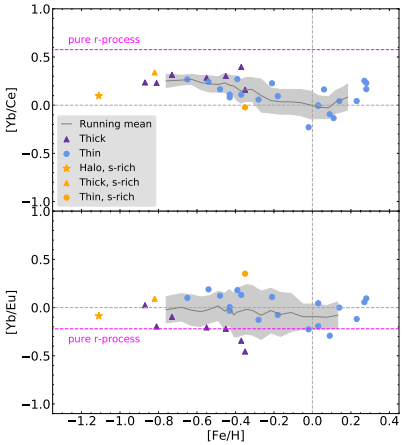

Fig. 7. [Yb/Ce] (*top*) and [Yb/Eu] (*bottom*) plotted towards [Fe/H]. The notation is similar to that in Fig. 6, and [Eu/Fe] abundances originate from Forsberg et al. (2019). The pure-*r*-process (solar) contributions, indicated in dashed magenta, were calculated using the values in Prantzos et al. (2020), as indicated in Fig. 6.

as neutron-star mergers. The ability to determine abundances of the *r*-process-dominated element Yb from near-infrared spectra for a wide range of metallicities up to super-solar values opens an additional Galactic chemical evolution channel from near-infrared spectra. This is significant both for the readily available near-infrared spectrographs and upcoming versatile instruments, such as the HIRES spectrograph for the ELT (Marconi et al. 2018).

Regarding the usefulness of having a wide range of neutron-capture elements in galactochemical research, we can consider our comparison of Yb to Ce and Eu: it becomes evident that the thick disk has a stronger enrichment by the *r*-process compared to the thin disk. The reverse holds for the thin disk, being more enriched by the *s*-process compared to the thick disk.

We have shown that with high enough spectral resolution and a careful analysis, the territory of the *r*-process can thus now be reached in the near-infrared. This will help to unravel regions previously obscured by dust, such as the Milky Way bulge. For future large near-infrared spectroscopic surveys, the Yb II line could therefore allow the *r*-process to also be studied in obscured stellar populations. Here, Yb can contribute a lot in deciphering the star formation history and assembly of the bulge.

Acknowledgements. M.M. acknowledges funding through VIDI grant "Pushing Galactic Archaeology to its limits" VI.Vidi.193.093, which is funded by the Dutch Research Council (NWO). R.F's and A.J's research is supported by the Göran Gustafsson Foundation for Research in Natural Sciences and Medicine. R.F. and N.R. acknowledge support from the Royal Physiographic Society in Lund through the Stiftelse Walter Gyllenbergs fond and Märta och Erik Holmbergs donation. This work used the Immersion Grating Infrared Spectrometer (IGRINS) that was developed under a collaboration between the University of Texas at Austin and the Korea Astronomy and Space Science Institute (KASI) with the financial support of the Mt. Cuba Astronomical Foundation, of the US National Science Foundation under grants AST-1229522 and AST-1702267, of the McDonald Observatory of the University of Texas at Austin, of the Korean GMT Project of KASI, and Gemini Observatory. These results made use of the Lowell Discovery Telescope (LDT) at Lowell Observatory. Lowell is a private, non-profit institution dedicated to astrophysical research and public appreciation of astronomy and operates the LDT in partnership with Boston University, the University of Maryland, the University of Toledo, Northern Arizona University and Yale University. This paper includes data taken at The McDonald Observatory of The University of Texas at Austin. This work has made use of the VALD database, operated at Uppsala University, the Institute of Astronomy RAS in Moscow, and the University of Vienna.

References

Abbott, B. P., Abbott, R., Abbott, T. D., et al. 2017, Phys. Rev. Lett., 119, 161101
Abdurro'uf, Accetta, K., Aerts, C., et al. 2022, ApJS, 259, 35
Afşar, M., Sneden, C., Wood, M. P., et al. 2018, ApJ, 865, 44
Biémont, E., Dutrieux, J.-F., Martin, I., & Quinet, P. 1998, J. Phys. B Atm. Mol. Opti. Phys., 31, 3321
Bisterzo, S., Travaglio, C., Gallino, R., Wiescher, M., & Käppeler, F. 2014, ApJ, 787, 10
Bland-Hawthorn, J., & Gerhard, O. 2016, ARA&A, 54, 529
Böcek Topcu, G., Afşar, M., Sneden, C., et al. 2019, MNRAS, 485, 4625
Böcek Topcu, G., Afşar, M., Sneden, C., et al. 2020, MNRAS, 491, 544
Brooke, J. S. A., Bernath, P. F., Western, C. M., et al. 2016, J. Quant. Spec. Rad. Transf., 168, 142
Burbidge, E. M., Burbidge, G. R., Fowler, W. A., & Hoyle, F. 1957, Rev. Mod. Phys., 29, 547
Busso, M., Gallino, R., & Wasserburg, G. J. 1999, ARA&A, 37, 239
Cescutti, G., Romano, D., Matteucci, F., Chiappini, C., & Hirschi, R. 2015, A&A, 577, A139
Corliss, C. H. 1973, J. Res. Natl. Bur. Stand. Sect. A, Phys. Chem., 77A, 419
Cowan, R. D. 1981, The Theory of Atomic Structure and Spectra, Los Alamos Series in Basic and Applied Sciences (Berkeley: University of California Press)

Cowley, C. R. 1984, Phys. Scrip. Vol. T, 8, 28
Cunha, K., Smith, V. V., Hasselquist, S., et al. 2017, ApJ, 844, 145
Drout, M. R., Piro, A. L., Shappee, B. J., et al. 2017, Science, 358, 1570
Forsberg, R., Jönsson, H., Ryde, N., & Matteucci, F. 2019, A&A, 631, A113
François, P., Depagne, E., Hill, V., et al. 2007, A&A, 476, 935
Grevesse, N., Asplund, M., & Sauval, A. J. 2007, Space Sci. Rev., 130, 105
Grevesse, N., Scott, P., Asplund, M., & Sauval, A. J. 2015, A&A, 573, A27
Grisoni, V., Cescutti, G., Matteucci, F., et al. 2020, MNRAS, 492, 2828
Gustafsson, B., Edvardsson, B., Eriksson, K., et al. 2008, A&A, 486, 951
Hasselquist, S., Shetrone, M., Cunha, K., et al. 2016, ApJ, 833, 81
Hawkins, K., Masseron, T., Jofré, P., et al. 2016, A&A, 594, A43
Honda, S., Aoki, W., Kajino, T., et al. 2004, ApJ, 607, 474
Humphreys, C. J., & Paul, E. J. 1959, Infrared atomic spectra, Technical Report 1, Naval Ordnance Lab., Corona, Calif.
Johnson, J. A. 2002, ApJS, 139, 219
Jönsson, H., Ryde, N., Nordlander, T., et al. 2017, A&A, 598, A100
Karakas, A. I., & Lattanzio, J. C. 2014, PASA, 31, e030
Kobayashi, C., Karakas, A. I., & Lugaro, M. 2020, ApJ, 900, 179
Kratz, K.-L., Farouqi, K., Pfeiffer, B., et al. 2007, ApJ, 662, 39
Kurucz, R. L. 2008, Robert L. Kurucz on-line Database of Observed and Predicted Atomic Transitions (Cambridge, Mass.: Smithsonian Astrophysical Observatory)
Lee, J.-J., Gullikson, K., & Kaplan, K. 2017, https://doi.org/10.5281/zenodo.845059
Li, G., Gordon, I. E., Rothman, L. S., et al. 2015, ApJS, 216, 15
Lomaeva, M., Jönsson, H., Ryde, N., Schultheis, M., & Thorsbro, B. 2019, A&A, 625, A141
Mace, G., Kim, H., Jaffe, D. T., et al. 2016, SPIE Conf. Ser., 9908, 99080C
Mace, G., Sokal, K., Lee, J.-J., et al. 2018, SPIE Conf. Ser., 10702, 107020Q
Majewski, S. R., Schiavon, R. P., Frinchaboy, P. M., et al. 2017, AJ, 154, 94
Marconi, A., Prieto, C. A., Amado, P. J., et al. 2018, SPIE, 10702, 619
McMillan, P. J. 2018, Res. Notes Am. Astron. Soc., 2, 51
Mårtensson-Pendrill, A.-M., Gough, D., & Hannaford, P. 1994, Phys. Rev. A, 49, 3351
Olmschenk, S., Hayes, D., Matsukevich, D., et al. 2009, Phys. Rev. A, 80
Park, C., Jaffe, D. T., Yuk, I.-S., et al. 2014, SPIE Conf. Ser., 9147, 91471D
Park, S., Lee, J.-E., Kang, W., et al. 2018, ApJS, 238, 29
Piskunov, N., & Valenti, J. A. 2017, A&A 597, A16
Prantzos, N., Abia, C., Cristallo, S., Limongi, M., & Chieffi, A. 2020, MNRAS, 491, 1832
Roederer, I. U., Preston, G. W., Thompson, I. B., et al. 2014a, AJ, 147, 136
Roederer, I. U., Schatz, H., Lawler, J. E., et al. 2014b, ApJ, 791, 32
Ryabchikova, T., Piskunov, N., Kurucz, R. L., et al. 2015, Phys. Scr, 90, 054005
Skúladóttir, Á., & Salvadori, S. 2020, A&A, 634, L2
Smith, V. V., Bizyaev, D., Cunha, K., et al. 2021, AJ, 161, 254
Sneden, C., Cowan, J. J., & Gallino, R. 2008, ARA&A, 46, 241
Sneden, C., Lawler, J. E., Cowan, J. J., Ivans, I. I., & Den Hartog, E. A. 2009, ApJS, 182, 80
Sneden, C., Lucatello, S., Ram, R. S., Brooke, J. S. A., & Bernath, P. 2014, ApJS, 214, 26
Stoehr, F., White, R., Smith, M., et al. 2008, ASP Conf. Ser., 394, 505
Tanvir, N. R., Levan, A. J., González-Fernández, C., et al. 2017, ApJ, 848, L27
Telting, J. H., Avila, G., Buchhave, L., et al. 2014, Astron. Nachr., 335, 41
Tody, D. 1993, ASP Conf. Ser., 52, 173
Valenti, J. A., & Piskunov, N. 1996, A&AS, 118, 595
Yuk, I.-S., Jaffe, D. T., Barnes, S., et al. 2010, SPIE Conf. Ser., 7735, 7735E

Printed by Media-Tryck, Lund 2023 NORDIC SWAN ECOLABEL 3041 0903

The Milky Way as seen through Neutron-Capture Elements

Through stars, the formation and evolution of the Milky Way goes hand-in-hand with the cosmic origin of the elements. As stars form, they carry chemical fingerprints of their birthclouds, providing us with chemical timestamps of the ancient Galaxy. This doctoral thesis presents studies of neutron-capture elements in red giant stars found in the most stellar rich parts of the Milky Way – the bulge and disk. The aim is to provide clues to help disentangle both the origin of heavy elements and the history of the Milky Way.

REBECCA FORSBERG, originally from Stockholm, started her studies of physics and astronomy at Lund University in 2014. Over the course of her time in Lund, she has found a strong passion both for the cosmic origin of elements, the Milky Way and its stars, as well as for science writing and communication, gardening, bikepacking, and long-distance running.

LUND UNIVERSITY

Faculty of Science
Department of Physics
Division of Astrophysics
Lund Observatory

ISBN 978-91-8039-715-5